THE UNIVERSITY OF SYDNEY

COPYRIGHT AND USE OF THIS THESIS

TIME-DEPENDENT BEHAVIOUR OF CONCRETE-FILLED STEEL TUBULAR ARCH BRIDGES

BY

YUE GENG

B.Sc. (Civil Engineering), Harbin Institute of Technology – Harbin, China
M.Sc. (Structural Engineering), Harbin Institute of Technology –Harbin, China

A thesis submitted in fulfilment
of the requirements for the degree of Doctor of Philosophy
School of Civil Engineering
The University of Sydney
Australia

THE UNIVERSITY OF
SYDNEY

CERTIFICATE OF AUTHORSHIP/ORIGINATLITY

I certify that the work in this thesis has not previously been submitted for a degree nor has it been submitted as part of requirements for a degree except as fully acknowledged within the text.

I also certify that the thesis has been written by me. Any help that I have received in my research work and the preparation of the thesis itself has been acknowledged. In addition, I certify that all information sources and literature used are indicated in the thesis.

Signed: Geng Yue (candidate) Date:.....

ABSTRACT

This thesis intends to formulate an accurate method of analysis to predict the long-term response of concrete filled steel tubular (CFST) arch bridges and to define a reliable simplified method to be used in routine design. It also aims at providing a better understanding of the occurrence of lateral creep buckling for CFST parabolic arches.

As part of this work, long-term experiments were conducted to investigate the creep and shrinkage behaviour of expansive concrete sealed inside steel tubes. For this purpose, eleven specimens were subjected to different levels of sustained axial loads applied at different ages of concrete. At the completion of the long-term experiments, specimens were tested to failure to evaluate how time effects influenced their ultimate response. The role of confinement at service load levels was then discussed based on the experimental measurements.

A comparative study was carried out to specify a suitable concrete model using available long-term tests for benchmarking purposes. The considered concrete models included the EC2 model, the AFREM model, the MC90 model and the B3 model. An extensive parametric study was then performed to evaluate the influence of time effects on the static response of CFST members with cross-sectional properties commonly used in real bridge applications. Different algebraic methods (i.e., the effective modulus method, the age-adjusted modulus method and the mean stress method) were applied to the long-term modelling of CFST members and their accuracy was investigated.

An accurate method was developed with the commercial finite element software ABAQUS to analyze the long-term response of CFST arch bridges. The method can account for the construction process, time effects, geometric nonlinearity and the ageing of the concrete. The method was validated using a representative bridge and the numerical results were benchmarked against real site measurements. As part of this work, the necessity of considering the variation of the time of first loading was discussed, and the effects of considering the presence of quasi permanent live loads on the long-term response was evaluated. For design purposes, a simplified method was provided to predict the long-term response of CFST arch bridges accounting for the aging of the concrete and the construction process.

A parametric analysis was conducted on single parabolic arches with fixed ends and subjected to vertical uniformly distributed loads to investigate the prebuckling deformation induced by time effects on their flexural-torsional stability. Considered parameters included the concrete age at first loading, the duration of the sustained load, the concrete strength, the steel strength, the ratio of the steel area over the concrete area at the cross-section, the slenderness ratio, and the span-to-rise ratio on the creep buckling behaviour of CFST arches.

It was pointed out that time effects had a pronounced influence on the lateral stability of slender parabolic arches with low steel strength and high span-to-rise ratio which subjected to uniformly distributed loads applied at early concrete ages and sustained for a long period of time.

PREFACE

This thesis is submitted in fulfilment of the requirements for the degree of Doctor of Philosophy at the School of Civil Engineering, The University of Sydney, Australia. Some of the work described in this thesis has been supported by papers that have been accepted in or submitted to journals, or presented or accepted in conferences, viz.:

Journal Papers:

Yuyin Wang, **Yue Geng**, Gianluca Ranzi, Sumei Zhang. (2011). Time-dependent behaviour of expansive concrete-filled steel tubular columns. *Journal of Constructional Steel Research*. **67**, No. 3, 471-483

Yue Geng, Gianluca Ranzi, Yuyin Wang, and Sumei Zhang. Time-dependent behaviour of concrete-filled steel tubular columns: analytical and comparative study. *Magazine of Concrete Research*. (Accepted).

Yuyin Wang, **Yue Geng**, Sumei Zhang. Experimental Study on Time-Dependent Behaviour of Axially-Loaded Concrete-Filled Steel Tubular Stubs with Expansive Additive. *China Journal of Highway and Transport*. (Accepted). (in Chinese)

Yuyin Wang, **Yue Geng**, Sumei Zhang. Comparison on the Concrete Models and the Simplified Analysis Methods. *Journal of Tianjin University*. (Accepted). (in Chinese)

Xinrong Wu, **Yue Geng**, Yuyin Wang. Analysis on Creep Buckling of Concrete-Filled Steel Tubular Arches under Uniformly Distributed Loads. *Progress in Steel Building Structures*. (Accepted). (in Chinese)

Yuyin Wang, **Yue Geng**, Gianluca Ranzi, Sumei Zhang. Time-dependent analysis of concrete-filled steel tubular arch bridges accounting for the construction sequence. (In preparation.)

Conference Papers:

Yue Geng, Wenwen Xiao, Jiajia Guo. (2009). Experimental study on long-term axially loaded concrete-filled steel tubular stubs with expansive additive. *Journal of*

Harbin Institute of Technology. 41, No. suppl. 2, 226-231. (in Chinese)

Yue Geng, Gianluca Ranzi, Sumei Zhang, Yuyin Wang. (2008) Time-Dependent Behaviour of Concrete-Filled Steel Tubular Columns: A Comparative Study Using Different Concrete Models. *Proceedings of the 20th Australasian Conference on the Mechanics of Structures and Materials*, Toowoomba, Australia, 2008, p 697-702.

Yuyin Wang, **Yue Geng**, Sumei Zhang and Zhonghua Hui. (2007). New Construction Process of A Five-Span Tied Rigid Frame Concrete Filled Steel Tubular Arch Bridge. Proceedings of 8th Pacific Structural Steel Conference - Steel Structures in Natural Hazards, PSSC 2007, Wairakei, New Zealand, **1**, 85-90.

Sumei Zhang, **Yue Geng**, Xiaolu Wang. (2007). Simulation on the Whole Construction Process of the Five-span Tied Rigid-frame CFST Arch Bridge. *6th International Conference on Steel and Structural Engineering*. Oxford, UK.

ACKNOWLEDGEMENTS

The research reported in this thesis was funded by the National Natural Science Foundation of China (No. 50608023), by the School of Civil Engineering of the Harbin Institute of Technology, by the School of Civil Engineering of the University of Sydney and by the Centre for Advanced Structural Engineering from the University of Sydney, and their support is greatly acknowledged.

I would also like to gratefully acknowledge the enthusiastic supervision of Prof. Zhang Sumei, A/Prof. Gianluca Ranzi, and Prof. Wang Yuyin, for their continuing guidance, patience and encouragement during my doctoral study.

My special thanks go to Mr. Hui Zhonghua, Mr. Zhang Xin and other designers in the China Railway 13th Bureau Group Co. for their help on the collection of the designing information of the CFST arch bridges.

I would like to express my gratitude to all the postgraduates in the Research Center of Metal & Composite Structures in the Harbin Institute of Technology and those in the Blue Room at the University of Sydney for their helps, especially Wu Xinrong, Liu Changyong, Zhang Xi, Saffat Al-deen, and Thanh Bihn Nguyen.

I would like to thank all professors, colleagues and friends who assisted me along the way until this dissertation has been completed and whose contributions are too numerous and diverse to mention in a few short paragraphs.

Finally, I am very grateful to my parents for their supports, understanding, endless patience and encouragement throughout this entire journey.

Geng Yue

January, 2011

TABLE OF CONTENTS

LIST OF FIGURES

LIST OF TABLES

CHAPTER 1 INTRODUCTION

1.1 BACKGROUND

Concrete-filled steel tubes (CFST) are becoming a very popular structural solution for arch bridges because of their high compressive strength as well as efficiency in construction. Up to date, there are more than 300 CFST arch bridges built in the world, among which more than 80 have a span longer than 150 m. In this context, the time-dependent behaviour of the core concrete is required to be considered in the design of large span CFST arch bridges as it can significantly increase arch deflections, redistribute stresses between steel and core concrete, and even lead to possible instability problems.

Up to date, no design guidelines are available for the design of CFST arch bridges. Provisions available in design codes of composite buildings are not suitable for the loading of concrete at its early ages, which is usually the case during the construction of CFST arch bridges. The time-dependent behaviour of the concrete core sealed inside the steel tube makes the guidelines available for reinforced concrete bridges unsuitable for CFST arch bridges.

Researchers have been experimentally and numerically investigating the long-term behaviour of CFST specimens for decades, trying to define accurate concrete models and formulate appropriate analysis procedures to capture the creep and shrinkage behaviour of the core concrete. Despite the research work devoted in the past few decades to investigate the time-dependent response of CFST arches, the following areas still require further attention:

1) Though expansive concrete has been extensively used in recent years in large-span CFST arch bridge applications, only very limited research has focused on the time effects induced in expansive concrete filled steel tubes (ECFST), and the only available long-term experimental results on ECFST columns are based on actions first applied at 28 days from concrete casting, despite the fact that current construction practice tends to load ECFST members at a concrete age much

earlier than 28 days due to stringent construction requirements.

2) At present there is no recommended concrete model to be used for the design of CFST arch bridges.

3) The investigation on the long-term response of CFST arch bridges needs to consider: i) their segmental construction process, ii) the varying concrete ages at which loads are first applied during construction, and iii) geometric nonlinearity. There is no research work carried out to date to account for the combined effects of all these factors with an accurate analysis procedure accounting for time effects.

4) No research has been carried out to date to investigate the influence of the time-dependent behaviour of the concrete core on the lateral stability of CFST arches.

1.2 OBJECTIVES OF THE THESIS

The work presented in this thesis intends to:

1) Identify a concrete model capable of adequately predicting the long-term response of CFST members filled with both normal and expansive concrete.

2) Provide an accurate method accounting for the construction process, the ageing of the concrete, the geometric nonlinearity and time effects to investigate the long-term response of segmentally constructed CFST arch bridges.

3) Identify an adequate simplified method of analysis for day-to-day routine design of CFST members and CFST arch bridges.

4) Investigate the influence of the prebuckling deformation induced by time effects on the lateral stability of single parabolic CFST arches.

1.3 THESIS OUTLINE

Chapter 2 conducts a survey of the CFST arch bridge applications to evaluate realistic

ranges of geometric and material properties to be adopted in parametric studies conducted later in this thesis. A review on the available literature regarding numerical and experimental investigating the time-dependent response of CFST columns and arch bridges is also provided.

Chapter 3 presents the long-term experiments on ECFST specimens and their ultimate failure tests. The time-dependent behaviour of eleven ECFST circular short columns subjected to sustained axial loads first applied at early concrete ages ($t_0 \leq 28$ days, where t_0 is the time of first loading) are investigated. After five months under sustained loads, these specimens are tested to failure to gain insight into the possible influence of time effects on the ultimate behaviour of ECFST specimens. Long-term deformations measured at different times, on specimens loaded at different ages, or subjected to different stress levels are compared to identify their influence on the time-dependent behaviour of ECFST members. Investigations on the confinement effects for ECFST specimens at service conditions are then provided based on the longitudinal and circumferential deformations measured on the steel tubes.

Chapter 4 provides the numerical analysis on CFST specimens. A comparative study is conducted on four concrete models (i.e. EC2, AFREM, B3, and MC90 model) to evaluate their accuracy. A cross-sectional analysis is carried out with the time-dependent behaviour of the concrete modelled by means of the integral-type creep law and implemented in the numerical solution by means of the step-by-step procedure. The numerical results have been compared against 81 long-term tests published to date to evaluate the accuracy concrete models in predicting the long-term response of CFST members. The 81 specimens have circular, square and rectangular steel sections filled with normal or expansive concrete of different strengths and subjected to both concentric and eccentric loading first applied at different concrete ages. An extensive parametric study has then been carried out to evaluate the long-term response of specimens whose geometries, material properties and loading conditions are outside the range of those used in the tests while still relevant for real applications. The accuracy of the algebraic methods, i.e. the Effective Modulus (EM) method, the Mean Stress (MS) method, and the Age-Adjusted Elastic Modulus (AAEM) method, is investigated based on the results

obtained using the step-by-step procedure.

Chapter 5 describes the refined method of analysis proposed to numerically analyze the long-term response of segmentally constructed CFST arch bridges. The FE commercial software ABAQUS is used to develop the model for CFST arch bridges and to perform the time-dependent analyses. The step-by-step method and the EC2 model are adopted to capture the timelong-term behaviour of the core concrete which is implemented in the analysis with the UMAT subroutine. Based on one representative bridge case, the reliability of the method is validated against measurements collected on site during construction. With this bridge case, time effects on the static behaviour of half-through CFST tied arch bridges are investigated. At the end of this chapter, a simplified analysis method which considers the time-dependent behaviour of the core concrete by changing the elastic modulus is presented for design purpose.

Chapter 6 shows the extensive parametric study conducted to investigate how time effects influence the lateral stability of single parabolic arches. Considered parameters include the duration of loading, the concrete ages when loads are first applied, the concrete strength, the steel strength, the steel area over concrete area at the cross-section, the slenderness of the arch, and the span-to-rise ratio. ABAQUS is also used to conduct the out-of-plane creep buckling analysis on single parabolic arches. With the UMAT subroutine, the time-dependent behaviour is still modelled by means of the step-by-step method based on the EC2 guidelines and the material nonlinearity under ultimate conditions is considered accounting for confinement effects.

Chapter 7 draws the conclusions and provides recommendations for future work.

CHAPTER 2 LITERATURE REVIEW

2.1 INTRODUCTION

This Chapter presents background information and the current state-of-the-art on the behaviour and design for the use of CFST members in bridge applications, with particular focus on arch bridges. In Section 2.2 different composite solutions adopted to date on real bridges are outlined and discussed. This is followed by a detailed description on the developments undergone over the years in the design and detailing of CFST arch bridges (Section 2.3) and by an extensive survey of CFST arch bridges built to date (Section 2.4). This detailed data was essential to direct the research work carried out as part of this thesis to address real issues currently faced by the construction industry. Section 2.5 discusses the significance of investigating the time-dependent response of CFST arch bridges, also supported by long-term measurements recorded on site during construction. The current procedures recommended in available guidelines for the prediction of the time-dependent behavior of CFST solutions are considered in Section 2.6 highlighting their inadequacies in dealing with CFST arch bridges. Finally, an overview of the current state-of-the-art related to the long-term modeling of CFST members and structures is presented in Section 2.7 to point out the need to develop the numerical models proposed in this thesis.

2.2 APPLICATIONS OF CFST IN BRIDGES

Concrete filled steel tubes (CFST) are members made of hollow steel tubes filled with concrete (also called core concrete). Typical cross-sections of CFST members used on recent projects are presented in Figure 2-1. Concrete filled steel tubes can combine the advantages of steel and concrete material. The encased core concrete prevents the thin-walled steel tube from local buckling. In return, the steel tubes provide confinement to the core concrete improving the compressive capacity and ductility of the CFST members. During construction, the hollow steel tubes can act as permanent formwork for the pumping of the core concrete, saving time and cost for

establishing and demoulding the temporary shoring systems. These advantages make the CFST members quite competitive in modern structural solutions especially when these members are mainly subjected to axial forces.

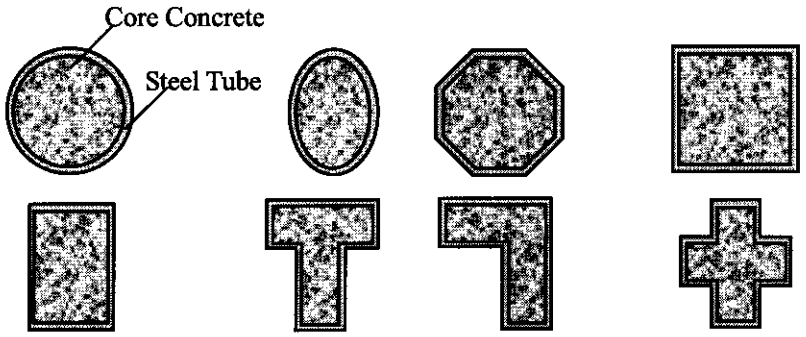

Figure 2-1 Various cross sections of CFST members

Considerable research efforts have been devoted over the past decades to investigate the static and dynamic behaviour of CFST columns, with significant contributions made particularly in Europe, Australia, and Asia. General reviews of the investigations have been presented by Tomii (1991), Shams & Saadeghvaziri (1997), Shanmugam & Lakshmi (2001), Uy (2005), Goode (2006), and Zhong (2006).

As a result, CFST members have gained their popularity in subway structures, towers, tall buildings and bridge applications. CFST members are mainly used as columns in high-rise buildings. A summary of such structures are presented by Uy (1997), Zhong & Zhang (1999) and Matsui (2006), which focused on CFST structures constructed in Australia, China and Japan. Examples of CFST applications in bridges include bridge piers, falseworks, main girders, pylons and main arch ribs in various types of bridges.

The usage of the CFST members in bridges can be traced back to the 19th Century. One of the earliest applications is the Severn Railway Bridge with the piers made of CFSTs. This bridge was built in 1879 in the UK (Zhong 1994). In this bridge, the concrete inside the steel tube was only used for the antirust purposes. Since 1982, Japanese engineers began to use CFST members as the bridge piers for ensuring sufficient stiffness under severe conditions of both the limited space and the high carrying loads. A summary of such bridge applications built in Japan is presented by

Kitada (1997). The Gan Haizi Bridge (under construction), a continuous span beam bridge located in the Si Chuan province of China, is another example of using CFST members as the piers in bridges (Figure 2-2). The trussed CFST piers have the maximum height of 107 m, and are composed of four 813 mm diameter steel tubes with the thickness of 14 mm filled with concrete with the cylinder characteristic compressive strength of 40 MPa (classified as C50 in Chinese guidelines) (Wu et al 2010, Jiang 2009).

Figure 2-2 Gan Haizi Bridge

In 1980s, Ohura invented a new construction method for the concrete arch ribs using the concrete filled steel tubes as falsework (Ohura & Kato 1993). The method was first adopted to construct the Joshi Bridge, on Sado Island, in Japan (Figure 2-3). This bridge has a span length of 82 m. The cross-section of the arch is formed by a hollowed box. During the construction, the thin-walled rectangular steel-arch tubes are used to span over the valley, after which the core concrete is filled into the steel tubes to obtain a more rigid steel-concrete composite structure (CFST members). Concrete is sequentially cast around the tubes using special traveling formwork. Since then, this method has been used to construct many concrete arch bridges in Japan, Europe and China. This kind of bridge is normally called steel tube reinforced concrete arch bridge or concrete self-shored arch bridge. The Wanxian Yangze River Bridge (located in Sichuan, China, finished in 1997) keeps the record of the longest span of this kind of bridge, with a span length of 420 m (Figure 2-4) (Liu et al 2002).

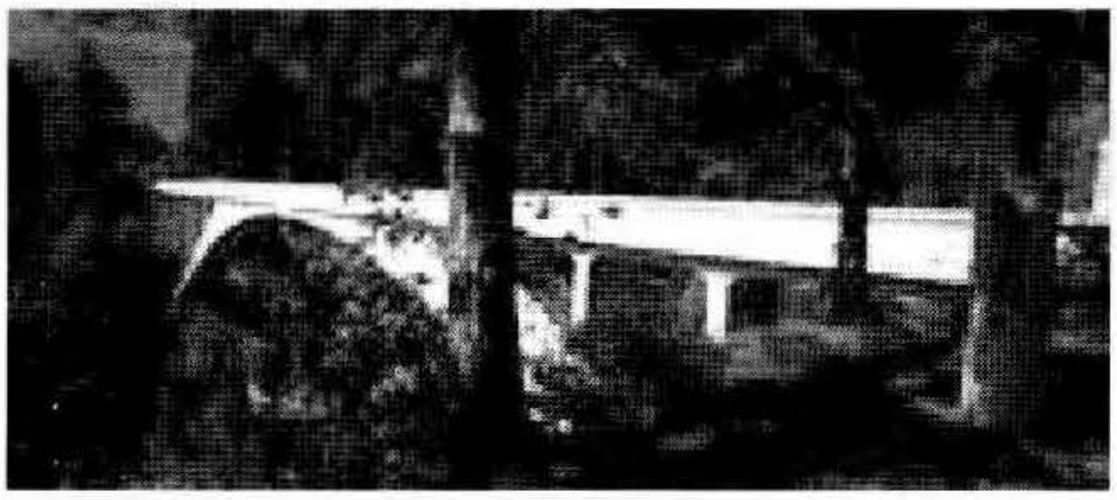

a) Whole Bridge

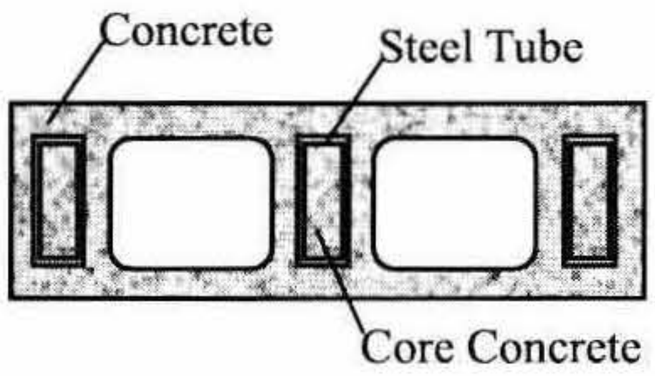

b) Cross Section of the Arch

Figure 2-3 Joshi Bridge

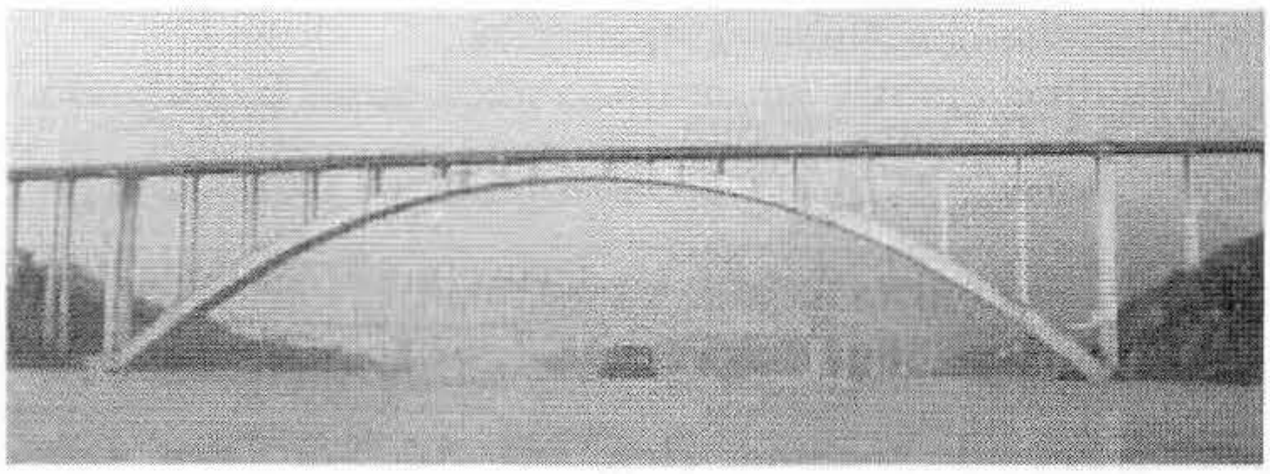

a) Whole Bridge

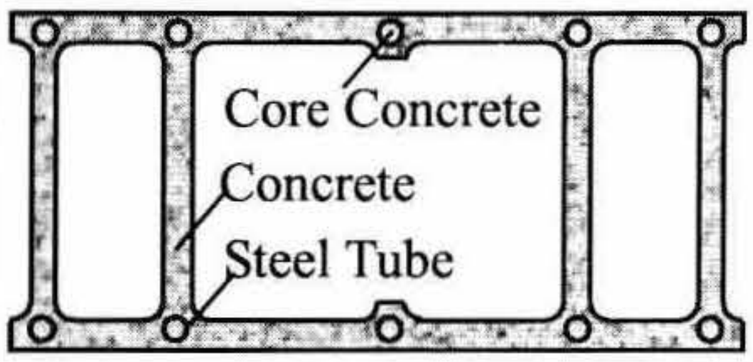

b) Cross Section of the Arch

Figure 2-4 Wanxian Yangze River Bridge

In 1996, the first CFST cable stayed bridge, called the Zi Dong Bridge, was opened to traffic in Guang Dong (China) (Figure 2-5). In this bridge, the 36 m high CFST pylons comprise steel tubes with a diameter of 1.84 m and a thickness of 25 mm. The core concrete has a cylinder characteristic compressive strength of 40 MPa (classified as C50 in accordance with Chinese guidelines) (Li 1997). The composite truss girder has 230 mm thick concrete deck working as the upper chord, and CFST members working as the bottom chords, the webs and the laterals, all of which are filled with concrete with a cylinder characteristic compressive strength of 40 MPa. The geometrical dimensions of the CFST members are 299 mm for the diameter of the bottom chords with the wall thickness of the steel tube of 12 mm and 140 mm for the diameter used for the webs and the lateral members with wall thickness of 10mm and 6mm, respectively. The Gan Haizi Bridge also uses the CFST members as the bottom chords and webs in the continuous truss beams with the diameter of 813 mm and 457 mm, respectively, and filled with concrete with a cylinder characteristic compressive strength of 50 MPa (classified as C60 in accordance with Chinese guidelines).

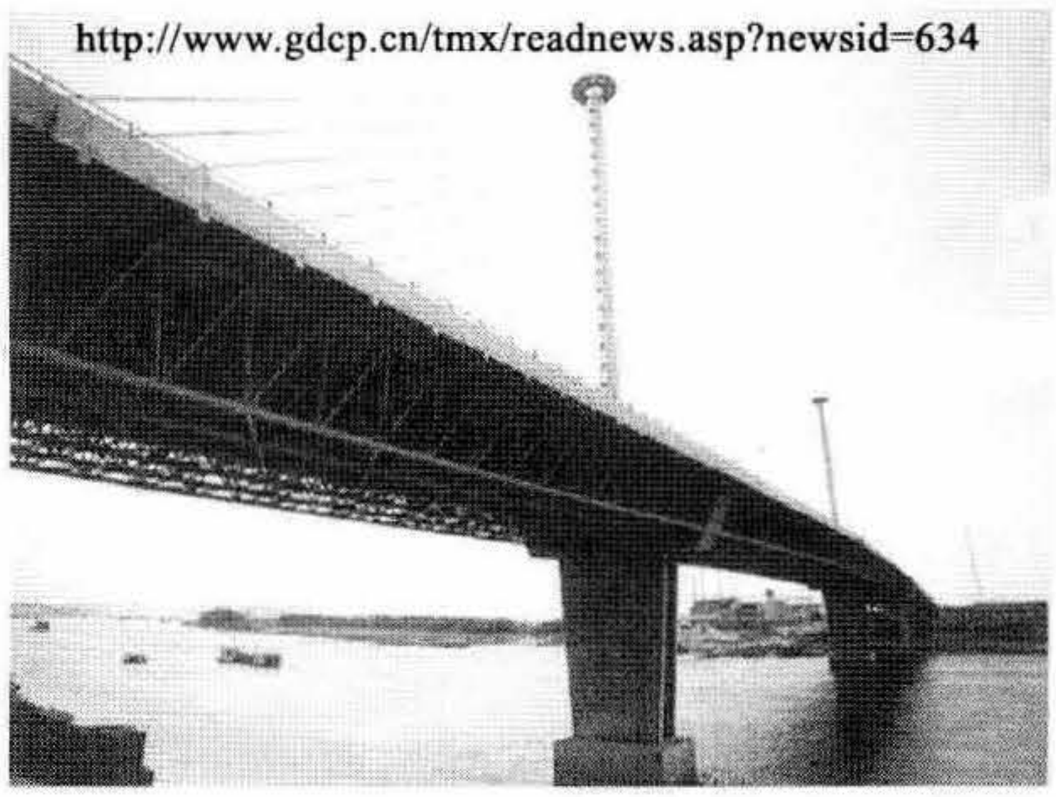

Figure 2-5 Zi Dong Bridge

Nakamura (2007) proposed the use of a single circular CFST member as the main girder in cable stayed bridges to resist the axial forces induced by the cables on bridge decks (Figure 2-6).

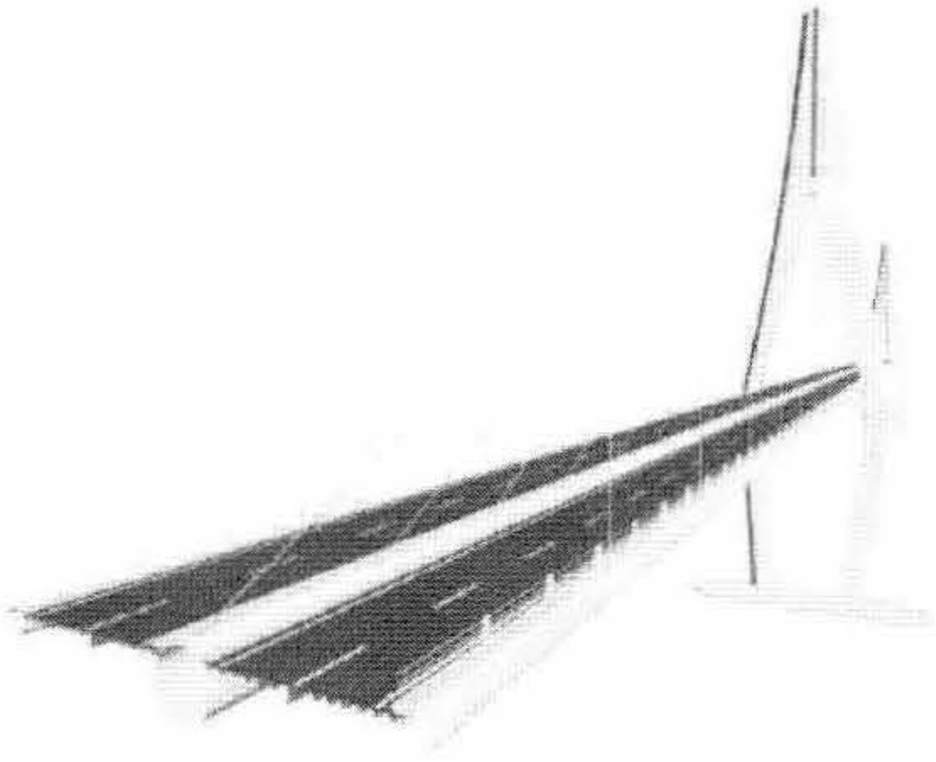

a) Whole Bridge

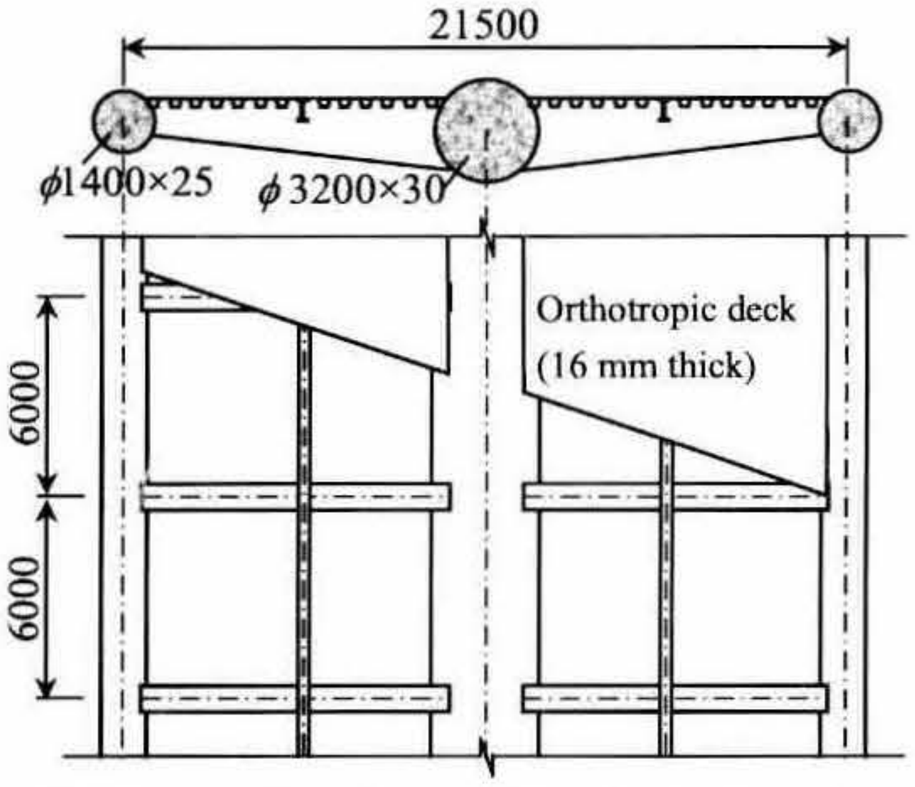

b) Cross Section of the Arch (mm)

Figure 2-6 Cable stayed bridge with three pipe girders in the deck (Nakamura 2007)

This bridge supports a four lane road with a main span of 500 m and a width of 21.5 m. The tower is proposed as an A-shaped tower with a height of 150 m, made of steel box columns. The centre pipe girder in the deck resists torsion caused by dead and live loads, and the stay cable system mainly resists bending moments. The center main girder in the deck is 3200 mm in diameter, and the edge pipe-girder is 1400 mm in diameter. The center girder and the two pipe-girders on each side are connected with the cross beams and the orthotropic steel deck (Figure 2-6 b)). The

stays go through the centre pipe-girders and are anchored inside the pipe. The three-pipe-girder bridge showed excellent aerodynamic stability during the wind tunnel tests.

Concrete filled steel tubes are also used as the bridge deck girders due to their advantages in strength, construction efficiency and ability of reducing the noise and vibration caused by trains and vehicles (Nakamura et al 2002). For example, such solution has been used for bridges supporting the Japanese rapid trains and referred to as the Bridge of Shinkansen (Figure 2-7). This bridge, completed in 2000, consists of three-span continuous girders with each span of 34–36 m long. The steel pipe adopted for the girder is 1.3 m in diameter with the maximum thickness of 22 mm and tensile strength of about 500 MPa. Studs and perfobond shear connectors were welded on the pipe girders. The construction of the bridge took 15 months. The total weight was only half of the conventional concrete bridges and the construction cost was substantially lower than that of the conventional railway bridges.

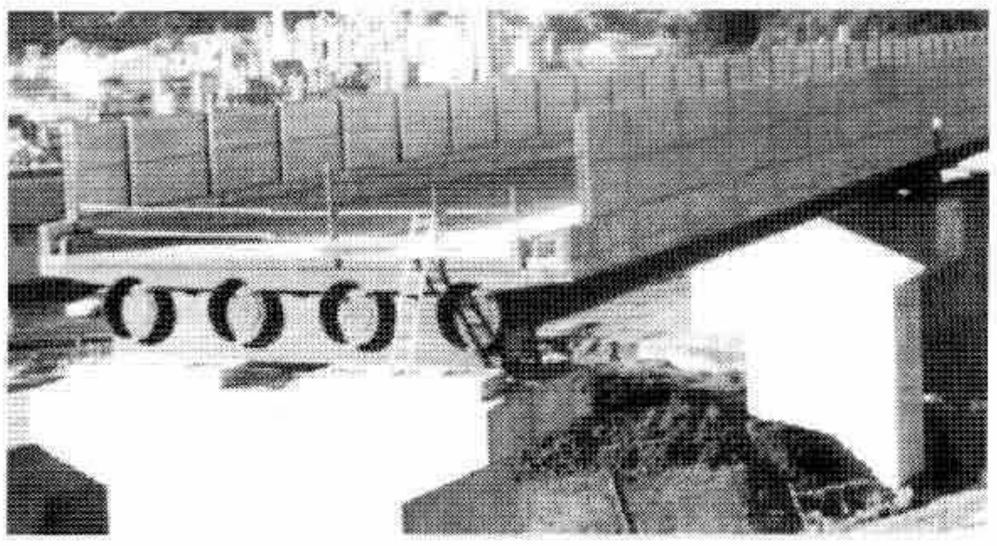

Figure 2-7 Bridge of Shinkansen (Nakamura et al 2002)

Among all possible applications of CFST members in bridges, their use as main arch ribs is the most extensive one. These bridges are called CFST arch bridges. Up to date, there are more than 300 CFST arch bridges built in the world, among which more than 80 have a span longer than 150 m. It is worth to notice that, unlike the steel tube reinforced concrete arch bridges (Figure 2-4), the CFST arch bridges uses the CFST members as the arch ribs whose structural behaviour is different from the one of concrete arches due to the fact that the concrete is encased inside the steel tubes. During the construction of CFST arch bridges, the hollow steel tubes are first

hoisted and erected to span the river or valley. After the closure of the hollow steel arches, the concrete is pumped inside the steel tube. The light weight and strong resistance of the steel tubes make it possible for the structure to span long distances and, because of this, construction techniques such as the slipform method are not needed. In the next sections, an extensive survey on CFST arch bridges is presented and representative bridges built using this form of construction are outlined.

2.3 DEVELOPMENT OF CFST ARCH BRIDGES

The first CFST arch bridge in the world was built in 1939 over the Icet River (Исеть) in Siberia, former Soviet Union, with a span length of 140 m (Figure 2-8). Compared to the steel arch bridge, this bridge is considered to be more economical by reducing 52% of the amount of steel and saving 20% of the cost (Cai 2007). The bridge is built with on-ground-type scaffolding method, with which the advantage of the CFST members in the efficiency and cost-effectiveness during the construction is not utilized.

Figure 2-8 First CFST arch bridge in the world (Cai 2007)

After this first bridge, no other CFST arch bridges were built for more than 50 years due to the limitations in the construction method. It was not until the 1990s that the CFST arch bridges started to become an attractive structural solution. Although this competitiveness is not predomingant in developed countries as the construction of this kind of bridge needs site pouring of the concrete, some applications have been constructed in Europe, Japan and America.

In 1998, one CFST arch bridge was opened to traffic in the Czech Republic crossing the new Brno-Vienna Expressway (Figure 2-9). This bridge has a span of 67.5 m, and the rise of the arch is 13 m. The circular arch has a radius of 74.75 m. It is

formed by a single steel tube with a diameter of 900 mm and a thickness of 30 mm (Strasky et al 2001). The deck is 10.9 m wide.

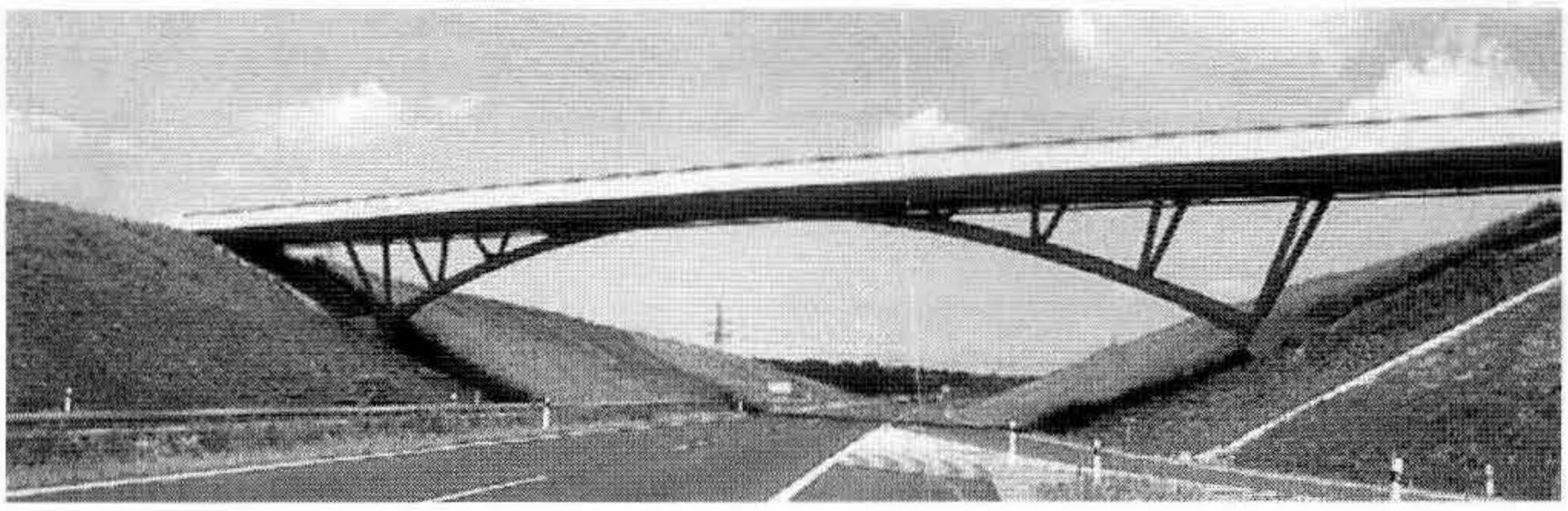

Figure 2-9 Arch bridge crossing the Brno-Vienna Expressway (Strasky et al 2001)

A CFST arch bridge called the Arco del Escudo (Escudo Viaduct) was built in Spain, and was designed by Manterola Armisen. This bridge was completed in 2001 (Figure 2-10). For this bridge, the 25.4 m wide and 229 m long composite superstructure is supported on two concrete filled steel double-tube arch ribs of 126 m span and 15.3 m rise (Šavor & Bleiziffer 2008).

Figure 2-10 Arco del Escudo Bridge (Šavor & Bleiziffer 2008)

In 2006, the world's longest CFST arch bridge without wind braces, i.e. the Second Saikai Bridge (Yoshmura et al 2006), was built in Japan with a span length of 230 m (Figure 2-11). The arch rib has a regular triangular truss cross-section consisting of three steel tubes with an outer diameter of 812.8 mm and a maximum thickness of 50 mm filled with high fluidity concrete. The bridge has a width equal to 20.2 m.

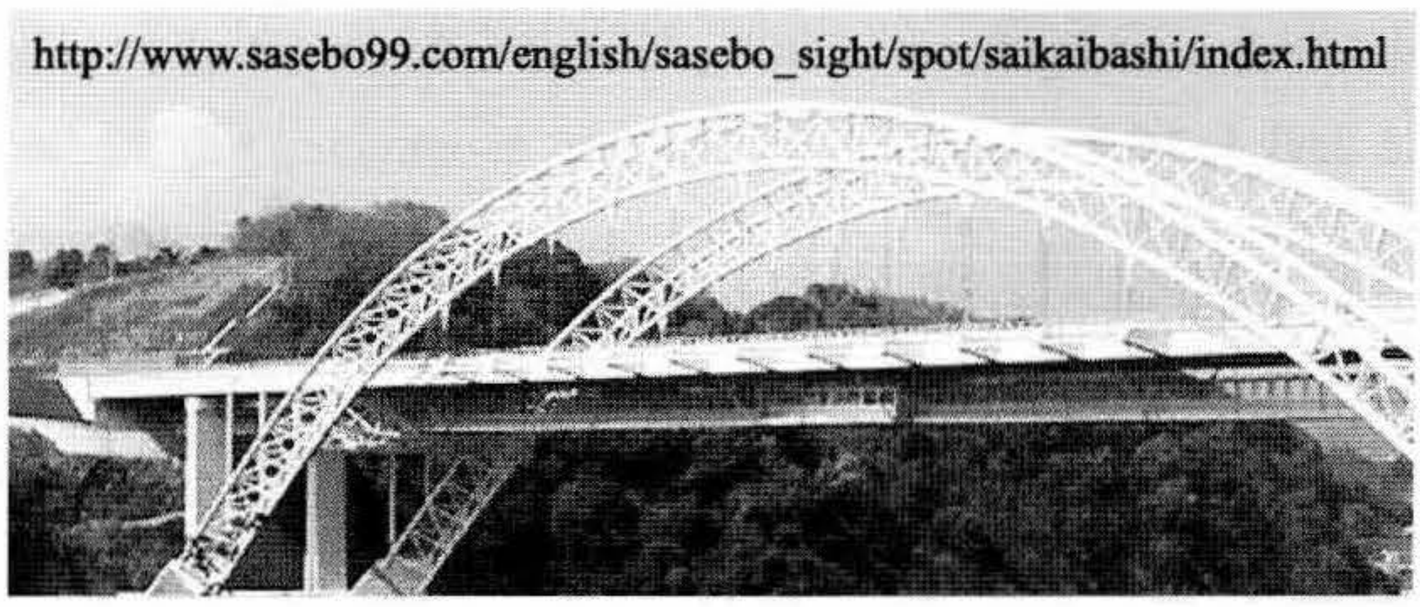

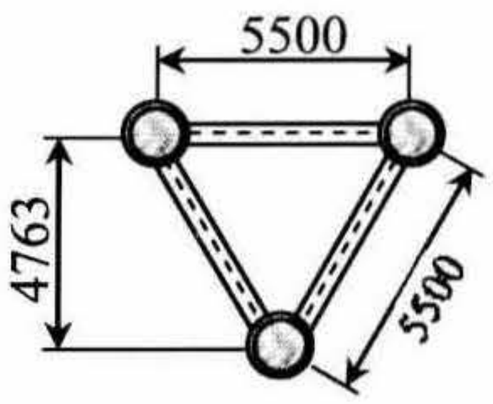

a) Whole Bridge b) Cross-section (mm)

Figure 2-11 Second Saikai Bridge

Some engineers choose to fill the hollow steel tubular arch ribs with concrete at their springings to prevent local buckling or to improve their impact resistance from vehicles. The Antrenas Tubular Arch Bridge (France, finished in 1994, see Figure 2-12) falls within this category (Virlogeux et al 1997). This 56 m span bridge has a deck width of 11.3 m. The parabolic steel arch has a circular cross-section of 1200 mm in diameter with the wall thickness of 32 mm.

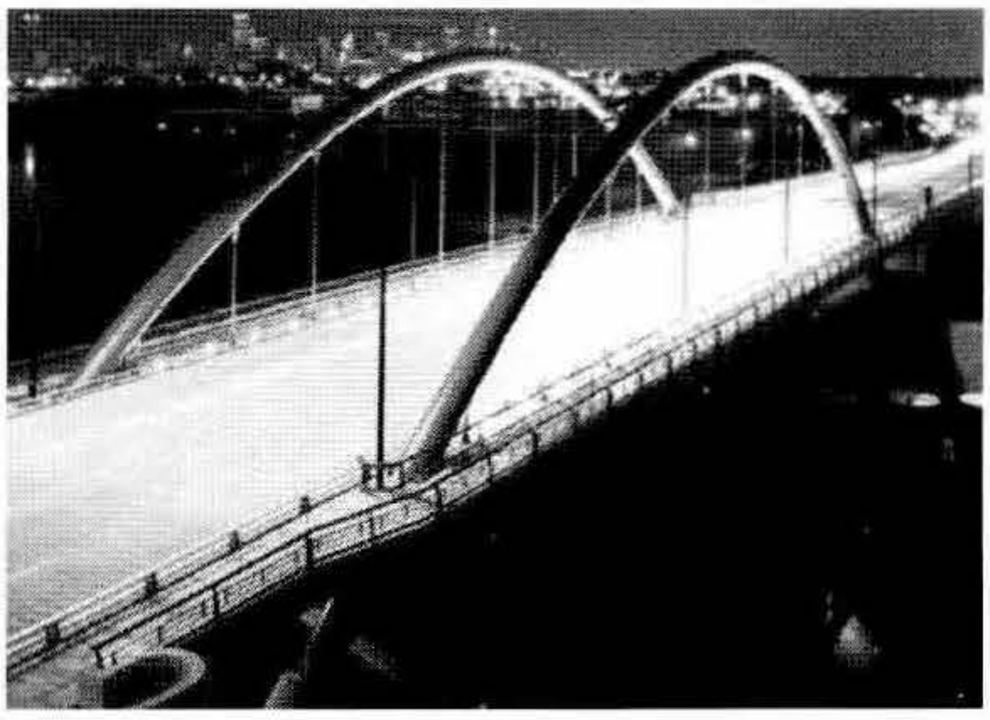

Figure 2-12 Antrenas Tubular Arch Bridge Figure 2-13 Damen Avenue Arch Bridge

Another example is the Damen Avenue Arch Bridge located in Chicago (US), and completed in 1998 (Figure 2-13) with a clear span length of 74 m, and a deck width of 21.9 m (Cassity 1999). The two ribs are fabricated from 1.2 m diameter steel pipe with a thickness of 25 mm that is formed into a compound circular curve using induction heat bending. Each rib is filled with concrete over a distance of 8m at each end to resist the higher thrust and moment near the springing.

Although there are some examples of CFST arch bridges in the developed countries, the arch spans of the bridges in these cases are relatively small, and the number of the bridges is limited compared to other bridge types or even concrete/steel arch bridges. In fact, the real development of the CFST arch bridge has been taking place in China. China is a mountainous developing country, in which a lot of streams and rivers rush through deep valleys, making arch bridges very competitive as they are economically applicable to span river valleys and deep ravines with high-gradient rocky riverbank and fast water flow. As a developing country, the concrete is still more economical than steel in China. Availability of more high-strength steels and concrete as well as the improved segmental hoisting and concrete pumping techniques further expanded the feasibility of CFST arch bridges. Since 1990, when the first CFST arch bridge, the Wang Cang East River Bridge, opened to traffic, more than 300 of this kind of bridges have been built in China, among which 85 bridges have a span longer than 150 m.

According to the location of the deck to the arch, the CFST arch bridges can be categorized into three types: the deck arch bridge, with the deck completely above the arch; the through arch bridge, with the deck located at the height of the arch springing; and the half-through arch bridge, with the deck passing through the arch at the mid height. Normally the decks above the arch are supported by concrete columns, while those beneath the arch are supported by suspension cables (also called suspenders). Figure 2-14 presents the development of CFST arch bridges in China during the past decades, in which 'Planned' depicts bridges under construction. It is clear that the span of the bridge become longer with time and the number of the bridge built every year is also increasing. So far, the longest span among CFST deck arches in the world is the 430 m long Zhi Jing River Bridge in Hubei Province (China), opened for service in 2009 (Figure 2-15). The truss arch ribs are 6.5 m high at the arch crown and 13 m high at the arch springing, and have a constant width of 4m throughout the arch length, comprising four 1.2 m diameter circular CFST arch ribs with a thickness of 24 (30, or 35) mm and webs formed by diagonal and vertical hollow steel tubes. The catenary arch rib has a rise-over-span ratio of 1/5.5. The distance between the two arch ribs is 13 m. Twenty wind braces

are installed between the ribs to ensure the lateral stability of the bridge (Wang & Hui 2010).

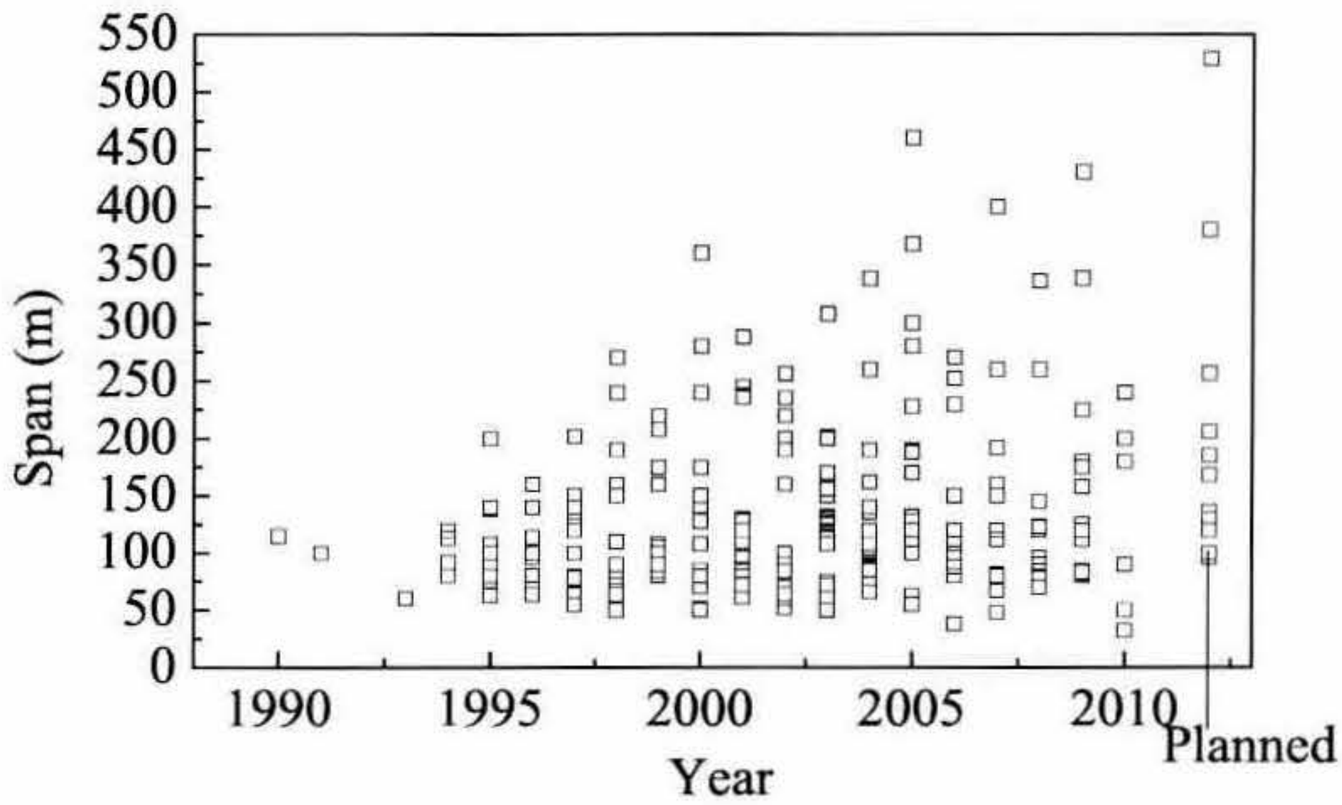

Figure 2-14 Development of the CFST arch bridges in China

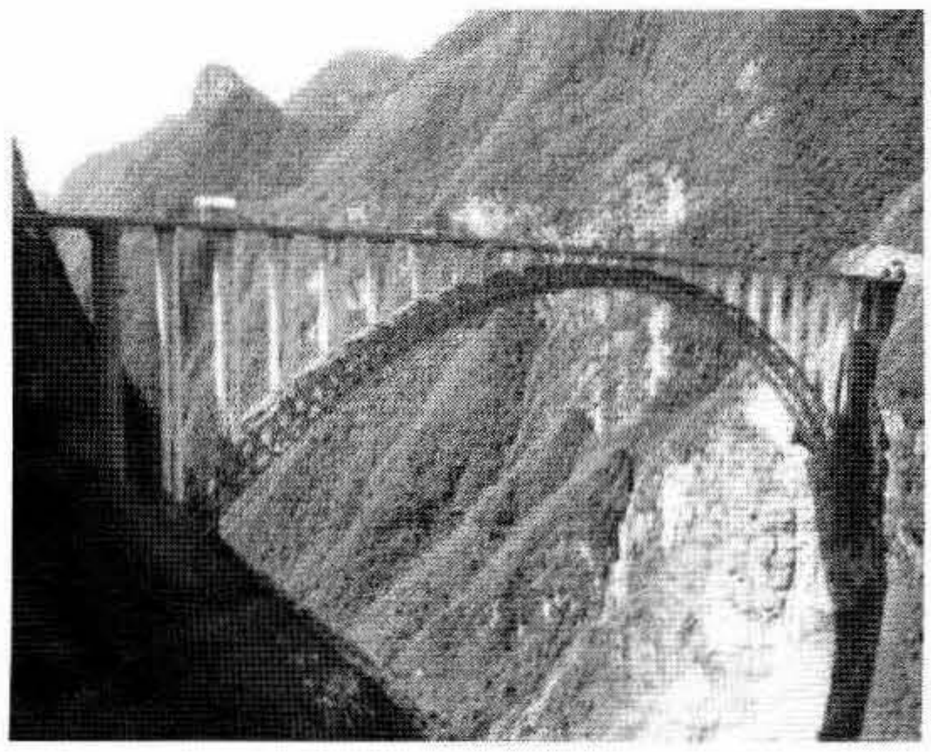

Figure 2-15 Zhi Jing River Bridge

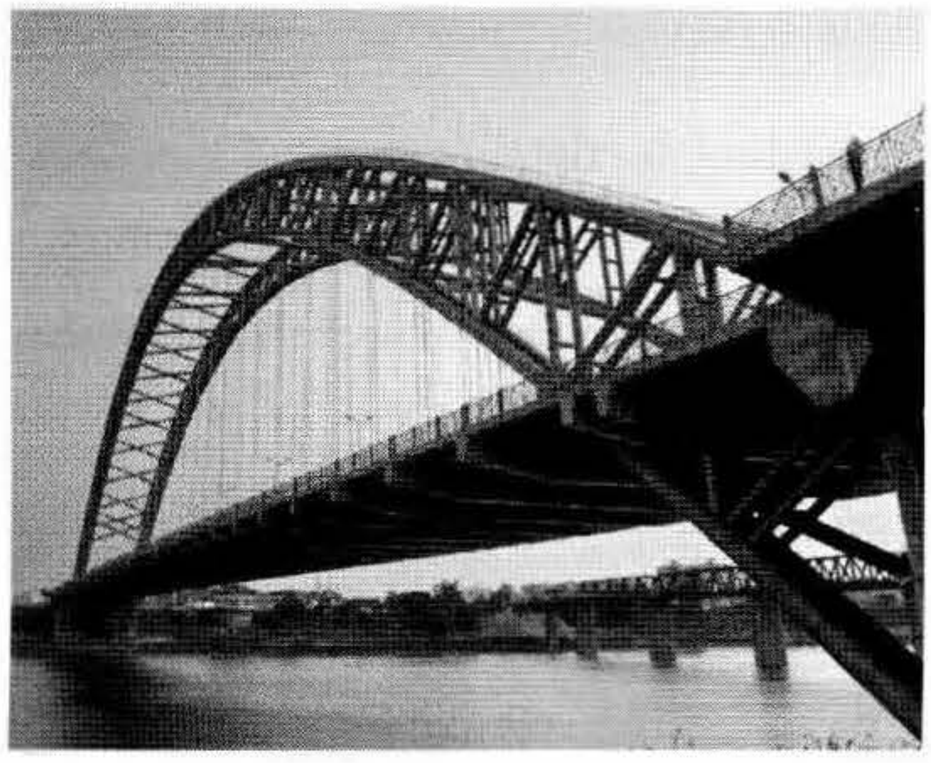

Figure 2-16 Yong River Bridge

The longest CFST through arch bridge in the world is the Yong River Bridge in Guangxi province (China), opened to traffic in 2004, with a span of 338 m and a deck width of 35 m (Figure 2-16). The rise over span ratio is 1/4.5. There are sixteen windbraces between the arch ribs to increase the lateral stability of the structure. The parabolic arch rib is 3m wide and 8~13.293 m high, consisting of bottom and upper dumbbell shaped CFST chords and diagonal and vertical hollow steel tubular truss webs. The circular steel tubes of the CFST chords are 1220 mm in diameter and 16(20) mm in thickness. These steel tubes are filled with concrete with cylinder characteristic compressive strength of 40 MPa.

The Wu Xia Long River Bridge, located in the Chong Qing province of China, and completed in 2004, is known as the world's longest CFST half-through arch with a span length of 460m (Figure 2-17). This is also the standing longest CFST arch bridge in the world. The truss arch possesses a catenary profile with a rise over span ratio of 1/3.8. The distance between the two arch ribs is 19.7 m with twenty-two windbraces placed between them. The truss arch rib is 7 m deep at the arch crown and 14 m deep at the arch springing, with a constant width of 4.14 m. It is composed of four circular CFST members with steel tubes of 1220 mm in diameter and 22(25) mm in thickness and hollow steel tubular webs of 610 mm in diameter and 12 mm in thickness.

The He River No. 1 Bridge (under construction) in the Si Chuan province of China, will soon break the world record as the longest CFST arch bridges with a span length of 529 m (Figure 2-18). The construction of this bridge started in 2009. This bridge is a half-through arch bridge. Four 1320 mm diameter CFST members filled with concrete of 50 MPa for cylinder characteristic compressive strength and hollow steel tubular webs constitute the 4 m wide and 8~16 m high catenary truss arch rib. The rise over span ratio is 1/4.5.

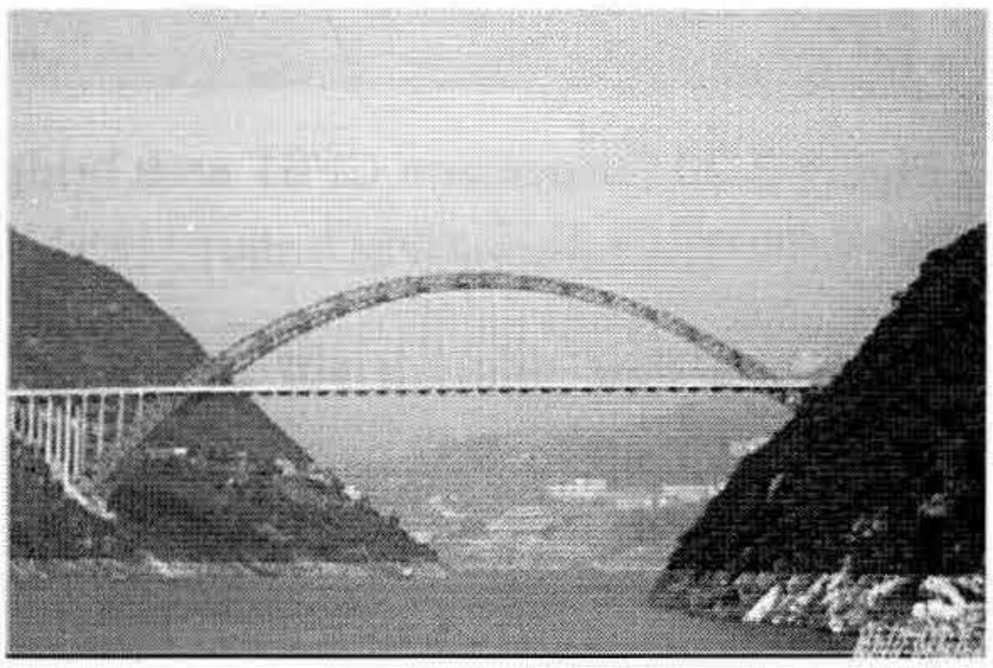

Figure 2-17 Wu Xia Long River Bridge

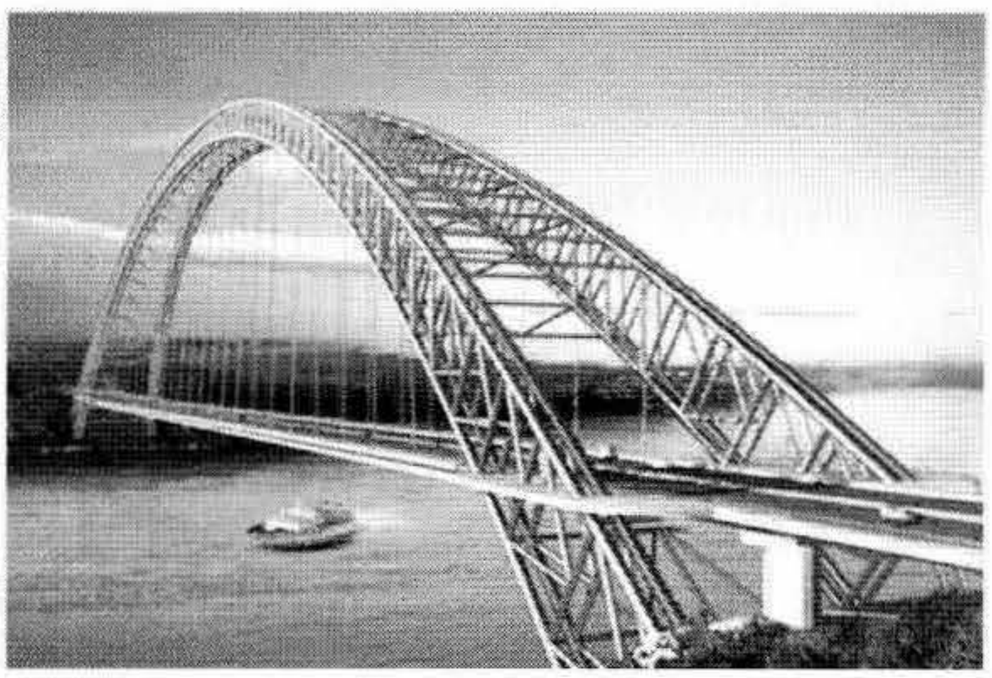

Figure 2-18 He River No. 1 Bridge

The Xiang Jiang Si Bridge, a cable-stayed CFST arch bridge built in the Hunan province of China, opened to traffic in 2007 (Figure 2-19). The center span is 400 m with two side spans of 120 m long. The tower is in H-shape with a height of 90 m. The distance between the two arch ribs is 34m, with eleven windbraces installed to

increase their lateral stability. As the main load bearing member, the parabolic truss arch rib with the rise over span ratio of 1/5.19 has six 850 mm diameter circular CFSTs (three in the upper chord with the steel tube thickness of 22 mm, 24 mm, or 28 mm and the other three in the bottom chord with the steel tube thickness of 20 mm, 24 mm, or 28 mm) connected with CFST solid webs in the horizontal direction and 450 mm diameter hollow circular steel tubular truss webs in the vertical direction, except for the part at the arch springing where the cross-section is fully filled with concrete to improve their impact resistance from boats and ships. The arch is 9 m high at the arch crown and 5 m high at the arch springing, and has a width of 3.55 m.

Nakamura et al (2009) presented new promising solutions combining the benefits of suspension and CFST arch bridges as depicted in Figure 2-20.

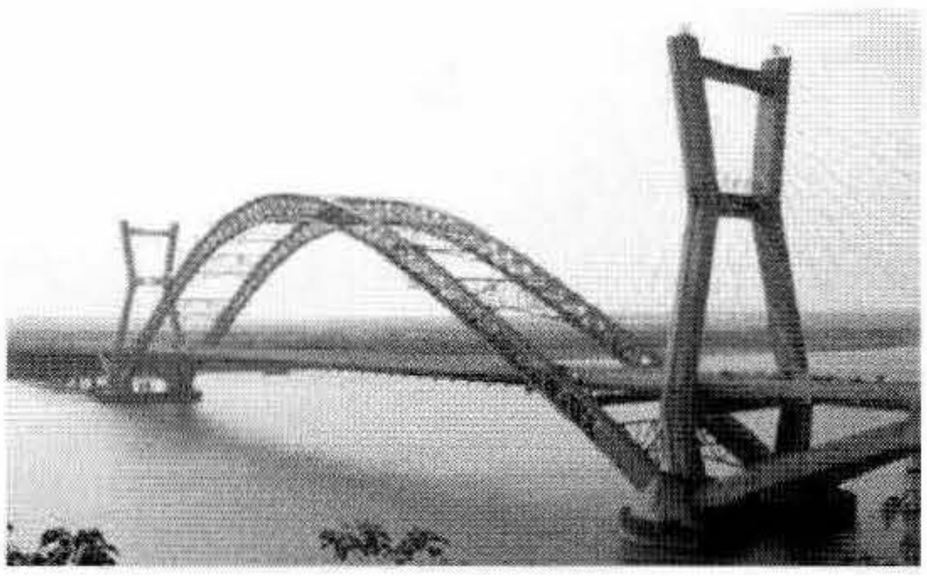

Figure 2-19 Xiang Jiang Si Bridge

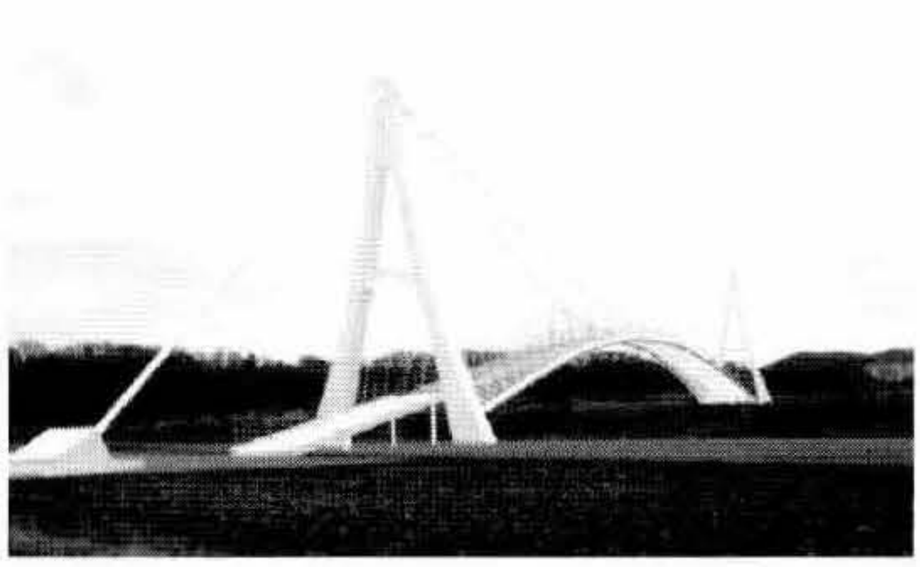

Figure 2-20 Suspension CFST arch bridge (Nakamura et al 2009)

2.4 SURVEY OF CFST ARCH BRIDGES

An extensive survey of the standing CFST arch bridges was conducted with the information collected through the website, the literature review or provided by some bridge designers in China. The designing information collected from 313 CFST arch bridges are presented in Appendix I, which is an update of the designing information reported in 2007 by Chen (2007) on 202 CFST arch bridges. In this section, an overview and discussion of the design information are presented, including the structural information of the bridge, and the geometries and material properties of the arch.

2.4.1 Structural Information

2.4.1.1 Bridge Type

Out of the 313 CFST arch bridges, 148 are half through arch bridges, 144 are through arch bridges, and the remaining 21 are deck bridges (Figure 2-21). For those bridges with a span longer than 150 m (defined as long span bridge in accordance with Chinese Code JTG D60-2004), there are 62 bridges half through bridges, 11 through arch bridges and 12 deck arch bridges. It can be seen that the number of the deck arch bridges is limited, being only 7% of the total number of built bridges and 15% of these bridges possess a span longer than 150 m. This is because, for this type of arch bridge, the elevation of the deck is high, making it only suitable for very deep valleys with steep walls (see Figure 2-15).

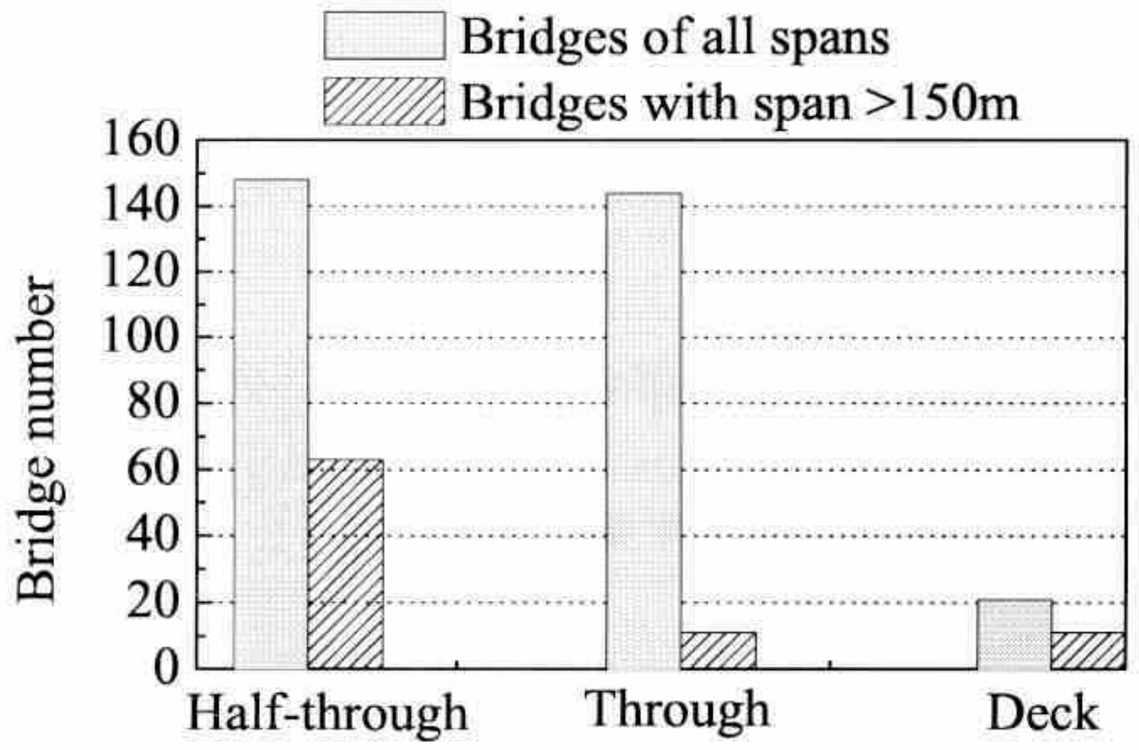

Figure 2-21 Different bridge types for CFST arch bridges

The use of the through arch bridges represents a competitive solution for small spans. More than 58% of the CFST arch bridges with a span smaller than 150 m are through arch bridges. They lose their competitiveness when moving to longer spans, because the limited clearance over the water cannot normally meet the navigation requirements for broad rivers. The half through arch bridge therefore is the dominant bridge type used for long span CFST arch bridges, representing more than 71% of the total number of built bridges.

2.4.1.2 Ratio of the span over width for the CFST arch bridges

In the designing of CFST arch bridges, the designers normally determine the width of the bridge according to the number of traffic lanes required, leading to a great

range of ratios of span length (l) over bridge width (b) (Figure 2-22). From Figure 2-22, it can be observed that the value of l/b gets larger as the span gets longer, meaning that the CFST arch bridges tend to be narrower compared to the longer spans. As a result, most of the CFST arch bridges with a span longer than 150 m will buckle in the lateral direction under ultimate loading, which may be further triggered by the increasing deformations produced by time effects.

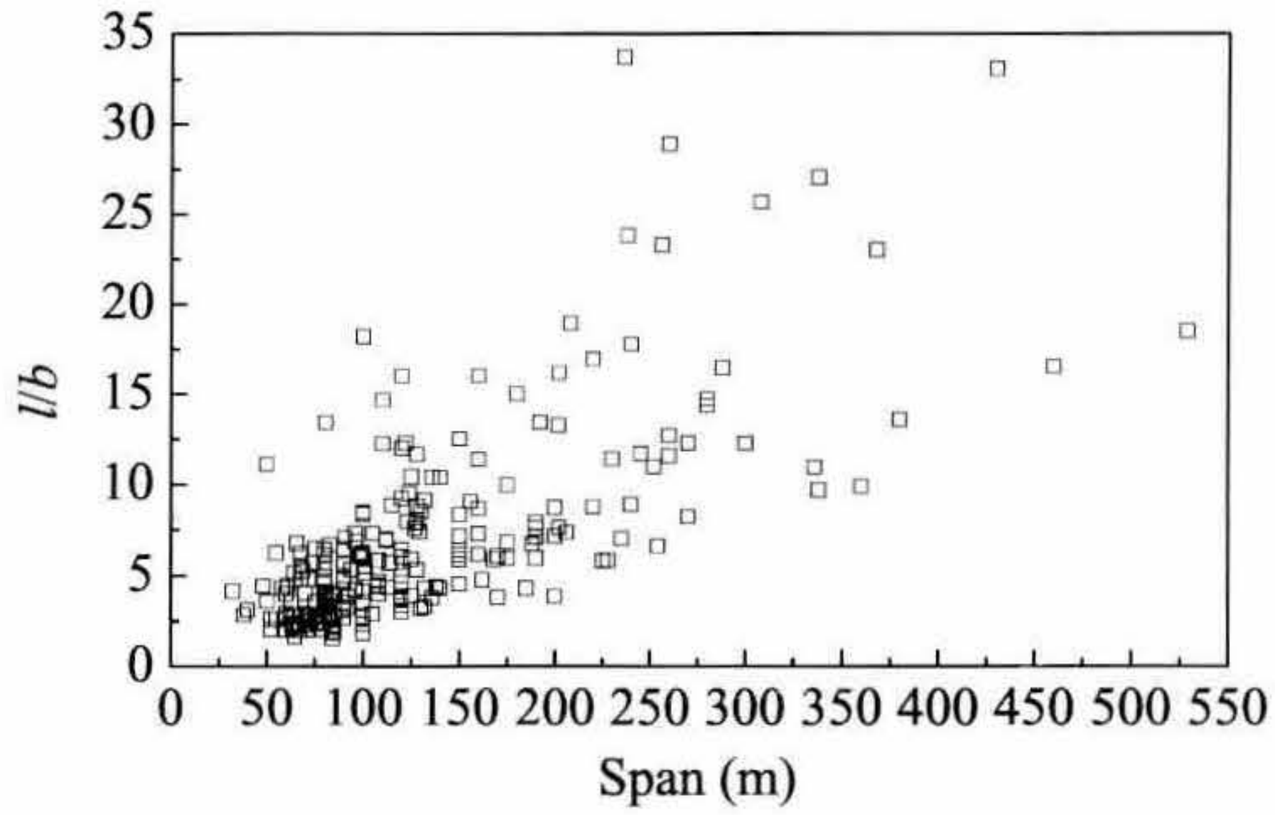

Figure 2-22 Ratio of width over span for bridges with different span length

2.4.2 Geometrical information for arches

2.4.2.1 Arch profiles

Designers are required to choose the arch profile carefully for CFST arch bridges to minimize the bending moment in arch ribs to fully utilize the load bearing capacity of CFST members when subjected to axial compression. For this purpose, it is normal to use an arch profile conforming closely to the dead-load thrust line. In such cases, if the rib is cambered for the dead load, there will be no bending in the rib under this load and the arch will be in pure compression. In particular, the circular arch ribs resist almost pure compression when under uniform distributed radial loading, the parabolic arches are ideal structures to support loading uniformly distributed along the span, and the catenary is the perfect curve for an arch subjected to uniform distributed loads along the arch profile (like the self-weight of the arch with uniform density and prismatic cross-section). The difference of the inner forces between these three arch profiles is not significant for small arch spans.

Figure 2-23 summarizes the number of CFST arch bridges with different arch profiles. In deck arch bridges, the catenary arch curve is the most used, being used in 85% of the total number of bridges. All deck bridges with a span longer than 150 m possess catenary arches. For half-through arch bridges, the catenary arch profile is more competitive than the parabolic one: 65 out of 107 half-through arch bridges have catenary arches. Its advantages become more pronounced with half-through arch bridges with a span longer than 150m, in which case the number of catenary arch bridges is almost three times of those with parabolic profiles. The use of the parabolic curve is more popular in through arch bridges (accounting for 72.6% of the total number) because the deck loading, distributed uniformly along the span, is more significant. Among the 311 bridges, only three bridges use circular arches, one deck bridge, one half-through bridge, and one through bridge, none of which has a span longer than 150m. Though the catenary curve and parabolic curve are almost equally popular in CFST arch bridges with all span lengths, the former one possesses the dominant number in bridges with a span length longer than 150 m.

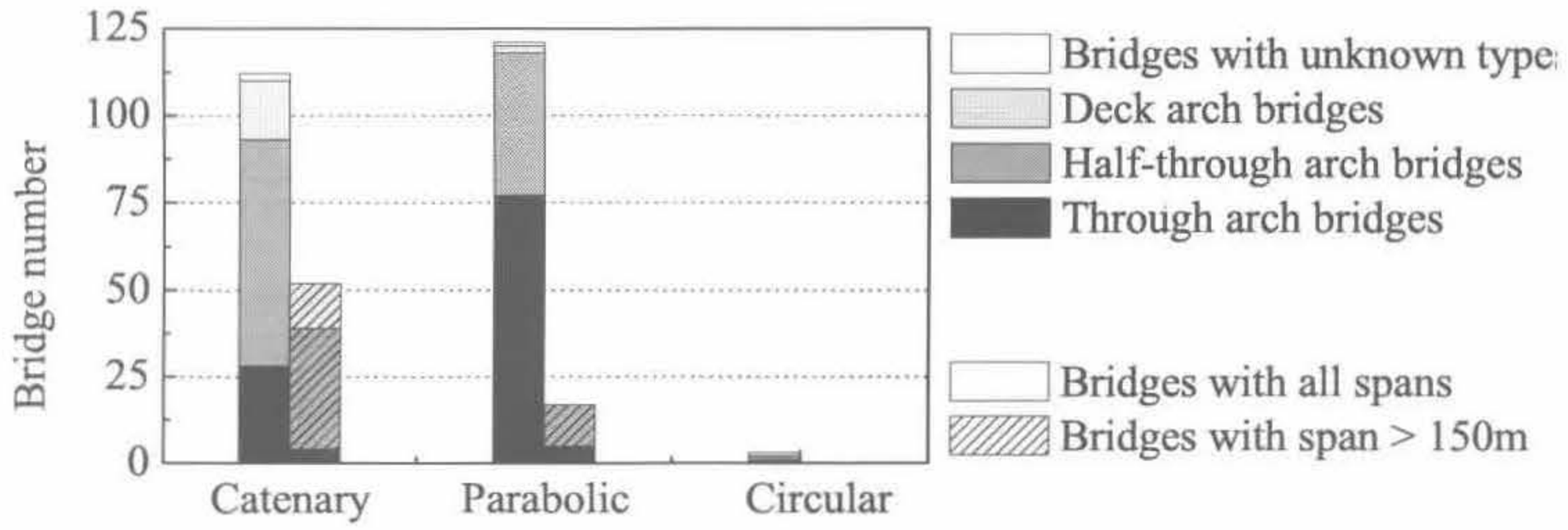

Figure 2-23 Different arch profiles for CFST arch bridges

2.4.2.2 Span-to-rise ratio

The flatter rise of the arch leads to higher horizontal thrust, causing difficulty in the design of buttress, foundation and the ties if adopted. The bending moment inside the arch ribs increases with the increasing span-to-rise ratio. A low value of the span-to-rise ratio, on the other hand, leads to higher material costs for the arch and causes difficulties in the construction of the arch as it becomes higher, also leading

to possible problemsn with lateral buckling. In this context, the span-to-rise ratio should always be carefully determined.

The span-to-rise ratio (*l/f*) for the standing CFST arch bridges covers the range 2-10 (Figure 2-24).

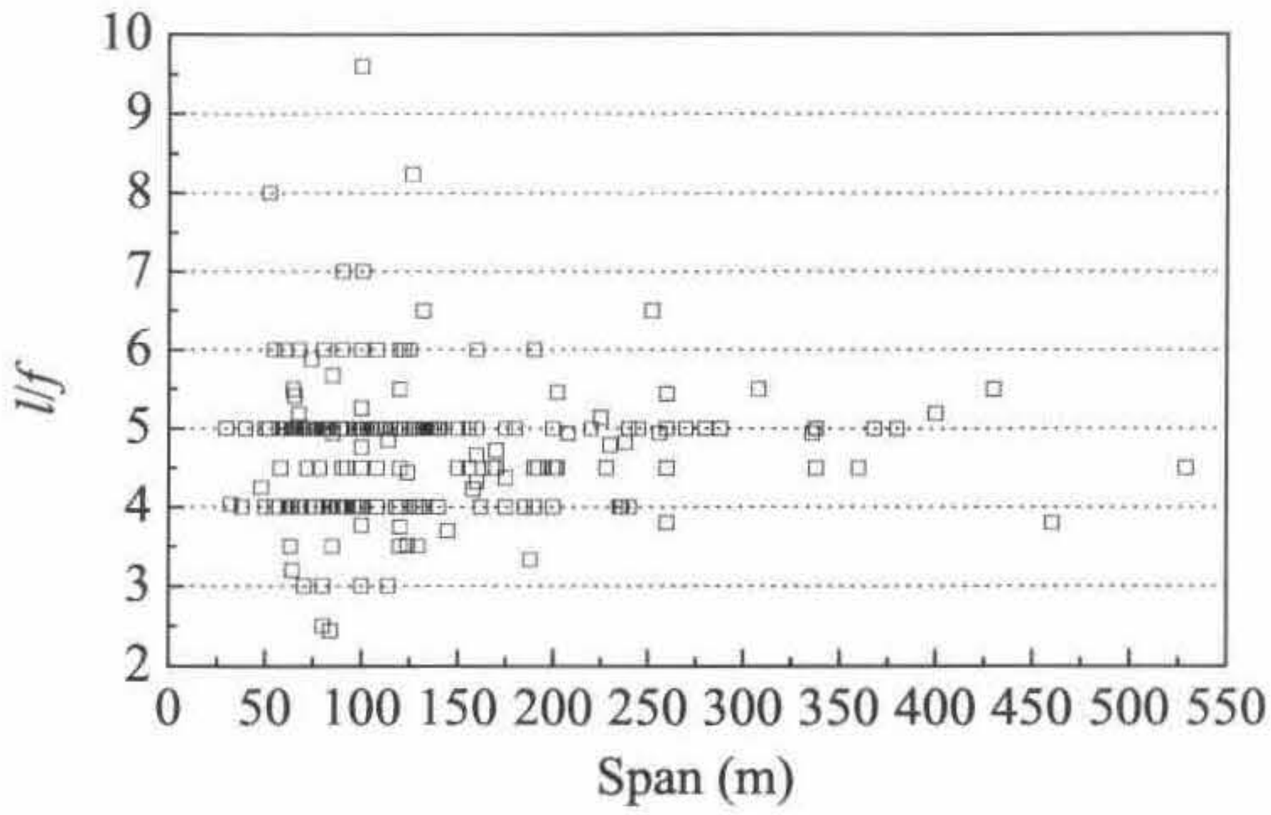

Figure 2-24 Ratio of span over rise for bridges with different span length

Most of the bridges, especially those bridges with a large span, have the span-to-rise ratio between 4 and 5.5 to achieve the best balance between cost and structural safety. For bridges with small spans, the ratio of span over rise tends to have a large variety to fulfill aesthetic needs.

2.4.2.3 Cross sections of the arch

A wide range of cross-sectional shapes can be used for the CFST arch member, including dumbbell shaped, trussed, circular, horizontal or vertical obround, cluster type, and rectangular, as presented in Figure 2-25. The number of bridges with different cross-sections is illustrated in Figure 2-26. The dumbbell shaped cross-section was adopted in the first CFST arch bridge, the Wang Cang East River Bridge. Since then, 114 CFST arches have been built using dumbbell shaped cross-sections. Despite its extensive use, this kind of cross-section is not recommended (Zhong 2000) as it commonly has a poor pouring quality of the concrete inside the web and the welding connection between the steel web and the steel tube has a high possibility of tearing up during the web concrete pumping.

Besides, the dumbbell shaped CFST members attract more bending moment along the arch compared to CFST members in a truss structure. The trussed arch is another popular arch type in CFST arch bridges, with a total number of 101 bridges being built. The trussed rib is more desirable for long span arches. Among the 44 CFST arch bridges with the span longer than 200 m, 41 are built in the trussed form. Dumbbell shaped cross section and single circular shaped one only suit for bridges with a span length shorter than 200 m. The latter one has 26 applications with the maximum span of 158 m, 92% of which have a span shorter than 100 m. The obround arch cross-sections are used in 23 bridges with a span length no longer than 150 m. In the 1990s, the designers tried to use the cluster type arch in CFST arch bridges but realised that it was not as effective as the trussed rib in resisting bending moments and it required complex connection detailing between the circular tubes. As a result, this kind of bridge was only used in 9 projects constructured between 1996 and 1999. After 2000, CFST arches with rectangular cross-sections appeared, with the total number of 7 bridges whose span length is limited to 100 m.

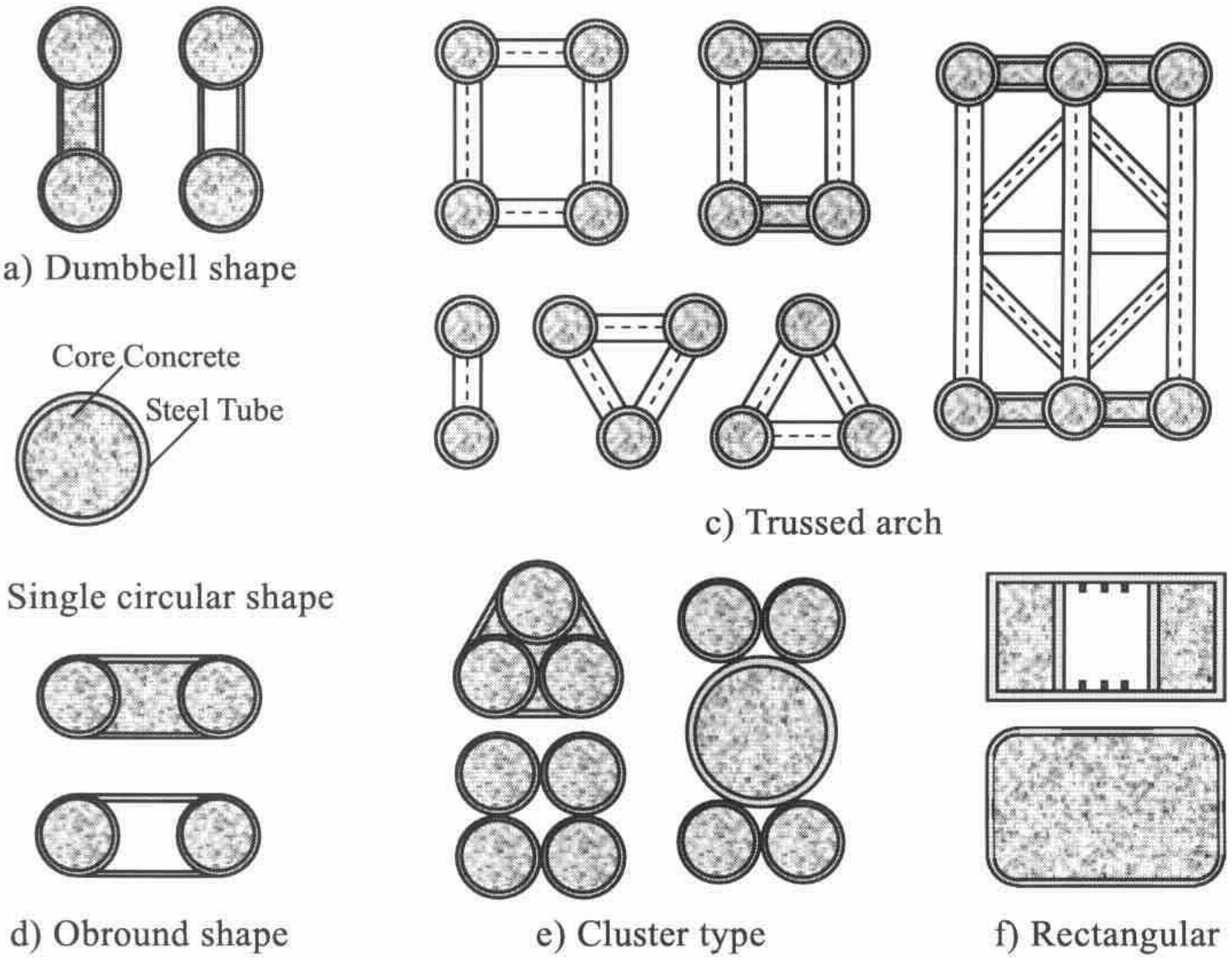

a) Dumbbell shape

b) Single circular shape

c) Trussed arch

d) Obround shape

e) Cluster type

f) Rectangular

Figure 2-25 Various cross sections of CFST members

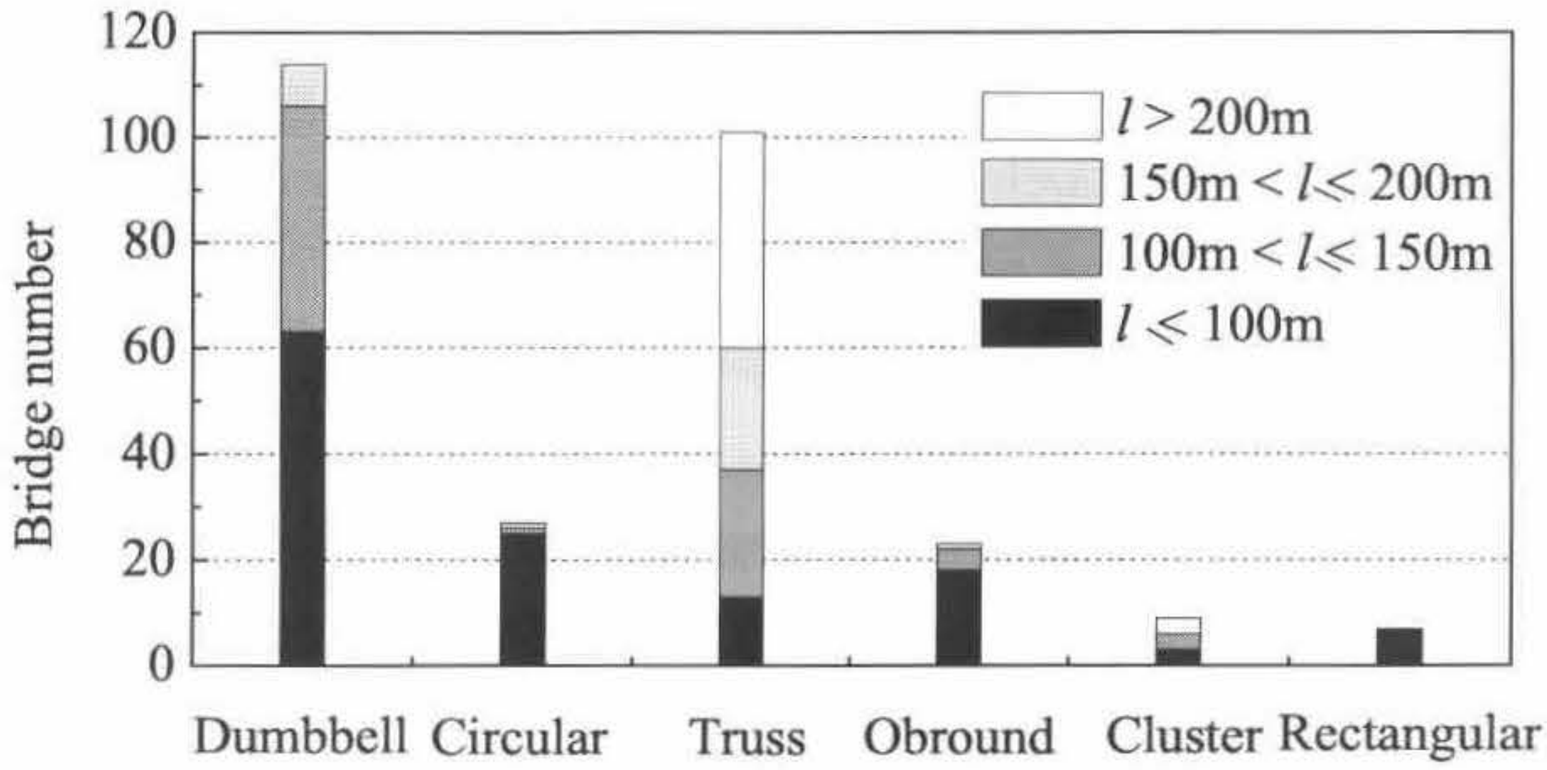

Figure 2-26 Different arch cross sections for CFST arch bridges

2.4.2.4 Ratio of steel area over concrete area

Figure 2-27 and Figure 2-28 illustrates the ratio of steel area over concrete area (α) at the cross section of CFST arches for bridges with different arch spans and opened to traffic in different years, respectively. It can be observed that the generally used ratios of α cover a range of about 0.04 to 0.16, which is relatively low compared to CFST tall buildings with the α ratio of 0.08~0.2.

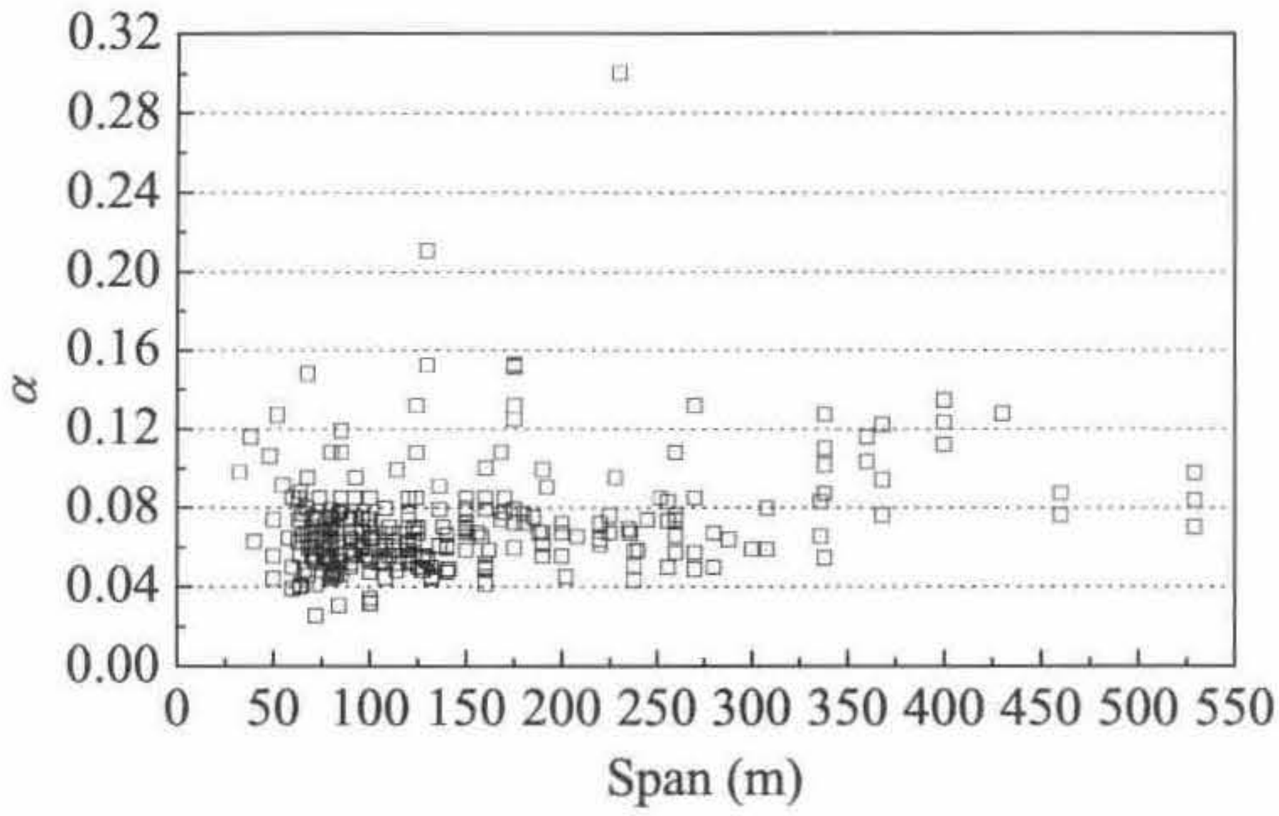

Figure 2-27 Ratio of steel area over concrete area at the cross-section of CFST members for arch bridges with different span length

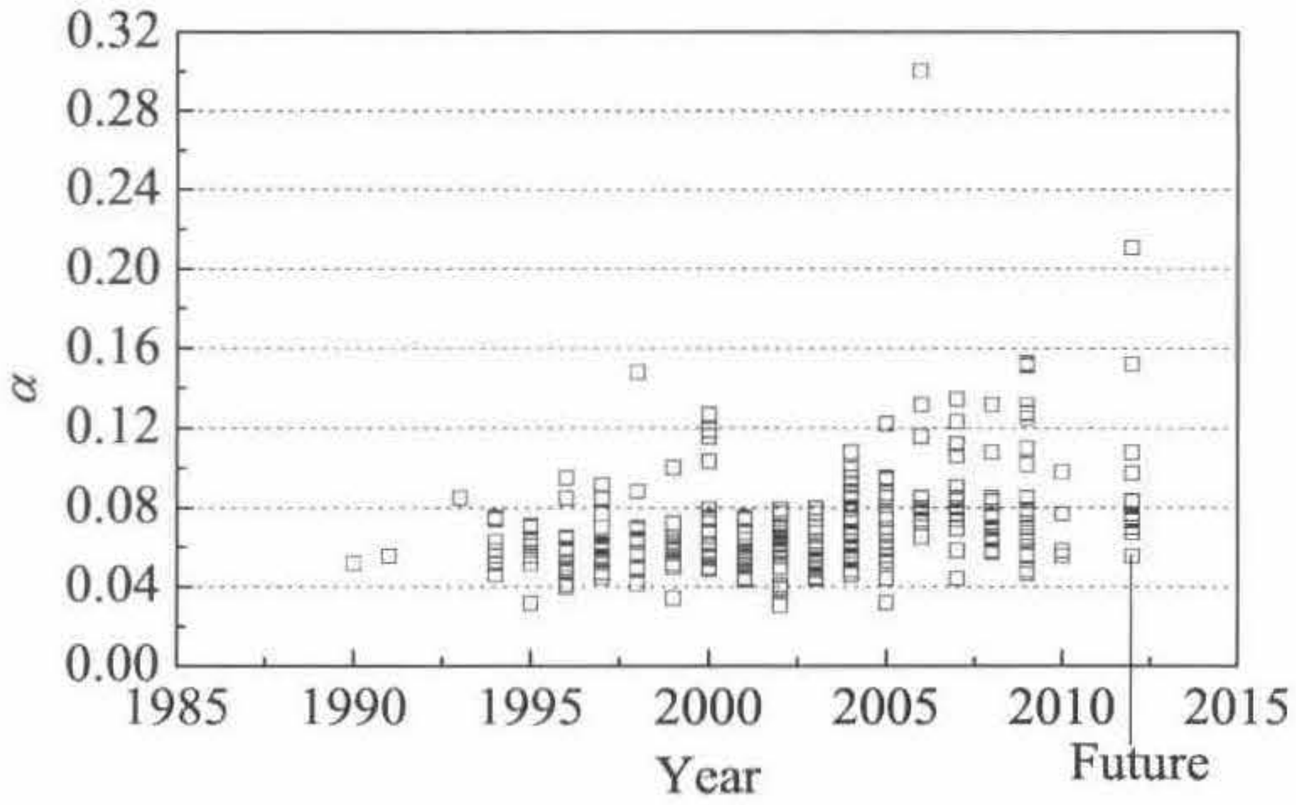

Figure 2-28 Ratio of steel area over concrete area at the cross-section of CFST members for arch bridges built in different years

Among all the CFST arch bridges, 85% have the α ratio smaller than 0.08, some even lower than 0.04. The value of α adopted in CFST arch bridges increases with the span length and with the year. Even for the 85 bridges with a span length longer than 150 m, only 3 bridges have a α ratio larger than 0.12, others are all within the range of 0.04~0.12. As a result, the time-dependent behaviour of the core concrete has a more considerable effect on static response of CFST arch bridges. The one bridge with the α ratio higher than 0.3 is the Second Saikai Bridge built in Japan and the Gao Yang Bridge, currently under construction in China, has a ratio for α of 0.21.

2.4.3 Material information

2.4.3.1 Steel

The application of steel tubes with different yield strength (f_y) in CFST arch bridges built in China is presented in Figure 2-29. Form Figure 2-29, it can be noted that steel with the yield strength of 345 MPa is the commonly specified material for the steel tubes used in CFST arches especially when the span of the bridge gets longer or the bridge is built more recently. The percentage of bridges using steel with a yield strength of 345 MPa is 83% (of the total number of bridges), 91% of bridges

with spans longer than 150m, and 92% of bridges opened to traffic after 2000. Only for one out of the 42 bridges completed after 2000 the steel has a yield strength of 235Mpa and its span is greater than 150 m.

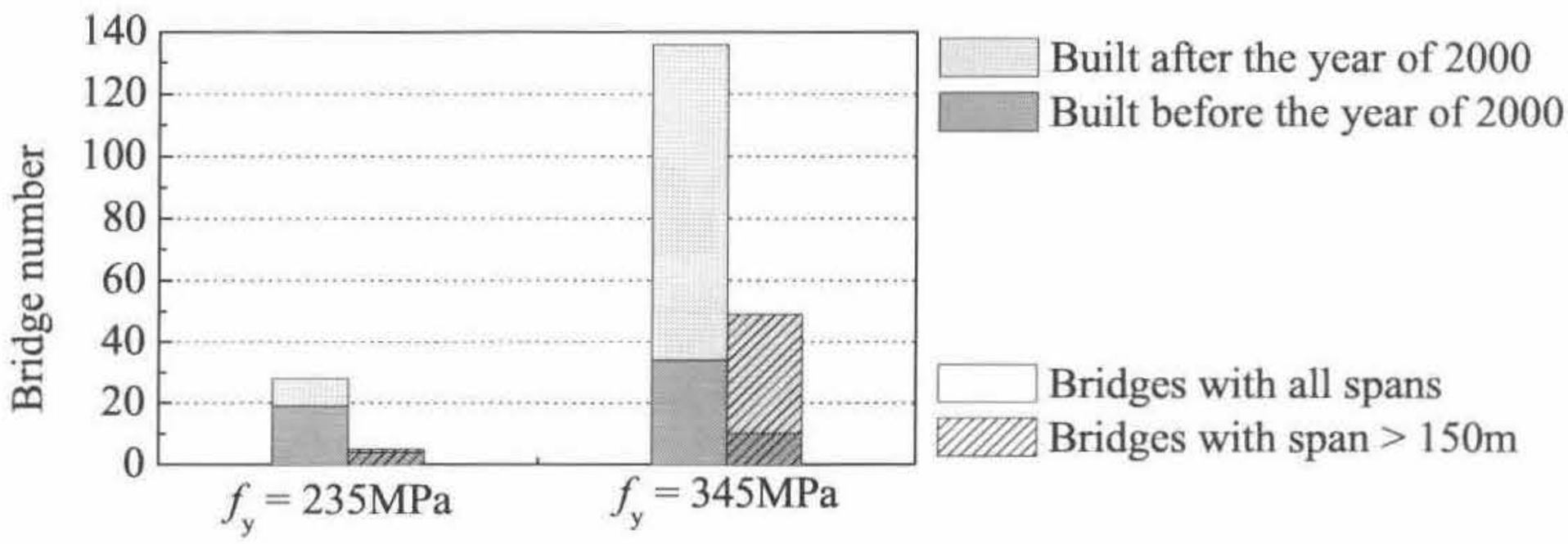

Figure 2-29 Application of steel with different strengths in CFST arch bridges

2.4.3.2 Core concrete

The concrete adopted to fill the steel tube in CFST arches have a cubic characteristic strength ranging from 30 MPa to 60 MPa, equivalent to a cylinder strength between 24.2 and 50 MPa. Figure 2-30 compares the number of CFST arch bridges using core concrete with different strengths. In this figure, the concrete strengths are graded following the Chinese Code (GB 50010-2002), with the characteristic strength being measured from concrete cubes with the dimensions of 150×150×150 mm ($f_{ck\text{-}cube}$). The corresponding cylinder characteristic strengths ($f_{ck\text{-}cylinder}$) are listed in Table 2-1 (CEB-FIP 1993).

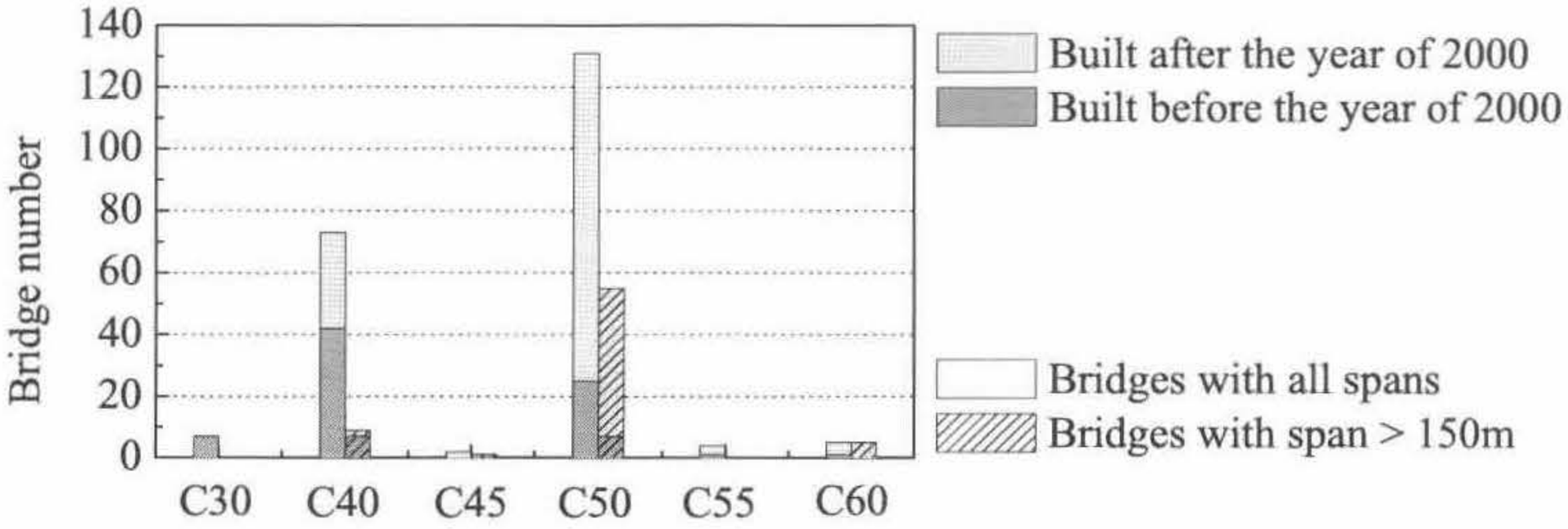

Figure 2-30 Application of concrete with different strengths in CFST arch bridges

Table 2-1 Characteristic strength values (MPa)

Concrete grade	C30	C40	C45	C50	C55	C60
$f_{ck\text{-}cube}$	30	40	45	50	55	60
$f_{ck\text{-}cylinder}$	24.2	32.3	36.2	40	45	50

From Figure 2-30 it can be noted that, as expected, the core concrete strength tends to increase for more recent bridges and with longer spans. C50 concrete (equivalent to a cylinder compressive strength of 40 MPa) is the most popular concrete grade in the standing CFST arch bridges, with 59% applications in the total number and 79% within bridges with the span longer than 150 m. C40 concrete (equivalent to a cylinder compressive strength of 32.3 MPa) is also commonly adopted in CFST arches, especially for those bridges built before 2000, among which 55% built with C40 concrete. There are 7 bridges which used C30 concrete to fill the steel tubes and their spans remained below 125 m. After 2000, C30 concrete (equivalent to a cylinder strength of 24.2 MPa) is no longer used for the main structural members, and CFST arches started to be filled with higher concrete compressive strength, i,e, C50~C60 (equivalent to cylinder strengths in the range of 45~50 MPa).

2.5 IMPORTANCE OF CONSIDERING TIME EFFECT ON STATIC RESPONSE OF CFST ARCH

As the span of CFST arch bridges increases in length, the time-dependent behaviour of the core concrete in arch ribs becomes significant in CFST arch bridges, causing increase in arch deflections, stress redistributions between steel and core concrete sections, and even instability problems for the arches. In this section, site measured data from real bridge applications is presented to highlight the importance of considering time-dependent behaviour of the core concrete during the design and construction of CFST arch bridges.

2.5.1 Increase in arch deflection

The creep and shrinkage of the core concrete increase the deformation of the CFST members leading to more considerable deflection in CFST arch applications. For example, the constructional-site-monitor system installed on the Nan Pu Bridge (Zhe Jiang, China, span length 308 m, open to traffic in 2003) detected that the displacement of the arch crown was increased by 20 mm due to the time-dependent behavior of the core concrete in arch ribs after 230 days from concrete pumping, equivalent to 20% of the total deflection caused by its self-weight (Zhang 2007). The arch of the Ya Ji Sha Bridge (Guang Dong, China, span length 360m, open to traffic in 2000) was detected to sag by 0.12 m after one year of operation (18 months under loading from the core concrete pouring) (Xin & Xu 2003). The increased deflection of the arch caused by the time-dependent behaviour of the core concrete need to be considered in the design as it can make the arch axis deviate from the dead-load thrust line inducing incremental moments along the arch. It is also important to consider the time-dependent deflection of the arch when determining the length and jacking forces of the suspenders during the construction to ensure the flatness of the bridge deck and to prevent concrete cracking of the deck.

2.5.2 Stress redistribution

The time effects of the core concrete modifies the initial stress and strain patterns at the steel and concrete cross-sections, relaxing the stresses in the core concrete due to imposed strains, and increasing the stresses in the steel tubes. Measurements obtained from on-site monitoring of the Qian Island Lake Bridge (Zhe Jiang, China, span length 252 m, open to traffic in 2006) indicate that the stress in the steel tube at the arch crown increased by 45% 140days after the core concrete pumped into arch ribs due to the time effect (Chen et al 2007).

Used as the template and falsework of the core concrete pumping, the steel tubes normally have a relatively high initial stress which will be further increased by time effects of core concrete sometimes causing unexpected steel yielding during the

bridge service life. An example in this sense consists of the Wanxian Yangze River Bridge (Si Chuan, China, span length of 420 m, open to traffic in 1997) (Gu et al 1999). Table 2-2 lists the predicted stresses in the steel tube at the arch crown of the top flange of cross-section during construction, at the end of the construction and after 200 days of operation, with or without the consideration of time effects of the core concrete, respectively, together with the measured data at the corresponding phases. In this table, the time was measured from the closure of the steel tubular arch ribs. It can be observed that without the consideration of time effects of core concrete, the predicted stress states in the steel tube are acceptable in all the phases. After considering creep effects of the core concrete, the steel tube with the yield stress of 345MPa yield at the end of the construction, and the measured stresses are even higher (already yielded at the completion of concrete casting). Thus, time effects have a considerable influence on static response of CFST arch ribs and need to be carefully accounted for in bridge design.

Table 2-2 Stress in steel tubes of top flange at arch crown (MPa)

Time	Elastic analysis (calculated)	Time-dependent analysis (calculated)	Measured
330 days (Completion of concrete casting)	281	328	356
495 days (Opened to traffic)	310	362	406
673 days (200 days under service)	310	383	448

2.5.3 Creep buckling

The CFST arches may become unstable due to creep buckling. There are two kinds of creep buckling problems as outlined by Bazant & Cedolin (2003).

One is for the situation when the dead-to-live load ratio is small. In this context, the stresses in the member under the dead load multiplied by its safety factor are within

the service stress range. In this case, the creep law of concrete is approximately linear and the failure of the column occurs in this case due to the application of a sudden overload representing the live load multiplied by its safety factor. The effect of creep is to increase the deflections due to initial imperfections prior to the application of the live load. During the failure process caused by the sudden overload, creep plays no role and the analysis may be carried out in the usual time-independent manner, although the nonlinear behavior of concrete under the overload needs to be taken into account. In this context, the purpose of the creep buckling analysis is to provide the initial conditions for the analysis of buckling due to the rapid overload. The increase of the member deflection due to creep prior to the overload must be taken into account in the analysis. Also, one may have to consider changes in the nonlinear properties caused by previous loading histories.

The other creep buckling problem relates to the case of large dead-to-live load ratio when dead load multiplied by its safety factor brings the material of the member into its nonlinear creep range. In this case, the members under sustained loads become generally unstable after a certain period of time which can be characterized in terms of a critical time. For this kind of problem, the creep analysis needs to be nonlinear.

For the CFST arch bridges with the span longer than 150 m, the stress level in the core concrete under service loading is normally within the linear creep range (less than 50% of the concrete strength), and the stability of the structures under earthquake load combination is the dominant designing case due to the low width to span ratio (Cui 2003, Zhao 2005), making the first creep buckling problem the critical one for this kind of structure.

2.6 CONSIDERATIONS ON THE LONG-TERM BEHAVIOUR OF CFST ARCH BRIDGES

Due to the necessity of considering the time-dependent behaviour of the core concrete in the design and the on-site monitor programmes of CFST arch bridges, an accurate prediction of the long-term response of CFST arches is required. There

is no current design guideline dealing with the design of CFST arch bridges. In 2008, the Highway Planning and Design Institute in Sichuan Provincial Communications Department wrote a design guide book for CFST arch bridges (Highway 2008). This book highlights that the creep and shrinkage in the core concrete of the arch rib should be considered in the design but no specific provisions were provided on how to consider such effects, leaving designers no choice but to refer to codes dealing with reinforced concrete bridges (JTG D62-2004) and standards on composite buildings (DL/T 5085-1999) to consider the long-term response of CFST arch bridges. The particularity of the time-dependent behaviour of CFST arches, when compared to the one of reinforced concrete bridges, relies on the absence of drying creep and shrinkage due to the presence of the steel tubes and on the use of different concrete mixes. Provisions available in design guidelines of composite buildings are not suitable for the loading of concrete at its early concrete ages. These three aspects related to the occurrence of creep and shrinkage in CFST arches are presented in detail in the following.

2.6.1 Creep and shrinkage

According to Neville (1995), the creep measured in a concrete specimen subjected to a sustained load consists of basic and drying creep. The former one is defined as the time-dependent deformation which occurs when concrete is loaded in a sealed condition so that moisture cannot escape while the latter one accounts for the additional creep induced from drying of the specimen. In the same way the two shrinkage components are defined as the drying shrinkage, which is associated with the loss of moisture from the concrete under drying conditions, and the autogenous shrinkage, which occurs as water is removed internally by chemical combination during hydration in a moisture sealed state (Bazant 1988).

The particularity of the time-dependent behaviour of CFST members relies on the fact that, being the concrete under sealed condition, no moisture exchange occurs with the environment. As a consequence of this, only basic creep and autogenous shrinkage will occur in the core concrete of CFST members, leading to a much smaller creep and shrinkage deformation compared to members with concrete

exposed to the air. Tan & Qi (1987) conducted comparative experiments on long-term deformation of circular CFST short columns and plain concrete short columns under the same stress level. Experimental results indicated that the long-term deformations of the CFST columns are only 74%~42% of that in the corresponding plain concrete ones after 60 days under sustained loading. Uy (2001) experimentally compared the shrinkage of the core concrete in square steel tubes with those exposed to the air, and found out that the growth rate of the shrinkage deformation in CFST specimens decreased much faster than in plain columns.

2.6.2 Concrete mix

Monitor programs carried out in construction sites of CFST bridges have pointed out that, for this structural form, there is the tendency of the concrete to separate from the hollow steel tubes. In some cases this behaviour may become sufficiently severe to affect the ultimate capacity of the structural system (Yang et al 2008). Some of the main reasons at the basis of this separation include poor pouring and curing conditions, shrinkage of the concrete core, and daily temperature fluctuations. A possible solution to address these problems is to add expansive additive to the concrete mix, therefore reducing the occurrence of shrinkage and preventing the separation between the steel and concrete components. These composite members are referred to as expansive concrete filled steel tubes (ECFST). This approach is commonly used for the construction of modern CFST large-span bridges. The amount of the expansive additive is generally around 13% of the cement weight with the minimum value of 11.3% (Han Jiang 3rd Bridge) and the maximum value of 15.2% (Nan Pu Bridge).

The existence of expansive admixture may lead to different mechanical performance of CFST members. Li & Wang (2002) reported that the microstructure of the expansive concrete is more condensed than that of normal concrete due to the confinement of the steel tube. Chang et al (2009) pointed out that the ultimate capacity of CFST short columns with expansive additive is higher than common CFST short columns. Wang (1994) observed that the rate of increase of the time-dependent deformations measured from CFST columns with the amount of the

expansion admixture in the core concrete of the order of 20% of the cement weight tended to decrease earlier than those with normal concrete in the long-term test. Ai (2007) compared the long-term deformation of one CFST column with expansive additive taking 6% of the weight of cement to the companion CFST column with normal concrete, and found that after 274 days under sustained loads, the incremental deformation of the specimen with expansive additive was 10% higher than the companion specimen. It can be noted that there is a high possibility that the time-dependent behaviour of the expansive concrete filled steel tubular specimens are different from the CFST specimens with normal concrete, which needs further experimental data on specimens with the amount of expansive additive normally adopted in CFST arch bridges to clarify.

2.6.3 Loading at early concrete ages

Current construction practice tends to load CFST arches at a concrete age well before 28 days due to modern stringent construction time. The core concrete in the bottom chords of the Nan Pu Bridge was pumped 12 days after the concrete pumping in the upper chord of the same rib, causing the compressive stress of the core concrete in the upper chord to increase by a maximum value of 6 MPa (Zhang 2007). The two 80 m span dumbbell shaped CFST arch bridges presented by Yin & Cao (2007) and by Yang & Yan (2008) had their three core concrete components pumped every 7 days. For the Jin Shan Bridge, the time interval between the two concrete pumping procedures on the same arch rib is only 4 days (Wang & Hui 2010). The construction sequence adopted for the Dong-Guan Waterway Bridge used intervals of only one day (see section 5.3.2). With loads applied at such early ages, the creep behaviour of the core concrete can have a more considerable effect on the static response of CFST arches, making the corresponding provisions in DL/T 5085-1999 provided based on experimental results of specimens loaded at 28 days unsuitable.

Based on the discussion in this section, it can be noted that the current codes cannot be used in the design of CFST arch bridges, and hence research work needs to be conducted to better understand the long-term behaviour of ECFST members subjected to sustained loading applied at an early concrete age.

2.7 LITERATURE REVIEW ON THE TIME-DEPENDENT ANALYSIS OF CFST ARCH BRIDGES

2.7.1 Concrete models

An accurate concrete model to describe the creep and shrinkage behaviour of the concrete material is the first step to well predict the long-term response of concrete members. For many decades, researchers have been dedicated to propose a proper mathematical model to predict the creep and shrinkage of concrete. Examples include the double power law for basic creep (Bazant & Osman 1976) which was adopted in ACI 209 code provisions (ACI 209 1992), the CEB-FIP Mode Code 90 (MC90) (CEB-FIP 1993), the Muller-Kuller model (MK) for the high performance concrete (Muller & Kuller 1996), the AFREM model for the high performance concrete (Le Roy et al. 1996), the GL2000 model (Gardner & Loackman 2001), the B3 model (Bazant & Baweja 2000), and the Euro Code model (EC2) (BSI 2004).

Table 2-3 lists the parameter ranges that the seven models mentioned above are restricted to, in which n denotes the stress level on the concrete; SFC stands for concrete containing an amount of silica fume equal to at least 5% of the weight of Portland cement; the cement types of I, II, III are for Portland cement concrete representing the general, low rate and high rate hydration speed of the cement, respectively; and '-' means the range of the corresponding parameter is not provided in the published paper. The following three concrete models have not been considered in the following predict the time-dependent response of concrete for CFST applications: (i) MK model because developed specifically for high-strength concrete; (ii) ACI model as not suitable for concrete loaded at a very early age and (iii) GL2000 model due to its very limited range of w/c ratio.

Table 2-3 Parameter ranges for different concrete models

Feature	B3	ACI	MC90	GL2000	AFREM	MK	EC2
t_0 (days)	≥1	≥7	≥0.5	≥1	-	≥0.5	≥0.5
RH (%)	-	> 40	40~100		-	-	-
n	≤0.45	≤0.5	<0.6	0.3~0.4	-	-	-
Temperature (°C)	-	21	-20~80		-	-	0~80
Cement type	I, II, III	I, III	-	I, II, III	SFC or non SFC	-	-
w/c	0.35~0.85	-	-	0.4~0.6	-	-	-
a/c	2.5~13.5	-	-	-	-	-	-
f_{c28} (MPa)	17~70	-	12~80	≤82	40~80	60~120	-
c (kg/m3)	160~720	-	-	-	-	-	-
Aggregate type	-	-	-	-	-	Quartzitic aggregates	-
Aggregate concentration	-	-	-	0.65~0.75	≥0.67	-	-

The concrete creep and shrinkage are affected by the degree of hydration and the composition of the concrete. The former one depends on the loading age of concrete (t_0), the size and shape of the member, the temperature and the duration of loading (t-t_0). The latter one depends on a number of factors including the type of cement, the type of aggregates, water-cement ratio (*w/c*), air-cement ratio (*a/c*), cement content (*c*). These factors also influence the concrete strength (f_{c28}) which sometimes researchers tend to use as the parameter to predict the long-term behaviour of concrete with different composition for simplification.

Table 2-4 presents the influential factors that the seven models considered and Table 2-5 details their main characteristics, where t_s is the age of the concrete when shrinkage starts, *RH* represents the relative humidity of the air, '√' depicts whether the corresponding factor is considered in the model, while '×' outlines that a factor is not included, and '-' stands for information not provided in the published paper.

Table 2-4 Parameters considered in different concrete models

Feature		B3	ACI	MC90	GL2000	AFREM	MK	EC2
t-t_0 (days)		√	√	√	√	√	√	√
t_0 (days)		√	√	√	√	√	√	√
t_s (days)		√	√	√	√	√	√	√
f_{c28} (MPa)		Mean strength	-	Mean strength	Mean strength	Characteristic strength	Mean strength	Mean strength
RH (%)		√	√	√	√	√	√	√
Member shape		√	√	×	×	×	×	×
Member size		√	√	√	√	√	√	√
Concrete temperature		×	×	√	×	×	√	√
Slump		×	√	×	×	×	×	×
Concrete mix	Cement content	√	√	×	×	×	×	×
	Air content	×	√	×	×	×	×	×
	a/c	√	√	×	×	×	×	×
	w/c	√	×	×	×	×	×	×
	Aggregate stiffness	×	×	×	√	×	×	×
	Cement type	×	×	√	√	×	√	√

Table 2-5 Equation components for different modes

Components	B3	ACI	MC90	GL2000	AFREM	MK	EC2
Autogenous shrinkage	×	×	Not differentiate	Not differentiate	√	Not differentiate	√
Drying shrinkage	√	√			√		√
Basic creep	√	Double power law	Not differentiate	Not differentiate	√	Not differentiate	Not differentiate
Drying creep	√	√			√		

From Table 2-4 it can be observed that the B3 and ACI models have the most comprehensive input of the factors influencing creep and shrinkage, while the other five concrete models have a lower level of complexity for thier input data. Table 2-5 indicates that among those four potential acceptable concrete models for long-term response prediction of CFST arch bridges, only the AFREM model separates between basic and drying creep as well as autogenous and drying shrinkage.

The other three concrete models require particular considerations on the specifications on their input data to model the time-dependent response of CFST arch bridges.

2.7.2 Basis of the Analysis

Different methods of analysis are available to capture the long-term behaviour of the concrete. including the step-by-step solution according to the integral-type creep model based on the principle of superposition (Bazant 1975), the step-by-step solution according to a rate-type creep model based on the Kelvin or Maxwell chain (Bazant 1994), and the algebraic methods such as the age-adjusted effective modulus method (Bazant 1972), the mean stress method (Bazant 1988), and the effective modulus method (McMillan 1916, Faber 1927).

For basic creep, Bazant et al (2008) pointed out that there is no evidence of systematic deviations from the principle of superposition, i.e., from the solutions based on aging linear viscoelasticity. The relaxation tests of sealed specimen at constant temperature are predicted by the principle of superposition from the compliance data as closely as it can be expected in view of the inevitable statistical experimental scatter (Bazant 1988).

The principle of superposition is considered valid if the following conditions are satisfied (Bazant 1988):

1) stress levels less than about 45% of the concrete strength.

2) appreciable reductions in strain magnitude due to unloading do not occur.

3) no significant change in moisture content distribution during creep occurs.

4) no large, sudden, stress increase long after the initial loading occurs.

In practice, all of these conditions may be violated to some extent, but experience has shown that conformity with the first and third conditions, which are the most important, is generally true in CFST arch bridge applications. The second and fourth conditions, which are less important, suffer more substantial violations in the real application, but experience has shown that strain predictions are still acceptable (Cluley & Shepherd 1996).

Among the formulations listed above, the step-by-step method according is considered to be accurate enough for time-dependent analysis on CFST arch bridges.

2.7.3 Experiments on long-term behaviour of CFST members

In 1980s, Tan & Qi (1987) carried out 40 long-term tests on circular CFST specimens subjected to both axial and eccentric loads. These samples were loaded at different ages of concrete varying from 28 days to 13 months. One decade later, Terry et al. (1994) conducted similar experiments on circular CFST samples axially loaded at an earlier age of the concrete, i.e. 18 days. Li & Gu (2008) and Xie & Yin (2009) experimentally measured the long-term deformation of circular CFST specimens with an age at loading of 14 days which subjected to eccentric and axial loading, respectively. Lin (2002) and Kwon et al. (2005) reported other long-term tests on circular columns axially loaded at 28 days after the casting of the concrete. The effect of decaying sustained loads on the overall long-term response was investigated experimentally by Ichinose (2001). The first tests on square CFST specimens were performed by Morino (1996). This test series included six concentrically loaded columns, two eccentrically loaded columns and one flexural member. In all cases the load was applied at 28 days after the concrete pour. Similar cross-sections were tested by Uy (2001) and Kwon et al (2007) applying axial loading at 14 and 28 days of age of the concrete respectively. In the experiments of Morino (1996), Uy (2001) and Kwon et al (2007), the stress level in the core concrete remained within 0.4 of the mean cylinder compression strength $f_{cm}(t)$.

Higher sustained loads were reported by Han & Yang (2003) and Han et al (2004) on square and rectangular CFST specimens reaching stress levels in the core concrete higher than $0.7f_{cm}(28)$.

Wang (1994) reported the first long-term tests on six expansive concrete filled steel tubular (ECFST) short columns with identical material and geometric properties. The columns were loaded at 28 days after concrete casting at different levels of sustained axial forces maintained for a period of 100 days. The expansive additive used in his specimens weighed 20% of the weight of cement. Following Wang's work, Chen supervised the experiments on the long-term response of nine ECFST stubs with a lower amount of expansive additive (12.5% of the weight of cement) subjected to different levels of axial loads applied at 28 days after concrete casting for 1710 days (Yao et al 2007, Hu 2007).

Zhou & Cao (2008) conducted long-term test on a scaled through tied CFST arch bridge for the main purpose of investigating the long-term behaviour of carbon fiber reinforced polymer suspenders. The long-term deflection of the arch as well as the stress variations in the steel tubes and core concrete were also measured during the test by dial gauges and vibrating wire strain gauges, respectively. The scaled bridge model has a span length of 10 m with the span-to-rise ratio of 4 and a width of 2.25 m. The parabolic arch has a single circular cross-section consisting of core concrete with 28 day characteristic cylinder strength of 40 MPa and steel tube with the outer diameter of 400 mm and the wall thickness of 3 mm. The expansive additive in the core concrete weighs 6% of the cement weight. The abutment of the model was pinned on the ground. The distributed loads were applied on the concrete deck 7 days after the core concrete was poured inside the steel tubes and lasted for 271 days. It was shown that the deflection of the arch at the end of the experiment was more than 2.3 times of the original one. The stresses in steel tubes increased by 203% at the arch springing, and by 536% at the arch crown.

Shao et al (2010) published their experimental work on a 1:5 scaled segmental arch rib (the arch crown part of 24m of the real bridge) of the Mao Cao Jie Bridge, the loads were applied in four steps with the value corresponding to the real bridge, i.e. the hollow steel tube stage, the CFST rib stage without installing bridge decks, the

bridge completion stage and the service stage, and then the loads were maintained for approximately two years to observe the long-term response before increasing the loads to its design level and maintained for another half an year. It was observed that more than 90% of the total concrete creep took place in the first year, and all creep development became very slow after 2 years. The maximum relaxation of creep-induced stress in the concrete was 52.7% of the initial value, and the maximum increment of stress in the steel tube was 27.3%.

In summary, extensive experimental work has been carried out to investigate the long-term behaviour of CFST specimens filled with common concrete, covering specimens with circular, square and rectangular cross-sections subjected to axial or eccentric loads with loading ages varying between 7 days and 341 days after concrete casting. Material properties considered consist of the mean cylinder strength at 28 days of concrete age (f_{cm28}) ranging from 15 MPa to 60 MPa, a ratio of the steel area over the concrete area (α) from 0.02 to 0.2, and stress levels in the core concrete from $0.1f_{cm28}$ to $1.1f_{cm28}$. Considerable time-dependent deformations were observed in all the experiments. However, only very limited research has focused on the time effects in ECFST applications, and the currently available experimental results on ECFST columns are obtained from tests with sustained loads applied at 28 days from concrete casting, despite of the fact that current construction practice tends to load ECFST specimens at a concrete age much earlier than 28 days due to stringent construction requirements.

2.7.4 Numerical analysis on long-term behaviour of CFST members

Many researchers have investigated the time-dependent response of CFST members by means of numerical simulations. For example, Terry et al. (1994), Uy (2001), Han et al. (2004) and Kwon et al. (2005) predicted the long-term response of CFST short columns with the core concrete time-dependent behaviour modelled in the format of the ACI-209 (ACI 1992). These analyses have relied on the use of the Age Adjusted Effective Modulus (AAEM) method to account for the concrete time effects. The final creep and shrinkage coefficients measured in these experiments varied with a range of ±25% partly attributed to the use of different concrete mixes,

aggregate sizes and types, and initial times of first loading. Kwon et al. (2007) reported some numerical work on the creep behaviour of CFST specimens based on the AAEM method while modelling the concrete time-dependent response using the Model Code 90 (CEB-FIP 1993) with the material coefficients identified from a regression analysis carried out on the experimental results to determine the basic concrete creep. Ichinose et al. (2001) utilised the Kelvin model to depict the concrete time-dependent behaviour and assumed the stress in the core concrete to decay with time following an exponential trend. Naguib & Mirmiran (2003) evaluated the long-term response of CFST specimens with and without the interface bond, using the rate of flow method and the double power law function for the basic concrete creep and using the step-by-step method to consider the stress redistribution taking place with time. Cheng et al. (2005) introduced a three-dimensional nonlinear laminated element for the long-term modelling. They assumed the creep behaviour to be described by the Kelvin model and implemented it numerically by means of the Euler algorithm. Gu et al. (2005) presented a creep function in the form of Dirichlet series with the coefficients regressed from the material experiment results for the concrete in the Wu Xia Long River Bridge. Based on this creep function and AAEM method, software is developed to theoretically study on the long-term behaviour of CFST arch bridges (Zeng & Gu 2005). Based on Burgers model, Wang (2006) proposed the formula to consider the creep of the sealed core concrete under three-dimensional compression. With this formula, the long-term response of circular and square CFST columns subjected to constant concentric and eccentric loading is theoretically analysed by means of the step-by-step method.

All the numerical studies draw the conclusion that the time-effects on the static response of CFST members is significant and should be taken into account in the design. However, researchers have performed numerical analyses to predict the long-term behaviour of CFST members based on different concrete models and analysis techniques usually applied to their specific sets of experimental results (Han & Wang 2007). Although extensive work is currently available in the literature to outline that different concrete models can lead to very different predictions of the

material responses (Brooks & Al-Qarra 1999, Howells et al. 2005, Sassone & Chiorino 2005, Geol et al 2007, ACI 2008, Bazant & Li 2008), only limited work has been carried out in general to identify how these variations in material predictions affect the structural response and long-term deformations in structural systems (Han & Wang 2007, Gilbert & Ranzi 2011). In the particular case of CFST members there is no recommended concrete model to be used by a designer for service calculations. In this context, comparative studies should be conducted on CFST members with different predictive material models and analysis methods to guide the design of CFST arch bridges.

2.7.5 Long-term analysis on CFST arch bridges

The core concrete inside the CFST arches is segmentally pumped into the steel tube. Several studies have been carried out to experimentally and numerically investigate the time-dependent behaviour of segmentally constructed reinforced concrete girder bridges or cable stayed bridges (such as Cluley & Shepherd 1996, Marí & Valdés 2000, Robertson 2005, Jung et al 2007 and Somja & Goyet 2008). It is commonly accepted that the segmental construction process need to be considered to predict the static response of bridges (Marí & Valdés 2000, Chiorino 2005, Somja & Goyet 2008). Liu et al (2002) developed a finite element model for the Wanxian Yangtze River Bridge, a 420m-span steel tube reinforced concrete deck arch bridge (Figure 2-4), accounting for time effects.

Methods of analysis with the capability of considering time-effects, the segmental construction process, the ageing of the concrete and the geometric nonlinearity are brought forward in all the papers mentioned above. However, programs developed in-house by research groups limit the use of the modeling in real bridge designs. The conclusions obtained from these papers does not represent the possible response of CFST arch bridges as their long-term behaviour is much smaller due to the fact that the core concrete is encased inside the steel tube. Unlike the stayed, girder or deck arch bridges, the stiffness of the piles and the restraint of the soil to the piles have a considerable influence on the static behaviour of the tied arch bridges (Wang & Hui 2010) and need to be considered in the analysis especially

during the construction process, making the finite element model of the through or half-through arch bridges more complex. As a result, it is necessary to conduct long-term analyses on tied CFST arch bridges using whole bridge models with the considerations on construction process.

An explicit model to simulate the long-term response of tied CFST arch bridges with full consideration of the construction process presents a challenge to researchers as it requires the ability to simulate the incorporated work of arches, piles, and ties, to depict the time-dependent behavior of the encased core concrete under the varying stress history, to consider the ageing of the concrete, to describe the varying stiffness of the structure during the staged construction process, and to take account of the geometric nonlinearity.

In this context, extensive research has been carried out in China to analyze the long-term response of CFST arch bridges introducing different levels of simplifications. Some researchers performed numerical studies under the assumption that all the loads were applied at the concrete age of 28 days to simplify the analysis process (Wu & Qu 1991, Xie & Qin 2001, Gu et al 2001, Cheng 2004, Yao 2006, Tian et al 2007, Wang et al 2007, and Shao et al 2010). Such simplification may not be reliable for CFST arch bridges as the core concrete ages can vary from 3 days to more than one year when loads are applied at different construction stages. Neglecting the variation of the concrete loading ages may lead to the underestimation of the static response in the initial construction stages and an overestimation at the end.

Zhang (2007) built a finite element model with ANSYS to analyze the long-term response of a CFST arch bridge with the consideration of the varying loading ages of the core concrete, but the bending moment on the arches was assumed to have no contribution on the long-term response, which has been proved to be not acceptable by Wang et al 2007. Geometric nonlinearity and the shrinkage effect were also neglected in Zhang's analysis.

In summary, none of the available research work has considered the ageing of the concrete, the geometric nonlinearity, and the incorporated contribution of the axial

forces and bending moment to the long-term response of the structure at the same time, and no research has been conducted to investigate the reliability of neglecting the variation of the loading ages of the core concrete during the construction process when predicting the long-term response of CFST arch bridges.

Although the live load needs to be considered in the quasi-permanent combination during the long-term analysis in accordance with Chinese guidelines (JTG D62-2004), many researchers investigated the long-term response of CFST arch bridges without their inclusion (Zhang et al 2001, Yu et al 2003, Cheng 2004, Xiong & Liu 2005, Tian et al 2007, Zhang 2007). No research work has been carried out to clarify the influence of the live load on the long-term response of the CFST arch bridges during operation.

It can be concluded that the time-dependent behaviour of the core concrete has a considerable influence on the arch deflections and can cause significant stress redistributions between steel and concrete components, which need to be considered in the bridge design.

2.7.6 Time effects on the stability of CFST members

The creep buckling behaviour of concrete columns have been investigated experimentally and numerically for decades (e.g. Bazant 1968, Bazant & Tsubaki 1980, Behan & O'Connor 1982, Minahen & Knauss 1993, Knalil et al 2001, Bradford 2005). It was shown that the time-dependent behaviour of concrete can have a considerable influence on the stability of the long columns. For example, a reinforced concrete columns with slenderness in the range of 18~63 can undergo a reduction in the load carrying capacity of 10-40% due to creep when subjected to sustained load of the order of 60% of its instantaneous critical loading. In 2006, Wang et al (2006) conducted theoretical and experimental analysis on shallow arches with a span-to-rise ratio of 25. Under sustained distributed loads of 79, 70 and 59% of their short-term buckling loads, the arches buckled after 70, 128 and 165 days, respectively. Bocklhold & Petryna (2008) conducted theoretical work on creep buckling of reinforced concrete shallow shells based on elasto-plastic

continuum damage theory for the concrete, a novel nonlinear creep model, and an efficient and locking-free continuum-based finite shell element.

However, not much research has focused on the creep buckling behaviour of CFST columns or CFST arches. Some researchers theoretically analyzed the stability of CFST long columns under sustained loading (Zhong 1987, Han & Yang 2003, Han et al 2004). It was noted that time effects of the core concrete can reduce the buckling load of CFST columns by a maximum of 25%. Liu (2008) numerically investigated the influence of the time-dependent behaviour of the concrete core on the in-plane stability of a 280m span CFST truss arch bridge which was subjected to sustained service loads for one year before reaching its critical loading. Results indicate that for arches with the span-to-rise ratio of 5, time effects have limited influence on the in-plane stability, causing only 0.11% reduction of the critical load. Wang et al (2011) developed the nonlinear in-plane equilibrium and buckling equations for CFST circular arches to investigate their creep buckling due to sustained loading. It was concluded that the time-dependent behaviour of the concrete core can cause a maximum decrease of 29% of the critical loads for CFST circular arches within the bridge designing life (i.e. 100 years).

In this context, no analysis has been conducted to date to investigate the influence of the time-dependent behaviour of the concrete core on the stability of CFST arches in the lateral direction which, as discussed in section 2.4.1.2, represents the main buckling mode for long-span CFST arch bridges.

CHAPTER 3 EXPERIMENTAL STUDY ON TIME-DEPENDENT BEHAVIOUR OF EXPANSIVE CONCRETE FILLED STEEL TUBULAR COLUMNS

3.1 INTRODUCTION

In CFST arch bridges, expansive additive is generally added in concrete inside the steel tubes to prevent the tendency of the concrete to separate from the steel. As pointed out in section 2.7.3, there is no experimental study carried out to investigate the time-dependent behaviour of this kind of members. In this context, this chapter intends to provide new experimental data describing the time-dependent behaviour of expansive concrete filled steel tubular (ECFST) circular short columns subjected to sustained axial loads first applied at early concrete ages ($t_0 \leq 28$ days, where t_0 is the time of first loading). The long-term deformation of eleven ECFST specimens was monitored over five months to study the influence of t_0 and of the applied stress level on their time-dependent behaviour. After five months under sustained loads, some of these specimens were tested to failure while the remaining ones were kept under sustained loads for a longer duration. The measured ultimate capacities of those specimens under sustained loading were compared against the one from the companion specimen (prepared with the same concrete mix at the same casting day) which was kept unloaded for the whole duration of the long-term tests to gain insight into the possible influence of time effects on the ultimate behaviour of ECFST specimens. Investigations on the confinement effect on long-term behaviour of ECFST specimens in service conditions are then provided based on the longitudinal and circumferential deformations measured on the steel tubes during the failure tests.

3.2 EXPERIMENTAL PROGRAMME

3.2.1 Preparation of Specimens

Eleven ECFST short columns were prepared for testing. For clarity these specimens have been subdivided into eight groups numbered from I to VIII. The details of specimens are listed in Table 3-1.

Table 3-1 Details of the tested ECFST specimens

Specimen	$D \times t_s \times L$ (mm)	α	N_L (kN)	t_0 (days)	Batches	n_L	$n_c(t_0)$	N_{ul} (kN)	K_f
I-1	140×2.63×420	0.079	303	5	Second	0.38	0.52	1350	1.125
I-2	140×2.63×420	0.080	303	5	Second	0.38	0.52	1200	1.000
II-1	140×2.62×420	0.079	304	7	Second	0.38	0.61	—	—
II-2	140×2.61×420	0.079	304	7	Second	0.38	0.61	—	—
III	140×2.62×420	0.080	290	27	First	0.33	0.38	1350	1.125
IV	140×2.66×420	0.079	290	27	Second	0.36	0.45	1300	1.120
V	140×2.60×420	0.080	441	30	First	0.50	0.58	—	—
VI	140×2.65×420	0.079	441	30	Second	0.55	0.68	—	—
VII-1	140×2.59×420	0.078	515	29	First	0.58	0.68	1350	1.125
VII-2	140×2.60×420	0.079	515	29	First	0.58	0.68	1350	1.125
VIII	140×2.65×420	0.080	0	—	First	0	0	1200	—

Some main test results are also included in Table 3-1, which will be illustrated later in this Chapter. Tabulated values include the outer diameter D, the thickness of the steel tube t_s, the length of the specimen L, the ratio of steel area over concrete area $\alpha = A_s/A_c$, the sustained axial force N_L, the concrete age at first loading t_0, the ratio of the sustained load over the cross-sectional ultimate capacity n_L (where $n_L = N_L/N_u$ and the ultimate capacity N_u is calculated at 28 days after the concrete casting), the initial stress level in the concrete $n_c(t_0) = \sigma_c(t_0)/f_{cm}(t_0)$ (where $\sigma_c(t_0)$ denotes the initial concrete stress of the time of first loading; $f_{cm}(t_0)$ defines the corresponding mean

cylinder compression strength), the tested ultimate failure load N_{ul}, and the ratio K_f of the ultimate failure load observed for specimens tested under sustained load (i.e. specimens I, III, IV, and VII) over the ultimate capacity of the specimen kept unloaded during the long-term tests (i.e. specimen VIII). The ratio K_f provides an overview of the effect of creep on the ultimate capacity of the ECFST specimens. The adopted ultimate capacity N_u has been calculated according to Zhong & Zhang (1992):

$$N_u = A_{sc} \cdot (1.212 + B\xi + C\xi^2) f_{ck} \tag{3-1}$$

where A_{sc} ($=A_s+A_c$) is the total area of the cross-section of the specimen, mm^2; f_{ck} denotes the characteristic compression strength of 150mm×150mm×300mm concrete prisms tested at 28days from concrete casting which can be converted to an equivalent cylinder concrete strength (f_{cm28}) as recommended in Chinese code (GB 50010 2002), MPa; $\xi = \alpha f_y / f_{ck}$ is defined as the confinement effect coefficient, in which f_y is the yield strength of the steel tube, MPa; $B = 0.1759 f_y / 235 + 0.974$, in which f_y is in terms of MPa, and $C = -0.1038 f_{ck} / 20 + 0.0309$, where f_{ck} is also in terms of MPa.

Eqn (3-1) well predicts the ultimate capacity of concrete filled tubes with the ratio α in a range of 0.04~0.2, and with the concrete strength f_{cm28} varying between 20 MPa and 70 MPa as specified in the Chinese code (DL/T 5085-1999).

As presented in Section 2.4, out of the 85 standing CFST arch bridges possessing a main span longer than 150 m, only 3 bridges have an α ratio larger than 0.12, others are all within the range of 0.04~0.12. In this context, the mean value of α=0.08 was adopted in the design of the specimens to reflect common construction practice. All specimens had a length-over-diameter ratio (L/D) of 3 to reduce end effects and to prevent slenderness effects on test results.

The hollow steel tubes used for the eleven specimens were cut from one single 6 m long cold rolled circular tube with an outer diameter of 140 mm and a wall thickness of 2.6 mm. A 160×160 mm steel plate of 10 mm thick was welded to the bottom end of each stub. During casting, the specimens were kept in a vertical position and the steel tubes were kept ungreased to reflect the common site practice. All the specimens

were cast on the same day in two batches. The concrete core was cast slightly higher than the steel tube to avoid the presence of gaps between the concrete core and the top steep plate before the top steel plates were welded. Immediately after the concrete pouring, the top surfaces of the specimens were tightly wrapped with plastic films to reflect the real situation in which the concrete core remains sealed during construction and in service. The plastic films were removed after 1 day and the top surfaces of the CFST specimens were ground plane and smooth. A 160×160 mm steel plate of 10 mm thick was then welded to the top of the steel tube to seal the concrete right after the smoothing operation was completed.

3.2.2 Material Properties

3.2.2.1 Steel coupon tests

Standard tensile tests were carried out on AG-250kNI tensile testing apparatus, Shimadzu Co. (Japan) to obtain the material properties of the steel tube. The sample preparation, the measurement of the geometrical properties of the coupons, and the testing speed have been carried out in accordance with Australian Code (AS 1391 2007). During the test, the deformation of the coupons was measured by strain gauges located in the middle of the coupon on both sides. A representative stress-strain curve recorded during these tests is presented in Figure 3-1 and the measured mechanical properties were: mean yield strength of 315MPa, elastic modulus of 1.79×10^5MPa and Poisson's ratio equal to 0.265.

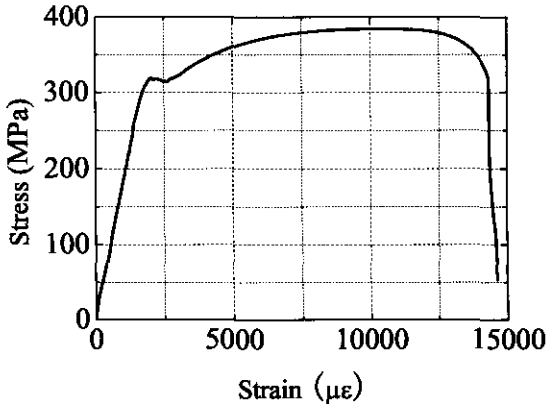

Figure 3-1 Typical stress-strain curve for the steel tube

3.2.2.2 Concrete cube tests

The concrete mix adopted for the specimens is outlined in Table 3-2, in which *w*, *c*, and *f* means the weight of the water, cement, and fine aggregate, respectively. The amount of expansive additive is 12% of the weight of the cement, reflecting the common specifications adopted in real CFST arch bridge applications.

Table 3-2 Concrete mix for the ECFST specimens

		Material (kg/m^3)							
w/c	*f/c*	*w*	Type I Cement	Fly ash	Superplasticizer	Air entraining agent	VEA expansive additive	Fine aggregate	Coarse aggregate
0.40	0.40	190	470	43	7.93	0.23	57	685	1013

Several concrete samples were prepared to measure the material properties, e.g. concrete strength and elastic modulus, at different instants of time. These included twelve cubes with the side length of 100 mm used to determine the cube strength ($f_{cu,100}$) at 3 days, 7 days and 28 days, respectively; three concrete cubes with the side length of 150 mm to evaluate the concrete strength at the time of the composite ultimate tests, i.e. approximately 150 days after the concrete casting; and nine concrete prisms with the dimension of 100 mm×100 mm×300 mm to measure the modulus of elasticity at 3 days, 7 days and 28 days, respectively.

The concrete were poured into conventional steel moulds and vibrated till fully consolidated. After completion of the casting, the top surfaces of the moulds were tightly wrapped with plastic films to reflect the sealing conditions. The concrete samples were removed from these moulds after one day and then completely sealed using plastic films.

Standard compression tests were carried out and the average strengths observed have been summarised in Table 3-3.

Table 3-3 Material property of core concrete in ECFST specimens

t (days)	Batches of concrete	Concrete Strength (MPa)			$E_c(t)$ ($\times 10^4$MPa)
		$f_{cu,100}$	$f_{cu,150}$	$f_{cm}(t)$	
3	Second	22.3	21.2	20.7	1.48
7	Second	26.5	25.2	23.6	2.94
28	First	44.9	42.7	37.2	3.31
	Second	38.7	36.8	32.7	
150	First	61.8	58.7	45.8	—

Based on guidelines (GB 50010 2002), the concrete strengths obtained from the 100 mm cube tests ($f_{cu,100}$) were multiplied with a factor of 0.95 to account for size effects and make them comparable with the capacities observed using the 150 mm cubes ($f_{cu,150}$). Equivalent cylinder strengths ($f_{cm}(t)$) have also been included in Table 3-3 in accordance with the conversion factors specified in CEB-FIP (1993).

3.3 LONG-TERM TESTS

3.3.1 Test Set-Up

3.3.1.1 Self-resisting loading frame

A self-resisting loading frame was designed to perform the long-term tests on ECFST specimens subjected to either axial or eccentric loads. Details and dimensions of the test rig are shown in Figure 3-2. With the proposed set-up two specimens can be tested simultaneously in each rig. The load was applied by a clamping force produced by tensioning the four pre-stressing bars against the two 40 mm thick load-bearing plates. The loading frames were verified and calibrated before the tests. It was shown that the proposed long-term testing set-up was capable of applying a constant sustained load up to 800 kN.

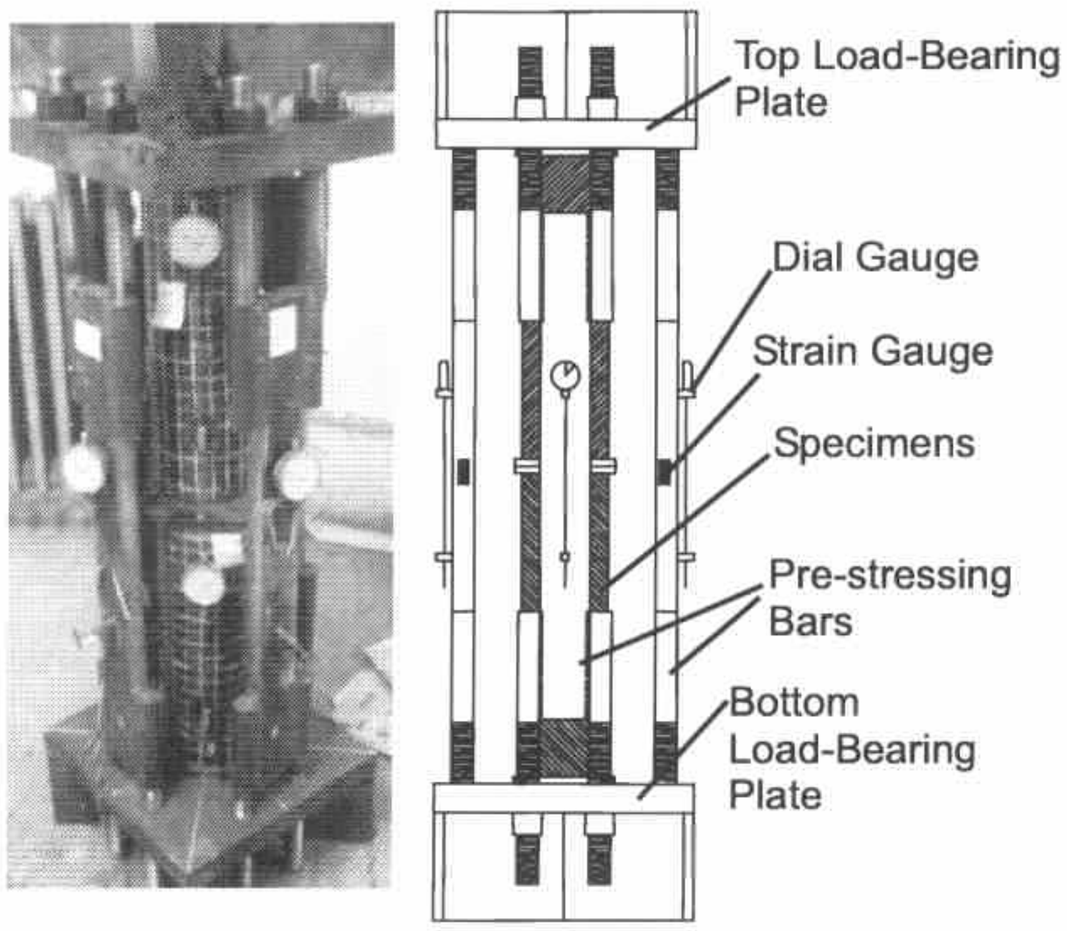

a) Loading rig

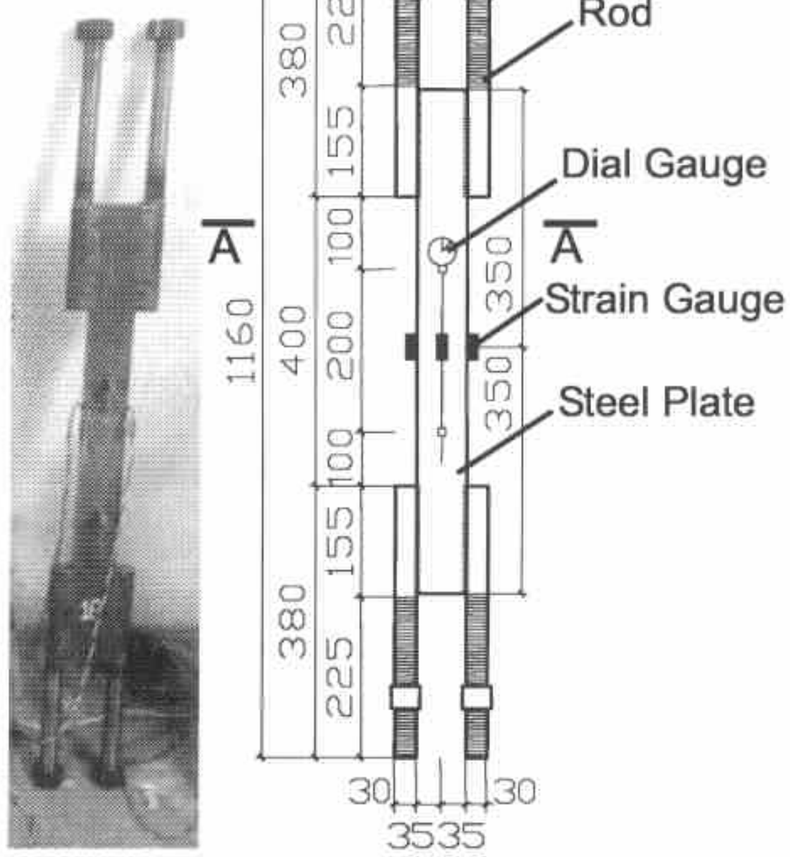

b) Pre-stressing bar

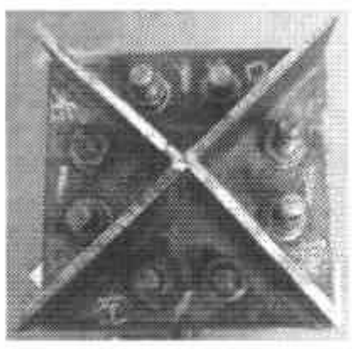

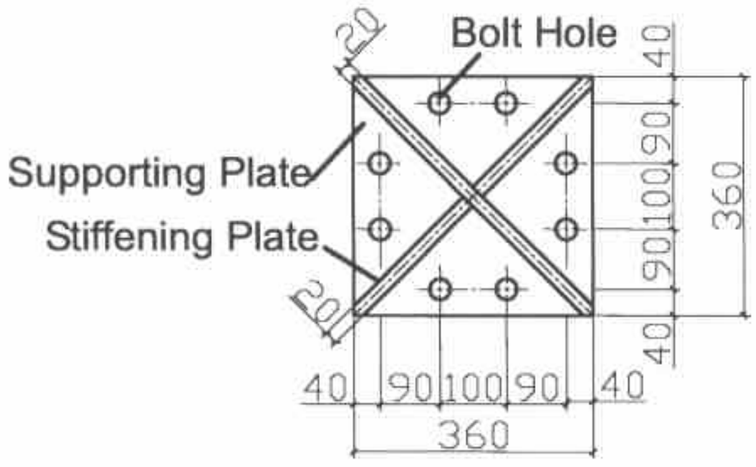

c) Load-bearing plate

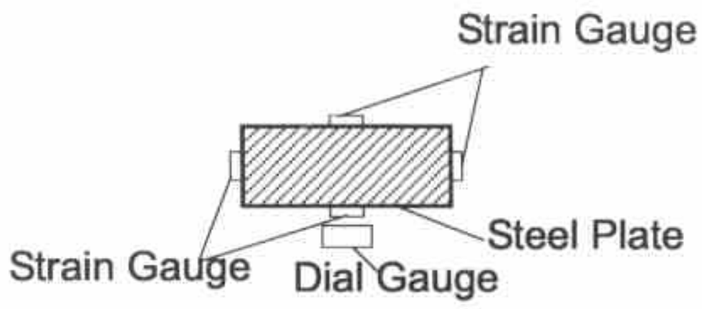

d) A-A section

Figure 3-2 Testing set-up

3.3.1.2 Loading process

Specimens included in sets I-VII were subjected to a sustained load for five months. In particular, specimens I, II, III and IV were first loaded at a concrete age of 5 days, 7 days, and 27 days respectively, with basically the same magnitude of the sustained load (N_L), while specimens III-VII were loaded at approximately 28 days after concrete casting with the stress level in the core concrete varying from 0.38 f_{cm28} to 0.68 f_{cm28}. Specimen VIII was maintained unloaded for the whole duration of the long-term tests.

The sustained load was applied by tensioning the prestressing rods (Figure 3-2(b)). This was achieved by tightening the nuts of the prestressing rods. During this process two nuts were screwed simultaneously each time with an increment of approximately 25% of the designed final sustained load. The nuts were carefully screwed in a given sequence to ensure the specimens remained axially loaded. After the beginning of the long-term test the nuts were tightened at different instants of time to ensure the sustained load remain constant. Such an adjustment was carried out three times a day during the first days of the long-term tests. After a period of two months the rate of creep development decreased and the required prestressing of the bars was carried out once a week. This approach enabled a constant sustained load to be applied for the whole duration of the long-term test with maximum deviation of 3.37% throughout the duration of the test.

3.3.1.3 Instrumentation

When the loads were first applied on the specimens, the tensile force resisted by each prestressing bar was measured by electrical resistance strain gauges and was worked out as the average value of the four gauges readings (Figure 3-2 (b, d)). The total applied load was calculated by combining the contributions of the four bars. One dial gauge, which was adopted to monitor the loading adjustment throughout the long-term test, was attached to the exterior surface of the steel plate (Figure 3-2 (b)) with a 200 mm gauge length. The combination of strain gauges and dial gauges was preferred because the strain gauges, though possessing a higher resolution, tend to be more sensitive to temperature variations and are likely to become unstable during long-term measurements.

The time-dependent deformations of the specimens were measured using two strain gauges (for short-term measurement) and two dial gauges (for long-term measurement) placed at 90° intervals around the specimens as illustrated in Figure 3-3. Also in this case the dial gauge had a gauge length of 200 mm.

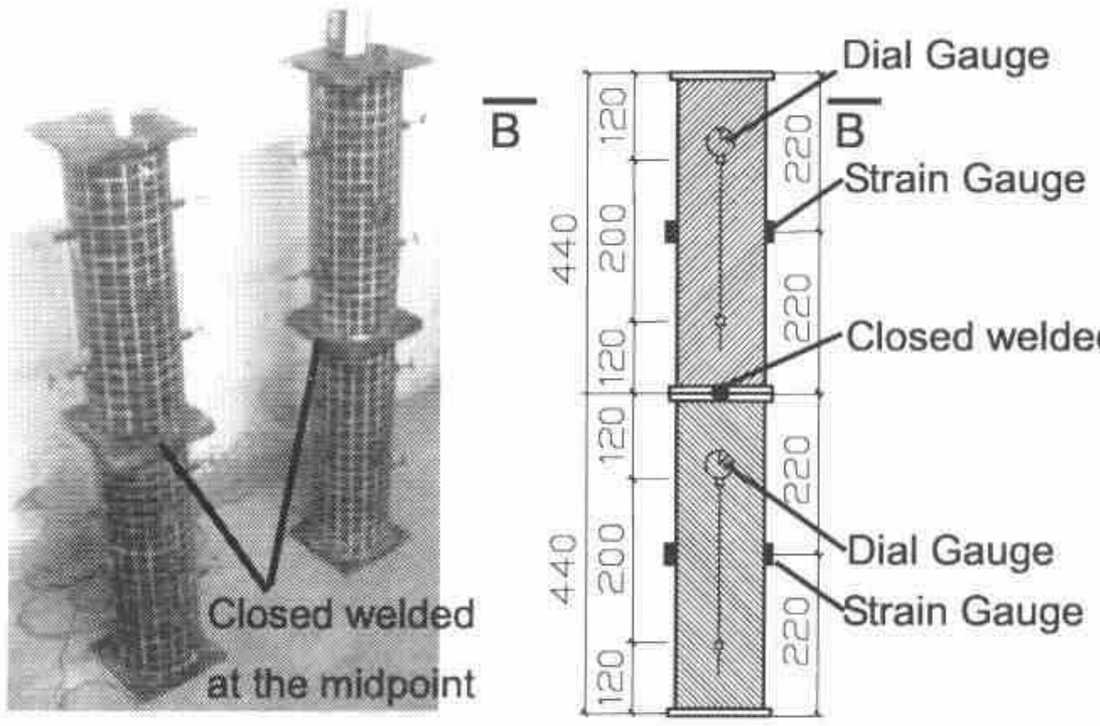

a) Specimens before long-term test b) B-B section

Figure 3-3 Instrumentation layout for the long-term test on ECFST specimens

3.3.2 Experimental Results

The measured incremental deformation caused by time effects (ε_{in}) for ECFST specimens are plotted in Figure 2-4. It appears that, independently from the time of loading, the deformation of the specimens kept increasing during the 5 months.

The rate of creep development was greater in the first couple of weeks and then started to reduce. After one month, the incremental deformations reached 60% of those recorded at the end of the experiment (i.e. after 5 months). The percentage increased to approximately 90% in 50 days. Unlike the results observed by Wang (1994), the rate of increase of the time-dependent deformations was similar to that experimentally observed in CFST specimens filled with normal concrete (Tan & Qi 1987; Kwon et al 2005, 2007; Ichinose et al 2001; Uy 2001; Han et al 2004). This difference could be attributed to the higher amount of expansive additive used in Wang's specimens.

As the steel tubes remained within linear-elastic range throughout the long-term tests, their stress increase can be considered to follow the same trend of the measured deformations.

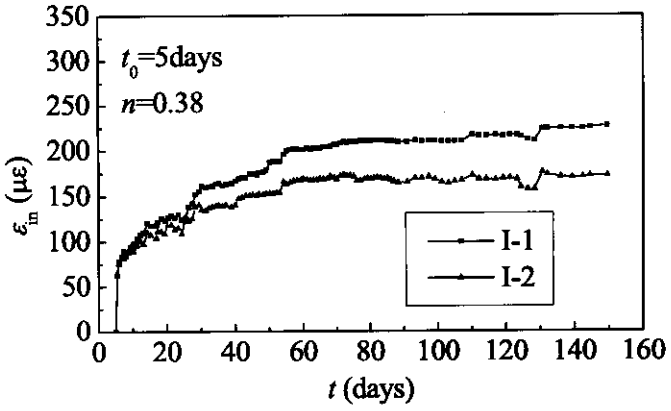

(a) Group I

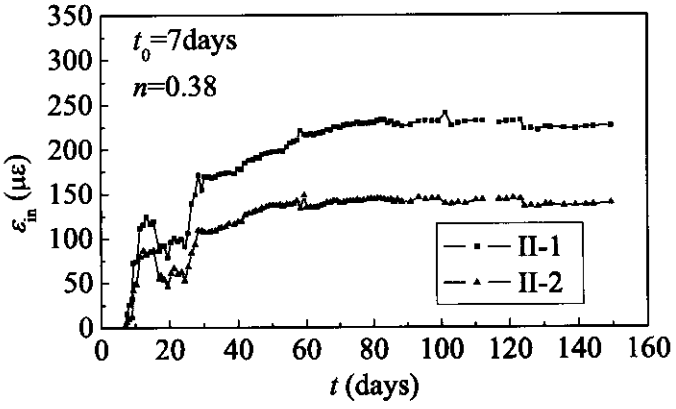

(b) Group II

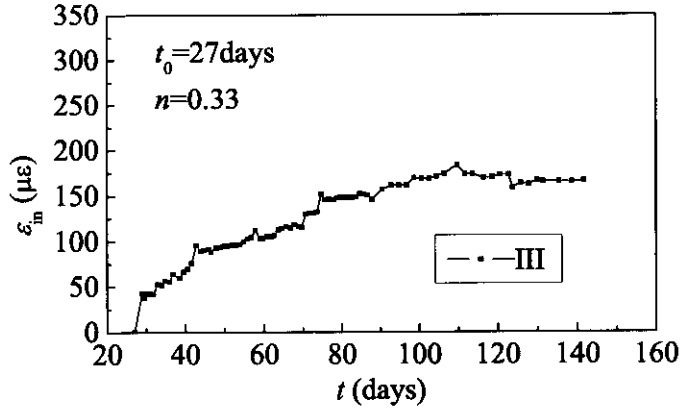

(c) Group III

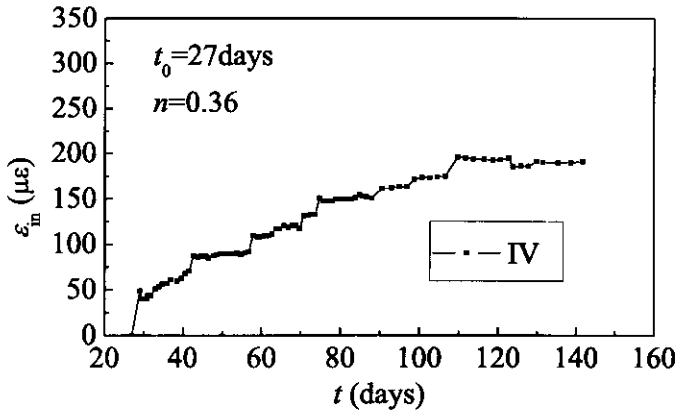

(d) Group IV

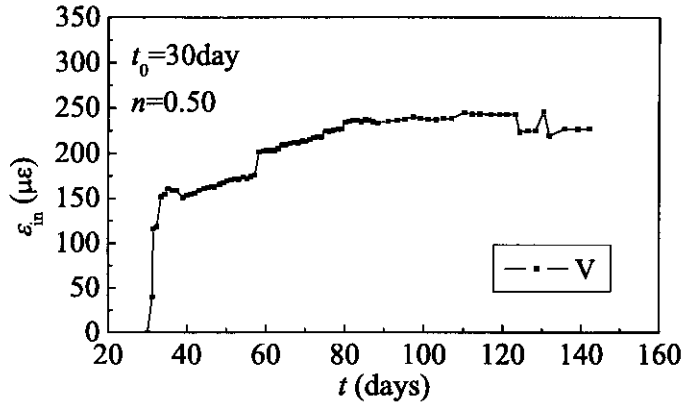

(e) Group V

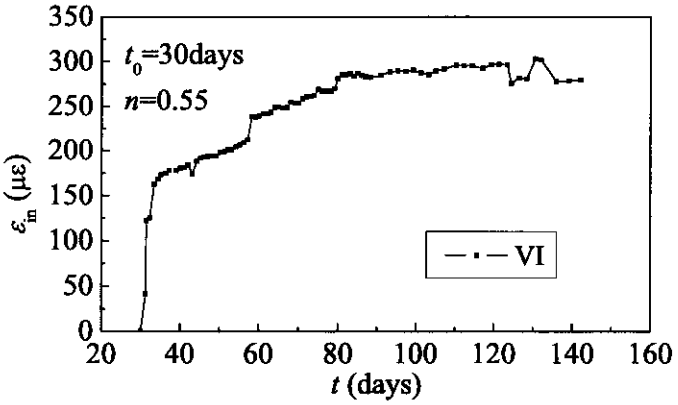

(f) Group VI

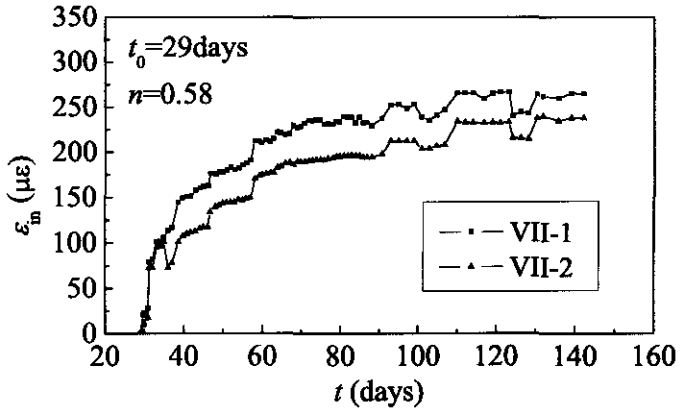

(g) Group VII

Figure 3-4 Long-term deformations measured during the long-term tests and comparisons with calculated predictions

The comparison between the instantaneous (elastic) deformations ε_e and their time-dependent (incremental) ones ε_{in} provides an effective estimate of the time effects on the deformation and stress distribution of ECFST specimens. For example, for specimens first loaded at 28 days from concrete casting (i.e. specimens III-VII), the time-dependent deformations are over 30% of the elastic ones after 5 months from casting, as shown in Table 3-4. Thus the long-term behaviour of the expansive concrete core causes considerable deformation increase and stress redistribution between steel tubes and concrete core, and should be considered in the design.

Table 3-4 Long-term deformations measured after 5 months for specimens loaded at 28 days

Specimens	III	IV	V	VI	VII-1	VII-2
ε_e (με)	434	522	691	774	860	764
ε_{in} (με)	191	166	227	280	265	238
$\varepsilon_{in}/\ \varepsilon_e$	43.9%	31.8%	32.8%	36.1%	30.8%	31.1%

Comparing Figure 2-4 (a-d) it can be noted that the deformation of the specimens loaded at an earlier concrete age increased faster and reached a higher final value than companion specimens first loaded at a later time. After 30 days under loading, the specimens loaded at 5 days after the concrete casting have the incremental deformations reached 70% of those recorded at the end of the experiment (i.e. after 5 months), while for those specimens loaded at 27 days, the percentage is only 50%. The mean value for the final incremental deformation of specimens with t_0=5 days

is 200 με, which is 12% higher than the one observed from specimens with t_0=27 days (178 με). It is also apparent that the deformation of the specimens increased more dramatically if the stress level in the concrete core is higher (Figure 3-4 (c-f)). A more detailed comparison is presented in Figure 3-5 to further investigate the influence of t_0 (time of first loading) and $n_c(t_0)$ (loading level on the core concrete as loads first applied) on the long-term response of ECFST specimens.

Figure 3-5 (a) illustrates the final incremental deformations ($\Delta\varepsilon_k$) measured for the ECFST specimens subjected to similar magnitude of sustained loading (specimens I-IV) and expressed as a function of the time of first loading (t_0). As expected, the magnitude of the long-term incremental deformation tends to increase for younger concrete ages of loading (t_0). The final measured incremental deformation ($\Delta\varepsilon_k$) for ECFST specimens first loaded at approximately 28 days (i.e. specimens III-VII) are plotted in Figure 3-5 (b) as a function of the initial stress level in the concrete core ($n_c(t_0)$), together with the results obtained by Wang (1994) and Yao (2006). Based on these results, it can be noted that, though the assumption of linear creep is usually acceptable for stress levels in compression lower than about one half of the compressive strength of the concrete (Gilbert & Ranzi 2011), the magnitude of the incremental deformation for ECFST specimens increases linearly with the stress level $n_c(t_0)$ even when the initial concrete stresses induced at the beginning of the experiments are of the order of $0.78f_{cm28}$. This indicates that the linear creep assumption may be applicable for higher stress ranges in ECFST specimens but further testing is required for an accurate evaluation of its upper limit.

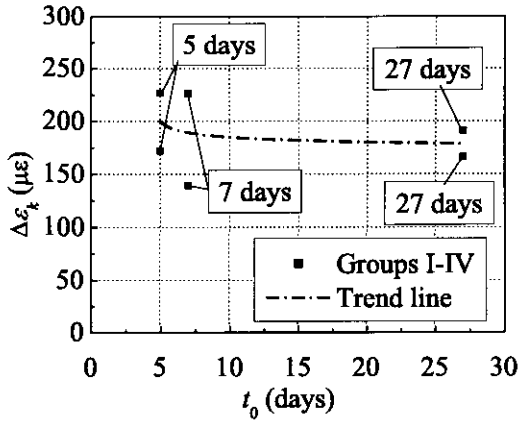

(a) Variation of the incremental deformations as a function of the t_0

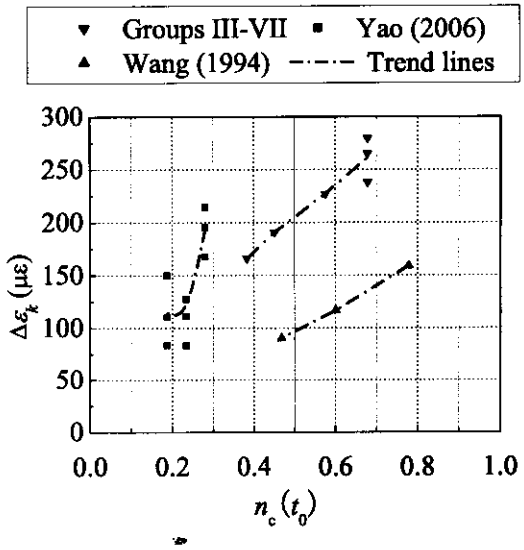

(b) Variation of the incremental deformations as a function of the stress level in the concrete component ($n_0(t_0)$)

Figure 3-5 Summary of the measured long-term response of the tested ECFST specimens

The variation of temperature recorded during the whole duration of the long-term tests is shown in Figure 3-6. The mean value measured during the 5 months period was 22.4°C.

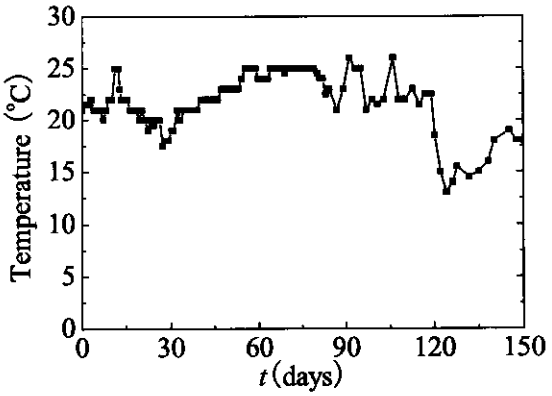

Figure 3-6 Variation of the temperature measured during the long-term test

3.4 ULTIMATE TESTS

3.4.1 Testing and Instrumentation Set-Up

At the end of the long-term tests, specimens I, III, IV, VII and VIII were tested to failure to investigate the influence of time effects on the ultimate capacity of ECFST specimens, while the remaining specimens were kept under sustained loading for a longer duration. For the ultimate tests two displacement gauges were placed at diametrically opposite positions of the column to monitor the deformation of the specimens (Figure 3-7). Eight electrical resistance strain gauges were attached to the exterior surface of the steel tube at the mid-height of the specimens equally spaced along the circumference as illustrated in Figure 3-7. Four strain gauges were attached in the longitudinal direction and the other four in transversal direction to measure longitudinal and circumferential deformations of steel tubes.

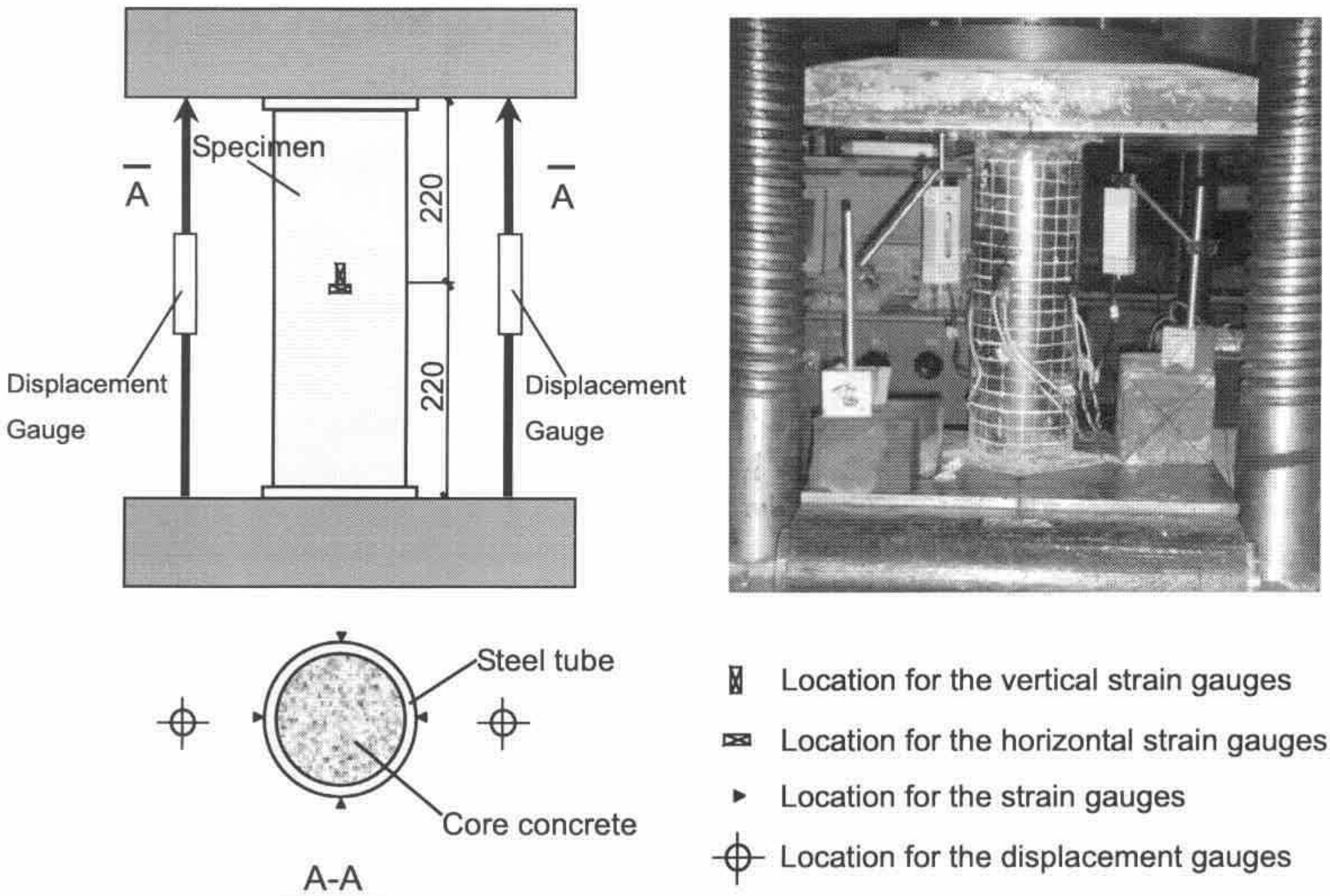

Figure 3-7 Typical layout of the ultimate experiment

In the first stage of the ultimate tests the specimens were loaded at 50 kN intervals as the specimens were in the elastic range. This rate was reduced to 25 kN when the

applied total load reached $0.75N_u$. At higher loads smaller increments were adopted to have sufficient data points to well define the 'knee' of the recorded load-strain curves. After reaching the peak load, the load cell readings continued to decrease while the deformation readings increased significantly. The test continued till the readings from the load cell reduced to 85% of the peak value. The test was then terminated.

3.4.2 Test Results

At the beginning of the test, all readings measured with the strain gauges as well as the dial gauges increased linearly with load, indicating that the specimens were deforming within the elastic range. As the load increased, the specimens began to exhibit nonlinear behaviour and, just before the loads reached the peak value, the specimens gave a slight 'crack' noise. The steel tubes then buckled locally at either end of the specimens followed by a shear-slip in the concrete core when the loads in the specimens began to drop.

All the specimens collapsed in a shear failure mode shown in Figure 3-8, indicating that time effects do not influence the mode of failure.

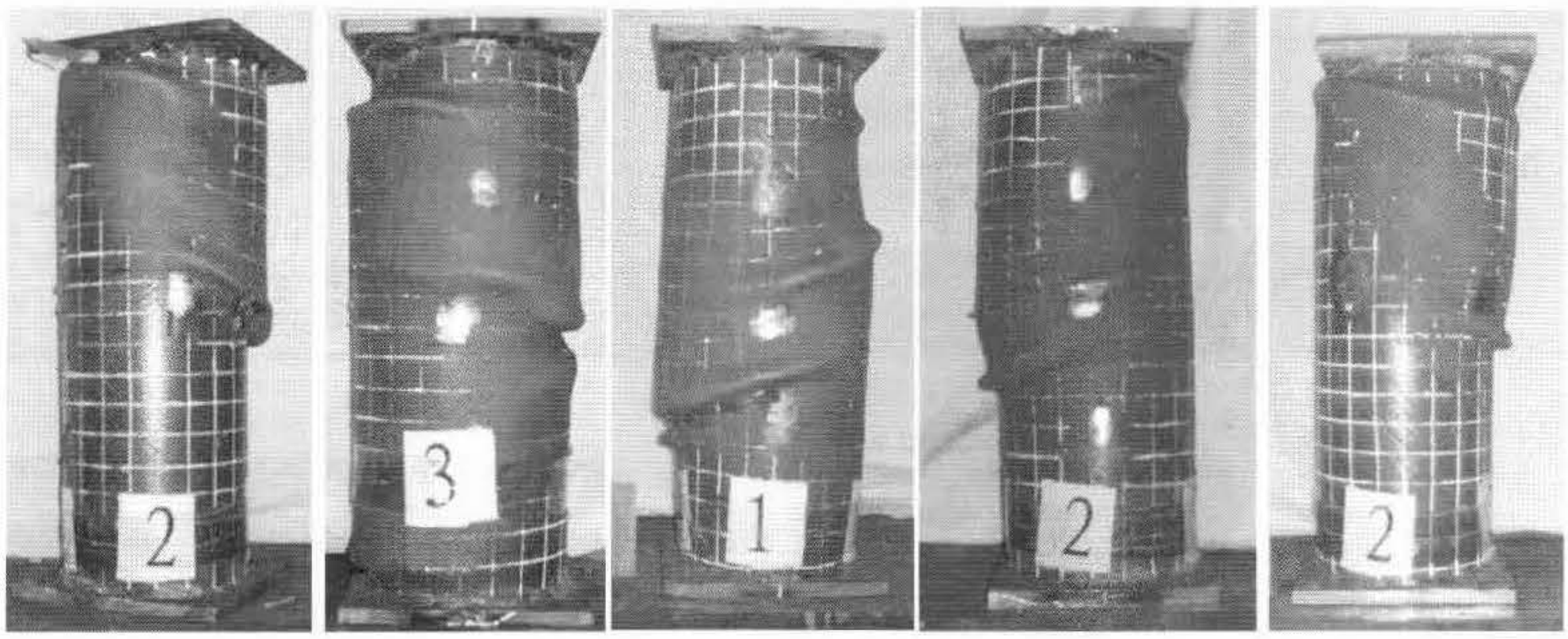

(a) Specimen I (b) Specimen III (c) Specimen IV (d) Specimen VII (e) Specimen VIII

Figure 3-8 Failure modes observed during the ultimate tests

Figure 3-9 shows comparison on the load-deformation curves of specimens subjected to sustained loading (i.e. specimens I, III, IV and VII), and the specimen maintained unloaded during the long-term tests (i.e. specimen VIII). The ratio of the

ultimate loads of those specimens under long-term loading over that of the specimen VIII has been depicted by the parameter K_f listed in Table 3-1.

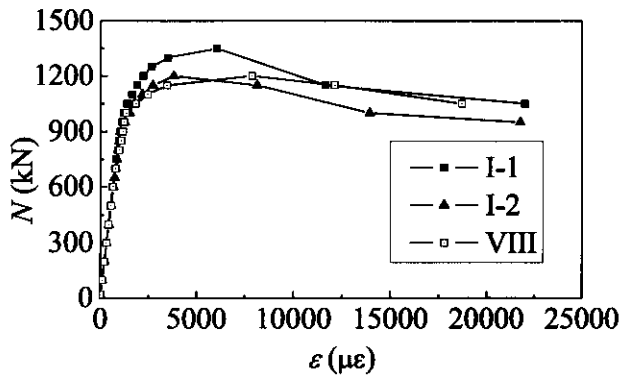

(a) Comparison between Specimens I and VIII

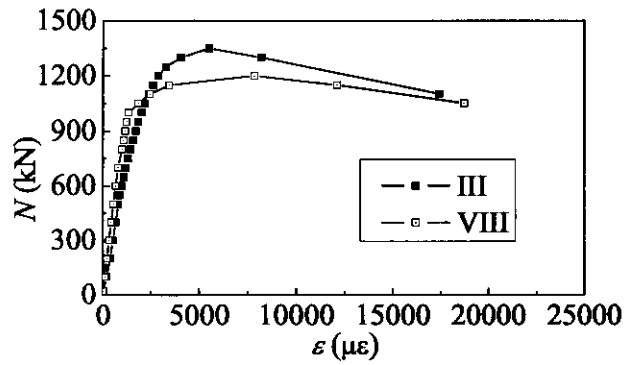

(b) Comparison between Specimens III and VIII

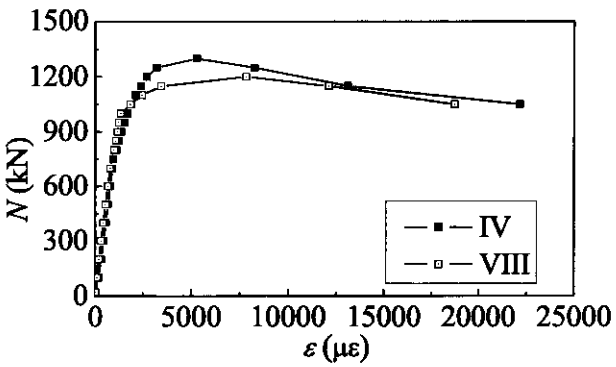

(c) Comparison between Specimens IV and VIII

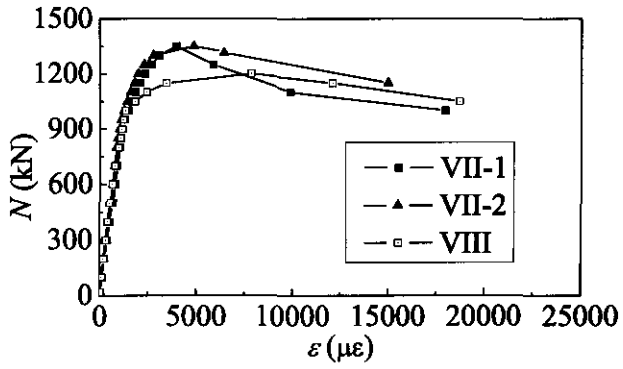

(d) Comparison between Specimens VII and VIII

Figure 3-9 Load versus axial deformation curves for ultimate tests

From these results it can be observed that the ultimate capacity of those specimens under long-term loading is higher than that of specimen VIII. Han & Yang (2003) and Zha et al (2010) also observed that for rectangular CFST specimens filled with normal concrete, the strengths of those specimens subjected to long-term loads were about 5~21% higher than those in the unloaded companion specimens. Such phenomena could be explained by the possible beneficial effects of the sustained loading on the strength of the concrete core, which were also observed in plain concrete tests by Freudenthal & Roll (1958), Dhir & Sangha (1972), and Cook & Chindaprasirt (1980) with the average increase in concrete strength ranging from 2% to 30% of the short-term one depending on the concrete strength, duration of load, level of stress and age at loading.

Such beneficial gain in strength could be induced by increased hydration in concrete: external pressure increases the solubility of unhydrated cement in the presence of water, which thus leads to increased hydration (Coutinho 1977). According to Hellesland & Green (1972), the explanation of the increase in strength caused by sustained load was also due to an improved healing of cracks perpendicular to the load, and to an increase in the van der Waals forces on bringing the gel particles closer together. More experiments need to be conducted with a wider parameter range to determine whether this beneficial effect is a common phenomenon in ECFST stubs.

3.5 CONFINEMENT EFFECT

The role of concrete confinement at service load levels was investigated based on the vertical and circumferential deformations measured from the steel tubes during the ultimate tests. To analyze the plane-stress conditions using strain gauges has been proved to be feasible even when the deformations of the materials are in the elasto-plastic range by Keil & Benning (1979).

In the initial stage of loading, the Poisson's ratio of the core concrete is lower than that of the steel tube; hence the steel tube tends to expand faster than the concrete. As the load increases, the longitudinal strain reaches a certain critical value at which the lateral deformation of the concrete equals to the deformation of the steel tube. After this point the concrete is subjected to a triaxial compression state and a tensile hoop stress develops in the steel tube. This can be observed experimentally by monitoring the circumferential strain in the steel tube (ε_{cc}). When the ε_{cc} in the steel tube becomes positive (i.e. in tension), the confinement effect starts to act on the concrete core. The calculation of the circumferential and longitudinal stresses requires the selection of a constitutive model to convert the experimentally observed deformations into corresponding stress states.

3.5.1 Material Property for Steel Tubes in Confinement Effect Analysis

The stress-strain curve for the steel under uniaxial stress can be simplified into three phases (Figure 3-10): the linear-elastic phase (line OA), the elasto-plastic phase (line AB) and the plastic phase (also called work hardening or strain hardening phase) (line BC). In Figure 3-10, f_p, f_y and f_u represents the proportional limit, the yielding strength, and the ultimate strength of the steel, respectively; the ε_p, ε_y, and ε_u are the corresponding strains; E_s is the elastic Young's modulus of steel; H denotes the plastic hardening modulus, which is defined as

$$H = \frac{d\sigma_{\text{plastic}}}{d\varepsilon_{\text{plastic}}} \tag{3-2}$$

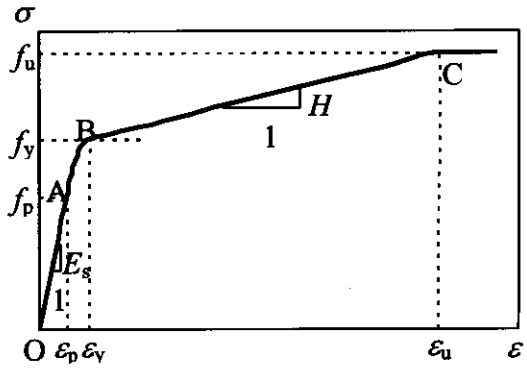

Figure 3-10 Theoretical stress-strain curve for the steel

The introduced material parameters were determined based on tensile coupon tests and their values are listed in Table 3-5.

Table 3-5 Regressed value for the parameters used in the constitutive model for steel tubes

E_s (MPa)	ε_p (με)	ε_y (με)	ε_u (με)	f_p (MPa)	f_y (MPa)	f_u (MPa)	H (MPa)
1.79×10^5	1507	2602	10088	261.0	315.1	384.5	8736

During the ultimate tests, the diametrical stresses in the steel tube were observed to remain small when compared to the values calculated in the longitudinal and circumferential directions. Based on this the steel component was considered to be under plane stress conditions with a nil value for the shear stress (τ_{xy}). Under this condition the stress-strain response for the steel can be described as follows.

3.5.1.1 Linear-elastic phase (OA)

Before reaching the proportional limit (f_p), the steel remains elastic (segment 'OA') and the stress-strain relationship follows Hooke's law (Boresi & Schmidt 2003):

$$\begin{bmatrix}\sigma_{cc}\\ \sigma_v\end{bmatrix}=\frac{E_s}{1-\mu_s^2}\begin{bmatrix}1 & \mu_s\\ \mu_s & 1\end{bmatrix}\begin{bmatrix}\varepsilon_{cc}\\ \varepsilon_v\end{bmatrix} \tag{3-3}$$

where μ_s denotes the Poisson's ratio of the steel plate, taking the value of 0.265 as obtained from the coupon test; ε_{cc}, ε_v, σ_{cc}, and σ_v represent the circumferential and

longitudinal strains and stresses, respectively. Based on the adopted sign convention a positive stress (strain) value depicts a tensile stress (strain).

3.5.1.2 Elasto-plastic phase (AB)

Beyond the proportional limit, the steel enters a nonlinear elasto-plastic phase (segment 'AB'). In this phase, the tangent modulus of the steel (E_s^t) decreases with the increase of the stress from the value of Young's modulus (E_s) to zero (at yielding). This can be represented using a formula proposed by Bleich (1952):

$$E_s^t = \frac{(f_y - \sigma_s)\sigma_s}{(f_y - f_p)f_p} E_s \tag{3-4}$$

where σ_s is the equivalent stress in the steel and can be determined from:

$$\sigma_s = \sqrt{\sigma_{cc}^2 + \sigma_v^2 - \sigma_{cc}\sigma_v} \tag{3-5}$$

In the elastic-plastic stage, the Poisson's ratio for steel also increases with stress. Zhong (1994) conducted 46 tests to investigate the increasing tendency of the Poisson's ratio for steel plate under plain stress. It was found that the Poisson's ratio reached a value of the order of 0.45 at the yielding point when the steel plate was under compression in one direction and tension in the other. The value for the Poisson's ratio of steel plate under such stress state in the elasto-plastic stage (μ_{sp}) can then be obtained by linear interpolation between the value at the proportional limit and that at the yielding point, based on:

$$\mu_{sp} = 0.185\frac{\sigma_s - f_p}{f_y - f_p} + 0.265 \tag{3-6}$$

In this context, the stress-strain relation for the steel plate in this phase can be determined using incremental theory which can be expressed as

$$\begin{bmatrix} d\sigma_{cc} \\ d\sigma_v \end{bmatrix} = \frac{E_s^t}{1-\mu_{sp}^2}\begin{bmatrix} 1 & \mu_{sp} \\ \mu_{sp} & 1 \end{bmatrix}\begin{bmatrix} d\varepsilon_{cc} \\ d\varepsilon_v \end{bmatrix} \tag{3-7}$$

where E_s^t and μ_{sp} can be calculated with Eqns (3-4) and (3-6), respectively; and $d\varepsilon_{cc}$, $d\varepsilon_v$, $d\sigma_{cc}$, and $d\sigma_v$ represent the incremental circumferential and longitudinal strains and stresss, respectively.

3.5.1.3 Plastic phase (BC)

With the Von Mises criterion adopted as the yield criterion for steel, the incremental stress-strain relationship for the steel in the plastic phase can be expressed based on the Prandtl-Reuss theory (Chakrabarty 1998) as:

$$\begin{bmatrix} d\sigma_{cc} \\ d\sigma_{v} \end{bmatrix} = \frac{2G}{\beta} \begin{bmatrix} (1+\mu_s)\frac{s_v^2}{\sigma_s} + 2\zeta & -(1+\mu_s)\frac{s_{cc}s_v}{\sigma_s^2} + 2\mu_s\zeta \\ -(1+\mu_s)\frac{s_{cc}s_v}{\sigma_s^2} + 2\mu_s\zeta & (1+\mu_s)\frac{s_{cc}^2}{\sigma_s} + 2\zeta \end{bmatrix} \begin{bmatrix} d\varepsilon_{cc} \\ d\varepsilon_{v} \end{bmatrix} \quad (3\text{-}8)$$

where G is the shear modulus of the steel; s_{cc}, s_v, and s_z are deviatoric normal stresses. These parameters can be calculated using:

$$G = \frac{E_s}{2(1+\mu_s)} \quad (3\text{-}9)$$

$$\zeta = \frac{H}{9G} \quad (3\text{-}10)$$

$$\beta = \frac{2}{3}(1-\mu_s)\left(1+\frac{H}{3G}\right) - (1-2\mu_s)\frac{s_z^2}{\sigma_z^2} \quad (3\text{-}11)$$

$$s_{cc} = \frac{2\sigma_{cc} - \sigma_v}{3}; \qquad s_v = \frac{2\sigma_v - \sigma_{cc}}{3}; \qquad s_z = -\frac{1}{3}(\sigma_{cc} + \sigma_v) \quad (3\text{-}12)$$

3.5.2 Confinement Effect of ECFST Specimens under Service Loading

Figure 3-11 presents the representative longitudinal and circumferential stresses in the steel tubes of ECFST specimens (specimens I, III and VIII) calculated using the strain gauge readings and the constitutive model for steel described in Section 3.5.1. In Figure 3-11, σ_v, σ_{cc}, and σ_s represent the mean value of the longitudinal, circumferential and equivalent stresses in the steel tube, respectively, while ε_v denotes the mean value of the longitudinal strains in steel tubes.

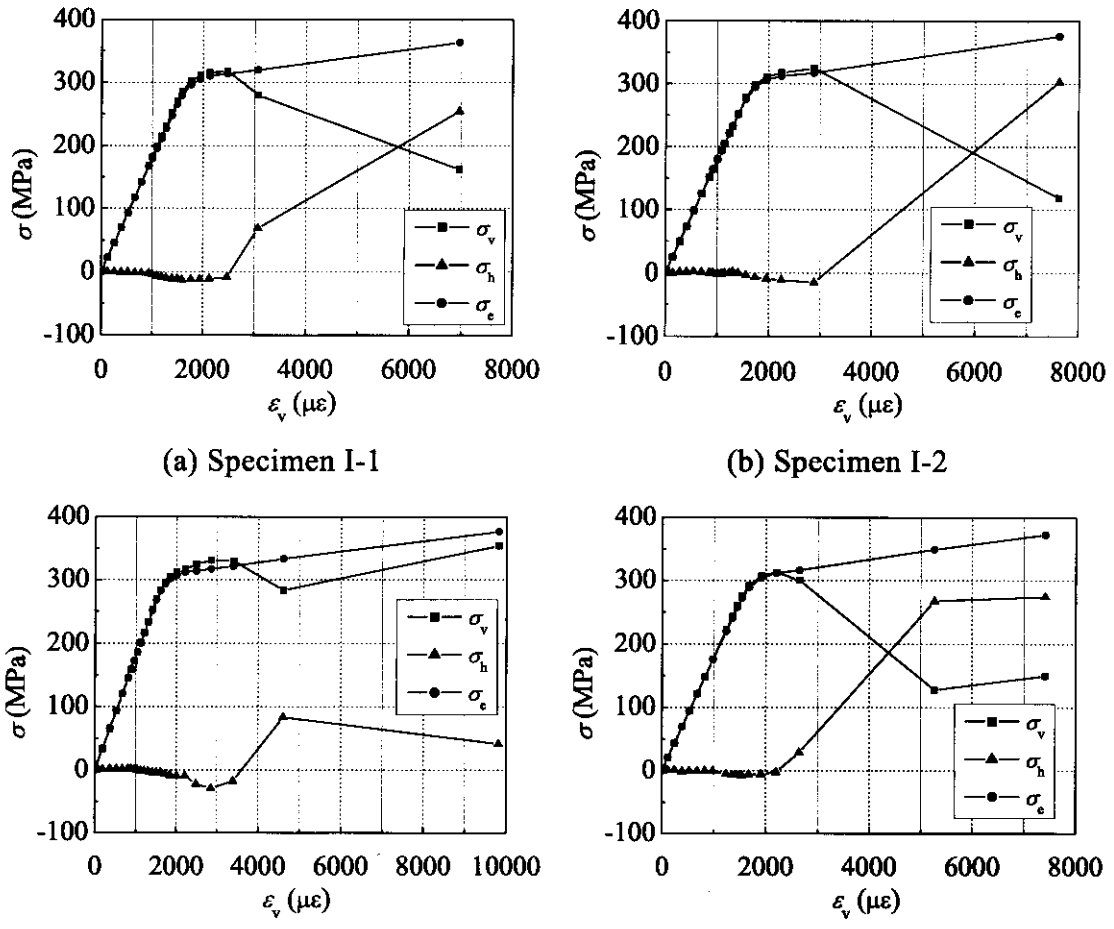

(a) Specimen I-1 (b) Specimen I-2

(c) Specimen III (d) Specimen VIII

Figure 3-11 Stress vs. vertical strain for steel tubes during ultimate capacity tests

Observing the variation of the longitudinal and circumferential stresses in each specimen, it can be noted that the circumferential stresses (σ_{cc}) in the steel tube are not significant at the beginning of the test and increase when the longitudinal stresses approach yielding (i.e. end of phase AB in Figure 3-10). In this process the confining effect on the concrete begins to develop. This indicates that within the parameter range adopted in the tested specimens, the confinement effect was not present in the long-term experiments.

3.6 CONCLUSIONS

This Chapter presented an experimental study on the time-dependent behaviour of ECFST columns with expansive core concrete. Eleven specimens were subjected to different levels of sustained axial loading over a period of 5 months with the concrete ages at first loading varying between 5 and 28 days. After the long-term tests, the ECFST specimens were tested to failure to evaluate the time effects on their ultimate capacity. The following conclusions were drawn from the results:

1) The development of the time-dependent deformations for ECFST specimens was similar to that experimentally observed in CFST specimens filled with normal concrete.

2) The long-term deformations measured for the ECFST specimens loaded at an earlier concrete age increased faster and reached a higher final value as expected. Based on the experimental measurements it was noted that the assumption of linear creep, usually considered acceptable for stress levels in compression lower than about one half of the compressive strength of the concrete (Gilbert & Ranzi 2011), appeared to be valid also for higher stress levels about 80% of the concrete strength. To better evaluate this upper limit in the case of composite columns further testing is recommended to be carried out.

3) The long-term behaviour of the expansive concrete core causes considerable deformation increase and stress redistribution between steel tubes and concrete core, and should be considered in the design.

4) The strength of the specimens subjected to sustained loading was higher than the one observed for the specimen remained unloaded during the long-term test. These results are consistent with other data published in the literature on normal concrete composite specimens and plain concrete specimens. It is recommended to carry out additional experiments to determine whether this beneficial effect is a characteristic of ECFST columns.

5) Based on the experimental measurements collected during the ultimate tests it was shown that confinement effects had no considerable influence on the

response of CFST specimens for load levels at which the steel was not yielded. This consideration is valid for composite columns with material properties similar to those adopted in the tests reported, i.e. steel yield stress of 235 MPa and concrete core characteristic strength of 40 MPa. In such cases the influence of confinement can be disregarded at service conditions.

CHAPTER 4 TIME-DEPENDENT BEHAVIOUR OF CONCRETE-FILLED STEEL TUBULAR COLUMNS: ANALYTICAL AND COMPARATIVE STUDY

4.1 INTRODUCTION

The work presented in this Chapter intends to (i) provide a unified method of analysis for both refined and simplified calculations, (ii) identify a concrete model capable of adequately predicting the long-term response of CFST members by performing a wide comparative study using available long-term experimental results for benchmarking purposes and (iii) recommend simplified methods of analysis for day-to-day routine design. This work focuses on CFST members filled with both normal and expansive concrete.

The numerical solutions have been obtained using a cross-sectional analysis. Four concrete models have been considered in this study, i.e. AFREM (Le Roy et al. 1996), B3 (Bazant & Baweja 2000), EC2 (BSI 2004) and MC 90 (CEB-FIP 1993). The numerical results have been compared against 81 long-term tests published to date and the performance of those concrete models is discussed. An extensive parametric study has then been carried out to evaluate the long-term response of specimens whose geometries, material properties and loading conditions are outside the range of those used in the tests while still relevant for real applications. Finally, under the consideration that for practical design purposes the use of the step-by-step procedure might be prohibitive, the accuracy of the algebraic methods, i.e. the Effective Modulus (EM) method, the Mean Stress (MS) method, and the Age-Adjusted Elastic Modulus (AAEM) method, has been evaluated with the step-by-step method on CFST specimens for a wide range of material and geometric properties. Based on these results design recommendations have been provided.

4.2 GENERAL METHOD OF ANALYSIS

4.2.1 Theoretical Model

Cross-sectional analysis provides a very effective tool in determining how stresses and strains vary with time when accounting for creep and shrinkage effects of the concrete for both reinforced concrete and composite applications (Gilbert & Ranzi 2011). With this approach, the system of governing equations describing the structural response of the cross-section is expressed in terms of variables defining the strain diagram which represent the unknowns of the problem. In the proposed derivation the cross-section is assumed to be symmetric about the y-axis and the orthogonal x-axis is selected as the reference axis (Figure 4-1 (a)).

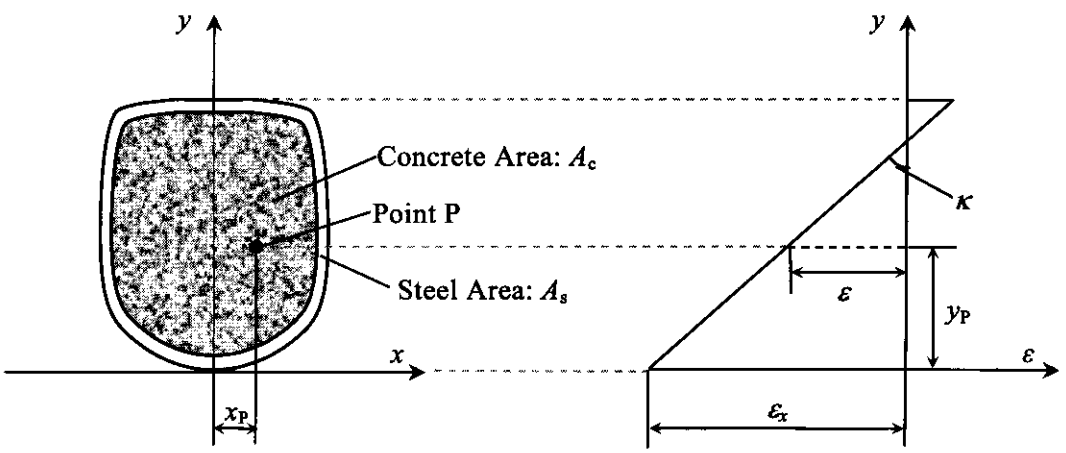

(a) Cross-section (b) Strain diagram

Figure 4-1 Generic cross-section of a CFST column

The proposed model relies on the assumption of Euler-Bernoulli beam theory, i.e. plane sections remain plane and perpendicular to the member axis also in its deformed shape. The strain diagram of a generic cross-section can then be identified by a single value of strain at any reference level (ε_x) and the curvature of the cross-section (κ) as presented in Figure 4-1 (b). These two unknowns are then determined based on equilibrium considerations enforcing horizontal and rotational equilibrium at the cross-section as:

$$\mathbf{r}_i = \mathbf{r}_e \tag{4-1}$$

in which $\mathbf{r}_i$ collect the internal cross-sectional resultants resisted at the generic time t while $\mathbf{r}_e$ represent the set of applied loads at the corresponding instant in time where

$$\mathbf{r}_i = \begin{bmatrix} N_i(t) \\ M_i(t) \end{bmatrix} = \begin{bmatrix} \int_A \sigma(t)\,\mathrm{d}A \\ \int_A y\sigma(t)\,\mathrm{d}A \end{bmatrix} \quad ; \quad \mathbf{r}_e = \begin{bmatrix} N_e(t) \\ M_e(t) \end{bmatrix} \tag{4-2}$$

in which $N_i(t)$ and $M_i(t)$ represents the internal axial force and moment at time t respectively, $\sigma(t)$ denotes the relevant stress at an arbitrary point P on the cross section with coordinates (x_P, y_P) as shown in Figure 4-1 (b), A is the total area of the cross section, $N_e(t)$ and $M_e(t)$ refer to external axial force and moment applied at time t respectively.

It is usually common to measure time t in days starting from the instant of concrete pouring. The proposed procedure is general and applicable to complex material representations in which case the integrals of Eqn (4-2) might need to be evaluated numerically.

4.2.2 Material Properties

4.2.2.1 Considerations on concrete models

The adopted concrete models are presented in Appendix II. The particularity of the time-dependent behaviour of CFST columns relies on the fact that, being the concrete under sealed condition, no moisture exchange occurs with the environment. As a consequence of this, only basic creep and autogenous shrinkage need to be considered in the modelling. These have been utilised when available in the adopted concrete model. For those models which do not separate between either basic and drying creep and/or autogenous and drying shrinkage, an infinite value is adopted for the hypothetical thickness or notional size, usually defined as the ratio between twice the concrete area and the exposed perimeter, in the calculation of the time-dependent material properties. Such a limit could be reached by considering a nil exposed perimeter, i.e. completely sealed conditions, in the expression of the notional size.

In particular, for the AFREM model, the available equations for basic creep and autogenous shrinkage have been included in the modelling. In the case of the EC2

guidelines the provided autogenous shrinkage has been included in the analysis while the creep response has been accounted for by adopting an infinite notional size for the concrete component to eliminate the effects of relative humidity, i.e. drying effects. Similarly, an infinite notional size of the core concrete is adopted also for the Model Code 90 (MC90) when considering both creep and shrinkage properties. In the use of the B3 model, basic creep has been included in the calculation and the volume to surface ratio of the core concrete is assumed to approach infinity for the shrinkage predictions. It is worth noting that the adopted assumption of using an infinite notional size for the concrete cancels the shrinkage effects in both MC90 and B3 models as these two models focus on the drying shrinkage component in their expressions. This limitation might become unacceptable when dealing with CFST specimens filled with high strength concrete when autogenous shrinkage becomes significant and needs to be accounted for.

4.2.2.2 Time-dependent constitutive model for concrete

The concrete time-dependent behaviour is modelled accounting for creep and shrinkage effects based on the integral-type constitutive law (CEB 1984) as:

$$\varepsilon_{tot}(t) - \varepsilon_{sh}(t) = \sigma_c(t_0) \cdot J(t,t_0) + \int_{t_0^+}^{t} J(t,\tau) d\sigma_c(\tau) \qquad (4\text{-}3)$$

where t is the time from casting of the concrete, t_0 is the time of first loading, $\varepsilon_{tot}(t)$ is the total axial strain which combines both stress-dependent and stress-independent strains, $\varepsilon_{sh}(t)$ is the shrinkage strain (while other stress-independent strains, e.g. thermal dilatation, could be modelled in a similar manner), $J(t,\tau)$ is the creep function defined as the strain at time t due to a constant unit stress acting from time τ to time t, and $\sigma_c(t)$ is the concrete stress calculated at time t.

The integral in Eqn (4-3) can be implemented with step-by-step procedure. The step-by-step procedure requires the integral included in Eqn (4-3) to be approximated by means of the trapezoidal rule (CEB 1984) subdividing the time domain t into discrete times t_j (i.e. t_0, t_1, t_2, ... t_i, ... t_k with $j = 1,\ldots,k$). With this discretisation Eqn (4-3) can be re-written as:

$$\varepsilon_{ck} - \varepsilon_{shk} \cong \sigma_c(t_0) J(t_k, t_0) + \sum_{j=1}^{k} \frac{1}{2} \left[J(t_k, t_j) + J(t_k, t_{j-1}) \right] \left[\sigma_c(t_j) - \sigma_c(t_{j-1}) \right] \quad (4\text{-}4)$$

where $\sigma_c(t_j)$ (also referred to as σ_{cj} in the following) represents the concrete stress calculated at time t_j, ε_{ck} is the total axial strain which combines both stress-dependent and stress-independent strains, ε_{shk} is the shrinkage strain, and $J(t_k,t_j)$ is the creep function which is defined as the strain at time t_k caused by a constant unit stress acting from time t_j to time t_k.

Collecting the terms of Eqn (4-4) the generic concrete constitutive law can be defined as:

$$\sigma_{ck} = E_{c1k} \varepsilon_{ck} + \sum_{j=0}^{k-1} \sigma_{cj} E_{c2kj} - E_{c1k} \varepsilon_{shk} \quad (4\text{-}5)$$

The main advantage of Eqn (4-5) relies on its ability to define the concrete behaviour based on both the step-by-step procedure as well as the algebraic methods. For the purpose of this study these include the Effective Modulus (EM) method, the Mean Stress (MS) method and the Age-Adjusted Effective Modulus (AAEM) method. In the literature, the algebraic methods have sometimes been referred to as 'simplified' to distinguish them from those requiring the time domain to be discretised with more than two instants (as in the case of the step-by-step procedure). For clarity, all notation of Eqn (4-5) is defined in Appendix III while all material parameters are calculated using concrete models considered in this study which include the AFREM model (Le Roy et al. 1996), B3 model (Bazant & Baweja 2000), EC2 model (BSI 2004), and MC 90 model (CEB-FIP 1993).

In the use of Eqn (4-5) it has been assumed that the time-dependent behaviour of the concrete is identical in both compression and tension. This is usually acceptable for stress levels in compression less than about one half of the compressive strength of the concrete, and for tensile stresses less than about one half of the tensile strength of the concrete, as recommended by Gilbert & Gianluca (2011). It is worth noting that comparisons with the long-term test results reported by Tan & Qi (1987), Wang (1994), Han et al. (2004), Yao (2006) and the experimental results presented in section 3.3.2 have highlighted that this assumption might also be applicable for

higher stress ranges for CFST specimens, but further tests are required to evaluate the accurate upper limit.

4.2.2.3 Constitutive models for steel tube and reinforcement

The steel tube and the reinforcing bars (if present) are assumed to behave in a linear elastic manner. The elastic modulus of the steel member is represented by E_s (subscript 's' for the steel section) while the contribution of the reinforcement is lumped into layers according to their locations where the total number of layers of reinforcement is referred to as n_r. In particular, the properties of each layer of reinforcement are defined by their area, elastic modulus and location with respect to the x-axis and are labelled as $A_{r(a)}$, $E_{r(a)}$ and $y_{r(a)}$, respectively. With this notation the subscript 'r' stands for reinforcement and $a = 1,\ldots,n_r$. Despite the fact that no reinforcement has been specified in the specimens considered, its presence has been included in the formulation for completeness.

4.2.2.4 Constitutive material representation in matrix form

The constitutive models of the materials forming the cross-section, i.e. concrete, and steel section, can be expressed in compact form at time t_j as follows

$$\mathbf{r}_{ij} = \mathbf{D}_j \boldsymbol{\varepsilon}_j + \mathbf{f}_{cj} - \mathbf{f}_{shj} \tag{4-6}$$

where $\mathbf{r}_{ij}$ collects the internal actions at time t_j and

$$\mathbf{D}_j = \begin{bmatrix} AE_j & BE_j \\ BE_j & IE_j \end{bmatrix};\ \boldsymbol{\varepsilon}_j = \begin{bmatrix} \varepsilon_{xj} \\ \kappa_j \end{bmatrix};\ \mathbf{f}_{cj} = \sum_{d=0}^{j-1} E_{c2jd}\mathbf{r}_{cd};\ \mathbf{f}_{shj} = \begin{bmatrix} A_c E_{c1j} \\ B_c E_{c1j} \end{bmatrix} \varepsilon_{shj} \tag{4-7a,b,c,d}$$

The definitions of AE_j, BE_j, and IE_j are presented in Appendix IV, $\boldsymbol{\varepsilon}_j$ groups the two unknowns identifying the strain diagram of the cross-section at time t_j and includes the relevant strain at the reference level (ε_{xj}) and the curvature of the cross-section (κ_j), $\mathbf{f}_{cj}$ and $\mathbf{f}_{shj}$ include the relevant terms to account for creep and shrinkage effects at time t_j, E_{c1j} and E_{c2jd} represent concrete material properties defined in Appendix III, A_c and B_c are the cross-sectional area and the first moment of area of the concrete component, and $\mathbf{r}_{cd}$ groups the concrete internal actions N_{cd} and M_{cd} calculated at time t_d and defined as

$$\mathbf{r}_{cd} = \begin{bmatrix} N_{cd} \\ M_{cd} \end{bmatrix} = \begin{bmatrix} \int_{A_c} \sigma_{cd} \, \mathrm{d}A \\ \int_{A_c} y\sigma_{cd} \, \mathrm{d}A \end{bmatrix} = E_{c1d}\mathbf{D}_c\boldsymbol{\varepsilon}_d + \mathbf{f}_{cd} - \mathbf{f}_{shd} \tag{4-8}$$

where $\mathbf{f}_{cd}$ and $\mathbf{f}_{shd}$ can be calculated by Eqns (4-7a,b,c,d), and

$$\mathbf{D}_c = \begin{bmatrix} A_c & B_c \\ B_c & I_c \end{bmatrix} \tag{4-9}$$

where I_c is the second moment of area of the concrete component.

Eqn (4-8) highlights how the concrete stress calculated at a generic time step d requires the knowledge of the concrete behaviour recorded over the previous d-1 steps as emphasised by the summation of concrete stresses over these d-1 instants. Obviously, in the case of the algebraic methods the maximum number of steps is limited to two.

4.2.3 Numerical Solution

Based on the material properties expressed in matrix form in Eqn (4-6), the equilibrium equations of Eqn (4-1) can be re-arranged as follows:

$$\mathbf{r}_{ej} = \mathbf{D}_j\boldsymbol{\varepsilon}_j + \mathbf{f}_{cj} - \mathbf{f}_{shj} \tag{4-10}$$

in which the time domain has been discretised into a number of instants t_j (with $j = 0,\ldots,k$) with the latter instant in time t_k being the one at which the structural response is sought while $\mathbf{r}_{ej}$ collects the external actions, i.e. external axial force (N_{ej}) and moment (M_{ej}), acting at time t_j and is defined as:

$$\mathbf{r}_{ej} = \begin{bmatrix} N_{ej} \\ M_{ej} \end{bmatrix} \tag{4-11}$$

The additional subscripts 'j' has been introduced for clarity to distinguish between variables calculated at different instants in time t_j (with $j = 0,\ldots,k$). The subscripts may be omitted for variables for which this distinction is meaningless, for example, for the material properties related to the steel section or reinforcement which do not vary with time.

The unknown strain vector $\boldsymbol{\varepsilon}_j$ can be obtained based on Eqn (4-10) as:

$$\boldsymbol{\varepsilon}_j = \mathbf{F}_j \left(\mathbf{r}_{ej} - \mathbf{f}_{cj} + \mathbf{f}_{shj} \right) \tag{4-12}$$

in which $\mathbf{F}_j$ is the inverse of matrix $\mathbf{D}_j$

$$\mathbf{F}_j = \frac{1}{AE_j\, IE_j - BE_j^2} \begin{bmatrix} IE_j & -BE_j \\ -BE_j & AE_j \end{bmatrix} \tag{4-13}$$

Finally, the stress distributions at time t_j can be determined recalling the specified material properties as

$$\sigma_{cj} = E_{c1j}\varepsilon_j + \sum_{i=0}^{j-1} \sigma_{ci} E_{c2ji} - E_{c1j}\varepsilon_{shj} \tag{4-14}$$

$$\sigma_{sj} = E_s \varepsilon_j \quad ; \quad \sigma_{rj(a)} = E_{r(a)} \varepsilon_j, \ a = 1,...,n_r \tag{4-15a,b}$$

where $\varepsilon_j = \varepsilon_{xj} + y\kappa_j = \begin{bmatrix} 1 & y \end{bmatrix} \boldsymbol{\varepsilon}_j$, σ_{sj} represents the stress in the steel tubes, and $\sigma_{rj(a)}$ denotes the stress in the a^{th} layer of steel reinforcements.

4.3 COMPARATIVE STUDY BASED ON LONG-TERM EXPERIMENTS

The tests presented in Section 2.7.3 have been used in the following to evaluate the adequacy of the concrete models considered in this study to predict the time-dependent behaviour of CFST members. In the cases where the experimental elastic modulus was not reported in the published work, its value was estimated based on f_{cm28} in accordance with the formula provided by the corresponding models. In the case of the AFREM model, for which no expression is provided for the calculation of the elastic modulus, the equations specified in the MC90 model have been used. Similarly, when not specified, an elastic modulus of 200,000 MPa was adopted for the steel in the analysis.

Comparisons with numerical results have been carried out considering either total or incremental deformations (or in some cases both) depending on the measurements reported from the experiments. Due to space limitations, only some selected and

representative comparisons performed for the whole duration of the test are presented while considerations on the whole set of tests are provided considering the deformation state measured at their end. Both normal and expansive concrete have been considered in this study as discussed in the following section.

It is worth noting that the confinement effect on the core concrete is not considered in this Chapter as not critical at service conditions. Analysis conducted in Section 3.5 have proved that within the scope of the tests conducted in Chapter 3, the confinement effects have a quite limited influence on the static behaviour of ECFST specimens under service loading. This is also supported considering the different values measured by researchers for concrete creep Poisson's ratio, e.g. (Kim et al. 2005). However, many specimens in long-term experiments carried out by Tan & Qi (1987), Han & Yang (2003), and Han et al. (2004) were subjected to high sustained load levels, in which cases the confinement of the core concrete by steel tubes may have occurred. It is normal practice to consider that after the axial stress in concrete reaches a value of approx. $0.75f_{ck}$, where f_{ck} is the characteristic compressive strength of cylinder concrete, the Poisson's ratio of the concrete starts to become larger than the one possessed by the steel (Neville 1995), soon after which the confinement effect begins to exist. Despite this consideration, it has been observed that unconfined concrete models also tend to provide satisfactory predictions for heavily loaded CFST samples, e.g. reaching concrete stresses of approx. $0.9f_{cm28}$.

4.3.1 Time-Dependent Deformations during the Long-Term Tests

The benchmarking experiments include circular, square and rectangular cross-sectional CFST specimens subjected to axial or eccentric loads with loading ages t_0 varying between 5 days and 341 days after concrete casting. Material properties considered in these tests consist of the mean cylinder strength at 28 days of concrete age (f_{cm28}) ranging from 15 MPa to 60 MPa, a ratio of the steel area over the concrete area (α) from 0.02 to 0.2, and stress levels in the core concrete from $0.1f_{cm28}$ to $1.1f_{cm28}$. This section presents an overview of how the considered concrete models perform in predicting both incremental and total time-dependent deformations, referred to as $\Delta\varepsilon(t)$ and $\varepsilon(t)$ respectively.

4.3.1.1 CFST specimens with normal concrete

The relevant material and cross-sectional properties of the presented tests are summarised in Table 4-1. Parameters specified (not yet defined) include: the thickness of the steel tube t_s, the elastic modulus of the steel tube E_s, the elastic modulus of the concrete at 28 days E_{c28}, the weight of the cement per cubic meter of concrete c, the initial stress level in the concrete component $n_c=\sigma_c(t_0)/f_{cm}(t_0)$ (where $\sigma_c(t_0)$ denotes the sustained stress resisted by the concrete at the time of loading), the eccentricity e, and the magnitude of the long-term axial force N. The latter is expressed as a function of the ultimate capacity N_u at 28 days, i.e. $n=N/N_u$, in which N_u is determined as Eqn (3-1) (Zhong & Zhang 1992).

Table 4-1 Material properties of selected test CFST specimens

Specimens	t_s	E_s	f_{cm28}	E_{c28}	c	Proportion of concrete*	α	t_0	N	n	n_c	e
	mm	MPa	MPa	MPa	kg			days	kN			mm
A-4	4	2.13e5	37.1	-	400	0.40:1:1.53:2.85	0.166	28	380	0.43	0.63	0
C-120-2.3	2.14	1.92e5	19.9	2.07e4	-	-	0.091	28	115	0.22	0.34	0
R-2	2.93	1.95e5	29.7	2.92e4	457	0.45:1:1.33:2.47	0.177	28	304	0.73	0.92	0
11	4.85	1.97e5	28.3	-	-	-	0.168	28	550	0.52	0.99	40
α=0.184	4.37	2.24e5	28.8	-	-	-	0.184	341	500	0.58	0.95	0
15	4.78	1.97e5	28.3	-	-	-	0.166	208	380	0.36	0.69	40

NOTE: * the proportion of concrete is specified in terms of the water-cement-sand-gravel ratios

The comparisons carried out on CFST columns prepared with normal core concrete and loaded at 28 days are illustrated in Figure 4-2. The long-term response of the tests shown in Figure 4-2 (a-c) consists of CFST specimens with different cross-sections, i.e. circular, square, and rectangular respectively, subjected to sustained axial loads applied at 28 days. The case of eccentric loading is presented in Figure 4-2 (d) which depicts the time-dependent variation of the maximum incremental deformation measured on the outside edge of the steel tube. In the tests shown in Figure 4-2 (c,d), the initial concrete stresses induced at the beginning of the experiments are of the order of $1.0f_{cm28}$.

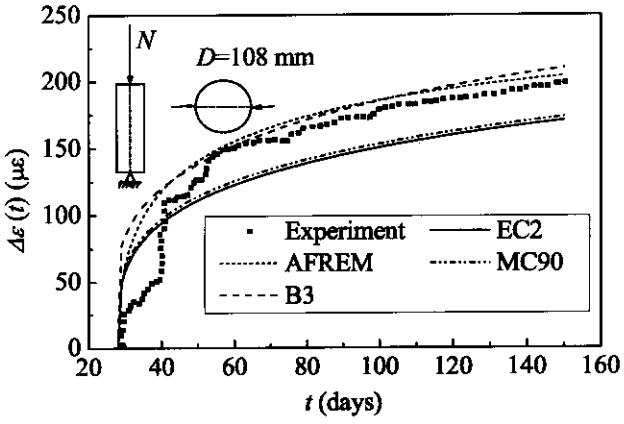

(a) Specimen A-4 (Lin 2002)

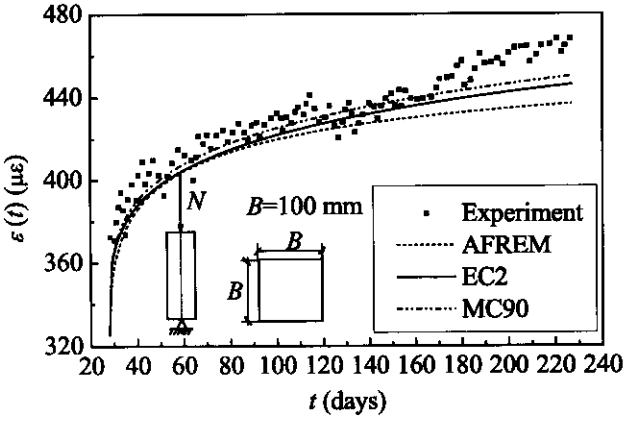

(b) Specimen C-120-2.3 (Morino et al 1996)

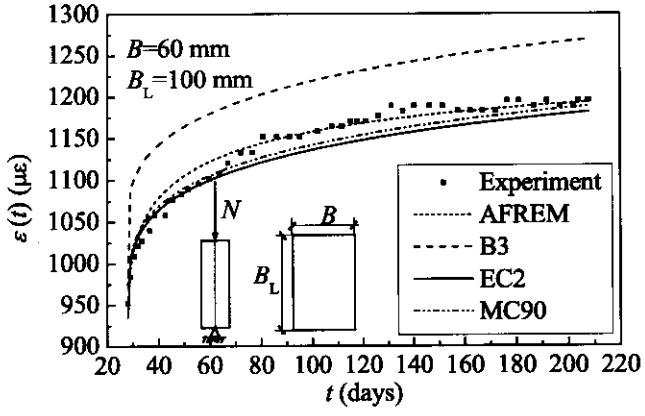

(c) Specimen R-2 (Han et al 2004)

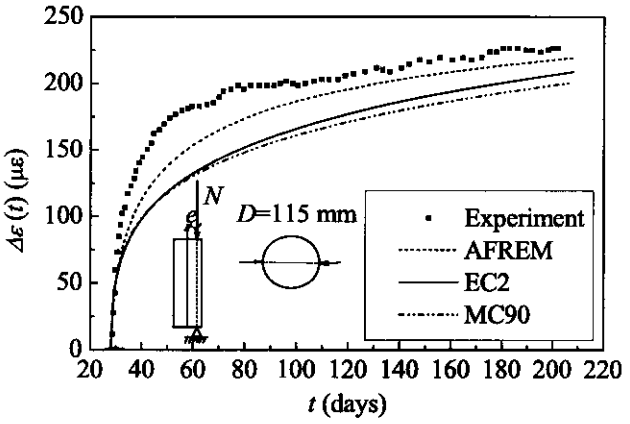

(d) Specimen 11 (Tan & Qi 1987)

Figure 4-2 Comparisons of calculated and measured deformations for CFST columns loaded at 28 days (normal concrete)

Despite the use of material models based on linear creep, the numerical simulations seem to well match the experimental results. Similar predictions were observed also in the whole set of experiments reported by Han & Yang (2003), Han et al. (2004) and Tan & Qi (1987). Hence, like the ECFST specimens, the CFST specimens filled with normal concrete also seems to have a higher upper limit for linear creep compared to plain concrete specimens, raising the question as to where to set the limiting stress level for the use of linear creep in CFST members. For these tests all concrete models considered provide a reasonable representation of the time-dependent response.

Specimens loaded at an older age of the concrete are considered in Figure 4-3 which presents typical comparisons carried out for two circular specimens tested under concentric and eccentric loading by Tan & Qi (1987). In this case, the time of loading occurred after 6 months from the casting of the concrete. Among the models considered, the AFREM one tends to excessively over-estimate the long-term incremental deformations while the remaining ones appear to provide a good estimate of the experimental behaviour.

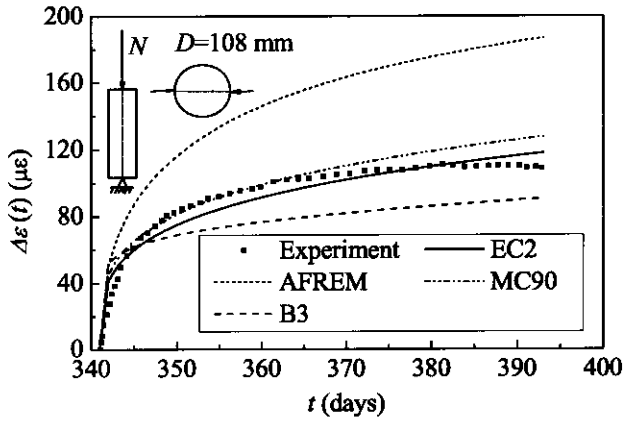

(a) Specimen α=0.184 (Tan & Qi, 1987)

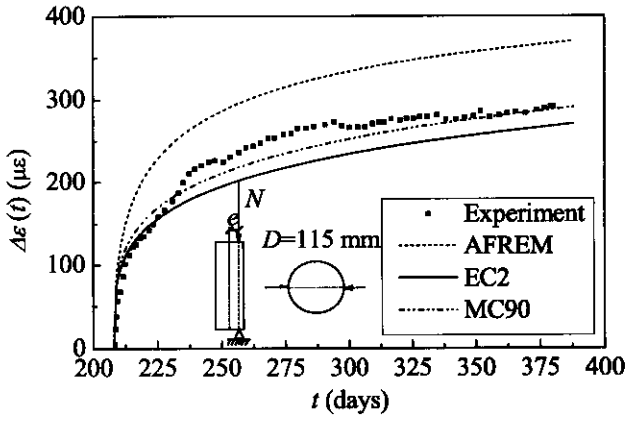

(b) Specimen 15 (Tan & Qi, 1987)

Figure 4-3 Comparisons of calculated and measured deformations for CFST columns loaded at $t_0 \geq 6$ months (normal concrete)

4.3.1.2 CFST specimens with expansive concrete

The predicted results are compared with the measured experimental data obtained in Chapter 3 to verify the adequacy of these concrete models in predicting the long-term response of ECFST specimens. The numerical results for ECFST specimens presented in this paper are shown in Figure 4-4.

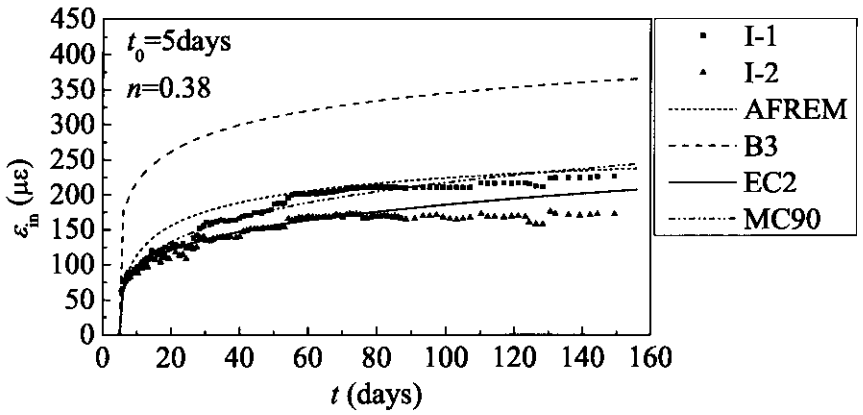

(a) Group I

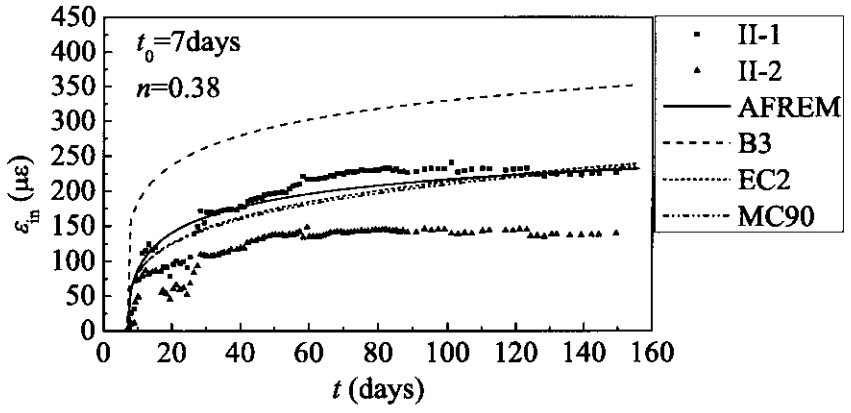

(b) Group II

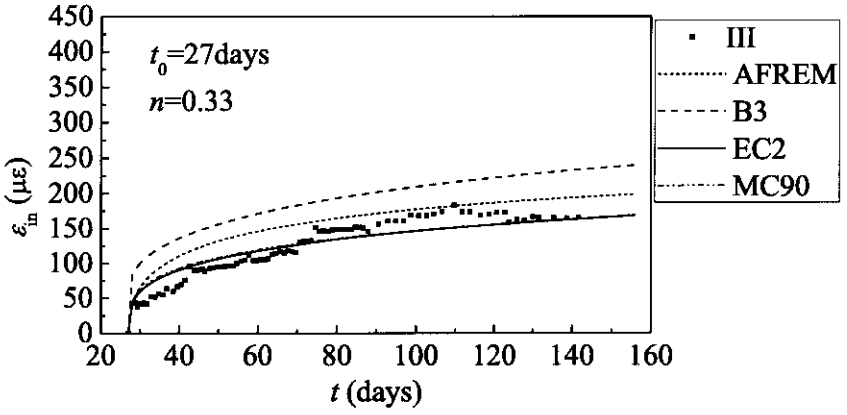

(c) Group III

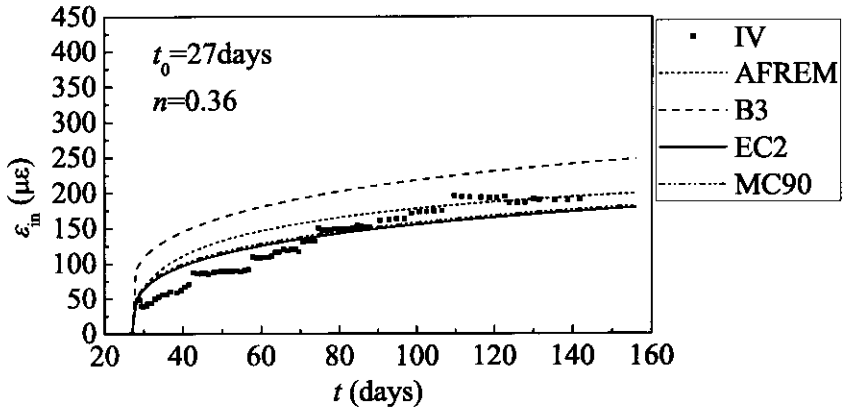

(d) Group IV

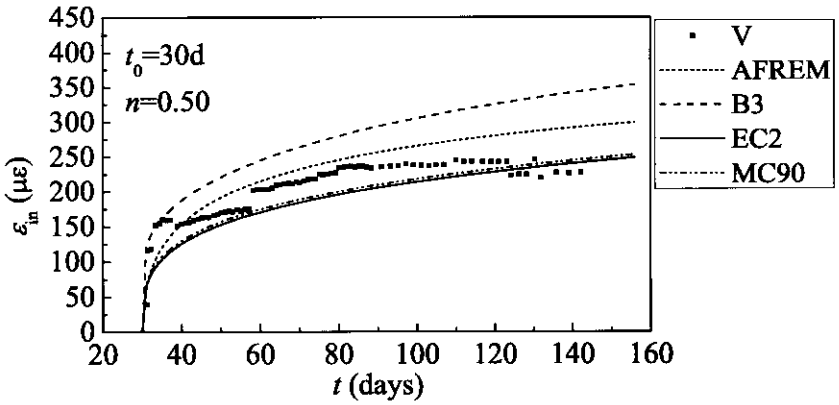

(e) Group V

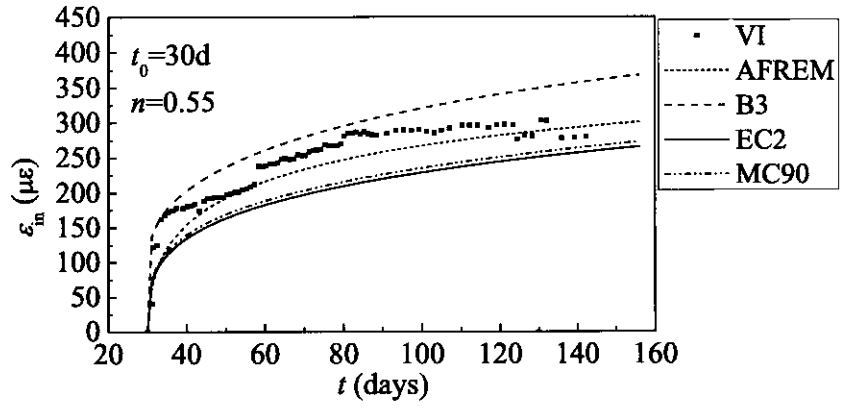

(f) Group VI

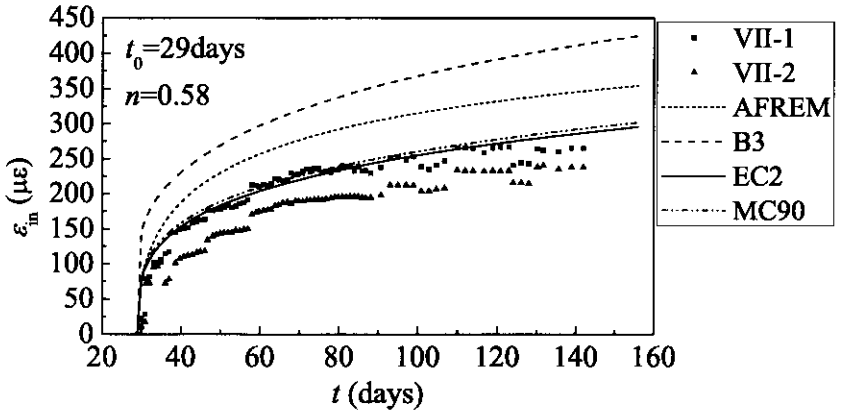

(g) Group VII

Figure 4-4 Long-term deformations measured during the long-term tests and comparisons with calculated predictions

The comparative results for ECFST specimens from Wang (1994) and Yao et al. (2007) are presented in Figure 4-5 and Figure 4-6, respectively, with the relevant material and cross-sectional properties summarised in Table 4-2.

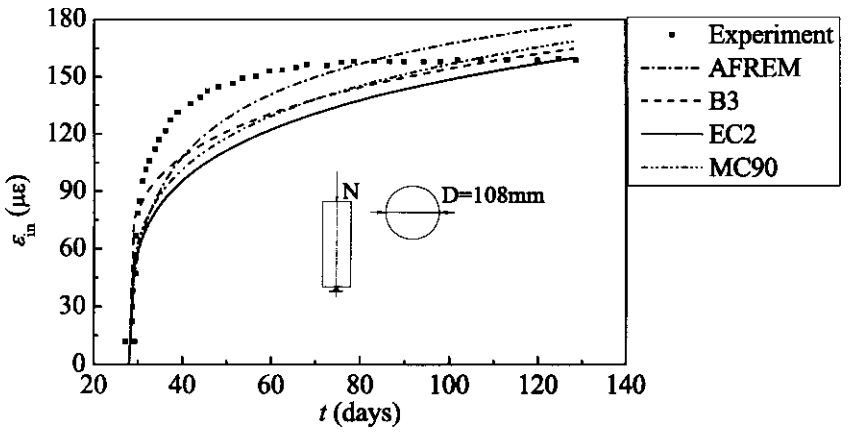

(a) Specimen CM1

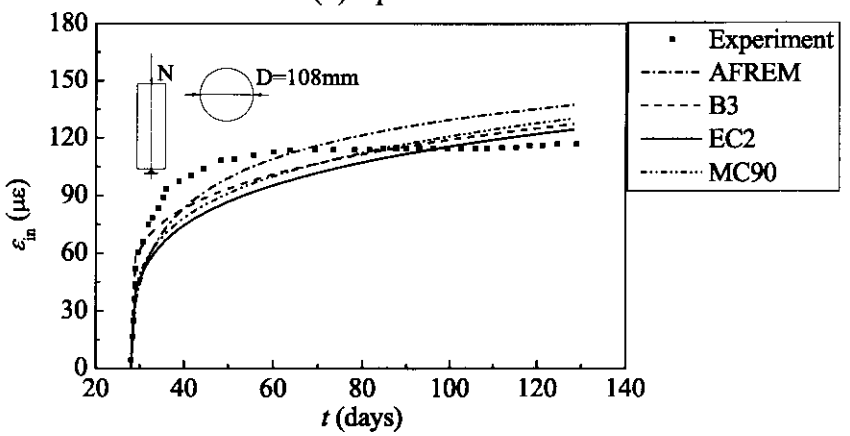

(b) Specimen CM2

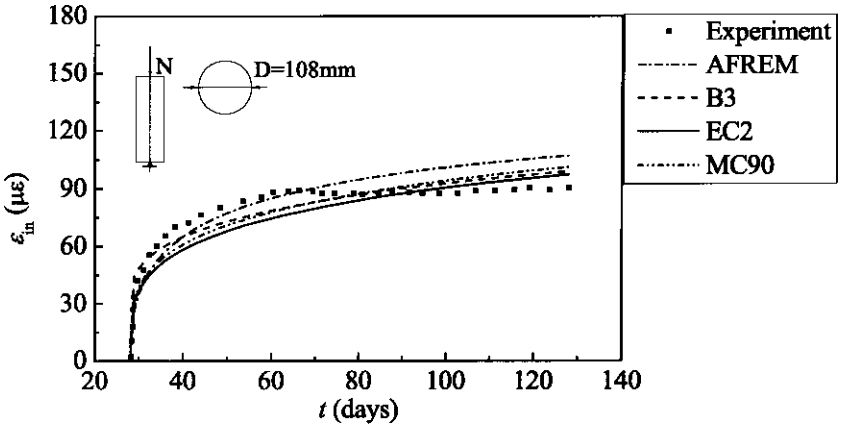

(c) Specimen CM3

Figure 4-5 Comparisons of calculated and measured deformations of ECFST columns tested by Wang (1994)

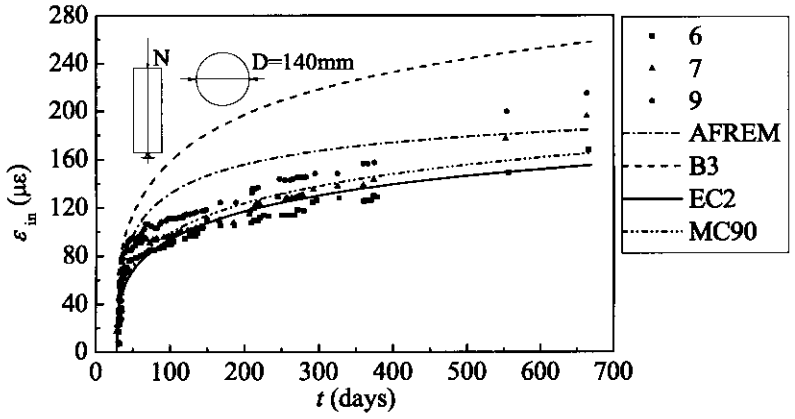

(a) Specimens 6, 7 and 9

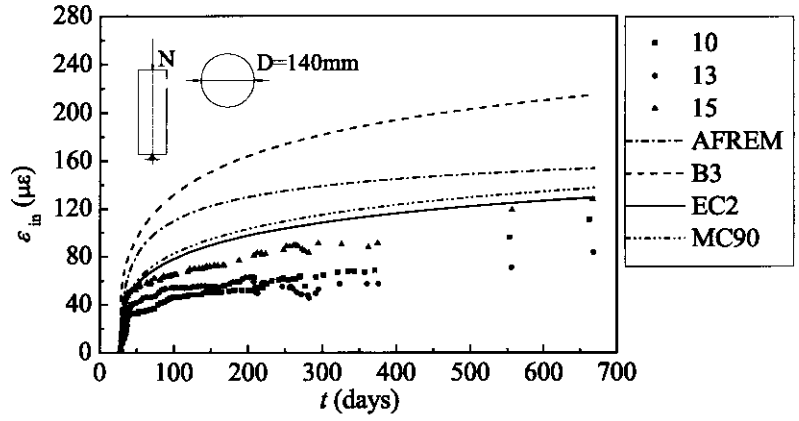

(b) Specimens 10, 13 and 15

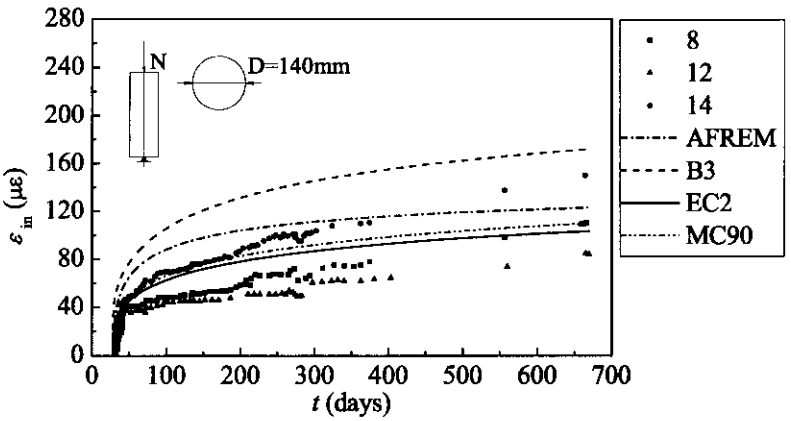

(c) Specimens 8, 12 and 14

Figure 4-6 Comparisons of calculated and measured deformations of ECFST columns tested by Yao et al. (2007)

Table 4-2 Material properties of test ECFST specimens

Specimens	t_s	E_s	f_{cm28}	E_{c28}	c	Proportion of concrete*	α	t_0	N	n	n_c	e
	mm	MPa	MPa	MPa	kg			days	kN			mm
CM1	4.5	-	29.3	-	-	0.45:1:1.84:3.56	0.190	28	400	0.52	0.78	0
CM2	4.5	-	29.3	-	-	0.45:1:1.84:3.56	0.190	28	307	0.40	0.60	0
CM3	4.5	-	29.3	-	-	0.45:1:1.84:3.56	0.190	28	240	0.31	0.47	0
6,7,9	2.5	-	43.3	3.92e4	390	0.47:1:2.00:2.45	0.075	28	242	0.19	0.28	0
10,13,15	2.5	-	43.3	3.92e4	390	0.47:1:2.00:2.45	0.075	28	202	0.16	0.23	0
8,12,14	2.5	-	43.3	3.92e4	390	0.47:1:2.00:2.45	0.075	28	162	0.13	0.19	0

NOTE: * the proportion of concrete is specified in terms of the water-cement-sand-gravel ratios

It can be observed that the B3 model overestimates the deformation of the ECFST specimens especially for those stubs loaded at very early ages, while the other three concrete models perform well in predicting the long-term response of these specimens and can be applied to predict the long-term response of ECFST members with the amount of the expansion admixture varying from 12% to 20% of the weight of cement and with sustained loads applied no later than 28 days after concrete

casting. Due to the incapability of the MC90 model to predict the autogenous shrinkage of the concrete, the EC2 and AFREM model are recommended for the long-term response prediction of ECFST structures with the concrete age at first loading $t_0 \leq 28$ days, considering the fact that the expansion admixture has the mean value of the order of 13% of the weight of cement in realistic situations. More experiments should be conducted for ECFST specimens with sustained loads applied at an old concrete age to further verify the reliability of these two models, as the AFREM model has been proved to have a poor performance in predicting the long-term response of CFST members with normal concrete when loads are applied more than 6 months after the concrete casting (i.e. $t_0 \geq 6$ months).

4.3.2 Final Deformations at the End of the Long-Term Tests

A second set of comparisons is carried out to study the ability of the different concrete models to predict the final deformation state at the end of the 81 long-term tests considered. This type of study is particularly useful for a designer who intends to know which model better estimates the long-term response at the end of the design life of a structure. This work is summarised in Figure 4-7 and Figure 4-8 where the experimental results are compared with the numerical values obtained using the four concrete models. Figure 4-7 shows the incremental deformations obtained for all the specimens and a regression line with the intercept equal to zero (dot-dashed) has been provided for each model to better highlight its accuracy. In Figure 4-7, black dots depict specimens whose values for ε_0 were reported in the literature, while square dots depict specimens for which this information was not provided. The correlation coefficient R^2 has been calculated based on

$$R^2 = \frac{m\left(\sum_{k=1}^{m} X_k Y_k\right) - \left(\sum_{k=1}^{m} X_k\right)\left(\sum_{k=1}^{m} Y_k\right)}{\sqrt{\left[m\sum_{k=1}^{m} X_k^2 - \left(\sum_{k=1}^{m} X_k\right)^2\right]\left[m\sum_{k=1}^{m} Y_k^2 - \left(\sum_{k=1}^{m} Y_k\right)^2\right]}} \tag{4-16}$$

where m defines the number of points included in the figure, X_k is the experimentally measured time-dependent deformation for specimen k, and Y_k represents the calculated time-dependent deformation for specimen k. In the case of perfect match between experimental and calculated results the regression line would be a straight line passing through the origin with a unit slope (straight solid line shown in Figure 4-7).

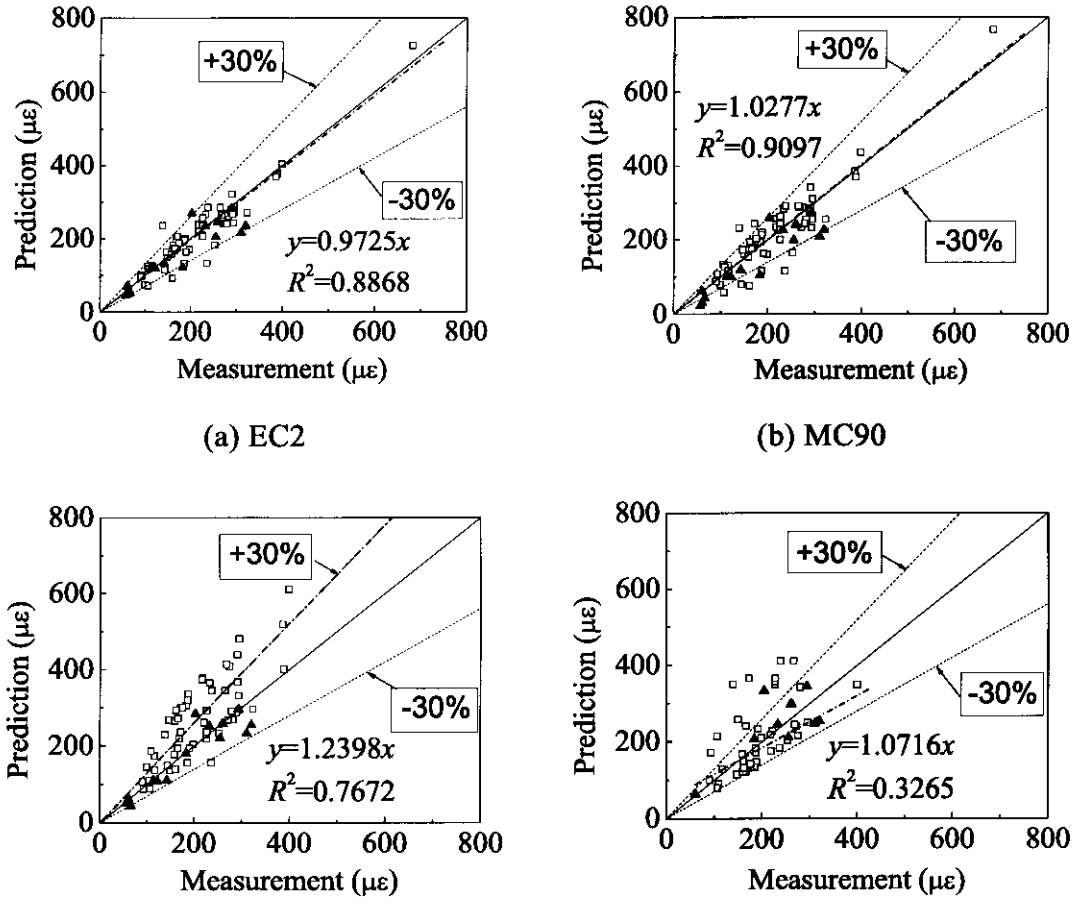

Figure 4-7 Comparison between the calculated and the experimental incremental deformations measured at the end of the 81 long-term tests (dot-dashed lines represent regression lines)

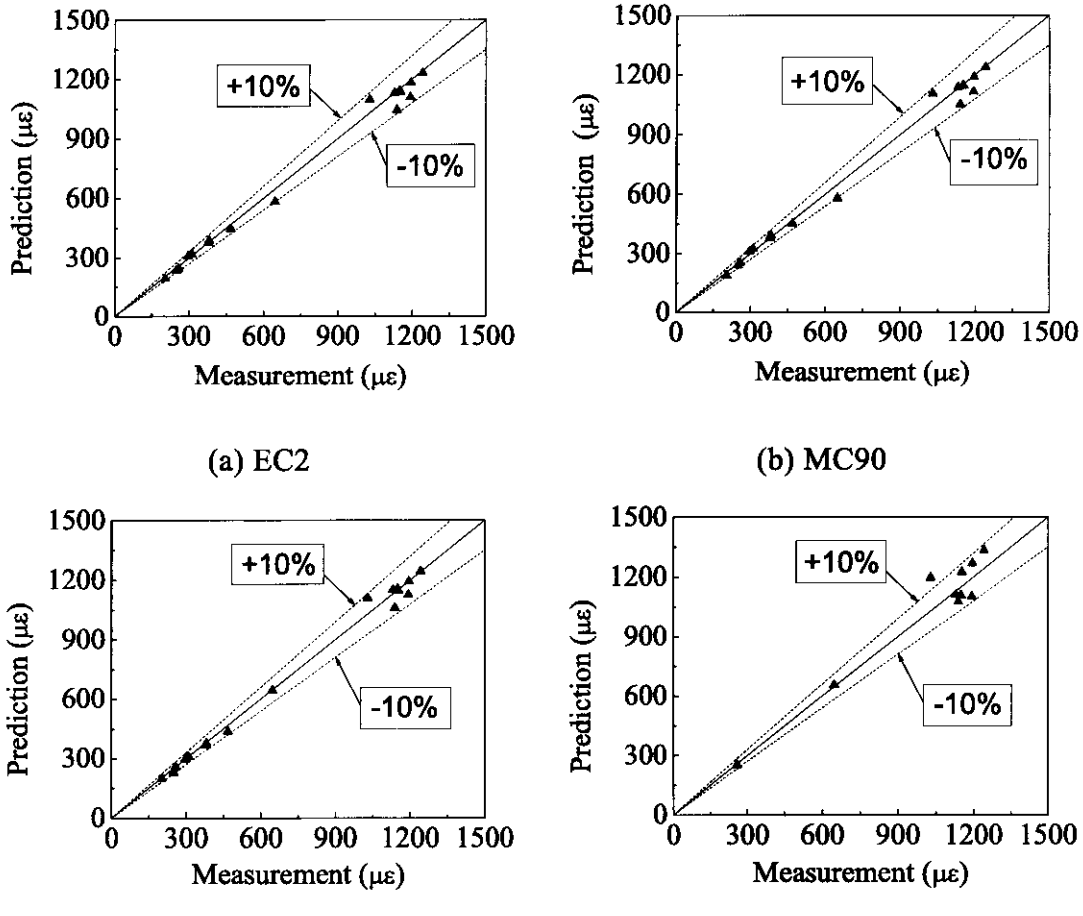

Figure 4-8 Comparison between the calculated and the experimental total deformations measured at the end of the long-term tests

In Figure 4-7, both regression lines of MC90 and of EC2 are close to the straight solid line even if with a scatter of approximately 30%. The high deviation of the calculated results with AFREM model from the experimental one are caused by the poor capacity of this model in predicting the long-term behaviour of CFST specimens loaded at an old age (i.e. with $t_0 \geq 6$ months).

Figure 4-8 depicts the variation of the total deformations for those specimens depicted with black dots in Figure 4-7. In this case, the scatter of results is significantly decreased due to the smaller magnitude of the incremental deformations.

Based on the comparisons carried out in this section, it can be concluded that the EC2 concrete model is capable of predicting very well the long-term behaviour measured in the reported experiments with a reasonable description of both creep and shrinkage behaviour for sealed concrete and will be used for the numerical work in the remaining part of this thesis. MC90 and B3 also lead to reasonable results even if producing larger discrepancy with measured experimental data. However, their inability to account for autogenous shrinkage prevents their use for the modelling of CFST specimens filled with high strength concrete, in which case autogenous shrinkage is significant. AFREM model was observed to largely overestimate the overall long-term response for specimens loaded at an older age of the concrete.

4.4 PARAMETRIC STUDIES

As presented in Section 2.4.2.4, current construction trend for arch bridge applications is to specify structural solutions with very low values for α which is well below those utilised to date in long-term tests. A very large number of CFST arch bridges (with main spans larger than 150 m) have been constructed in China with α values in the range of 0.04-0.08 (Figure 4-9) while those utilised in experiments vary between 0.08 and 0.2. To provide an overview of the long-term response observed in these laboratory tests, the ratio of the final measured incremental deformation ($\Delta\varepsilon_k$) over the instantaneous one observed at the time of loading (ε_o) has been plotted in Figure 4-10 (a) as a function of the α value corresponding to the specimen considered to enable a comparison between different test results. This variation has been illustrated in Figure 4-10 (b) as a function of the duration of loading (t-t_0). Only tests for which the total deformations are reported (Han & Yang 2003; Han et al. 2004; Kwon et al. 2005, 2007; Morino et al. 1996; Uy 2001) have been considered in Figure 4-10. It can be observed that for all the specimens, the time-dependent deformation accounts for more than 20% of the elastic one with peak values up to 40-50% for specimens with low α values and loaded even after 6 months from the concrete pour.

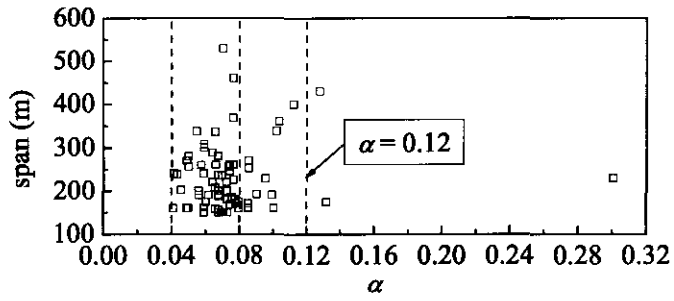

Figure 4-9 Values for α (the ratio of steel area over concrete area for the CFST cross-section) related to some CFST arch bridges built in China

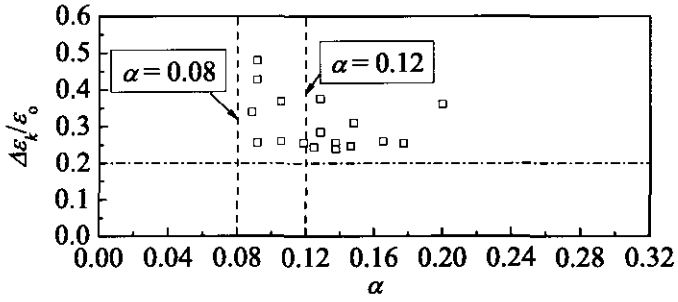

(a) Variation of the incremental deformations (non-dimensionalised with the instantaneous one) as a function of the value for α

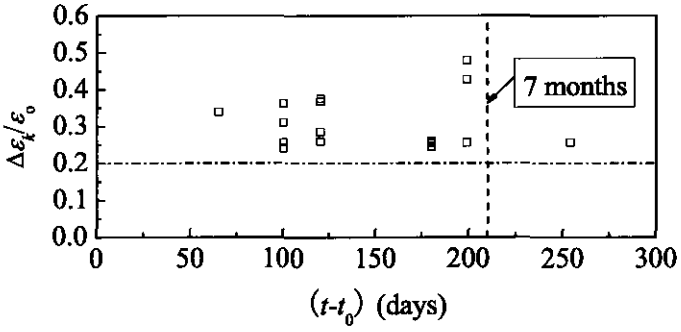

(b) Variation of the incremental deformations (non-dimensionalised with the instantaneous one) as a function of the duration of loading (t-t_0)

Figure 4-10 Summary of CFST long-term tests expressed in terms of values for α and the duration of loading

Considering that the long-term experiments carried out to date do not provide information for cross-sections with low values for α (Figure 4-10 (a)) and for long duration of sustained loading (Figure 4-10 (b)), an extensive parametric study based

on 270 CFST specimens has been carried out with the step-by-step method and modelling the time-dependent behaviour using the EC2 model as previously recommended. In the following only representative results from this extensive study are presented.

Figure 4-11 illustrates the effects of how the ratio of time-dependent (incremental) deformation $\Delta\varepsilon_t$ over the elastic one ε_o varies for different values for α and different durations of sustained loading (t-t_0). For illustrative purposes, the results provided in Figure 4-11 consist of CFST columns loaded axially at an age of concrete equal to 28 days. Figure 4-11 well depicts how time effects are more pronounced for cross-sections with low values of α. Considering a sustained load applied for a period of 50 years, the incremental deformation for a CFST column with α=0.04 becomes more than 80% of the elastic one, while the deformation of the column with α=0.2 only increases by 35%. The consequences of this behaviour may further be exacerbated by the possible occurrence of second order effects originated from these additional deformations. It can also be observed that during the first 1.5-7 months of loading the increase in deformation is of the order of 20-50% of the instantaneous one. These results are in good agreement with those already observed in the experimental measurements shown in Figure 4-10. After 7 months, the CFST columns still have a considerable increase in deformation (Figure 4-11). For example, for a column with α=0.04, the incremental deformation at 50 years is nearly twice the value calculated at 7 months.

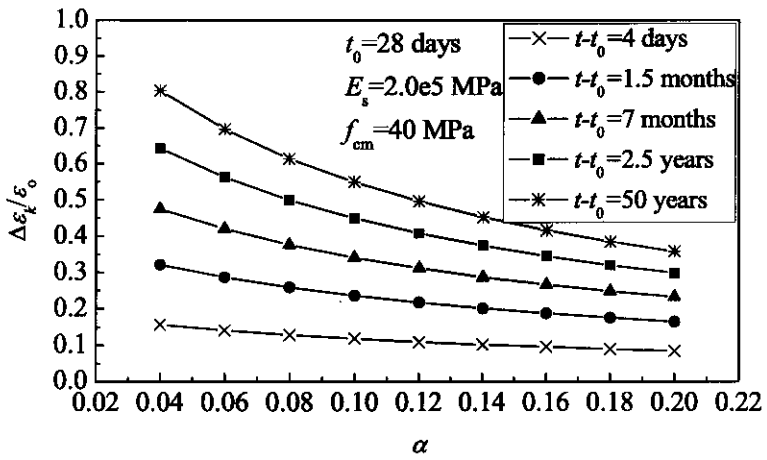

Figure 4-11 Parametric study: variation of $\Delta\varepsilon_t/\varepsilon_o$ with t-t_0 and α

Figure 2-6 provides an overview of how the time-dependent behaviour of CFST, expressed in terms of $\Delta\varepsilon_k/\varepsilon_o$ at 50 years after the casting of the concrete, is affected by varying the time of loading (t_0) from 3 days to 3 years. As expected, the long-term deformation increases significantly for concrete members loaded at an earlier age. If the loads are applied 3 days after the concrete casting, the total deformation after 50 years can increase by 105% for columns with α=0.04 (Figure 4-10). This value is 30% higher than the one obtained when loads are applied at 28 days (with a corresponding increase of 80% as discussed in Figure 4-11). After 180 days, the influence of the time of loading (t_0) on the long-term deformation becomes relatively insignificant. Though the total deformation keeps reducing as the time of loading increases, columns loaded at 3 years after concrete casting can still exhibit long term deformations of the order of 20% of the elastic ones during their in-service condition.

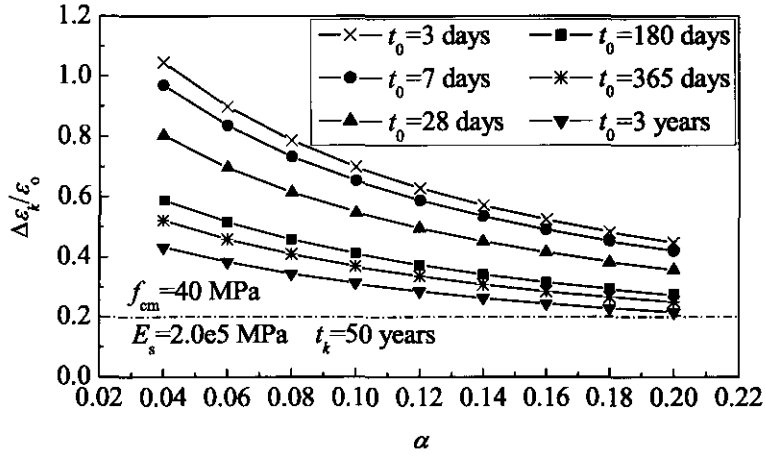

Figure 4-12 Parametric study: variation of $\Delta\varepsilon_k/\varepsilon_o$ with t_0 and α

All results discussed till now have combined the effects of both basic creep and autogenous shrinkage. To gain insight into the differences between the two, Figure 4-13 depicts the magnitude of the shrinkage deformation ($\Delta\varepsilon_{shk}$) as a function of the elastic one (ε_o). In these simulations it is assumed that the shrinkage starts one day after concrete casting, while the instantaneous deformation (used as reference) is calculated at a concrete age of 28 days. The long-term response has been calculated at 50 years of the age of concrete for different values of n_c, f_{cm28}, and α.

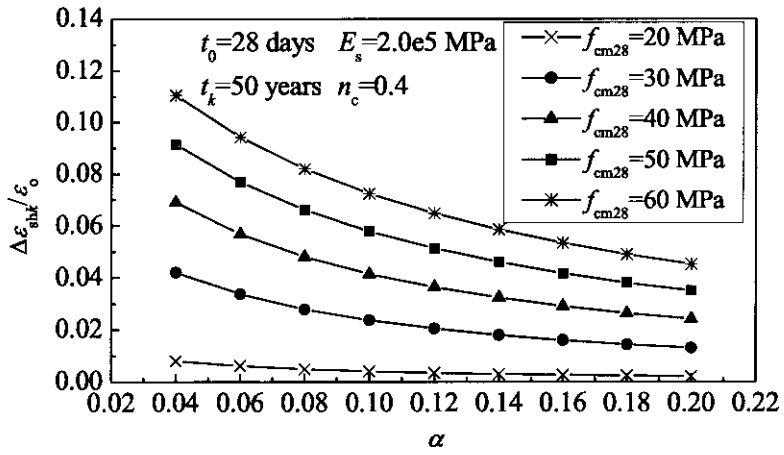

(a) Variation of $\Delta\varepsilon_{shk}/\varepsilon_o$ with f_{cm} and α

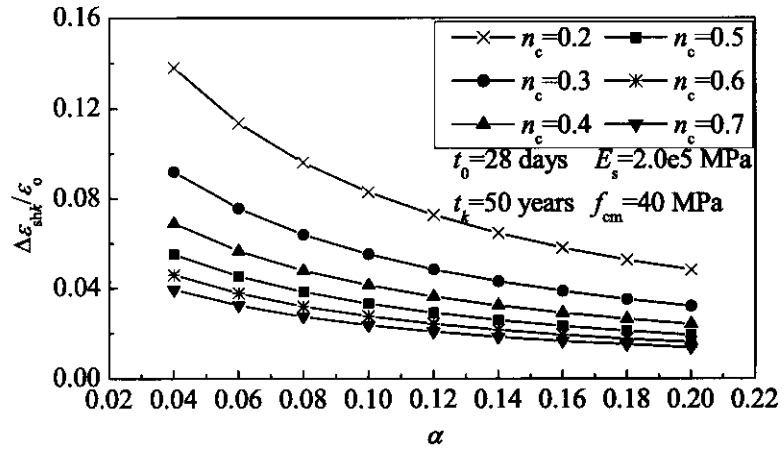

(b) Variation of $\Delta\varepsilon_{shk}/\varepsilon_o$ with n_c and α

Figure 4-13 Typical layout of the ultimate experiment

Based on Figure 4-13 $\Delta\varepsilon_{shk}/\varepsilon_o$ increases for decreasing values of n_c and α. A similar trend is noted for increasing values for f_{cm28}. Comparing Figure 4-11 and Figure 4-13, it can be observed that for normal strength concrete, shrinkage has a quite limited contribution to the overall deformation when compared to creep. For example, for a specimen with f_{cm28}=40 MPa and with α=0.04, the deformation after 50 years caused by shrinkage which started one day after the concrete casting only

accounts for 7% of the elastic one (see Figure 4-13 (a)), while the total deformation increases by 80% if the sustained load (equivalent to n_c=0.4) is applied to a column at 28 days after the concrete casting (Figure 4-11). This implies that the shrinkage deformation remains below 4% of the total deformation. This example is representative of typical bridge application as the adopted combination of f_{cm28}=40 MPa, α=0.04, n_c=0.4, t_0=28 days is common. Figure 4-13 also highlights that for increasing concrete strengths the effects induced by shrinkage tend to become more pronounced.

4.5 TIME ANALYSIS USING THE ALGEBRAIC METHODS

The use of the step-by-step procedure to model the time-dependent behaviour of the concrete is adequate to perform extensive parametric studies while it might not be practical for day-to-day design applications. In fact, an analysis carried out at a particular instant in time t_k requires the knowledge of the concrete behaviour recorded over the previous k-1 steps and these calculations can lead to extremely high computational costs. For this purpose, the use of the algebraic methods, i.e. Effective Modulus (EM) method, Mean Stress (MS) method and the Age-Adjusted Effective Modulus (AAEM) method, to predict the long-term response of CFST members is evaluated in the following. This has been carried out by comparing the results obtained using the step-by-step procedure with those calculated with the algebraic methods for the 270 CFST columns considered in the previous section. The EC2 model has been used to describe the time-dependent behaviour of the concrete. When applying the AAEM method two different expressions have been adopted for the age coefficient χ, i.e. one using the equation provided by Bazant & Baweja (2000) and one based on Brooks & Neville (1976). For clarity, the results obtained with these two expressions for χ have been referred to as AAEM-Bazant method and AAEM-Neville method respectively.

Figure 4-14 summarises the results of this study highlighting the envelope of maximum and minimum differences (expressed as a percentage) between the deformations calculated using the step-by-step procedure and the algebraic methods at 50 years of age for the concrete. Based on the results obtained it has been noted

that variations for α values lead to errors within 1%. For this reason only variations related to the time of loading t_0 and mean concrete strength f_{cm28} have been reported in Figure 4-14 which highlights that all four algebraic methods produce acceptable results. In particular, the AAEM-Bazant method achieves the accuracy with the step-by-step method with maximum errors within 5% for all the 270 specimens investigated. The maximum variations observed with the MS and the AAEM-Neville methods are equal to 5.4% and 6.9% respectively. The EM method has a deviation of the order of 10% calculated for low ages of loading. This difference tends to decrease as t_0 increases. In fact, for loads applied at 28 days the EM method has a difference of only 5% from the step-by-step procedure. It is worth mentioning that the EM method is particularly attractive for its simplicity of use. It is also worth highlighting that both AAEM method and EM method have the tendency to underestimate the time-dependent deformations while the use of the MS method gives overestimations which might be preferable in the sense of safety. Based on this latter consideration it can be concluded that the MS method should be used for quick design calculations. Obviously, considering the variability of the concrete properties the EM method could also be regarded as acceptable for simple calculations. Nevertheless, in the case of slender structural systems in which instability problems might be the governing design criteria or where there are critical service conditions it is still recommended to utilise more refined analysis methods, for example using the step-by-step procedure.

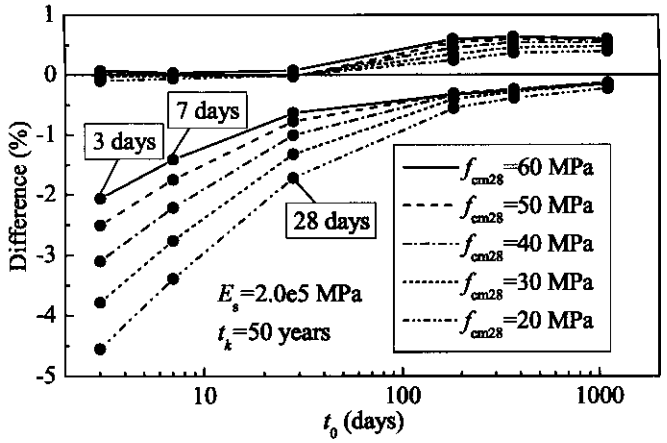

(a) AAEM – Bazant Method

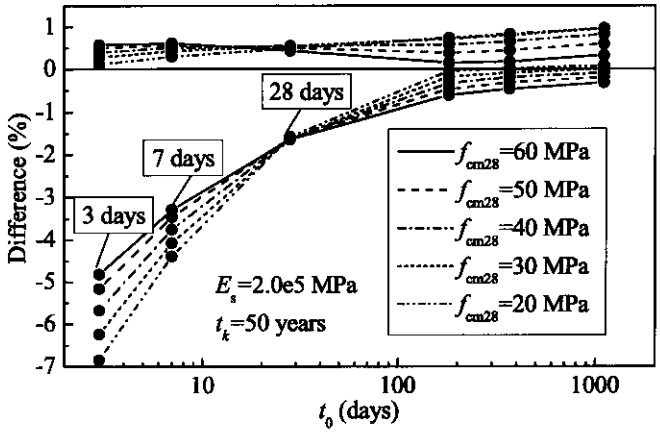

(b) AAEM – Neville Method

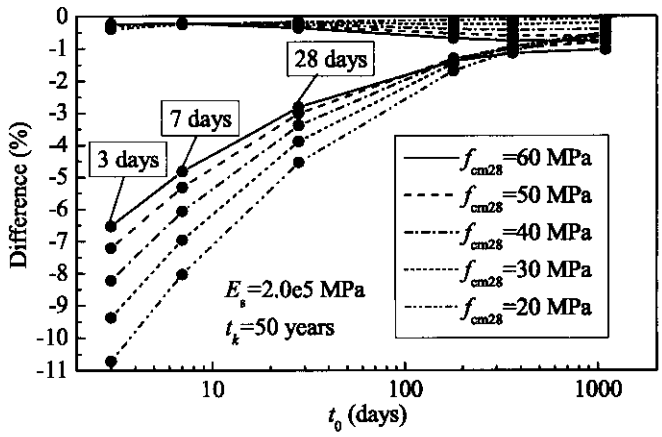

(c) EM Method

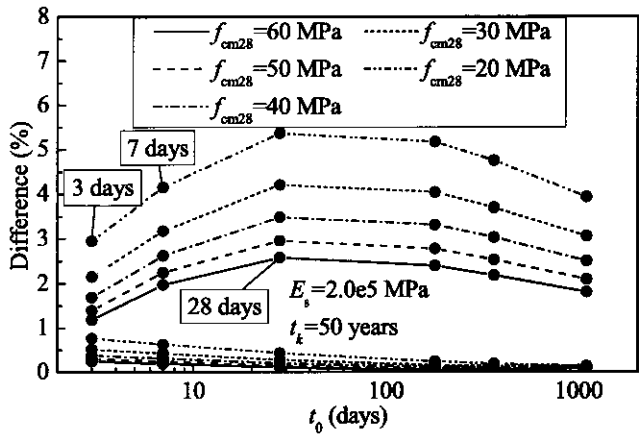

(d) MS Method

Figure 4-14 Variation between the long-term deformations calculated using the algebraic methods and the step-by-step procedure

4.6 CONCLUSIONS

This Chapter has focussed on the long-term behaviour of CFST columns. A unified method of analysis has been proposed and its ability to well depict the time-dependent response of CFST members has been investigated using 81 long-term tests available in the literature for benchmarking purposes. An extensive parametric study has then been carried out to highlight the considerable time effects on CFST members and to investigate the influence of the steel-concrete area ratio (α), the duration of loading, and the age at first loading (t_0) on the time-dependent response of realistic CFST columns for which no experimental results are currently available. Finally, four algebraic methods have been discussed and their accuracy has been evaluated against the results calculated using the step-by-step procedure. The following conclusions were drawn from the results:

1) The EC2 concrete model has been shown to exhibit a remarkable ability to predict the long-term deformations of CFST specimens with both normal and expansive core concrete and its use is recommended for this structural system. To account for the sealed conditions of CFSTs a nil exposed perimeter has been included in the input data.

2) When predicting the long-term response of the CFST structures, superimposed dead and quasi-permanent live loads applied after completion of the structure need to be carefully taken into account, as actions applied at a very old concrete age can induce considerable long-term deformations.

3) Shrinkage in the core concrete has limited influence on the overall deformation if the core concrete has normal strength.

4) All algebraic methods produce acceptable results with the AAEM method yielding the smallest error. Both AAEM method and EM method tend to underestimate the time-dependent deformations, while MS method generally producing overestimations of these. At the same time it was recommended to use more refined analysis methods for slender structural systems. The EM method was recommended for simple design calculations because of its simlicity and acceptable accuracy.

5) Further long-term experimental tests were recommended to be carried out using cross-sections with small α values, longer test duration and early ages of first loading, which are representative of current industry practice adopted for CFST members.

6) Further work is also required to identify the upper stress limits for using linear creep assumptions in composite columns and how these would interact with confined affects at high levels of load.

CHAPTER 5 TIME EFFECTS ON STATIC RESPONSE OF CONCRETE-FILLED STEEL TUBULAR ARCH BRIDGES

5.1 INTRODUCTION

As discussed in Section 2.7.5, there is no work carried out to date investigating the time-dependent behaviour of segmentally constructed CFST arch bridges including the effects of the ageing of the concrete, geometric nonlinearity, and combination of axial and flexural actions. No previous research has carefully evaluated the influence on the calculated long-term response of neglecting the loading ages of the core concrete during the construction of CFST arch bridges. In this context, the purpose of this Chapter is to present an accurate method of analysis to investigate the long-term response of CFST arch bridges using the EC2 model and the step-by-step method. The material property of the concrete with the capability of considering the varying concrete ages at loading in different construction stages is implemented with the commercial finite element package ABAQUS using its UMAT subroutine.

The FE modelling is implemented using a real long-span CFST arch bridge as case study to investigate the influence of time effects of the core concrete on its long-term response. For this purpose, the whole bridge is specified in the finite element model. Its results are benchmarked against readings measured on construction sites to validate the ability of the proposed analysis method to capture the real structural response. The necessity of considering the variation of the time of loading of the core concrete during construction is then discussed. The influences of geometric nonlinearities are also investigated. Finally, a simplified method is provided for design purposes to predict the long-term response of CFST arch bridges using commercial finite element programs taking into account concrete ageing and the construction process.

5.2 IMPLEMENTATION OF THE STEP-BY-STEP METHOD WITH ABAQUS

The development of a refined model for the prediction of the long-term behaviour of CFST arch bridges accounting for the various phases involved during construction represents a challenge for researchers as it requires to account for: (i) an accurate detailing in the model of the arch, piles, and ties, (ii) the time-dependent behavior of the core concrete during its varying loading and stress history, (iii) varying ages of the concrete core, (iv) the varying stiffness of the structure during construction, and (v) geometric nonlinearity. For this purpose, the FE commercial software ABAQUS is used to develop a model for CFST arch bridges. The step-by-step method and the EC2 model have been shown in the previous chapter to provide an adequate representation of the long-term response of CFST members with both normal and expansive core concrete and, for this purpose, have been implemented with ABAQUS for the long-term analysis of CFST arch bridges. The proposed FE model is able to account for the five factors (i)-(v) listed above.

The CFST structural system is modelled using the beam element B31 available from the ABAQUS library, and the step-by-step method is introduced based on the following assumptions:

1) The long-term behaviour of the core concrete under shear forces is not considered in this analysis.

2) The elastic strain is small.

3) The time-dependent behaviour of the concrete is identical in both compression and tension (usually acceptable for stress levels less than about one half of the strength of the concrete, as recommended in Gilbert and Ranzi (2011)).

4) The stress level in the arch ribs at service conditions is sufficiently low to assume the creep behaviour to remain linear.

5) No cracks occur in the core concrete during the analysis.

The first assumption is generally acceptable for slender beams. The other four

assumptions are acceptable as the arch is mainly subjected to compression, and the stress levels in both compression and tension are less than one half of the tensile strength of the concrete for CFST arch bridges during construction or at service conditions, as discussed in the following sections.

Each construction stage is discretised into k steps based on a geometric progression (Eqn (5-1)) as follows:

$$(t_k - t_0) = 10^{\frac{1}{m}}(t_{k-1} - t_0) \tag{5-1}$$

$$m = \frac{k-1}{\log(t_k - t_0) - \log(t_1 - t_0)} \tag{5-2}$$

where t_i (with $i = 0,...,k$) define the time at instant i, and the coefficient m is determined by setting t_1-t_0=0.01 days, where t_0 depicts the age of first loading. Rewriting Eqn (4-4) at time t_{k-1}:

$$\varepsilon_{ck-1} - \varepsilon_{shk-1} \cong \sigma_c(t_0)J(t_{k-1},t_0) + \sum_{j=1}^{k-1}\frac{1}{2}\left[J(t_{k-1},t_j) + J(t_{k-1},t_{j-1})\right]\left[\sigma_c(t_j) - \sigma_c(t_{j-1})\right] \tag{5-3}$$

and subtracting Eqn (5-3) from Eqn (4-4), the incremental form of the discretised equation can be expressed as:

$$\Delta\sigma_{ck} = E_{c1k}\left[\Delta\varepsilon_{ck} - \Delta\varepsilon_{shk} - \Delta\varepsilon_{dk}\right] \tag{5-4}$$

where

$$\Delta\varepsilon_{dk} = \sum_{j=1}^{k-1}\left(E_{c2kj}\cdot\Delta\sigma_{cj}\right) \tag{5-5}$$

$$E_{c1k} = \frac{2}{J(t_k,t_k) + J(t_k,t_{k-1})} \tag{5-6}$$

$$E_{c2kj} = \begin{cases} 0 & \text{for } k = 1 \\ \dfrac{J(t_k,t_j) + J(t_k,t_{j-1}) - J(t_{k-1},t_j) - J(t_{k-1},t_{j-1})}{2} & \text{for } k > 1 \end{cases} \tag{5-7}$$

The constitutive model for the core concrete accounting for creep and shrinkage effects can then be described as:

$$\Delta\boldsymbol{\sigma}_{ck} = \mathbf{D}_{ck} \cdot \Delta\boldsymbol{\varepsilon}_{ck} \tag{5-8}$$

and

$$\Delta\boldsymbol{\sigma}_{ck} = \begin{Bmatrix} \Delta\sigma_{ck} \\ \Delta\tau_{c1} \\ \Delta\tau_{c2} \end{Bmatrix};\ \mathbf{D}_{ck} = \begin{bmatrix} E_{c1k} & & \\ & G_c & \\ & & G_c \end{bmatrix};\ \Delta\boldsymbol{\varepsilon}_{ck} = \begin{Bmatrix} \Delta\varepsilon_{ck} - \Delta\varepsilon_{shk} - \Delta\varepsilon_{dk} \\ \Delta\gamma_{c1} \\ \Delta\gamma_{c2} \end{Bmatrix} \tag{5-9a,b,c}$$

$$G_c = \frac{1}{2 \cdot J(t_k, t_k) \cdot (1 + \nu_c)} \tag{5-10}$$

where $\Delta\sigma_{ck}$, $\Delta\tau_{c1}$, and $\Delta\tau_{c2}$ represent the incremental normal stress and shear stresses in two directions, respectively; $\Delta\varepsilon_{ck}$, $\Delta\gamma_{c1}$, and $\Delta\gamma_{c2}$ depict the incremental normal strain and shear strains in two directions, respectively; E_{c1k} and $\Delta\varepsilon_{dk}$ can be determined according to Eqn (5-5) and Eqn (5-6); $\Delta\varepsilon_{shk}$ and $J(t_k, t_k)$ are determined with model EC2; G_c denotes the shear modulus of the core concrete; and ν_c=0.17 is the Poisson's ratio of the core concrete.

The constitutive mode of Eqn (5-8) is implemented in ABAQUS using the UMAT subroutine, following the flowchart presented in Figure 5-1.

5.3 OVERVIEW OF THE CASE STUDY

As outlined in Section 2.4, half-through CFST arch bridges with catenary truss arches represent a popular structural solution for long CFST arch bridges (i.e. with a span longer than 150 m). In this context, the Dong-Guan Waterway Bridge, located in the Guangdong Province (China) and opened to traffic in 2005, is adopted in the following to outline the use of the proposed FE model as representative of this form of construction.

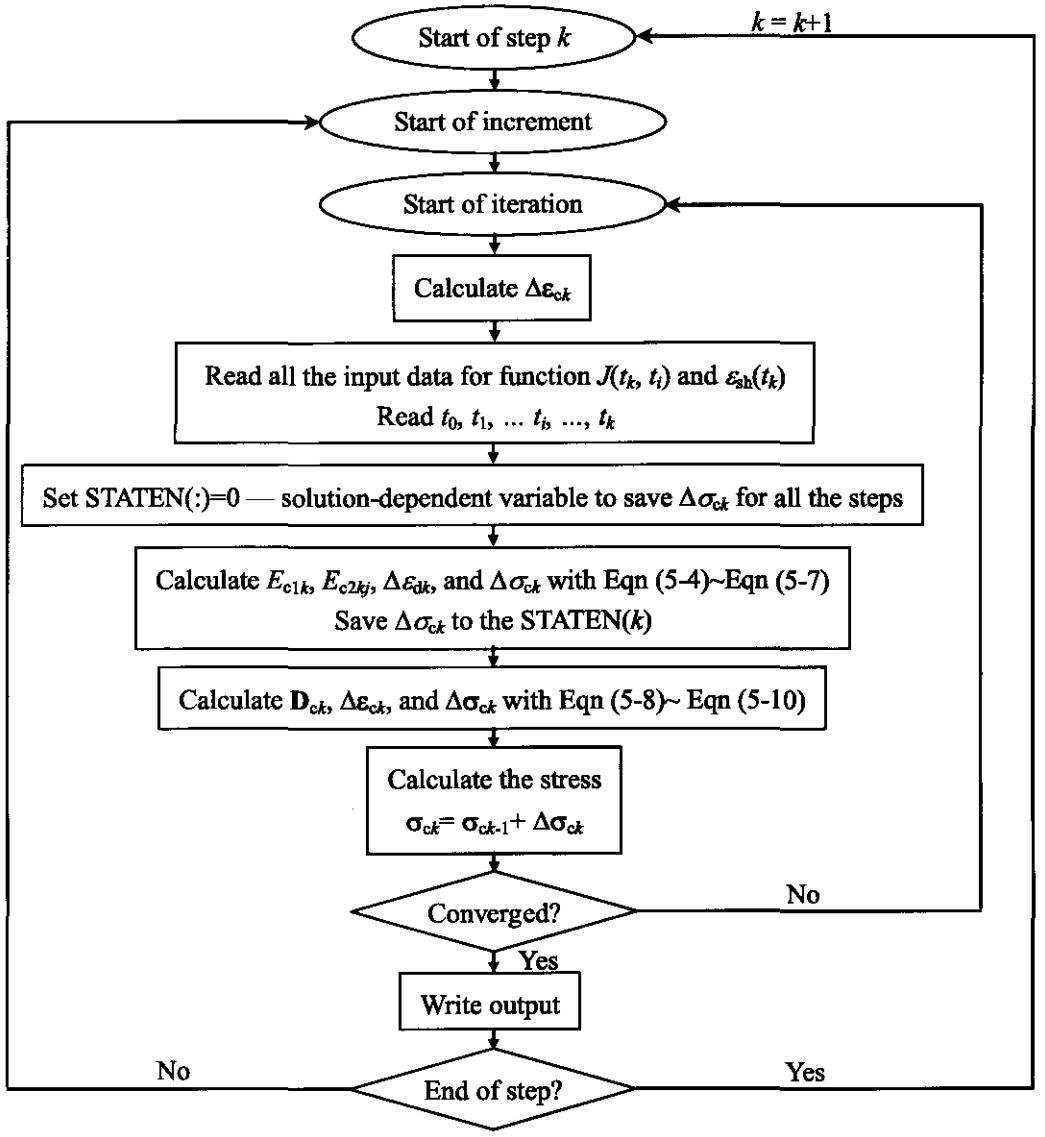

Figure 5-1 Flowchart to implement the step-by-step method in ABAQUS

5.3.1 Description of the bridge

5.3.1.1 Overview

The Dong-Guan Waterway Bridge consists of two independent and identical half-through CFST arch bridges (Figure 5-2). For each bridge, the distance between the two arch ribs is 19.5 m. Its deck is 53.6 m wide and its span lengths are 50 m, 280 m and 50 m, respectively.

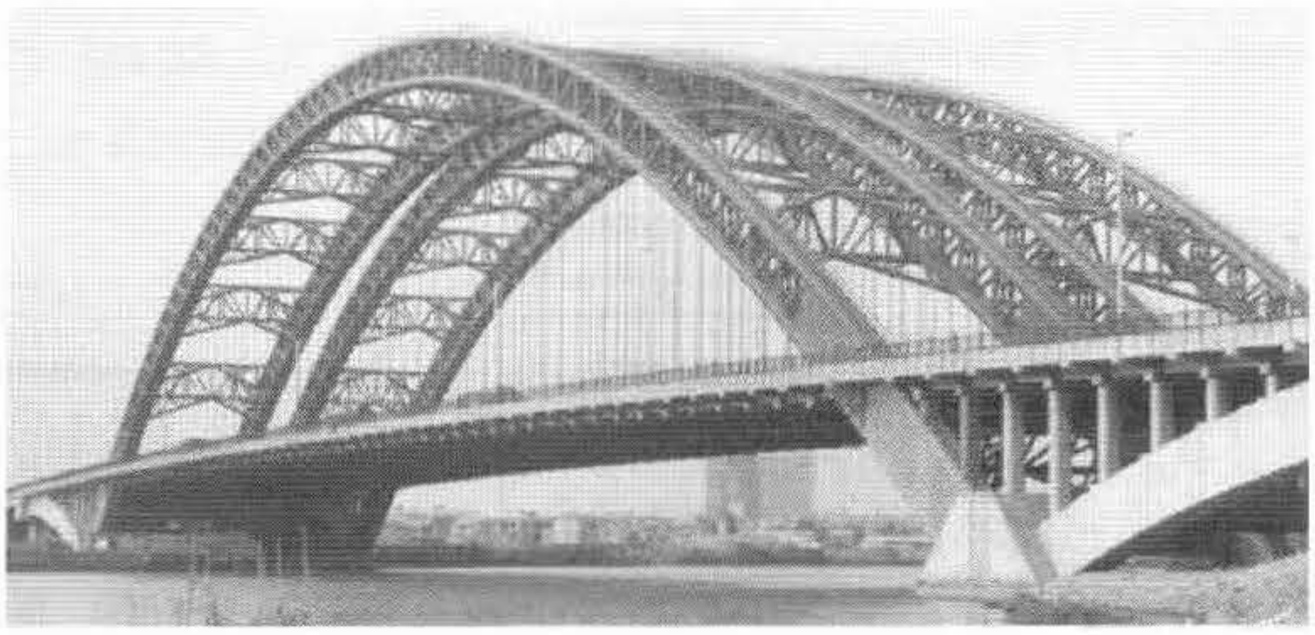

(a) Actual Bridge

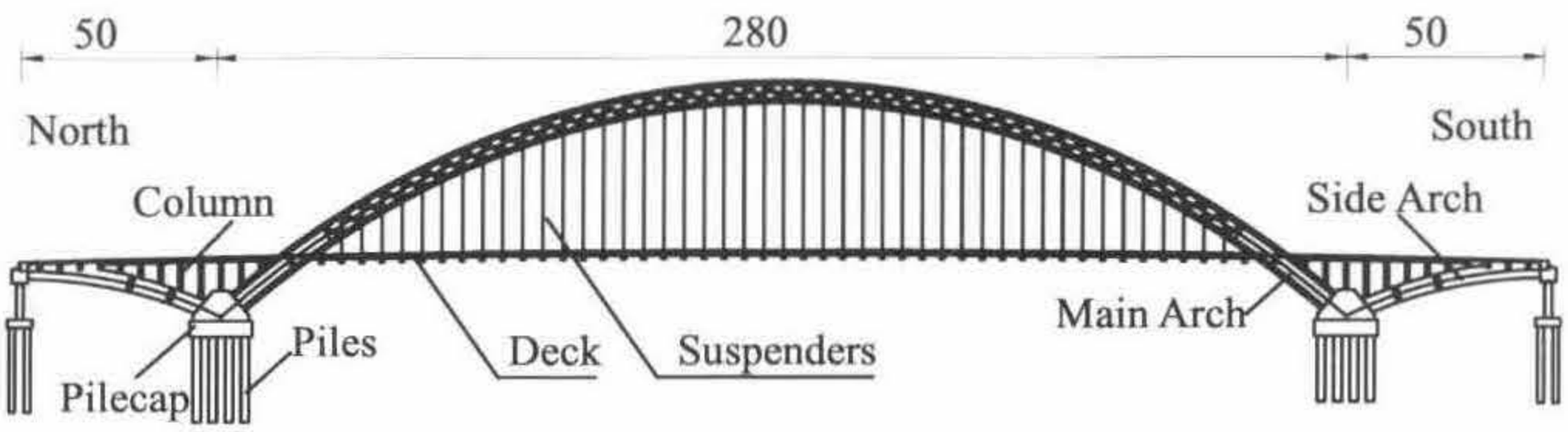

(b) Elevation view of the Dong-Guan Waterway Bridge (Unit: m)

Figure 5-2 Dong-Guan Waterway bridge

5.3.1.2 Main arch ribs

The rise over span ratio of the main arch is 1/5, and the arch axis follows the following catenary equation with the cartesian coordinates shown in Figure 5-3:

$$y = f + \Delta f - \frac{f + \Delta f}{m - 1} \cdot \left[\mathrm{ch}\left(k \cdot \xi\right) - 1 \right] + 3.689 \tag{5-11}$$

$$k = \ln\left(m + \sqrt{m^2 - 1}\right) \tag{5-12}$$

$$\xi = \frac{L - 2x + 8.5}{L}, (4.25 \le x \le 275.75) \tag{5-13}$$

where $f = 54.3$ m depicts the vertical distance from the arch springing to the arch crown; $\Delta f = 0.45$ m represents the camber of the arch at the crown; $m = 1.5$ is a constant coefficient; and $L = 271.5$ m denotes the distance between the two arch springings for the main arch (see Figure 5-3).

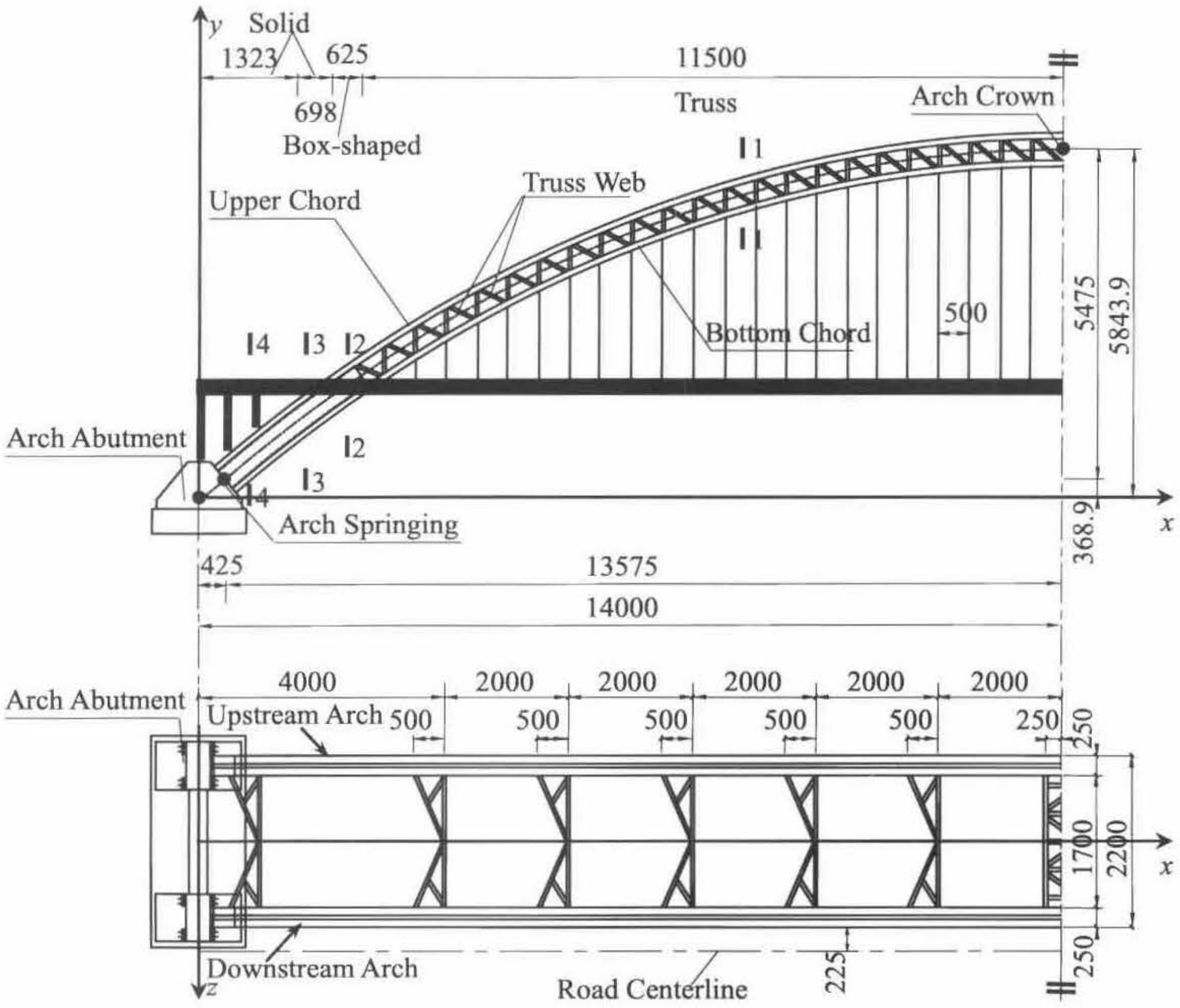

Figure 5-3 Details for the main arch (Unit: cm)

Thirteen wind braces, i.e. one I-type wind brace at the arch crown and twelve K-type ones located symmetrically with respect to the arch crown, are placed between the arch ribs to ensure the lateral stability of the bridge during construction and service life (Figure 5-3). These braces are formed with transverse hollow steel tubes (with the diameter and thickness of 670 mm and 12 mm, respectively) and diagonal members (with hollow tubes with diameter and thickness of 351 mm and 10 mm, respectively).

Three kinds of cross-sections (i.e. truss, box-shaped and solid, see Figure 5-4) with the same outside dimensions are adopted for the main arch at different locations along the bridge length (Figure 5-3). Within the central segment of the truss 230 m long (115 m for half of the span), the top and bottom chords consist of two horizontal

dumbbell-shaped CFST members while the truss webs are formed with diagonal and vertical hollow steel tubes (Figure 5-4 (a)). Outside the central segment and above the deck, the hollow steel tubular truss webs are filled with concrete with the box shape detailed in Figure 5-4 (b). The cross-section of the truss specified below the deck is filled with concrete (Figure 5-4 (c), (d)) to protect the arch from damage from possible ship collisions. The only difference between cross-section shown in Figure 5-4 (c) and the one in Figure 5-4 (d) relies on the thickness of steel tubes, which is 16 mm and 18 mm, respectively. The steel adopted for arch ribs and wind braces has a yield strength of 345 MPa and the encased core concrete has a cylinder characteristic compressive strength of 40 MPa.

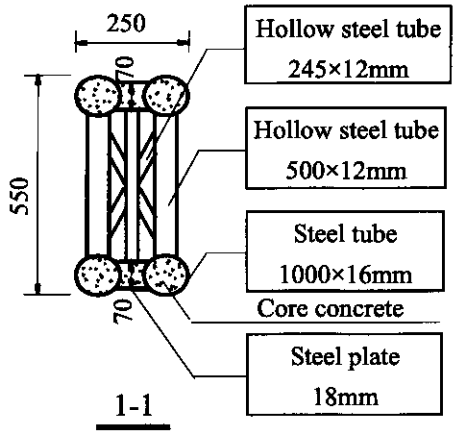

(a) Truss Cross-Section
(1-1 in Figure 5-3)

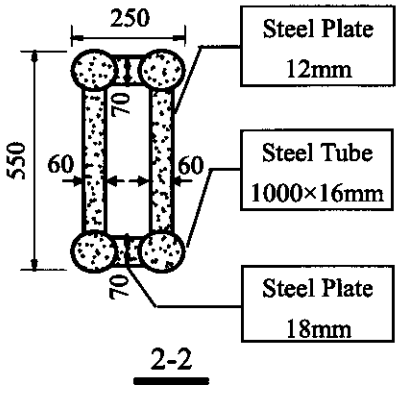

(b) Box-Shaped Cross-Section
(2-2 in Figure 5-3)

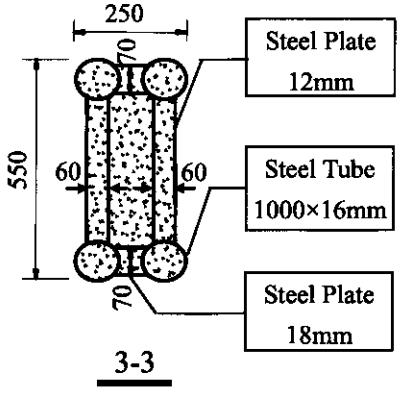

(c) Solid Cross-Section
(3-3 in Figure 5-3)

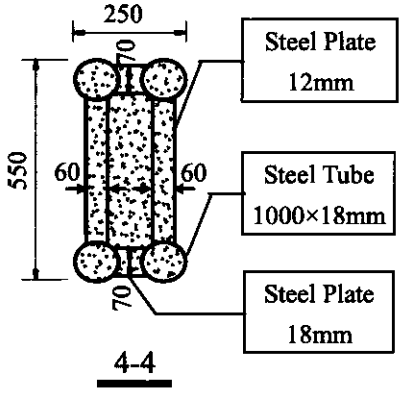

(d) Solid Cross-Section
(4-4 in Figure 5-3)

Figure 5-4 Details for the cross-sections of the main arch (Unit: cm)

5.3.1.3 Ribs of the side arch

Reinforced concrete is used for the side arches which possess a rise over span ratio of 1/9.819 (Figure 5-5). The arch axis follows the catenary equation:

$$y = f - \frac{f}{m-1} \cdot \left[\mathrm{ch}\left(k \cdot \xi\right) - 1 \right] + 2.448 \tag{5-14}$$

$$k = \ln\left(m + \sqrt{m^2 - 1}\right) \tag{5-15}$$

$$\xi = \frac{L - 2x + 10.65}{L}, \left(5.325 \le x\right) \tag{5-16}$$

where $f = 9.1\mathrm{m}$ depicts the vertical distance from the arch springing to the arch crown; $m = 1.9$ is a constant coefficient; $L = 89.35\mathrm{m}$ denotes the distance between the two arch springings for the main arch.

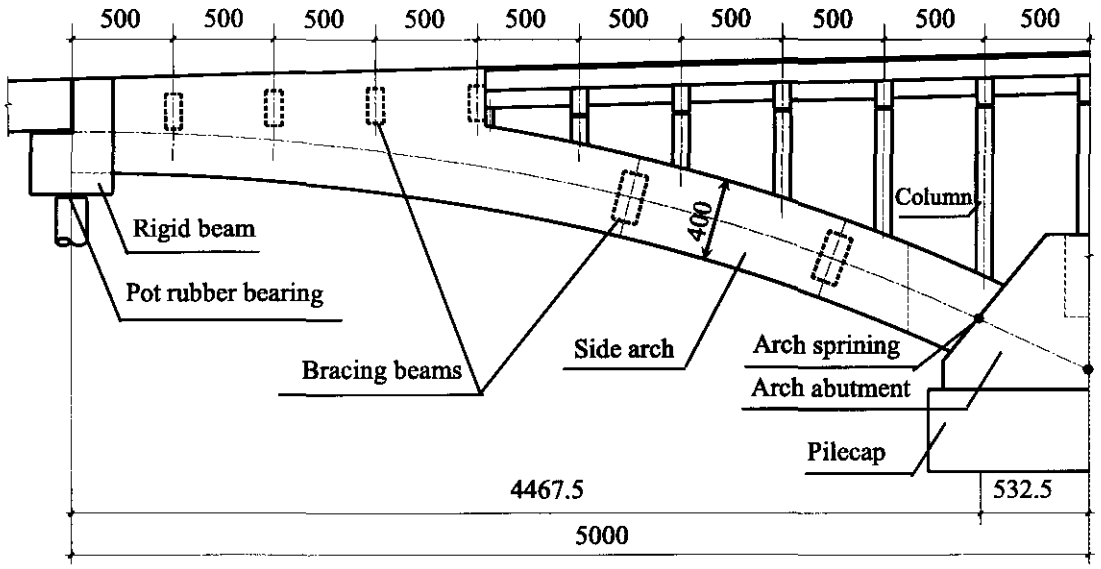

Figure 5-5 Details for the side arch (Unit: cm)

The side arch has a 4 m × 2.5 m solid rectangular cross-section which is enlarged to 4 m × 3.19 m at the arch crown to resist the pre-compressive stress from the ties. To ensure the stability of the side arch, connections at different locations along the arch are provided between the two ribs. These occurred at the arch crown with a rigid

cast-in-situ beam, and along the remaining of the arch with four precast reinforced concrete beams (1.7 m high and 0.8 m wide) regularly spaced at 5 m and two concrete beams (2.4 m high and 1.2 m wide equally) spaced along the rest of the side arch axis.

Concrete with a cylinder characteristic compressive strength of 32.3 MPa is used for the side arches and the bracing beams. The main reinforcement has a yield strength of 335 MPa.

5.3.1.4 Bridge decks and their supports

The bridge deck consists of transverse beams, longitudinal beams, carriageway slabs, footpath boards, and deck pavement (Figure 5-6). In the main arch part, there are forty-seven concrete transverse beams and two steel transverse beams placed at a distance of 5 m. The steel transverse beams are set at the intersection of the arch and the deck with a distance of 7.5 m from their adjacent beams. Ten concrete transverse beams, including four beams used as the bracing between arches, are built on the side arches.

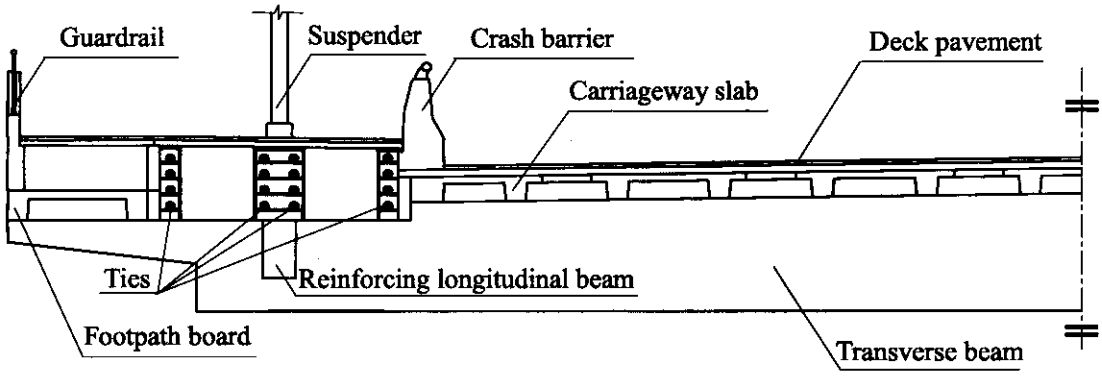

Figure 5-6 Details for the bridge deck

Longitudinal beams are cast between two adjacent transverse beams at the location of the suspender to increase the robustness of the bridge deck. Seven carriageway slabs, and two footpath boards are supported on the transverse beams, all of which are precast π-shaped reinforced concrete slabs with a thickness of 0.35 m. The slabs and boards are covered by pavements, the layers of which are (from bottom to the top): cast in-situ steel-fiber reinforced concrete with reinforcing bar mesh, waterproofing layer, and SMA (Stone Mastic Asphalt) pavement.

The concrete adopted for the transverse beams, the longitudinal beams, and the concrete slabs have a cylinder characteristic compressive strength of 28.3MPa. The main reinforcement has a yield strength of 335 MPa.

Sixteen flexible ties passing through the springings of the main arch are anchored at the crown of the side arch to bear the outward-directed horizontal forces at arch springings of the main arch (see Figure 5-6). Guide rollers are installed on each transverse beam to reduce the friction between the ties and the concrete. The ties are numbered in Figure 5-7 for referencing in the site monitoring measurements.

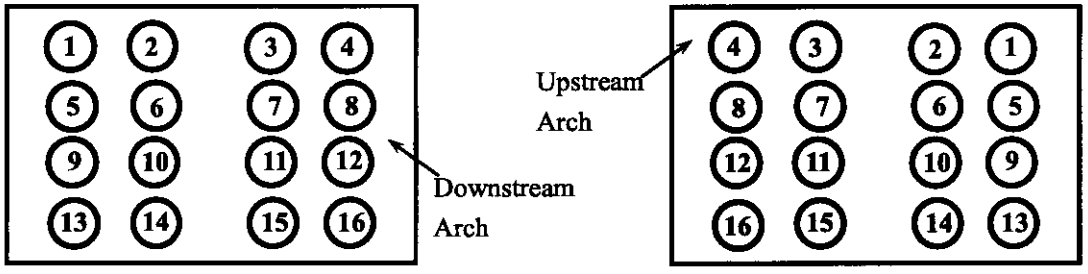

Figure 5-7 Layout of the Ties

The transverse beams are connected to CFST main arches with flexible suspenders. Each transverse beam is hung by one suspender at each end, except for the beams intersecting the arch which have two suspenders at a distance of 500 mm from each end. The transverse beams on the side arch are supported by concrete columns with obround cross-sections and dimensions of 0.8×1.5 m. Their concrete cylinder characteristic compressive strength is 32.3 MPa and the yield strength of the steel bars is 335 MPa.

5.3.1.5 Bridge piles

Each abutment of the arch is supported by twenty-four bored piles with diameter of 1.85 m and length varying between 20.5~22.9 m (17.0~18.6m) on the north (south) side. The top of the piles is located about 6.6 m below the riverbed. Reinforced concrete pile caps are provided over the twenty-four pile group (Figure 5-8). The piles are embedded in slightly weathered mudstone at their bottoms. The concrete of the piles and their caps has a cylinder characteristic compressive strength of 24.2 MPa. The main reinforcement in the piles has a yield strength of 335 MPa. The rigid

cast-in-situ end beams at the arch crown of the side arches are supported by pot rubber bearings placed on the pile caps.

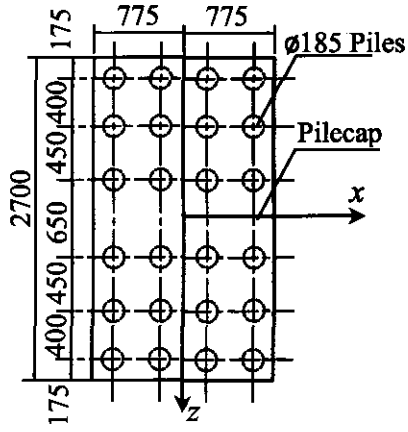

Figure 5-8 Layout of the Piles (Unit: cm)

5.3.2 Bridge Construction Process

The hollow steel tubular arches for the Dong-Guan Waterway Bridge are erected with the cableway system and fixed with tiebacks depicted in Figure 5-9.

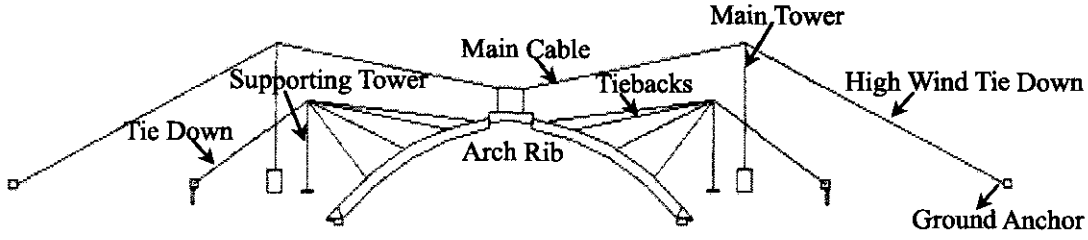

Figure 5-9 Assembling method for the hollow steel arch ribs

This kind of cantilever construction method is commonly used for the closure of hollow steel arch ribs. Sometimes the main tower may also be used as the supporting tower to reduce costs. The extensive analysis work carried out by Geng et al. (2010) has shown that the assembling process of the hollow steel arch ribs does not significantly affect the stress in the arch ribs at the completion of the construction. The hollow steel arches are modified to match the designed profile before the arch segments are welded together and the tiebacks are loosened. Because of this, the assembling process of the hollow steel arches is neglected in this analysis. The construction process considered in the following starts at the closure of the hollow steel tubular arches.

Like most of the half-through CFST tied arch bridges, the Dong-Guan Waterway bridge are constructed in the following steps: construction of the bridge foundation and pile caps, closure of the hollow steel tubular arch ribs, pouring core concrete inside the arch ribs segmentally, installing the suspenders, assembling the precast concrete transverse and longitudinal girders in the floor system, placing the precast concrete slabs, and, at last, laying the floor pavement. The transverse beams and slabs are all constructed symmetrically from the arch springings to the arch crown. The sequence of the core concrete pouring is presented in Figure 5-10.

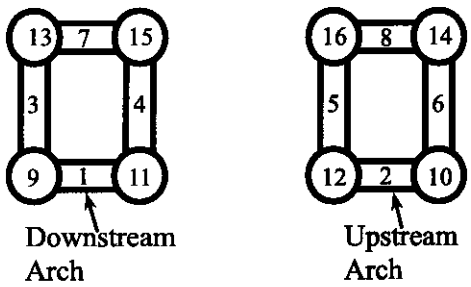

Figure 5-10 Number of the concrete components

Based on the instants in time at which site measurements were carried out, the time domain of the construction process is discretized into 27 steps (see Table 5-1, in which the number of the ties and concrete components are presented in Figure 5-7 and Figure 5-10, respectively). In Table 5-1 the time is measured from the closing of the arch ribs.

5.3.3 Site Monitoring

Extensive site monitoring has been carried out on the Dong-Guan Waterway Bridge. For the purpose of this study, only the measurements related to the displacements of the main arches, the stretching forces in the ties, and the stress levels in the steel tubes are included and considered in the following.

The displacement of the main arch is monitored using a TCA1800 Total Station. In order to provide an adequate representation of the displacement of the arches, one monitor point was selected for each steel arch segment, making a total of 11 monitor points on the arch rib as specified in Figure 5-11.

Table 5-1 Construction process for the Dong-Guan Waterway Bridge

Construction Steps	Construction Content	Time (days)
1	Closure of the hollow steel tubular arches, pour the center concrete core at the arch foot part.	0
2	Stretch the ties of No.1, pour concrete components of 1, 2	1
3	Stretch the ties of No.4, pour concrete components of 3~6	2
4	Pour concrete components of 7, 8	3
5	Stretch the ties of No.5	4
6	Stretch the tie of No.8 for the downstream arch, and pour concrete component of No.9	5
7	Stretch the tie of No.8 for the upstream arch, and pour concrete component of No.10	6
8	Stretch the tie of No.13 for the downstream arch, and pour concrete component of No.11	7
9	Stretch the tie of No.13 for the upstream arch, and pour concrete component of No.12	8
10	Stretch the tie of No.16 for the downstream arch, and pour concrete component of No.13	9
11	Stretch the tie of No.16 for the upstream arch, and pour concrete component of No.14	10
12	Stretch the tie of No.9 for the downstream arch, and pour concrete component of No.15	11
13	Stretch the tie of No.9 for the upstream arch, and pour concrete component of No.16	12
14	Place the four bracing beams on the side arches	15
15	Install suspenders and concrete transverse beams on the main arch (the two beams at the arch crown are not installed), and stretch the ties of No.12	25
16	Install the rest two concrete transverse beams on the main arch, and install the transverse beams on the columns of side arches	28
17	Place the slabs on the side arches, and stretch the ties of No.2	46
18	Place 33 sections of slabs on the main arches*, and stretch the ties of No.3	61
19	The slabs on the main arches are all placed in position except for the four sections adjacent to the steel transverse beams and the four sections at the arch crown, and stretch the ties of No.6	62
20	Finish the construction of precast concrete slabs except for the four sections adjacent to the steel transverse beams	65
21	Stretch the ties of No.7	67
22	Install the two steel transverse beams, and lay the rest concrete slabs	78
23	Pour concrete for the 10cm thick cast-in-situ concrete slabs, and stretch the ties of No.10	91
24	Lay the pavement of the deck floor	93
25	Stretch the ties of No.11	95
26	Stretch the ties of No.14	101
27	Stretch the ties of No.15	103

NOTE: * One section of slabs is the slabs between two transverse beams.

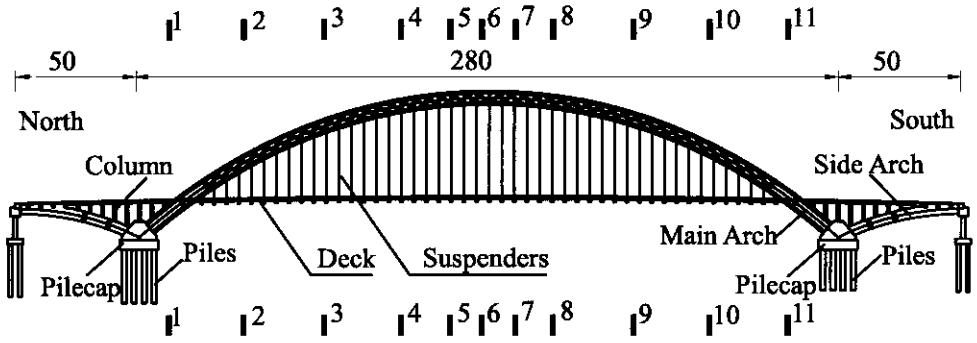

Figure 5-11 Locations for the displacement monitor points (Unit: m)

The stress in the steel tubes is measured with vibrating-wire strain gages produced by CEKON. These were placed around the cross-section (Figure 5-12) at the arch crown, at the quarter points along the bridge length, and at the arch springings.

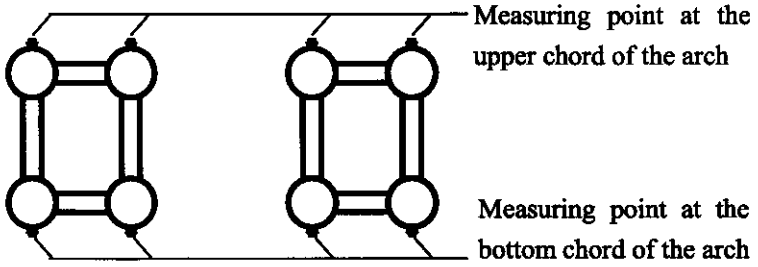

Figure 5-12 Layout of the strain gauges on the steel tubes at each cross-section

The stretching forces of the ties are measured with feed-through sensors produced by the CEKON. In particular, ties No. 2, No. 7, No. 12, and No. 13 (Figure 5-7) are measured during the construction (i.e. one tie for each layer). The total stretching forces are specified in Table 5-2. Considering that the ties in the same layer have a very close loss of prestress, the other three ties are assumed to have the same value with the measured one in the analysis. The measured values are only available from the 21th construction step when all four monitored ties are stretched. Due to this lack of data, the total stretching forces of the ties used in the analysis for the initial twenty steps are determined by making the arch springings return to their designed position.

Table 5-2 Stretching forces in the ties during construction (kN)

Construction Steps	Measured Inner Forces				Stretching Forces Used in Analysis
	N2	N7	N12	N13	
1	0	0	0	0	0
2	0	0	0	0	3806
3	0	0	0	0	7612
4	0	0	0	0	7612
5	0	0	0	0	11438
6	0	0	0	0	15263
7	0	0	0	0	15263
8	0	0	0	3374	18852
9	0	0	0	3403	18882
10	0	0	0	3372	22438
11	0	0	0	3344	22376
12	0	0	3625	3398	26232
13	0	0	3454	3388	26232
14	0	0	3454	3396	26232
15	0	0	3445	3384	23091
16	0	0	3479	3415	23091
17	3578	0	3457	3394	26478
18	3438	0	3448	3390	29652
19	3450	0	3434	3379	32944
20	3465	0	3410	3364	32944
21	3430	3597	3625	3374	36727 (measured)
22	3414	3531	3454	3403	36242 (measured)
23	3386	3512	3454	3372	39867 (measured)
24	3393	3486	3445	3344	39699 (measured)
25	3578	3456	3479	3398	43148 (measured)
26	3438	3597	3457	3388	46051 (measured)
27	3450	3531	3448	3396	49193 (measured)

5.4 FINITE ELEMENT MODELING

5.4.1 Material Properties

The core concrete inside the arch ribs is modelled accounting for creep and shrinkage effects using the step-by-step method. Except for the core concrete, the materials are considered in the elastic range when the bridge is under service loading. The elastic modulus, density and Poisson's ratio for the steel take the

values of 2.06×10^5MPa, 7800kg/m^3, and 0.283, respectively, while those for the concrete are 3.4×10^5MPa, 2600 kg/m^3, and 0.167, respectively. To simplify the analysis, the reinforced concrete members are modeled as equivalent beam or shell members.

5.4.2 Main Arch Ribs

The following assumptions are adopted in the simulation of the main arch ribs:

1) Plane sections remain plane (i.e., linear strain distribution); and

2) there is perfect bond between the steel tube and the core concrete.

All members of the main arch ribs are simulated by Timoshenko beam elements B31 except for the diagonal and vertical hollow steel tubular webs which are modelled by means of truss elements T3D2.

For the truss part of the arch, the dumbbell-shaped top/bottom chord is divided into four components (Figure 5-13): the dumbbell-shaped hollow steel tube, the two concrete cores inside the circular steel tubes and the concrete web. For the box-shaped part, the whole cross-section is divided into nine components: the box-shaped hollow steel tube, the four concrete cores inside the circular steel tubes, and the four concrete webs. For the solid part of the arch, one central concrete component is added to the box-shaped cross section. The various components of the cross-sections have been connected by means of rigid bars to ensure plane sections to remain plane before and after the analysis.

The stiffness properties of the steel components with generic shaped cross-sections (shapes other than rectangular and circular ones) are calculated and the obtained stiffness of the section (EA), bending stiffness (EI) and torsional rigidity (GJ), etc. are used to define these cross-sections (SIMULIA 2007 a).

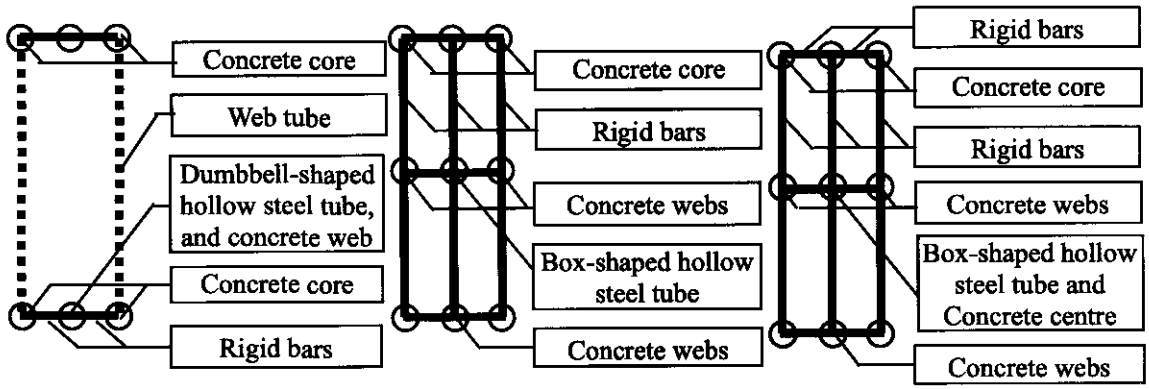

(a) Truss cross section

(b) Box-shaped cross section (2-2 in Figure 5-4)

c) Solid cross section (3-3 and 4-4 in Figure 5-4)

Figure 5-13 Finite element components of the main arch

5.4.3 Bridge Decks and Their Supporters

The transverse and longitudinal beams in the floor system are simulated with Timoshenko beam elements B31, and the deck slabs are with 4-node shell elements S4. The technique of 'Generalized Cross-Sections' is adopted for the simulation of the π-shaped cross-section. The self-weight of non-structural elements, such as the 5 cm thick SMA pavement, the light fixture, and the guardrails, etc, are included in the analysis increasing the density of the cast-in-situ slabs. The reinforced concrete slabs are simplified into one material defined by equivalent rigidities and self-weight, for which the concrete elastic modulus and Poisson's ratio are adopted.

The sixteen ties for each arch are simplified into one tie bar with equivalent rigidity, and are simulated with the truss element T3D2 specifying that the element can carry only tension forces. The designed value for the prestressing forces in the tie is 3800 kN. At each construction step, the stretching force in the equivalent tie is the sum of the forces in sixteen ties as listed in Table 5-2. Changes in the axial forces induced in the tie are implemented in the FE model varying the air temperature at each construction step, adopting a thermal expansion coefficient of 1.17×10^{-5} 1/°C for the ties.

The suspenders are simulated using truss elements T3D2 enabling the member to resist only tensile forces. The columns supporting the transverse beams at the side arch are built with Timoshenko beam elements B31.

5.4.4 Pile Foundation and Boundary Conditions

The rigid cast-in-situ beams are fixed in the y direction at the crown of the side arches and the piles under them are neglected. The piles under the arch abutment are simulated with Timoshenko beam elements B31 based on the assumption that plane sections of the 24 piles remain plane before and after deformations. The reinforced concrete piles are simplified into one material with equivalent rigidities and self-weight, for which the concrete elastic modulus and Poisson's ratio are adopted. A length of 22.9 m is specified for the piles on the north side and 18.6 m for those on the south side. The piles are fixed at their bottom ends as they are embedded in a slightly weathered mudstone. During the construction, the soil restrains the lateral deformation of the piles. Such interaction is implemented using the spring element SPRING1, whose positions and stiffness are determined according to the Chinese Code 'Code for design of ground base and foundation of highway bridges and culverts' (JTG D63 2007).

The properties of the soil present around the piles are listed in Table 5-3, in which the coefficient m relates to the spring stiffness. In the simulation, the soil is divided into several layers, with depth of about 1 m per layer.

Table 5-3 Properties of the soil

Soil profile	Soil type	Coefficient m (kN/m^4)	Thickness on the north side (m)	Thickness on the south side (m)
1st	Silt	3000	2.92	5.86
2nd	Silty fine sand	6000	6.1	4.5
3rd	Medium-coarse sand	20000	2.8	2.7
4th	Highly weathered mudstone	25000	1.2	—
5th	Moderately weathered mudstone	30000	6.3	1.0
6th	Slightly weathered mudstone	—	3.58	4.54

In each layer, two springs are set for one pile, one in the x and one in the z direction. The positions of the springs in the y direction are determined based on the following equation.

$$y_i = \frac{b+2a}{3(a+b)} g h_i + h_0 \tag{5-17}$$

where y_i represents the distance from the surface of the riverbed to the spring in the i^{th} soil layer (expressed in m); b is the distance from the top of the pile to the bottom of the soil layer (m); a denotes the distance from the top of the pile to the top of the soil layer (m); g depicts the acceleration of gravity (N/kg); and h_i=a-b depicts the thickness of the i^{th} soil layer (m); h_0 defines the distance from the riverbed to the top of the piles (m).

The stiffness of the spring is determined as follows:

$$k = h_i C_y b_0 \tag{5-18}$$

$$C_y = m y_i \tag{5-19}$$

$$b_0 = \begin{cases} K_r K_0 (d+1) \le 2d & \text{for } d \ge 1.0 \\ K_r K_0 (1.5d+0.5) \le 2d & \text{for } d < 1.0 \end{cases} \tag{5-20}$$

$$K_0 = \begin{cases} 1.0 & \text{for } L_1 \ge 0.6h_1 \\ b_2 + \frac{1-b_2}{0.6} \cdot \frac{L_1}{h_1} & \text{for } L_1 < 0.6h_1 \end{cases} \tag{5-21}$$

$$h_1 = 3(d+1) \le h_0 \tag{5-22}$$

$$b_2 = \begin{cases} 1.0 & \text{for } n=1 \\ 0.6 & \text{for } n=2 \\ 0.5 & \text{for } n=3 \\ 0.45 & \text{for } n \ge 4 \end{cases} \tag{5-23}$$

where k denotes the stiffness of the spring in the i^{th} soil layer (kPa); h_i represents the thickness of the i^{th} soil layer (m); m is a constant coefficient depending on the soil type, the value of which is listed in the Table 5-3; y_i depicts the distance from the

surface of the river bed to the position of the spring (m); K_f defines the coefficient depending on the shape of the cross-section of the piles, 0.9 for the circular pile; d is the diameter of the pile (m); L_1 represents the clear space between two adjacent piles in a row parallel to the direction of the horizontal loading (m); n denotes the number of piles in the row parallel to the direction of the horizontal loading; and h_0 is the distance from the riverbed to the top of the pile (m).

The simulation of the piles and the restraint effect of the soil to the piles well represent the real situation. The predicted horizontal displacement of the arch springings is -2~4 mm during the construction which matches well with the site monitored results of -2~5 mm for the arch springings on the upstream side and -2~3 mm for those on the downstream side.

5.4.5 Construction Process

The 'Model Change' technique (SIMULIA 2007 b) is adopted to simulate the variation of the stiffness and the self-weight for both arch ribs and the bridge deck during the construction. At the start of the analysis, all the parts of the bridge are first 'removed (or deactivated)' except for the foundation of the bridge. The structural parts are gradually 'added (or reactivated)' following the construction steps presented in Table 5-1. After the parts are 'removed (or deactivated)', these are not included in the analysis (i.e. their stiffness and self-weight are ignored) till they are 'added (or activated)' at a certain step.

The whole finite element model for the Dong-Guan Waterway Bridge is presented in Figure 5-14.

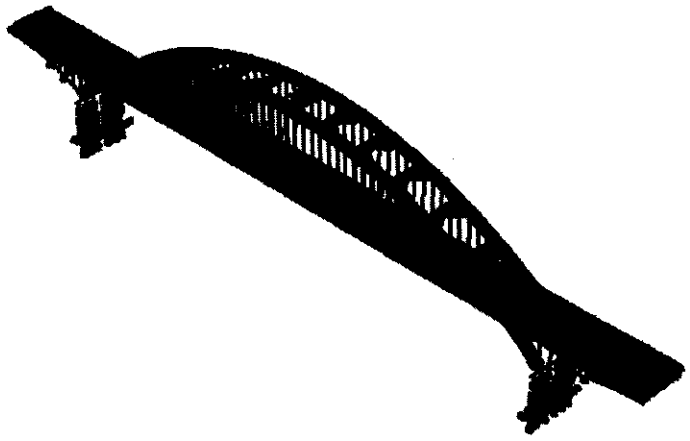

Figure 5-14 Finite element model for the whole bridge

5.5 VALIDATION OF THE NUMERICAL MODEL

To verify the reliability of the proposed finite element model, the monitored displacements and stresses of the arch ribs during the construction are adopted as benchmark data. Both analysis with and without the consideration of the geometric nonlinearity is considered to investigate its influence on the static response of the CFST arch bridges under service loading.

Figure 5-15~Figure 5-18 present the typical comparisons for the displacements of the arch ribs and stresses in the steel tubes during the construction. In these figures, scattered solid points represent the measured results, solid lines depict the calculated results accounting for geometric nonlinearity, dashed lines denote the numerical results without geometric effects, and dash-dot lines describe the results obtained without considering time effects. In the adopted sign convention positive (negative) stresses are tensile (compressive), while positive (negative) displacements depict upward (downward) movements.

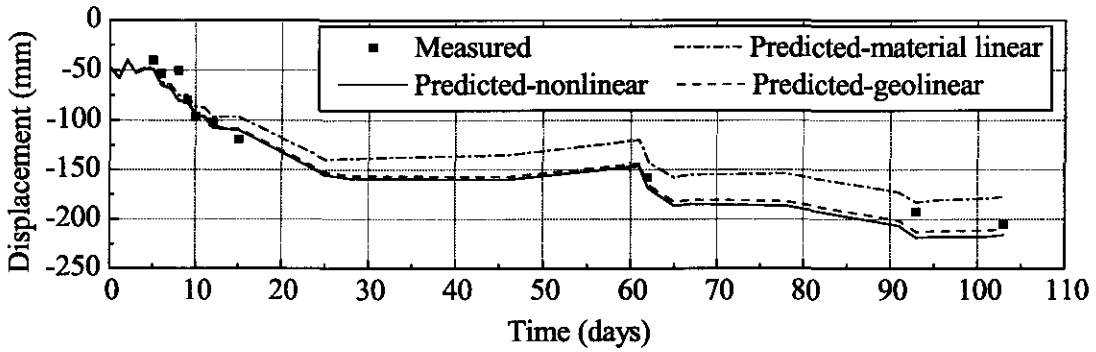

(a) Displacement at arch crown

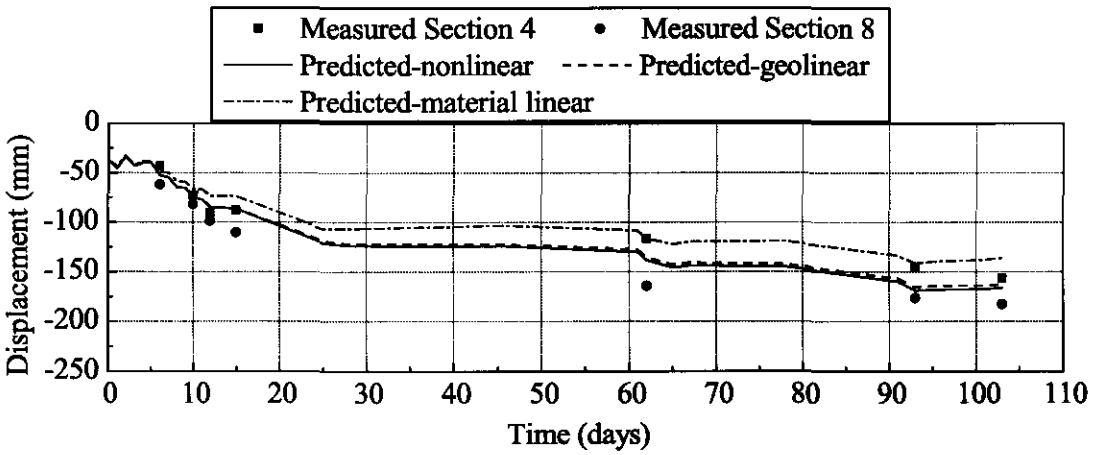

(b) Displacement at sections of 4 and 8 (see Figure 5-11)

Figure 5-15 Comparison on displacements of arches during the construction

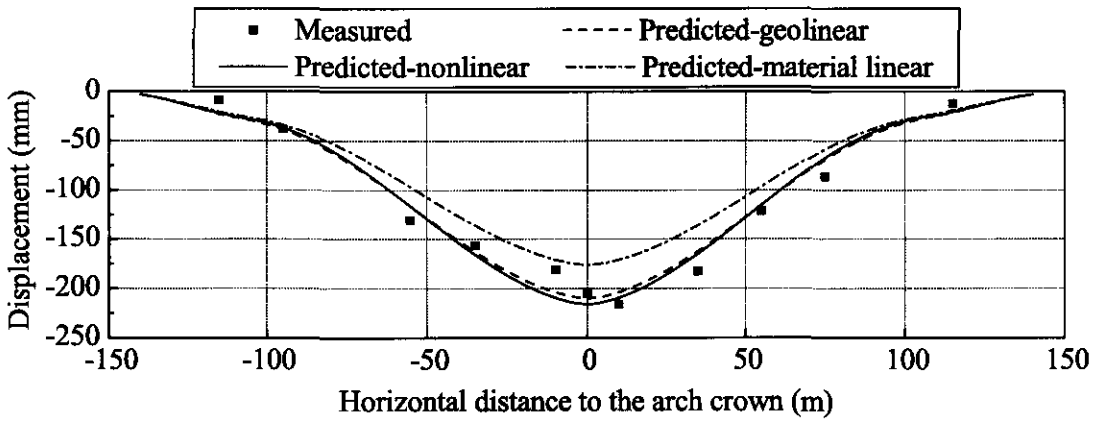

Figure 5-16 Comparison of displacement of arches at the end of the construction

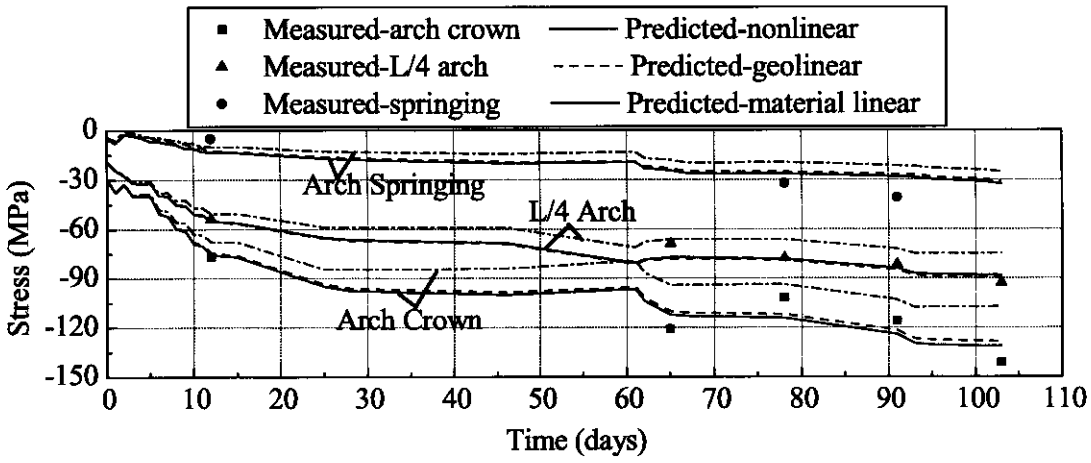

(a) Stress at the upper chord of the arch ribs

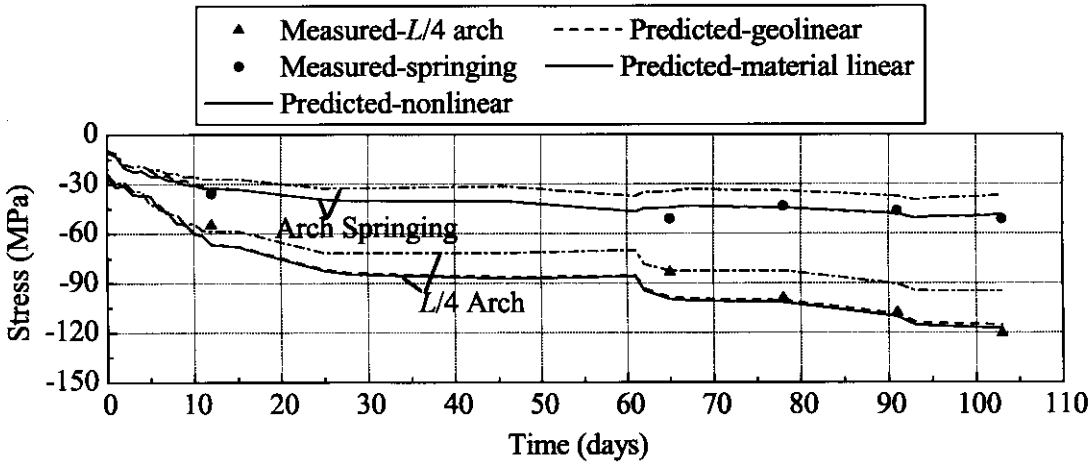

(b) Stress at the bottom chord of the arch ribs

Figure 5-17 Comparison on stresses of arches during the construction

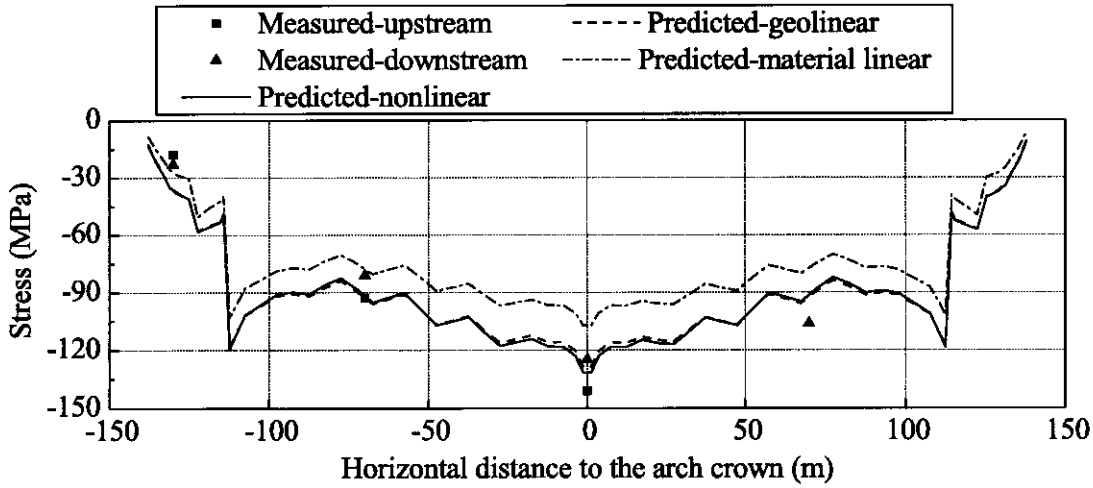

(a) Stress at the upper chord of the arch ribs

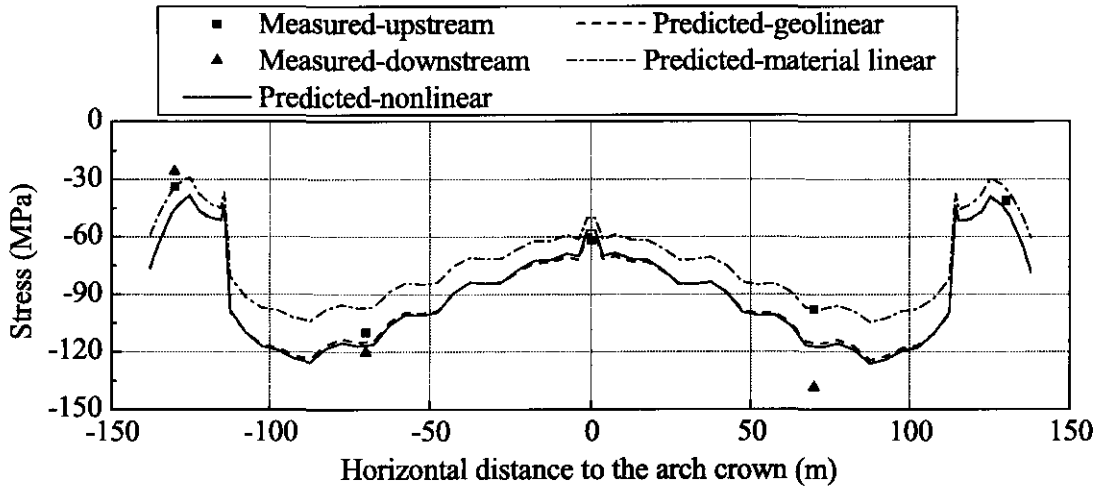

(b) Stress at the bottom chord of the arch ribs

Figure 5-18 Comparison on stresses of arches at the end of the construction

In particular, Figure 5-15 describes how the displacements at specific points of the arch ribs developed during the construction process. In Figure 5-15, the locations of sections 4 and 8 are illustrated in Figure 5-2. Due to the symmetry of the structure, only the analysis curves for section 4 are presented. Figure 5-16 is plotted to describe the total deflection of the arch ribs at the end of the construction. The stresses in the upper and bottom chords of the steel arches during the construction are illustrated in Figure 5-17, with the stress at the arch crown, at the quarter points and at the arch springing shown in the same graph. The vibrating-wire strain gages at the arch crown of the bottom chords broke during the concrete pumping process, so the measured stresses at the arch crown are missing in Figure 5-17 (b). During the whole construction process, the stress in the steel tubular arches at the arch springing is relatively low compared to those at the arch crown or quarter points because the arch has a much larger cross-section at the arch springing than at the arch crown or at quarter points (see Figure 5-4). Figure 5-18 shows the distribution of stresses in the steel tube along the upper and bottom chords at the end of the construction.

All numerical results are determined at the same location of the arch where the measurements were taken. The reference arch profile for the displacement measurements (i.e. the arch profile for which the displacements are considered to be

zero) is the one exhibited before the tiebacks were loosened. The measurement of the stress in steel tubes also starts before loosening the tiebacks.

Observing Figure 5-15~Figure 5-18, it can be noted that the geometric nonlinearity has a quite limited influence on the static response of the CFST arch bridges at service conditions. With the consideration of geometric nonlinearity, the predicted displacements at the arch crown and at sections 4 and 8 are only 2.8% and 2.2% higher, respectively, than those obtained without the consideration of the geometric nonlinearity. The maximum differences between the predicted stresses with and without the consideration of geometric nonlinearity are only 2.2%, 1.4%, and 4.1% for upper chords at arch crown, quarter points and arch springing, respectively, and 3.7%, 1.6%, and 0.6% for the bottom chords at the corresponding locations. Thus, in the simplified method provided for the designing purpose, the geometric nonlinearity is neglected.

From Figure 5-15~Figure 5-18 it can also be observed that the predicted results match well with the monitored results with the maximum deviation of 10.6% and 8.8% for the displacements and stresses, respectively. The proposed finite element model can capture the development of the stress and displacement of the arches during the construction, and provides good predictions of their distribution along the arch length. The deviation between the predicted results and measured ones is acceptable considering the fact that the influence of the temperature variation and the temporary constructional live loading on the static response of the bridge cannot be considered in the prediction due to the lack of detailed loading information. It is worth pointing out that the site readings may be affected by noise in the recorded signals as well.

During the construction of CFST arch bridges, the time-dependent behaviour of the core concrete significantly influences the static response of the structure. Before the transverse beams are hoisted, the time-dependent behaviour of the core concrete can cause an increase in arch displacements of the order of 17% of the instantaneous value at the corresponding construction step (Figure 5-15). Such time effects need to be considered in the monitor programme to determine the jacking forces of the suspenders and the elevation of the transverse beams to ensure the flatness and the

serviceability of the bridge deck. At the end of the construction, the displacement at the arch crown is increased by 21.9% of the instantaneous value due to time effects (Figure 5-16). The maximum stress increase in the steel tube occurs at the location with the highest value of initial compressive stress (Figure 5-18). For the upper chord this occurs at the arch crown and for the bottom chord at the location connecting the first wind brace above the deck (about 100 m from the arch crown, see Figure 5-3). The maximum increase of the stress in the steel tubes of the upper and bottom chords is 22.6% and 19.0% of the instantaneous values, respectively.

5.6 DISCUSSIONS

5.6.1 Time Effect on the Static Response of CFST Arch Bridges under Service Conditions

With the consideration of the construction process and the ageing of the concrete, the analysis is performed to investigate how time effects influences the static response of CFST arch bridges at service conditions for their entire service life (100 years). This is carried out using the Dong-Guan Waterway Bridge as a study case. In the analysis, the bridge is subjected to the long-term load combination specified by Eqn (5-24) (JTG D62-2004), with the live loading applied as the quasi-permanent distributed loads on the whole bridge deck.

$$S_{ld} = S_{Gk} + \sum_{j=1}^{n} \phi_{2j} S_{Qjk} \tag{5-24}$$

where S_{ld} represents the long-term load combination; S_{Gk} denotes the characteristic dead loads; $\phi_{2j}S_{Qjk}$ depicts the quasi-permanent value for the jth live load; ϕ_{2j} is the quasi-permanent coefficient for the jth live load, 0.4 for the road traffic load, 0.4 for the pedestrian path load, and 0.75 for the wind load; S_{Qjk} defines the jth characteristic live load.

It is worth to notice that the Chinese Code (JTG D62-2004) requires to take the live loading into account in the long-term effect analysis to consider the fact that there is always heavy traffic in China and quite a number of bridges are working at

overloaded conditions. Since most of the CFST arch bridges are built in China, the Chinese Code is adopted in the analysis.

Figure 5-19 and Figure 5-20 depict the time-dependent changes produced on the displacement and the stress distributions of the main arch rib after 100 years at service conditions. It is apparent that time effects in the core concrete significantly change the initial stress and strain states in the cross-sections, increase the displacement of the arch, enhance the stress in the steel tube, and relax the stress in the core concrete. The long-term displacement at the arch crown is 46.1% of the instantaneous one, indicating the importance of considering time effects when specifying the camber of the arch ribs. The most dramatic stress redistribution occurs at the place of maximum initial stress (about 100 m from the arch crown where the first wind brace above the deck intersecting with the arch ribs, see Figure 5-3), with a maximum of 51.2% increase in the steel tube and 61.9% decrease in the core concrete when compared to the instantaneous values. The stresses in the steel tubes and core concrete along the whole arch are lower than one half of the material compressive or cracking strength, indicating that the assumptions adopted in this Chapter (section 5.2) are reasonable.

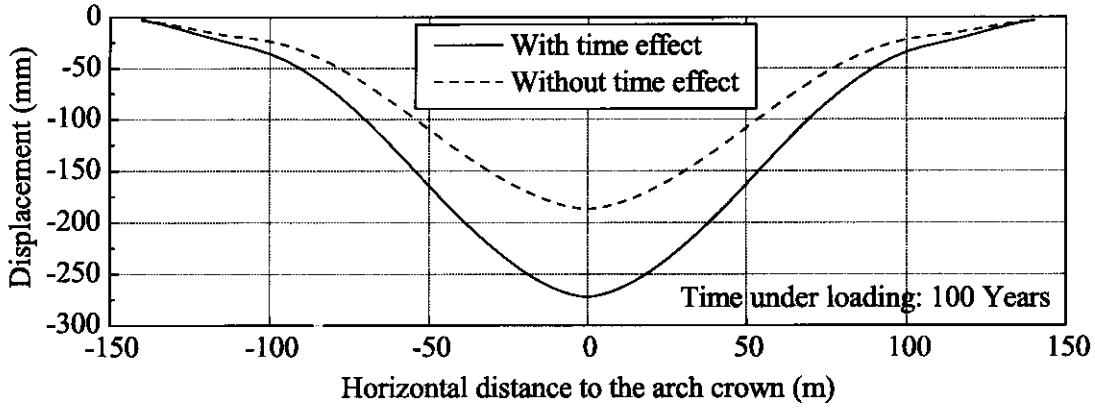

Figure 5-19 Time effects on the displacement of CFST arches under service loading

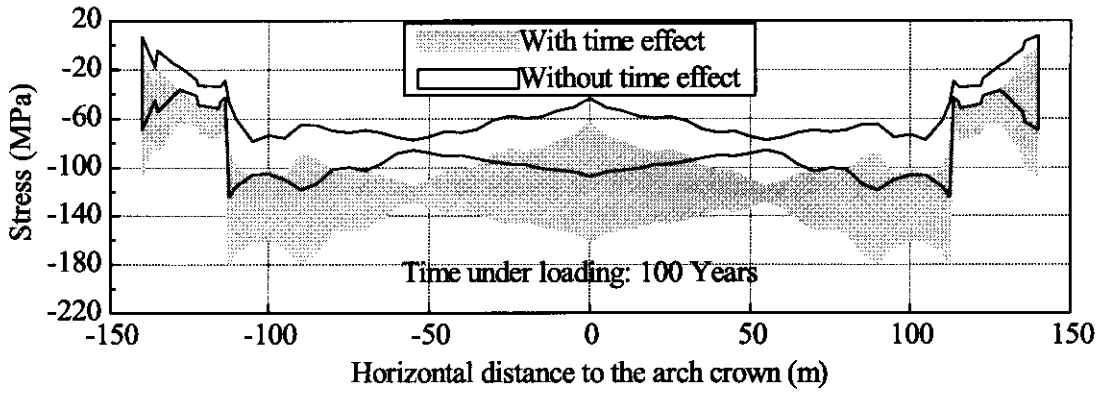

(a) Comparison on the stress envelop in steel tubes of the arch ribs

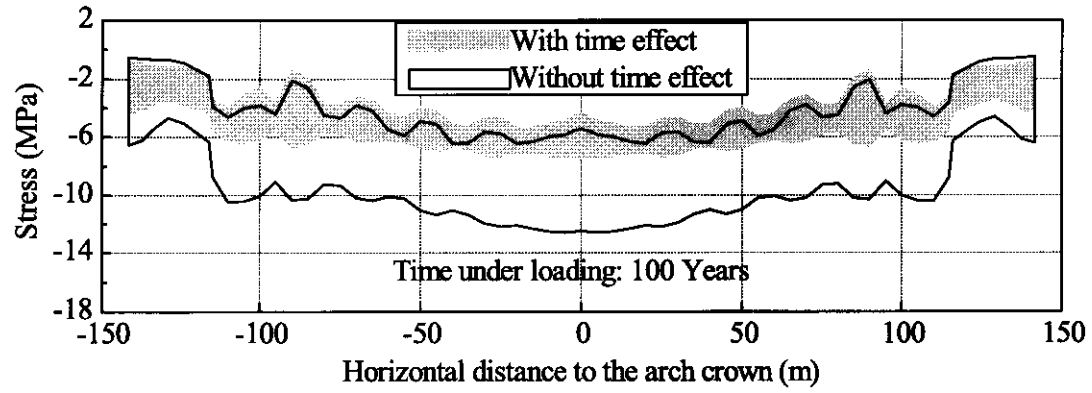

(b) Comparison on the stress envelop of core concrete inside the upper chord

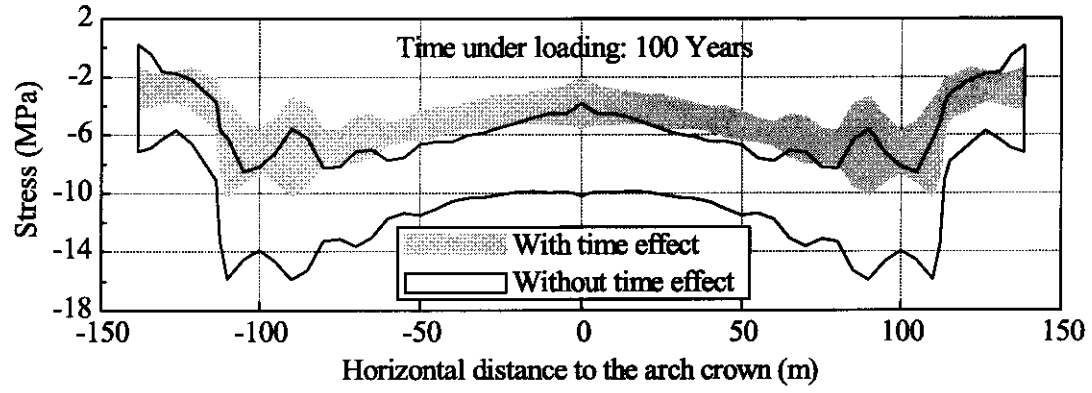

(c) Comparison on the stress envelop of core concrete inside the bottom chord

Figure 5-20 Time effects on the stress of CFST arch ribs under service loading

Figure 5-21 compares the predicted inner forces in the main arch ribs subjected to service loading for 100 year calculated with and without time effects. In Figure 5-21 (b), positive moments cause the arch to sag. It can be noted that the time effects of the core concrete have limited influence on the axial forces along the arch, with

0.7% difference in maximum, but have considerable influences on the bending moment in the arch rib, reducing the negative values by 8.3% of the initial ones and increasing the positive values by a maximum of 64.7% of the initial ones, causing the bending moment diagram to shift upwards in Figure 5-21 (b).

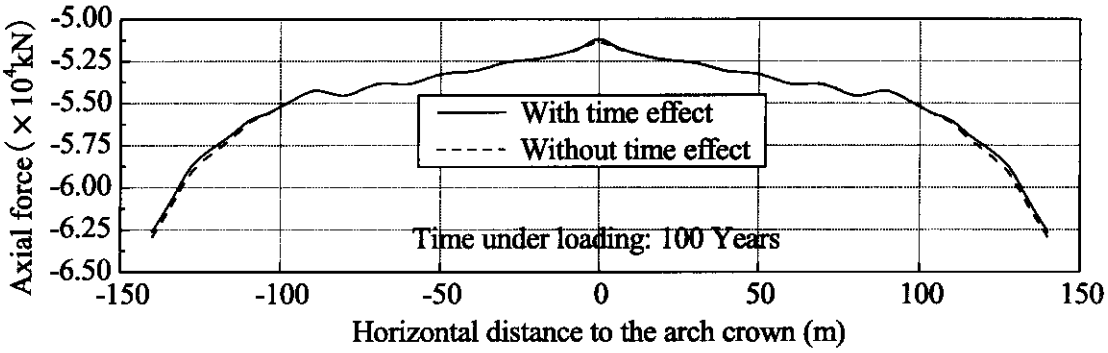

(a) Comparison on the axial forces along the arch ribs

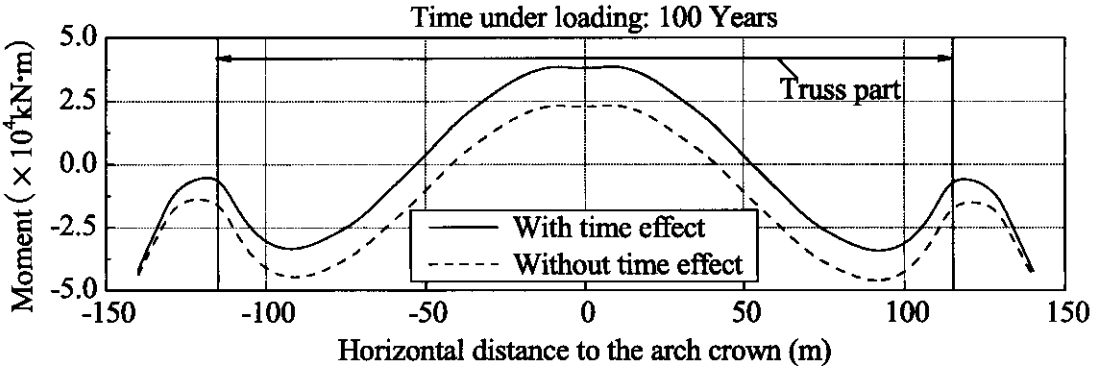

(b) Comparison on the bending moments along the arch ribs

Figure 5-21 Time effects on the inner forces of CFST arch ribs under service loading

The significant differences between the bending moment distributions calculated with and without the consideration of time effects are mainly induced for two reasons. The first one is caused by the time-dependent deflection developed along the arch profile which increases the amplitude of the bending moment. Figure 5-22 presents the bending moment distribution diagrams obtained with all the loads applied at 28 days after concrete casting to indicate how the increase in deflection influences the bending moment distribution along the arch. The second one relates to the shift in the stiffness centre of the section. During construction, the bottom

chords are pumped first and the stiffness centre of the cross-section is located below the geometric centre (Figure 5-23), producing a negative additional bending moment ($N \cdot e$) almost constant along the arch. The time-dependent behaviour of the concrete reduces the distance between the stiffness and the geometric centres, and hence reduces the additional negative bending moment (i.e. causing the bending moment diagram to shift upwards and horizontally). Comparing Figure 5-22 and Figure 5-21 (b), it can be noted that the second reason is more important than the first one. In Figure 5-22 the maximum difference between the bending moments obtained with and without consideration for time effects is 11%, which is much smaller than the differences presented in Figure 5-21.

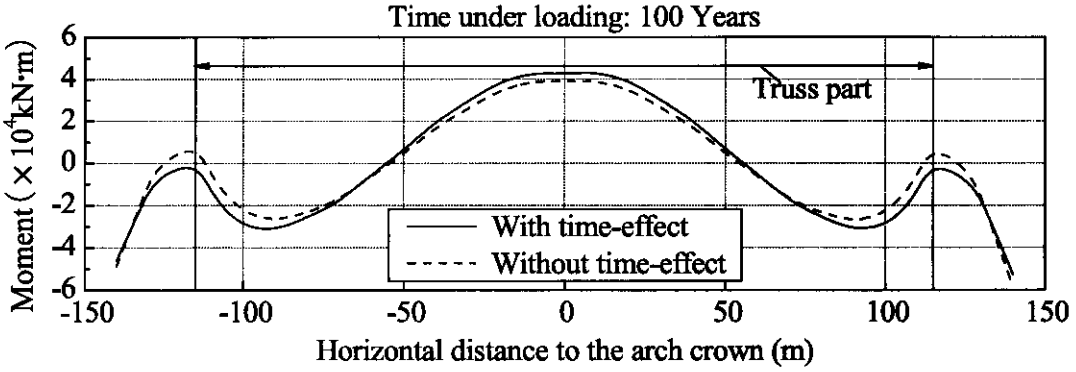

Figure 5-22 Bending moment curves of CFST arches obtained without the consideration of construction process

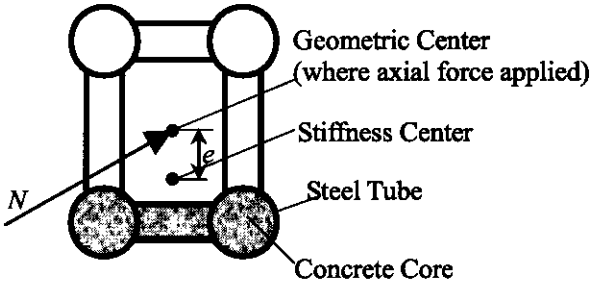

Figure 5-23 Location of the stiffness centre of the arch rib during construction

The comparison of Figure 5-22 and Figure 5-21 (b) also highlights that the construction process needs to be considered in the time-dependent analysis on trussed CFST arch bridges, otherwise incorrect conclusions may be drawn.

5.6.2 Necessity of Considering the Variation of Loading Ages during Construction

Though it is commonly accepted that the segmental construction process needs to be considered when predicting the static response of bridges (Marí and Valdés 2000, Chiorino 2005, Somja and Goyet 2008), many researchers conducted the long-term analysis of CFST arch bridges considering the time-dependent construction process based on the assumption that the age of the concrete at loading (t_0) is always 28days (Wu & Qu 1991, Xie & Qin 2001, Gu et al 2001, Cheng 2004, Yao 2006, Tian et al 2007, Wang et al 2007, and Shao et al 2010). This means that the aging of the concrete material is neglected, which is not acceptable as some loads are applied at very early concrete ages especially during the core concrete pouring procedure.

To prove the necessity of considering the ageing of the core concrete, the predicted displacement and stress envelops obtained with the consideration of the varying loading ages of the core concrete are compared with those obtained by assuming t_0=28days for the main arch of the Dong-Guan Waterway Bridge under service loading for 100 years considering the whole construction process (Figure 5-24 and Figure 5-25). The differences between the predicted results at different locations along the bridge are listed in Table 5-4, in which the t_{0a} represents the predicted results with consideration of the concrete ageing, t_{028} depicts those obtained by setting t_0=28days, and the difference is presented in percentage with the positive value representing that the results obtained with t_{0a} is higher than those obtained with t_{028}. It can be noted that the long-term response of the arch increases when accounting for the actual times of loading. Comparing the results calculated at t_0=28 days to those obtained based on the actual time of loading ages, the latter can be 20.2% higher for the displacement at the arch crown, 48.9% higher for the stress in the steel tube, and 39.8% lower for the stress in the core concrete. The maximum difference for the stresses in the steel tube and core concrete appear around the arch rib intersecting with the first wind brace above the deck (about 100m from the arch crown, see Figure 5-3).

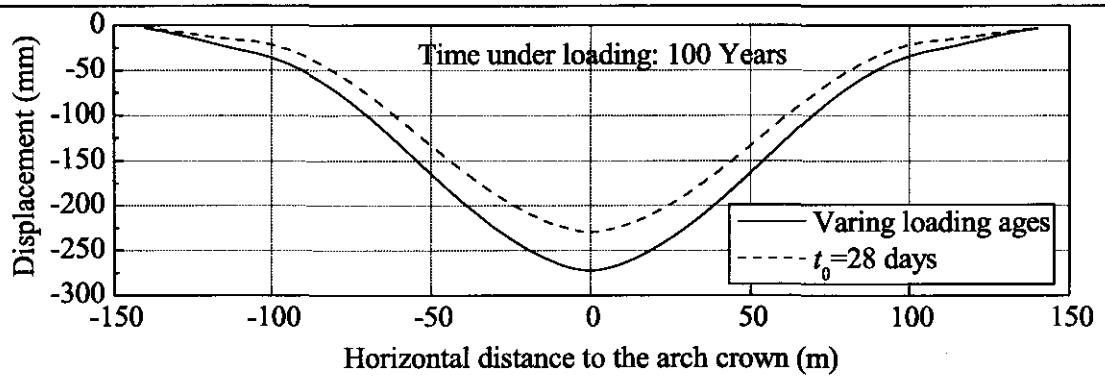

Figure 5-24 Comparison of the predicted displacement of CFST arch ribs with and without the consideration of the varying loading ages

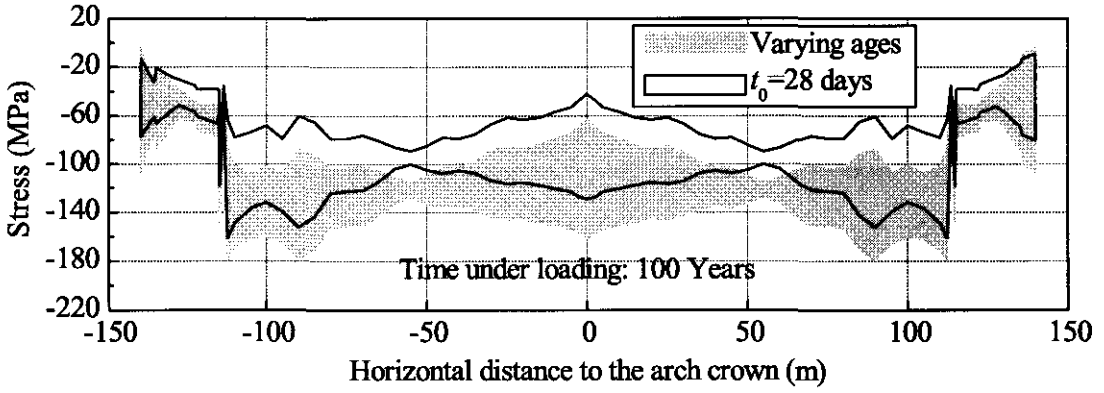

(a) Comparison on the stress envelop in steel tubes of the arch ribs

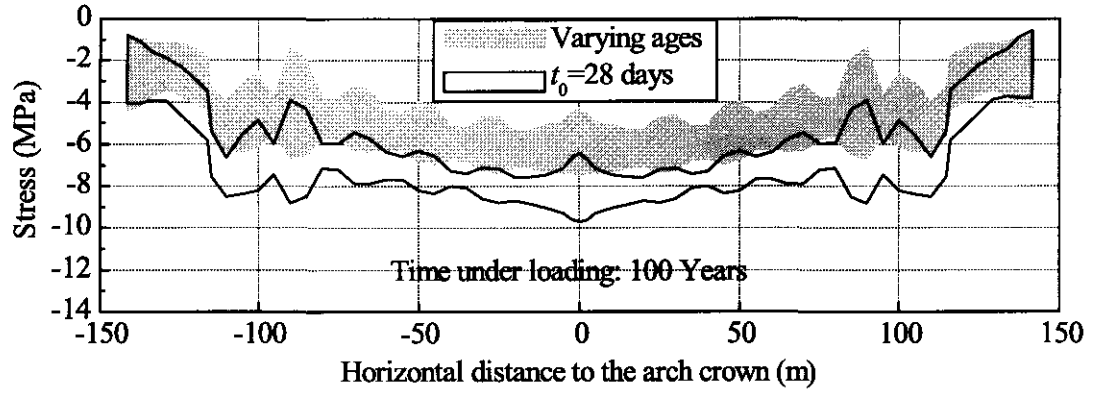

(b) Comparison on the stress envelop of core concrete inside the upper chord

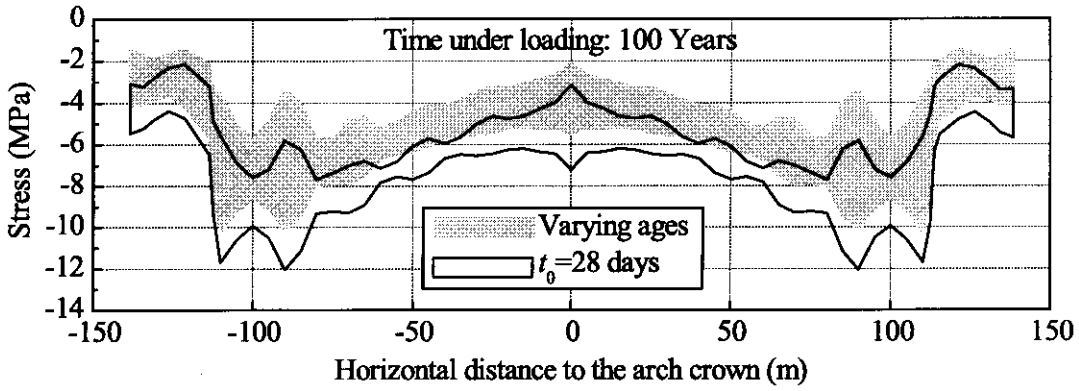

(c) Comparison on the stress envelop of core concrete inside the bottom chord

Figure 5-25 Comparison of the predicted stress in CFST arch ribs with and without the consideration of the varying loading ages

Table 5-4 Difference between stress envelop predicted with and without the consideration of concrete ageing (MPa)

Location		Steel tube		Core concrete			
				Upper chord		Bottom chord	
		Max	Min	Max	Min	Max	Min
Arch springing	t_{0a}	-3.7	-106.9	-0.8	-4.3	-1.4	-4.2
	t_{028}	-9.3	-80.9	-0.6	-3.8	-3.3	-5.7
	difference	-59.9%	32.1%	47.5%	14.6%	-56.7%	-26.2%
L/8	t_{0a}	-107.6	-161.4	-3.1	-6.3	-5.1	-9.2
	t_{028}	-73.9	-136.5	-5.5	-8.4	-6.9	-10.6
	difference	45.7%	18.3%	-44.3%	-24.2%	-26.5%	-13.0%
L/4	t_{0a}	-101.9	-151.1	-3.2	-6.2	-4.8	-7.9
	t_{028}	-76.7	-121.7	-5.4	-7.9	-7.0	-9.3
	difference	32.9%	24.2%	-41.7%	-20.7%	-31.6%	-14.6%
3*L*/8	t_{0a}	-99.2	-136.9	-5.2	-7.4	-3.8	-5.5
	t_{028}	-75.2	-107.8	-6.8	-8.1	-5.7	-6.5
	difference	31.8%	27.1%	-30.0%	-16.5%	-32.1%	-14.6%
Arch crown	t_{0a}	-63.3	-161.1	-4.4	-7.5	-2.1	-5.5
	t_{028}	-42.5	-128.9	-6.4	-9.7	-3.2	-7.2
	difference	49.0%	25.0%	-31.8%	-23.2%	-33.5%	-23.5%

5.6.3 Contribution of the live loading to the long-term response of the CFST arch bridges

Though the live loading is required to be applied on the bridge in the form of quasi-permanent combination during the long-term analysis by the Chinese Code (JTG D62-2004), many researchers investigated the long-term response of CFST arch bridges under service loading without the consideration of the live loading arguing that the live loads are small compared to the dead ones and are applied at a very old concrete age (Zhang et al 2001, Yu et al 2003, Cheng 2004, Xiong & Liu 2005, Tian et al 2007, Zhang 2007).

To clarify the contribution of the live loading to the long-term response of the CFST arch bridges, analyses are performed to compare the increase in the displacement (ΔD) and the stress redistribution in steel tubes and core concrete ($\Delta\sigma$) caused by the time-dependent behaviour of the core concrete after the completion of the bridge construction. In this case, the bridge is subjected to its self-weight (curves called 'without live loading') and to the live load combination as defined in Eqn (5-24) (curves called 'with live loading') (Figure 5-26 and Figure 5-27).

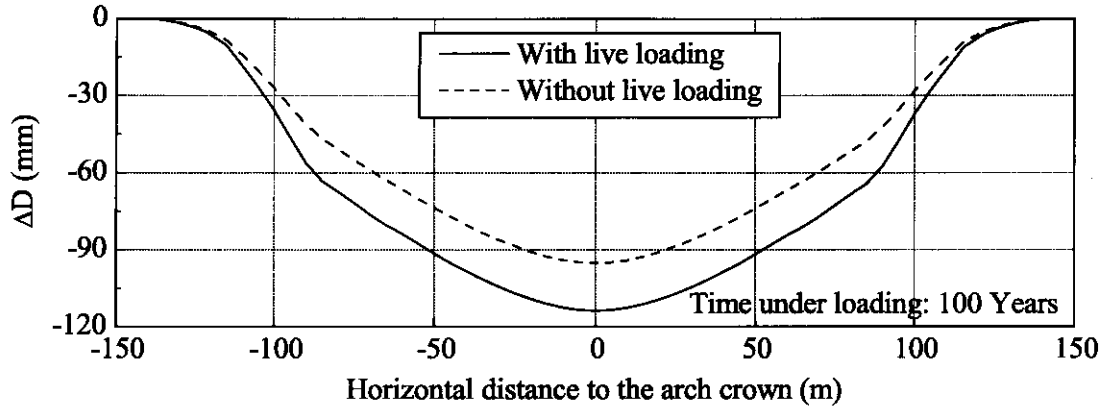

Figure 5-26 Contribution of live loading to the incremental displacement of CFST arch ribs caused by time-dependent behaviour after construction

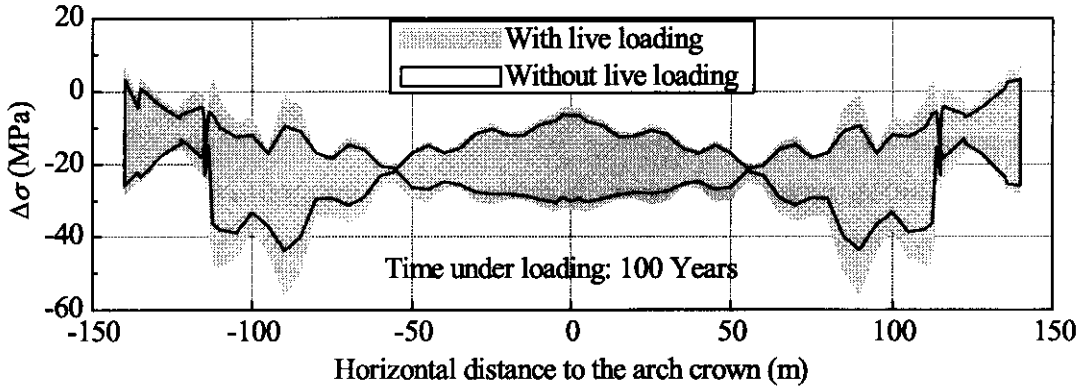

(a) Comparison on the stress envelop in steel tubes of the arch ribs

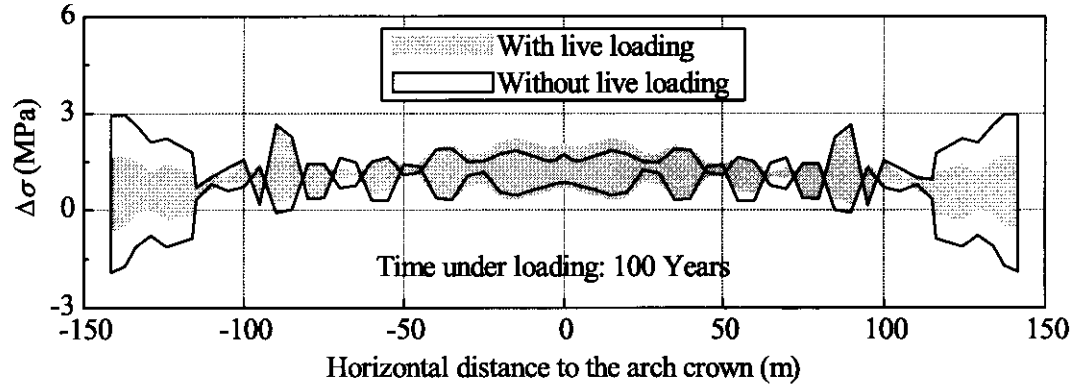

(b) Comparison on the stress envelop of core concrete inside the upper chord

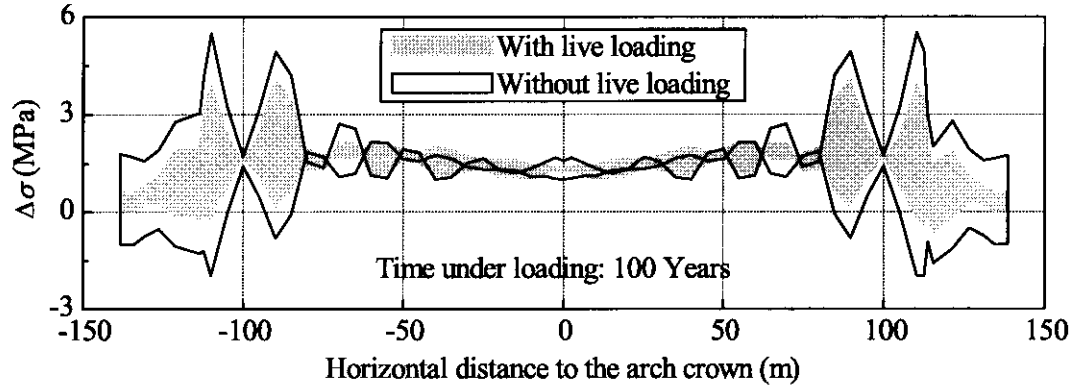

(c) Comparison on the stress envelop of core concrete inside the bottom chord

Figure 5-27 Contribution of live loading to the incremental stress of CFST arches caused by time-dependent behaviour after construction

It is obvious that the increase of the displacement and the transformation of the stress between the steel tube and the core concrete predicted with the consideration of the live loading is considerably more critical than those obtained with only self-weight applied. The incremental time-dependent displacement (ΔD) caused by quasi-permanent live loading takes 16.4% of the total displacement increment at the arch crown, and 22.7% at $L/4$ along the arch. The live loading significantly affects the stress distribution in the arch rib occurs, with a maximum increase of 24.7% for the steel tube and maximum reduction of 41.3% in the core concrete taking place near the intersection of the first wind brace above the deck (about 100m from the arch crown, see Figure 5-3),

5.7 SIMPLIFIED METHOD FOR THE LONG-TERM ANALYSIS OF CFST ARCH BRIDGES

Using the step-by-step procedure to model the time-dependent behaviour of the concrete may not be practical for day-to-day design applications despite its high accuracy. With step-by-step method, an analysis carried out at time t_k requires the knowledge of the concrete behaviour recorded over the previous k-1 steps and these calculations can lead to extremely high computational costs especially for complicated structures like CFST arch bridges. Even with commercial finite element programs, the use of the step-by-step method represents still a complicated task for designers. In this context, a simplified method with an easier analysis procedure is presented in this section. The simplified method is based on the following assumption.

1) The geometric nonlinearity is neglected.

2) Shrinkage of the core concrete is neglected.

3) All the assumptions listed in section 5.2 are satisfied.

The first two assumptions have been proved to be acceptable in section 5.5, and section 4.4, respectively. The effective modulus (EM) method which has been proved to have an acceptable accuracy in predicting the long-term response of

CFST members is recommended for design. Section 4.5 has shown that for the widely adopted concrete strength in CFST arch bridge application (i.e. with a cylinder compressive strength of 40MPa), the results calculated using the EM method have a maximum deviation of about 8% from those obtained with the step-by-step procedure. The accuracy of using EM method to predict the long-term response of CFST arch bridges can be further increased by subdividing the time interval t-t_0 into sub-intervals as the construction process has to be divided into steps. In this context, the EM method is adopted in the simplified method.

When using the simplified method, the time discretisation is based on the construction steps. The loads are applied incrementally at each construction step. The long-term response of the structure at the n^{th} step is then the sum of all the predicted results obtained from n steps. Figure 5-28 presents the flow chart to determine the long-term response of CFST arch bridges at step n, in which t_i is the age of the concrete at step i, the value of which differs for different core concrete components as these are pumped at different times; $\triangle N(t_i) = N(t_i) - N(t_{i-1})$ denotes the new loads applied on the arches at step i; and $\triangle \mathbf{R}(t_i)$ collects all the static responses of the arches at step i including the stresses in the steel tube and core concrete, and displacements.

With the simplified method, long-term analysis is conducted at several instances during the construction process of the Dong-Guan Waterway Bridge and the results are compared with those obtained from step-by-step method to verify the reliability of the simplified method (Figure 5-29 and Figure 5-30). Observing these two figures, it can be noted that the simplified method tends to underestimate the time-dependent behaviour of the core concrete, leading to lower predicted values for both displacements and stresss in the steel tube. The differences between the predicted results obtained by the simplified method and those obtained with the step-by-step method are relatively large at the beginning of the construction (up to 13%) and tend to decrease with time (around 5% at the end of the construction). This is reasonable as the deviation of the effective method is higher for CFST specimens with early concrete ages at loading (around 10% when loads are applied 3 days after concrete casting) and tends to decrease for loads applied at a relatively

old concrete age (less than 5% if the age at loading is older than 28 days) (see section 4.5).

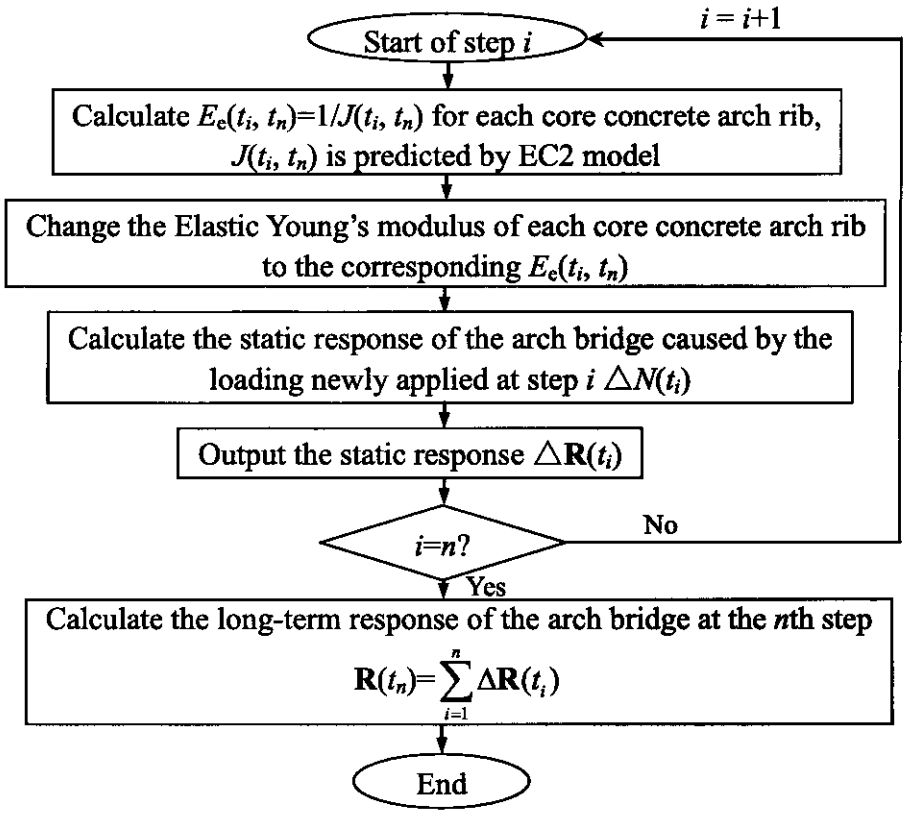

Figure 5-28 Flow chart for long-term analysis of CFST arch bridges at step n with the consideration of construction process and concrete ageing.

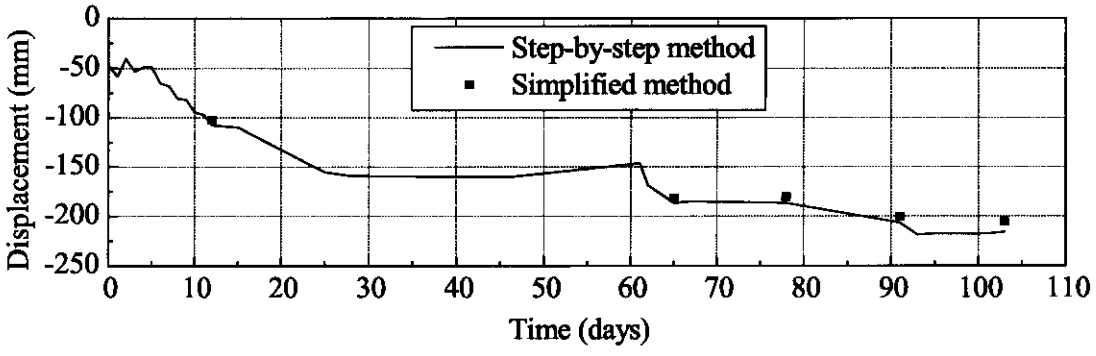

(a) Displacement at arch crown during the construction process

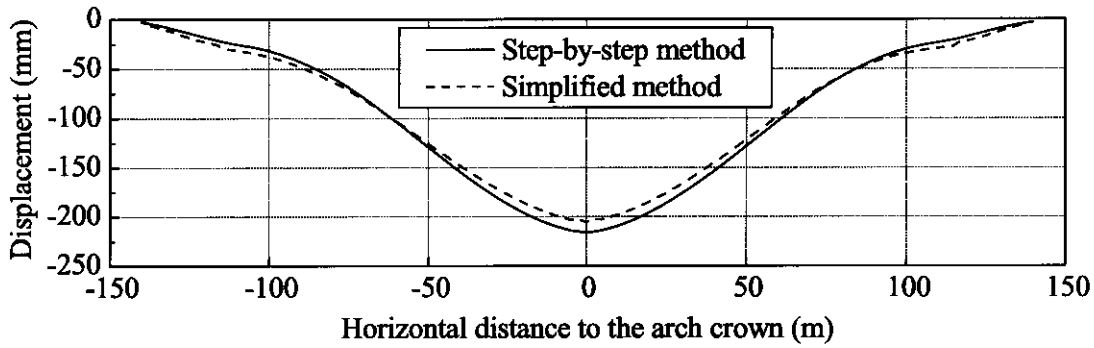

(b) Displacement of the arch at the end of the construction

Figure 5-29 Validation of the simplified method in predicting the displacements of arch ribs

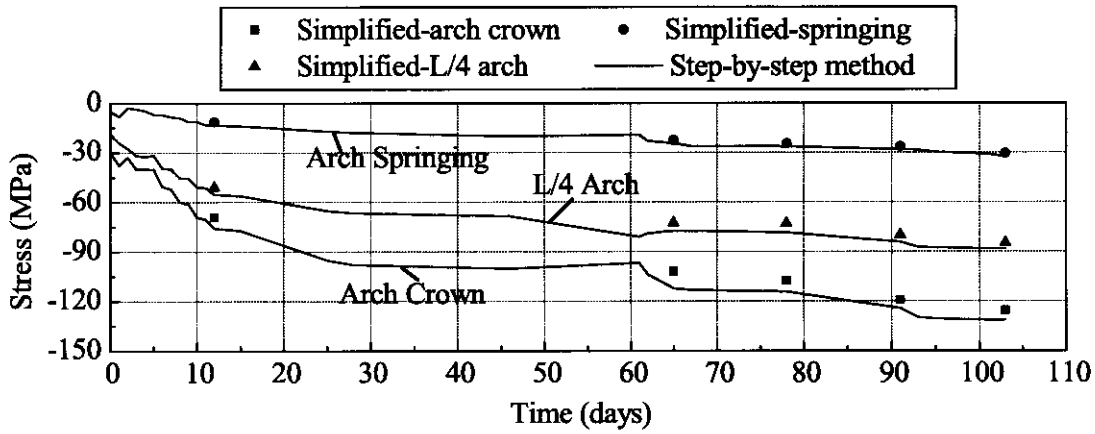

(a) Stress at the upper chord of the arch ribs

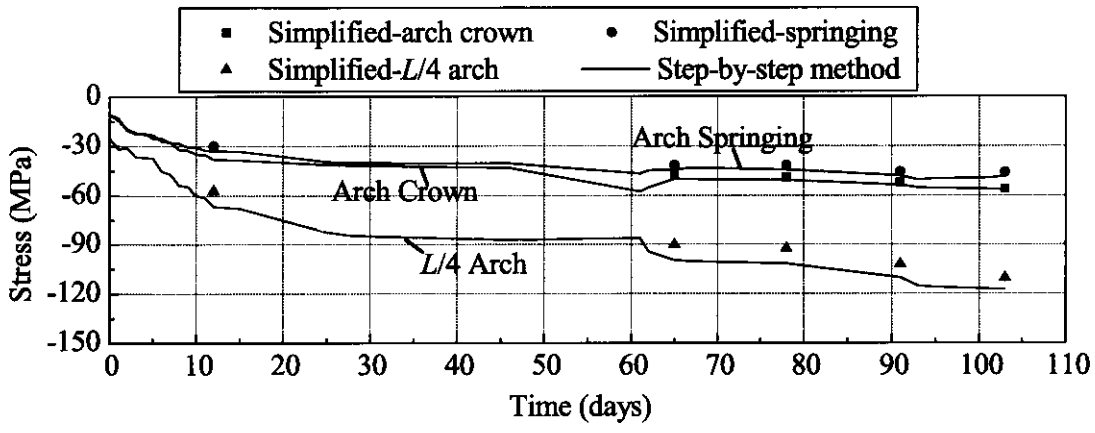

(b) Stress at the bottom chord of the arch ribs

Figure 5-30 Validation of the simplified method in predicting the stress of arch ribs

The results calculated using the simplified method have an acceptable agreement with those obtained with the step-by-step method, with a maximum deviation of 4.9% for the long-term displacements and 4.5% for the stress predictions at the end of the construction. Based on this, the simplified method can be used for predicting the long-term response of the CFST arch bridges in design.

5.8 CONCLUSIONS

An accurate finite element analysis method has been proposed to predict the long-term response of CFST arch bridges. It has been developed using the commercial FE software ABAQUS. This method is capable of accounting for the construction process, the ageing of the concrete, the geometric nonlinearity and time effects. Using the Dong-Guan Waterway Bridge as a study case, the analysis method has been validated against measurements collected on site during construction. Based on the proposed numerical results it has been shown the necessity of considering the time-dependent behaviour of the core concrete, the influence of accurately modelling the time of first loading during construction, and the importance of accounting for live loads in heavily loaded bridges. Finally, a simplified analysis method, which considers the time-dependent behaviour of the core concrete by changing the elastic modulus, has been presented for design purpose. The reliability of the simplified method has been validated comparing its results with those predicted with the step-by-step method. In summary, the main outcomes of this Chapter can be detailed in the following points:

1) The finite element model has been presented to account for the time-dependent behaviour of the core concrete in arch ribs. The concrete behaviour has been described using EC2 and implemented by means of the step-by-step method. The proposed model has been shown to be adequate to predict the long-term response of CFST arch bridges.

2) It has been highlighted that time effects have a significant influence on displacements, stress distributions, and bending moment diagrams of CFST arches during the construction and service life.

3) The construction process, including the variation of the loading ages during this stage, has a significant influence on the long-term response of the CFST arch bridges and its effects need to be considered in design.

4) Live loads are recommended to be included in the quasi-permanent combinations used for the predictions of the long-term response of CFST arch bridges, especially for bridges with heavy traffic loads.

5) The geometric nonlinearity has limited influence on the static response of the CFST arch bridges at service conditions.

6) The effective modulus method has been shown to be a reliable simplified method to be used in design to determine the long-term response of CFST arch bridges.

CHAPTER 6 TIME EFFECTS ON THE LATERAL STABILITY OF PARABOLIC CFST ARCHES SUBJECTED TO DISTRIBUTED LOADS

6.1 INTRODUCTION

The time-dependent behaviour of the core concrete has a significant influence on the static behaviour of CFST arches, in particular producing long-term deformations, stress redistributions between the steel and the concrete components and variations in the internal moment distributions. In this context, these effects might also affect the stability of CFST arches. Wang et al (2011) numerically analyzed time effects on the in-plane buckling of CFST arches and pointed out that when subjected to long-term loading the stability of the structure can decrease by 30% in maximum. Unfortunately, no work has been published to date on the time-dependent out-of-plane instability of CFST arches (section 2.7.6).

The purpose of this Chapter is to numerically investigate the effects of prebuckling deformations induced by time effects on the flexural-torsional buckling of single parabolic CFST arches with single circular cross-sections fixed on both ends and subjected to loads uniformly distributed along their span. Such investigation is important to gain better insight into the creep buckling of large span CFST arch bridges ($l \geq 150$ m) considering that: i) several large span CFST arch bridges have been built to date without wind bracing for aesthetic purposes (with longest span of 240 m); and ii) arch bridges, even with wind braces, are prone to lateral buckling when possessing low width-to-span ratio (see section 2.4.1.2).

For this purpose, a finite element model is built to perform buckling analyses using the commercial software ABAQUS. The time-dependent behaviour of the core concrete is implemented with a UMAT subroutine based on EC2 guidelines and the step-by-step method. The analysis also accounts for material nonlinearities. An extensive parametric study is conducted to evaluate the influence of the concrete age at first loading (3 days~3 years), the duration of the sustained load (100 days~100

years), the concrete strength (20 MPa~70 MPa), the steel strength (235 MPa~420 MPa), the ratio of the steel area over the concrete area at the cross-section (0.04~0.2), the slenderness (60~150), and the span-to-rise ratio (3~10) on the creep buckling behaviour of CFST arches.

6.2 FINITE ELEMENT MODELLING

6.2.1 Loading Process

The arch is fixed at both ends, and the loads are uniformly distributed along the arch span. The analysis starts with the application of service loads (P_L) (Figure 6-1) which are maintained constant over a period of t-t_0 days, after which they are increased at time t till the critical level (P_{cr}) is reached when the arch buckles (reaching an ultimate state condition for the bridge).

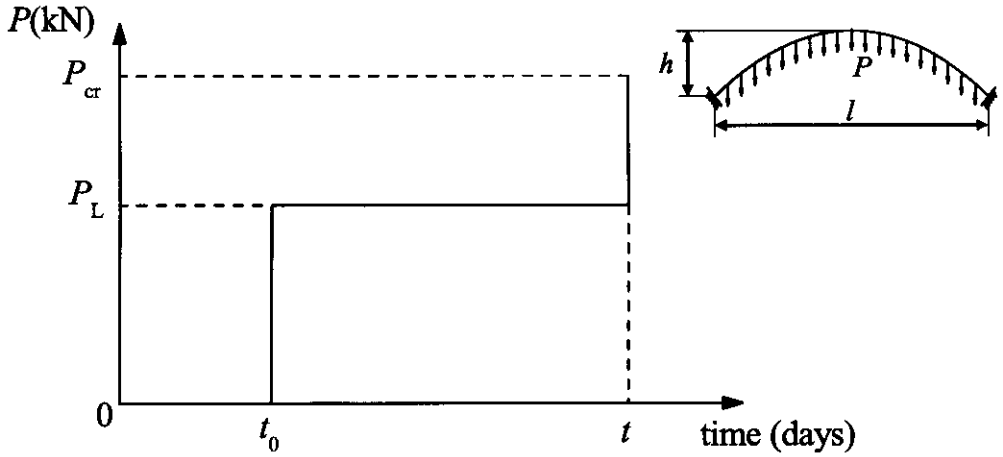

Figure 6-1 Loading process for the parametric analysis

According to the analysis results presented in Chapter 5, the stress in the core concrete is lower than 50% of the cylinder compressive strength for large-span CFST arch bridges subjected to service loading. In this context, for ease of comparisons, the value of the sustained load is expressed in terms of the maximum initial compressive stress calculated in the concrete equal to 50% of the concrete strength.

6.2.2 Material Property

6.2.2.1 Concrete

The creep of the concrete core are within linear range throughout the long-term loading phase in the analysis, hence the concrete model with the time effects considered by step-by-step method and the EC2 model as presented in section 5.2 is adopted in this part (which is also referred to as the time-dependent model in the following).

Concrete in tension is assumed to carry no load. When the concrete reaches a stress greater than 55% of its compressive strength, it is modeled by means of the constitutive equations proposed by Han (2007) to account for material nonlinearities and the possible confinement effects. The equations are presented in the following, among which σ_{cr} is the peak value of the stress in stress-strain curve, and ε_{cr} is the corresponding strain:

$$y = 2x + x^2 \qquad (x \le 1) \qquad (6\text{-}1)$$

$$y = \begin{cases} 1 + q \cdot \left[(x)^{0.1\xi} - 1 \right] & (\xi \ge 1.12) \\ \dfrac{x}{\beta \cdot (x-1)^2 + x} & (\xi < 1.12) \end{cases} \qquad (x > 1) \qquad (6\text{-}2)$$

and

$$x = \frac{\varepsilon}{\varepsilon_{cr}} \qquad (6\text{-}3)$$

$$\varepsilon_{cr} = \varepsilon_{cc} + \left[1400 + 800 \cdot \left(\frac{f_{ck}}{24} - 1 \right) \right] \cdot \xi^{0.2} \quad (\mu\varepsilon) \qquad (6\text{-}4)$$

$$\varepsilon_{cc} = 1300 + 12.5 \cdot f_{ck} \quad (\mu\varepsilon) \qquad (6\text{-}5)$$

$$y = \frac{\sigma}{\sigma_{cr}} \qquad (6\text{-}6)$$

$$\sigma_{cr}=\left[1+\left(-0.054\cdot\xi^2+0.4\cdot\xi\right)\cdot\left(\frac{24}{f_{ck}}\right)^{0.45}\right]\cdot f_{ck} \tag{6-7}$$

$$q=\frac{\xi^{0.745}}{2+\xi} \tag{6-8}$$

$$\beta=\left(2.36\times10^{-5}\right)^{\left[0.25+(\xi-0.5)^7\right]}\cdot f_{ck}{}^2\cdot3.51\times10^{-4} \tag{6-9}$$

$$\xi=\frac{A_s\cdot f_y}{A_c\cdot f_{ckp}} \tag{6-10}$$

where the input variables required for the analysis consist of: characteristic compressive strength of 28-day standard cylinders f_{ck} (MPa); area of steel A_s (mm^2); area of concrete A_c (mm^2); yield strength of steel f_y (MPa); and characteristic compressive strength at 28 days for 150 mm cube f_{ckp} (MPa) (which corresponds to f_{ck} as presented in Table 6-1 calculated based on (CEB-FIP 1993, GB 50010 2002)).

Table 6-1 Characteristic strength values (MPa)

Concrete grade ($f_{ck\text{-}cube}$)	C30	C40	C45	C50	C55	C60
$f_{ck\text{-}prism}$	20	26.8	29.6	32.4	35.5	38.5
f_{ck}	24.2	32.3	36.2	40	45	50

To account for the time-dependent deformation occurred over time the instantaneous stress-strain curve of the material, here expressed using Han's model, is shifted horizontally by an amount $\Delta\varepsilon_1$ to ensure that the concrete still resists the same stress (Figure 6-2). For this purpose, referring to the stress and strain resisted by the concrete at the end of the last time step of the time analysis as σ_1 and ε_1, respectively, $\Delta\varepsilon_1$ can be obtained with Eqn (6-11) and Eqn (6-3) should be replaced with Eqn (6-12):

$$\Delta\varepsilon_1=\varepsilon_1-\varepsilon_{1H} \tag{6-11}$$

$$x = \frac{\varepsilon - \Delta\varepsilon_1}{\varepsilon_0} \tag{6-12}$$

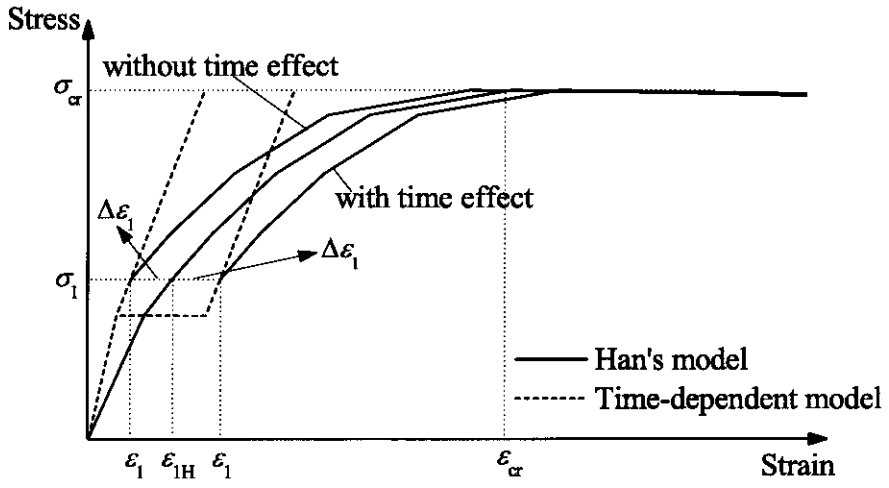

Figure 6-2 Stress-strain curve for concrete core

Figure 6-2 exaggerates differences between curves for clarity. In fact, within the range of the parameters considered in this Chapter, the maximum difference of predicted for the strains obtained using the time-dependent model and the instantaneous relationship of Han is 9.2%.

Re-arranging Eqn (6-1) in terms of x leads to:

$$x = -1 + \sqrt{1 + y} \tag{6-13}$$

ε_{1H} can be calculated as follows (Eqn (6-3) and Eqn (6-6)):

$$\varepsilon_{1H} = -\varepsilon_0 + \varepsilon_0 \cdot \sqrt{1 + \frac{\sigma_1}{\sigma_0}} \tag{6-14}$$

which can be substituted in Eqn (6-11) to calculate $\Delta\varepsilon_1$ as:

$$\Delta\varepsilon_1 = \varepsilon_1 + \varepsilon_0 - \varepsilon_0 \cdot \sqrt{1 + \frac{\sigma_1}{\sigma_0}} \tag{6-15}$$

6.2.2.2 Steel

Han (2007) refined the plastic phase of the stress-strain curve for the steel under uniaxial stress as presented in section 3.5.1 into three phases (Figure 6-3): i.e. the yield plateau phase (line *bc*), the strain hardening phase (line *cd*), and the perfect plastic phase (line *de*).

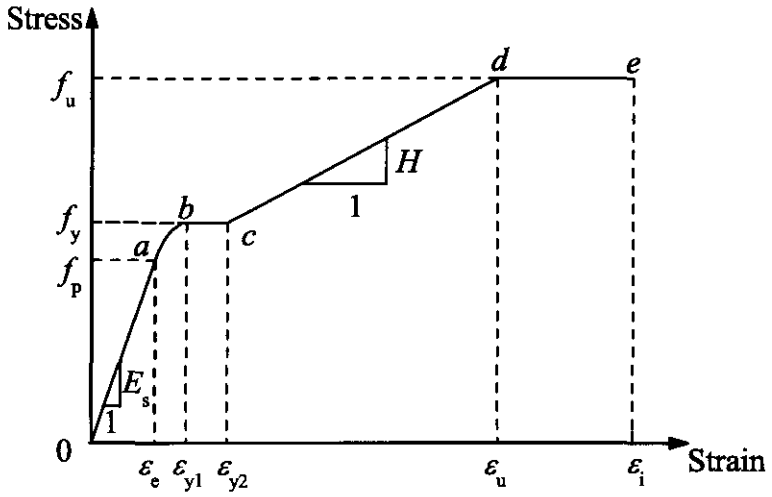

Figure 6-3 stress-strain curve for steel under uniaxial stress

In Figure 6-3, f_p, f_y and f_u represent the proportional limit, the yielding strength, and the ultimate strength of the steel, respectively; the ε_e is the strain corresponding to the proportional limit; ε_{y1} and ε_{y2} are the strains at the start and end of the yield plateau, respectively; ε_u and ε_i denote the strains at the start and end of the perfect plastic phase, respectively; E_s is the elastic Young's modulus of steel; and H defines the plastic hardening modulus. The elastic modulus (E_s) and Poisson's ratio (v) for the steel are taken as 2.06×10^5 MPa and 0.283, respectively. The yield strength has been varied in the range 235-420 MPa (i.e. actual values considered inluded 235 MPa, 345 MPa or 420 MPa). The values for the other factors can be calculated as follows (Zhong 1994):

$$f_p = 0.8 f_y \tag{6-16}$$

$$f_u = 1.6 f_y \tag{6-17}$$

$$\varepsilon_e = f_p / E_s \tag{6-18}$$

$$\varepsilon_{y1} = 1.5\varepsilon_e \tag{6-19}$$

$$\varepsilon_{y2} = 10\varepsilon_{y1} \tag{6-20}$$

$$\varepsilon_u = 100\varepsilon_{y1} \tag{6-21}$$

6.2.3 Modelling of the Arch

The arch used in the following parametric analysis is expressed by a parabolic equation:

$$y = \left(\frac{l}{f}\right) \cdot \left[1 - 4 \cdot \left(\frac{x}{l}\right)^2\right] \tag{6-22}$$

where l denotes the span length of the arch (m), f represents the span-to-rise ratio, x and y depicts the coordinates of the nodes in x and y direction, respectively, with the Cartesian coordinates shown in Figure 6-4 (a).

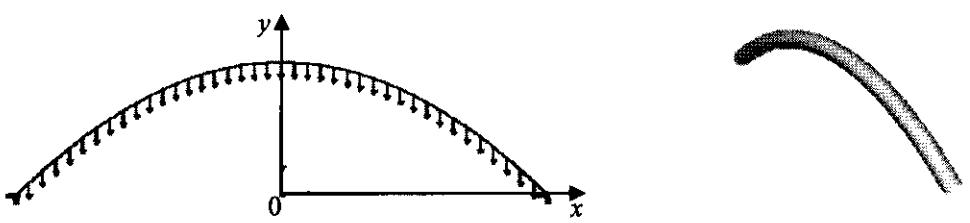

(a) Elevation view (b) Isometric view with cross-section

Figure 6-4 Finite element model for the arch

Similar to the simulations presented in Chapter 5, the following assumptions are adopted in the modelling of the arches in this Chapter:

1) Plane sections remain plane (i.e., linear strain distribution); and
2) Perfect bond between the steel tube and the core concrete in both long-term and buckling analyses.

The core concrete and the steel tubes are modelled separately using Timoshenko

beam elements (B31), adopting the same mesh refinement for the two components. The mesh refinement is carefully chosed to achieve a balance between the efficiency of the calculation and the accuracy of numerical results. The steel and concrete elements are using the same group of nodes to ensure the two materials to behave in full shear interaction. The arch model is presented in Figure 6-5. Imperfections are introduced in the model based on the shapes exhibited by critical buckling modes (i.e. the first eigenmode, see Figure 6-5) with the maximum perturbations of 1/1000 of the arch length.

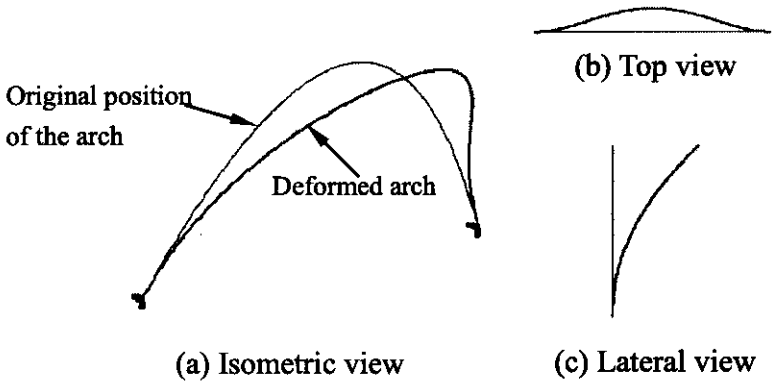

Figure 6-5 First buckling mode of the arch

6.3 INFLUENCE OF PREBUCKLING DEFORMATION INDUCED BY TIME EFFECTS ON LATERAL STABILITY OF CFST ARCHES

The time effects increase the lateral deflection of the arches, therefore triggering the structure to buckle with critical loads lower than the instantaneous ones. Such decrease of critical loads are well depicted by Figure 6-6 using arch cases with the α ratio of 0.2, span-to-rise ratio of 3, steel yield strength of 235 MPa, and concrete cylinder strength of 50 MPa. The loads are applied at 3 days for all the cases and sustained for 100 years for cases with the consideration of time effects. In Figure 6-6, P represents the loads applied on the arch, Δ denotes the corresponding lateral deflection at the arch crown, P_{cro} depicts the instantaneous critical loads, P_{cr} means the critical loads obtained with time effects. It can be noted that the decrease of the critical loads becomes pronounced for slender arches.

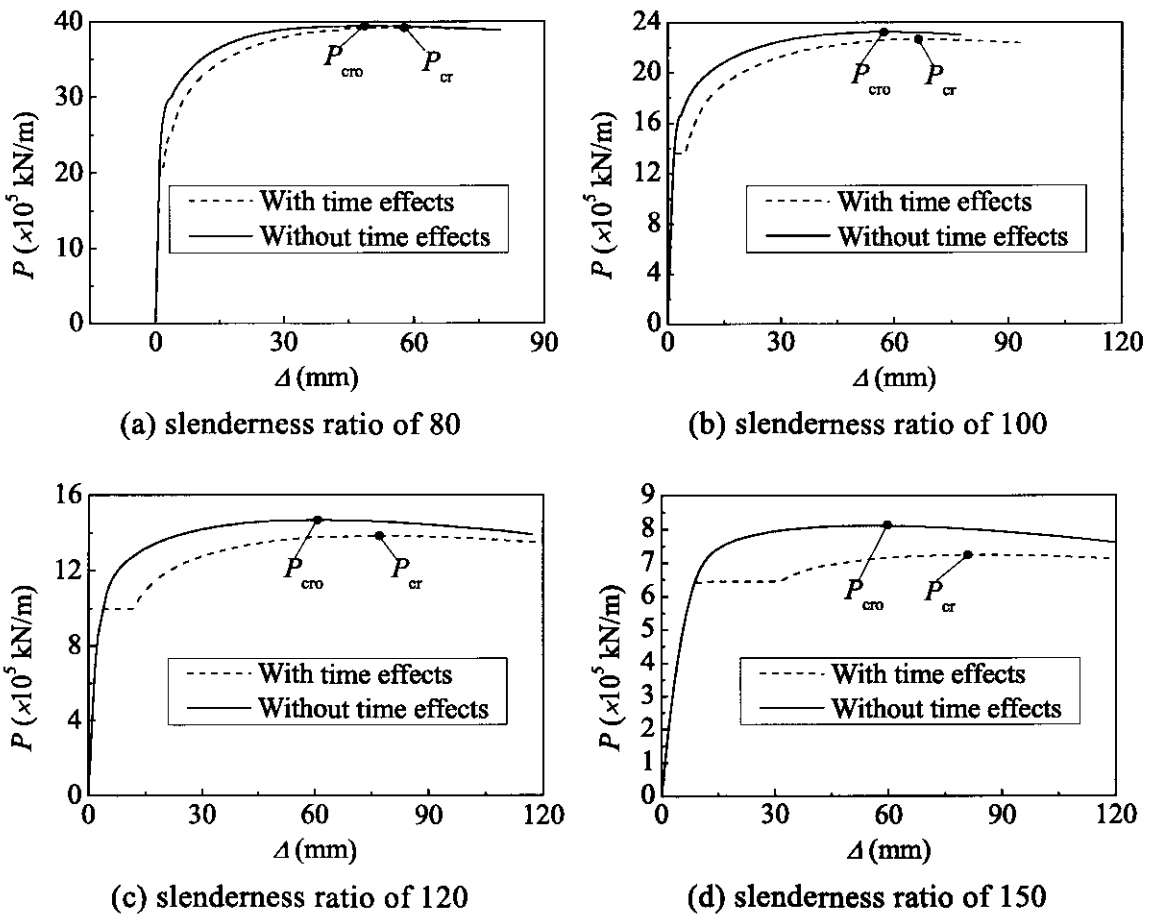

(a) slenderness ratio of 80

(b) slenderness ratio of 100

(c) slenderness ratio of 120

(d) slenderness ratio of 150

Figure 6-6 Buckling and postbuckling behaviour of CFST arches subjected to uniformly distributed vertical loads with and without the consideration of time effects

Whithin the range of parameters considered in this analysis (with concrete age at first loading from 3 days to 3 years, the duration of the sustained load 100 days~100 years, the concrete strength grade between 20 MPa and 50 MPa, the steel strength 235 MPa~420 MPa, the ratio of the steel area over the concrete area at the cross-section from 0.04 to 0.2, the slenderness of 60~150, and the span-to-rise ratio between 3 and 10), the maximum influence of the prebuckling deformation induced by time effects on the lateral buckling behaviour of CFST parabolic arches are presented in Figure 6-7, in which $\Delta P_{cr}= P_{cro}-P_{cr}$, P_{cro} defines the instantaneous value for critical buckling loads and P_{cr} is the critical buckling loads accounting for time effects.

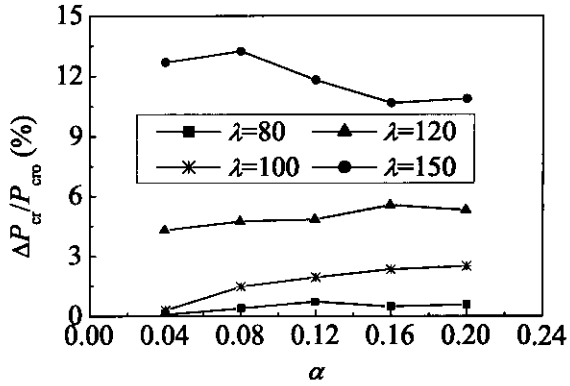

Figure 6-7 Maximum value of $\Delta P_{cr}/P_{cro}$ for different λ and α

It can be observed that time effects can reduce the critical buckling loading by 13% in maximum when compared against its instantaneous value. In this context, time effects need to be considered for the design of large span CFST arch bridges.

6.4 PARAMETRIC STUDY

In the parametric study, the ranges of the parameters are determined according to the designing information gathered from 313 bridges, including the concrete grade ($f_{ck\text{-}cube}$, see Table 6-1 for the corresponding characteristic cylinder compressive strength), the yield strength of the steel (f_y), the age at loading (t_0), the time under loading (t-t_0), the ratio of steel area over concrete area (α), the slenderness ratio (λ), and the span-to-rise ratio (f).

In the following, only representative comparison results are presented. Large-span CFST arch bridges with design life of 100 years are normally constructed with steel with yield stress f_y of 345 MPa and concrete core strength f_{ck} of 40 MPa. Their span-to-rise ratios are generally in the range of 4-5.5 with most loads being applied after 28 days from concrete casting. In this context, the selected results presented in the following have been calculated with: different values for α and λ, f_y=345 MPa, f_{ck}=40 MPa, t-t_0=100 years, t_0=28 days, and f=5. In the last part of this section, the envelop of the possible influence of time effects on the occurrence of lateral stability in CFST arches in investigated for different values for α and λ.

Analysis results indicate that the prebuckling deformation has limited influence on lateral buckling capacity of CFST arches with $\lambda \leq 80$. The difference between the critical loads obtained with and without the consideration of time effects is less than 1% for these members. In this context, only comparison results for arches with λ ratios of 100, 120, and 150 are presented in the following. The decrease of the critical buckling loads induced by time effects is presented in the form of $\Delta P_{cr}/P_{cro}$, in which $\Delta P_{cr} = P_{cro} - P_{cr}$, P_{cro} defines the instantaneous value for critical buckling loads and P_{cr} is the critical buckling loads accounting for time effects.

Figure 6-8 illustrates how the critical loads of the arches decrease for different values of α, different concrete ages at loading (t_0) and different slenderness ratio (λ).As expected, the slender arches subjected to long-term loading applied at an early concrete age are more prone to creep buckling problem. A maximum decrease in critical loading of 4% is observed for arches with λ equal to 150 and sustained load applied at 28 days after concrete casting, while for arches with λ=100 it becomes 2%. These percentages are calculated with reference to the instantaneous buckling load, i.e. ignoring time effects. If the loads are applied 3 days after the concrete casting, the critical loading can increase up to 8% for arches with λ=150, while its value reduces to less than 1% for the same arch subjected to long-term loads first applied at 3 years.

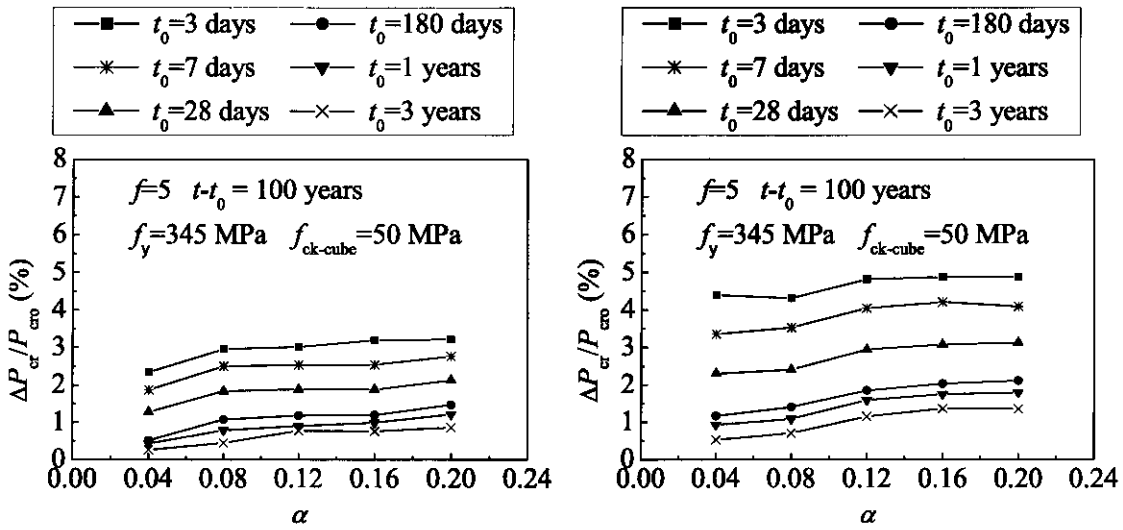

(a) λ = 100

(b) λ = 120

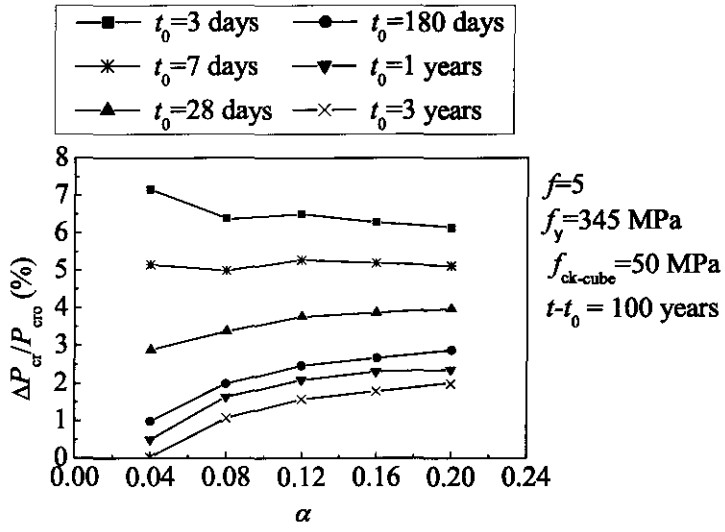

(c) $\lambda = 150$

Figure 6-8 Parametric study: variation of $\Delta P_{cr}/P_{cro}$ with t_0, λ and α

The α ratio has limited effect on the creep buckling behaviour of CFST arches, despite the fact that time effects in CFST members with lower α ratio are considerably more pronounced. This is because the long-term loads are higher for the arches with higher values for α, which induce more additional moments. As a result, the arches with high values for α ratios are more prone to creep buckling problems, unless the increased time effects overcome the effects caused by the additional moments. This is depicted in Figure 6-8 (a) in which the diagram decreases with increasing α ratios for arches subjected to long-term loading at early concrete ages, while increases for arches with old loading ages.

The duration of the loading (t-t_0) is another factor that considerably affects the lateral creep buckling behaviour of CFST arches (Figure 6-9). Figure 6-9 indicates that with long-term loads sustained for 100 days, the decreases of the critical loads of the members are only half of the value for those subjected to long-term loads for 100 years. It is also worth noticing that with the long-term loads applied at 28 days, the maximum decrease of the stability induced by time effects is only 4% when compared to the instantaneous results, while early applied long-term loads can lead to a maximum decrease of 8% (Figure 6-8 (c)). Disregarding the early concrete loading age may lead to an unsafe design solution.

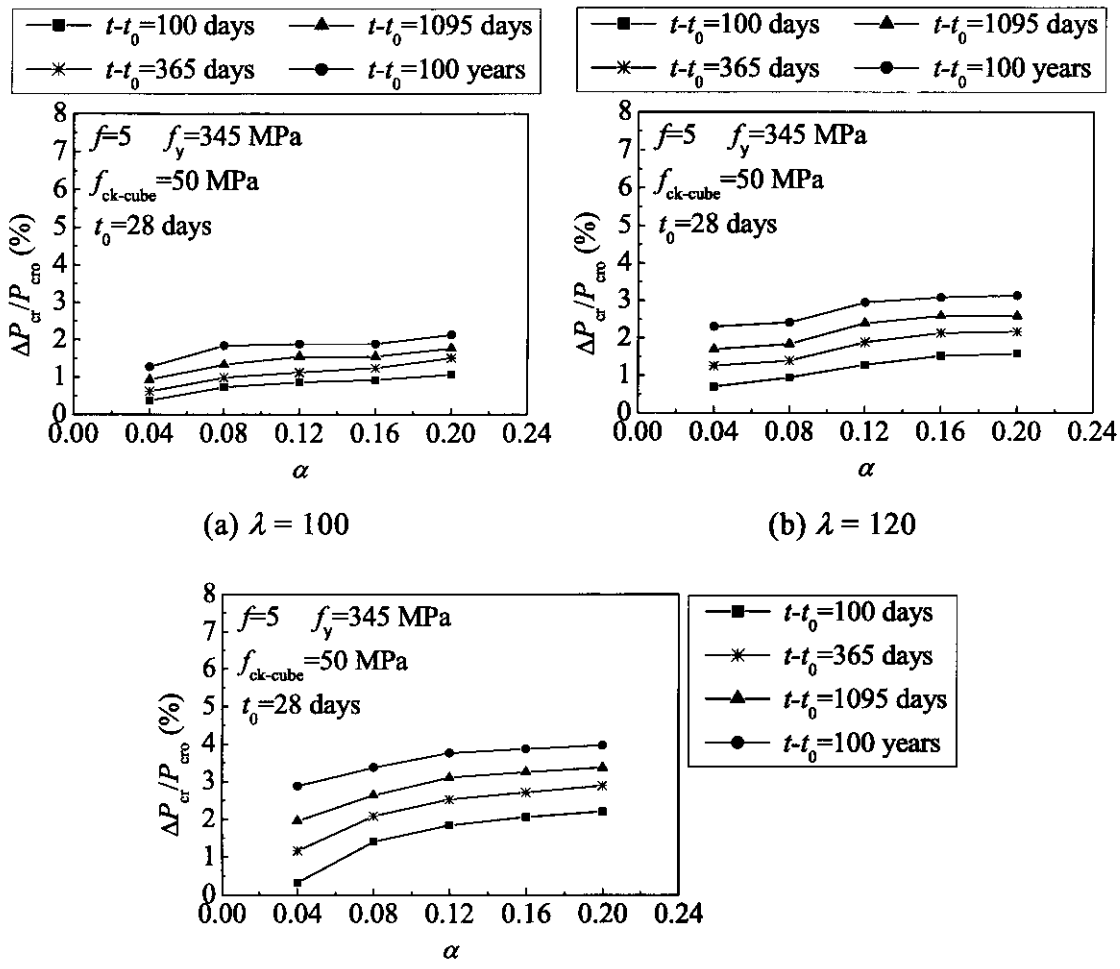

Figure 6-9 Parametric study: variation of $\Delta P_{cr}/P_{cro}$ with t-t_0, λ and α

The yield strength of steel (f_y) and the span-to-rise ratio (f) only have a notable influence on the creep buckling behaviour of slender CFST arches (with λ = 150) (Figure 6-10 and Figure 6-11). The decrease in the lateral stability is more pronounced for arches adopting steel with lower yield strength or with higher span-to-rise ratio.

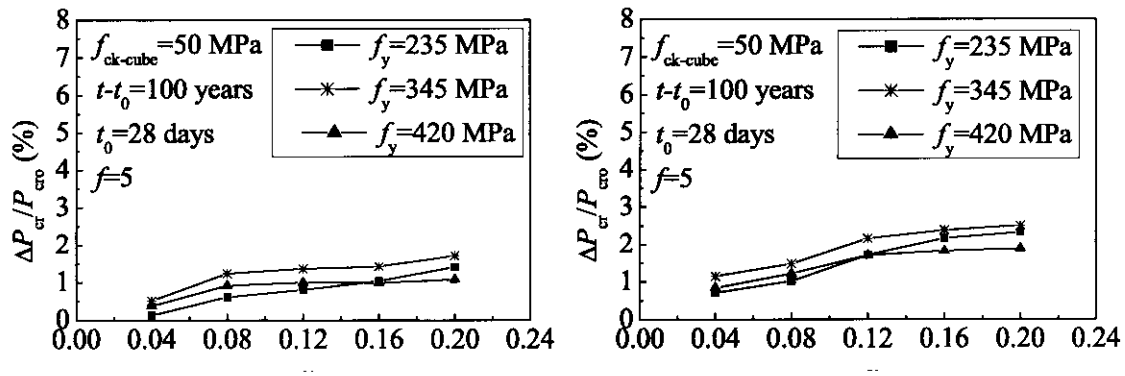

(a) λ = 100 (b) λ = 120

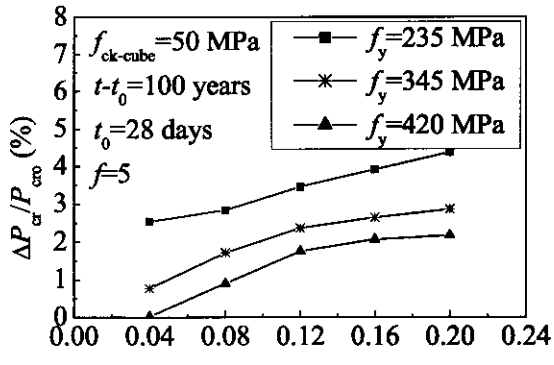

(c) λ = 150

Figure 6-10 Parametric study: variation of $\Delta P_{cr}/P_{cro}$ with f_y, λ and α

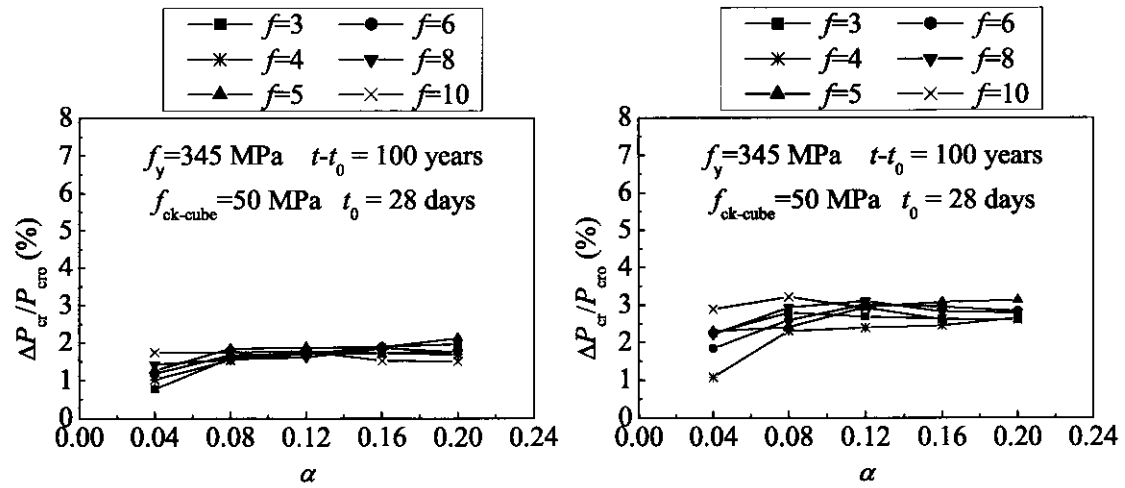

(a) λ = 100 (b) λ = 120

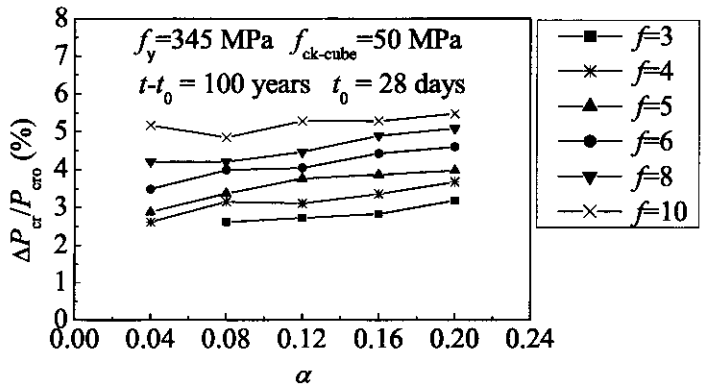

(c) $\lambda = 150$

Figure 6-11 Parametric study: variation of $\Delta P_{cr}/P_{cro}$ with f, λ and α

The concrete strength has only limited influence on the stability of single parabolic CFST arches (Figure 6-12).

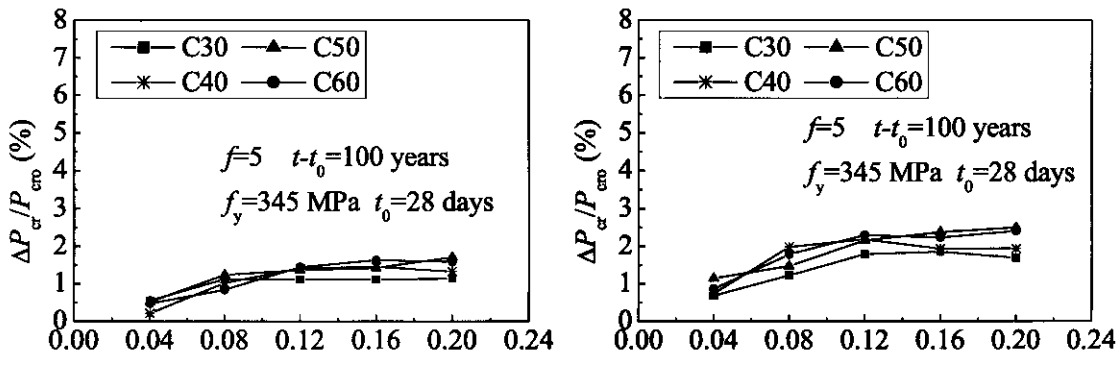

(a) $\lambda = 100$ (b) $\lambda = 120$

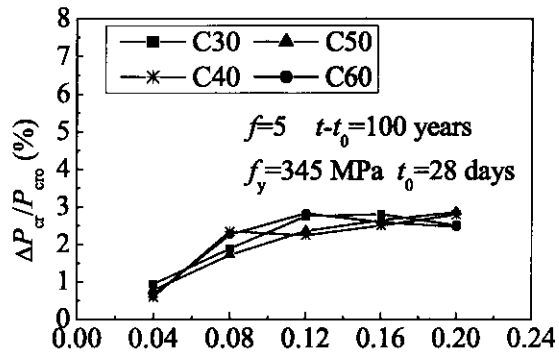

(c) $\lambda = 150$

Figure 6-12 Parametric study: variation of $\Delta P_{cr}/P_{cro}$ with $f_{ck\text{-}cube}$, λ and α

6.5 CONCLUSIONS

An extensive parametric analysis was conducted to investigate the creep buckling behaviour of single parabolic CFST arches subjected to uniformly distribute vertical loads. In the analysis, the time-dependent behaviour of the core concrete was considered by means of the step-by-step method when the material properties were calculated using EC2 guidelines. The confinement effects of the CFST members under ultimate conditions were also taken into account. The following conclusions were drawn based on these results:

1) Prebuckling deformations induced by time effects had a considerable influence on the lateral stability of single parabolic arches with large slenderness ratio and subjected to long-term loads applied at early concrete ages and sustained for a long period of time.

2) The yield strength of the steel and the span-to-rise ratio only had a considerable influence on the creep buckling behavoiur for slender arches (with slenderness ratios larger than 150). The decrease of the critical loading induced by time effects was more considerable for arches adopting steel with lower yield strengths or with higher span-to-rise ratios.

3) Concrete strength and the steel area over concrete area ratio at the cross-section had limited influence on the creep buckling behaviour of the arches.

4) Within the ranges of parameters normally adopted in CFST arch bridge applications, the prebuckling deformations induced by time effects can lead to instability problems in fixed single arches reducing their buckling load by a maximum of 13% when compared against its instantaneous values.

CHAPTER 7 CONCLUSIONS

7.1 CONCLUDING REMARKS

This thesis presented experimental and numerical work aiming at gaining insight into the long-term behaviour and possible creep buckling of CFST arch bridges. This work was carried out by developing an accurate method of analysis to predict their time-dependent response and proposing an adequate simplified method to be used in daily design routine. This work also provided a deeper understanding of the possible occurrence of creep buckling in CFST arches.

The time-dependent behaviour of ECFST specimens was experimentally investigated. Eleven short columns were subjected to different levels of sustained axial loading over a period of 5 months with the concrete ages at first loading varying between 5 and 28 days. After the long-term tests, the ECFST specimens were tested to failure to evaluate how time effects influence their ultimate capacity. The ultimate strength of the specimens subjected to sustained loading was higher than the one noted for the specimen maintained unloaded during the long-term tests. This consideration was experimentally observed up to sustained loads producing stresses about 70% of the concrete strength. These results were consistent with other data published in the literature on normal concrete composite specimens and plain ones. Experimental results also showed that the assumption of linear creep could be applicable for ECFST members with initial concrete compressive stresses of the order of 80% of the concrete strength. Based on the experimental measurements collected during the ultimate tests it was shown that confinement effects had no considerable influence on the response of CFST specimens for load levels at which the steel was not yielded. This consideration is valid for composite columns with material properties similar to those adopted in the tests reported, i.e. steel yield stress of 235 MPa and concrete core characteristic strength of 40 MPa. Based on these considerations its influence could be disregarded at service conditions.

A comparative study was carried out to evaluate the ability of the four concrete

models (i.e. EC2 model, AFREM model, MC90 model, and B3 model) to well depict the time-dependent response of CFST members. A unified method of analysis was proposed for both refined and simplified calculations. The EC2 concrete model, which possesses a reasonable description of both creep and shrinkage behaviour for sealed concrete by considering a nil exposed perimeter, was shown to predict the long-term deformations of CFST specimens well with both normal and expansive core concrete and its use was recommended for this structural system.

Four algebraic methods were discussed and their accuracy was evaluated against the results calculated using the step-by-step procedure. The algebraic methods included the EM method, the MS method and the AAEM method. The latter was implemented using the expressions for the aging coefficient proposed by Bazant and Baweja (2000) and Brooks and Neville (1976). It was observed that all algebraic methods produced acceptable results with the AAEM method yielding the smallest error. Despite this, the EM method was recommended for its ease of use and acceptable accuracy. At the same time it was recommended to use more refined analysis methods for slender structural systems.

Using the Dong-Guan Waterway Bridge as a study case, a refined finite element model was built to investigate time effects on the static response of CFST tied arch bridges. The material property for the core concrete was developed using the step-by-step method based on the guideline of EC2 model and was implemented in the commercial finite element program ABAQUS with the UMAT subroutine. The method had the capability of accounting for the construction process, the aging of the concrete, the geometric nonlinearity and time effects. The accuracy and adequacy of the proposed FE model were validated against on-site readings measured on the Dong-Guan Waterway Bridge. A simplified method of analysis was presented for daily design routine. It was still capable of accounting for the construction process and the aging of the concrete. Its main advantage relied on its ability to be easily implemented in general commercial finite element programs. Its reliability was verified by comparing its results with those calculated using the step-by-step method.

Time effects were shown to have considerable influence on the static response of CFST arches during the construction and service life, highlighting the necessity to

account for these in design to ensure the structural adequacy of the bridge. The inclusion of live loads was considered in the prediction of the long-term response of CFST arch bridges subjected to heavy traffic. It was shown that shrinkage in the core concrete had limited influence on the overall deformation of normal strength core concretes.

An extensive parametric study was performed to investigate the occurrence of creep buckling of CFST arches. It was pointed out that time effects had a pronounced influence on the lateral stability of slender parabolic arches with low steel strength and high span-to-rise ratio which subjected to uniformly distributed loads applied at early concrete ages and sustained for a long period of time.

7.2 RECOMMENDATIONS FOR FURTHER RESEARCH

This study highlighted the need to carry out further long-term experimental tests considering cross-sections with small α values and first loaded at early concrete ages, being representative of current industry detailing practice adopted for CFST members.

It is recommended to carry out additional experiments to determine the possible beneficial effects on the strength of CFST members when its core concrete is subjected to sustained loads over an extended period of time and then unloaded.

Further work is also required to identify the upper stress limits for using linear creep assumptions in composite columns and how these would interact with the occurrence of confinement at high levels of load.

REFERENCES

ACI Committee 209. (1992). *Prediction of creep, shrinkage, and temperature effects in concrete structures*, American Concrete Institute, Farmington Hills, Michigan, ACI 209R-92.

ACI Committee 209. (2008) *Guide for modeling and calculating shrinkage and creep in hardened concrete*. American Concrete Institute, Farmington Hills, Michigan, ACI 209.2R-8.

Ai D. H. (2007). Experimental study on creep of concrete filled steel tubular short columns under sustained axial loading. Sichuan Structural Material. No. 5, 217-218. (in Chinese).

AS 1391 2007. (2007). Metallic materials-Tensile testing at ambient temperature, Australian Standard, Australia

AS 5100.5 2004. (2004). Bridge design-Part 5: Concrete. Committee BD-090. Australian Standard. Standards Australia International Ltd. 2004, Australia.

Bazant Z. P. (1968). Creep stability and buckling strength of concrete columns. *Magazine of Concrete Research*. **20**, No. 63, 85-94.

Bazant Z. P. (1972). Prediction of concrete creep effects using age-adjusted effective modulus method. ACI Journal. No. 69, 212-217.

Bazant, Z.P. (1975). Theory of creep and shrinkage in concrete structures: A precis of recent developments, *Mechanics Today*, (ed. by S. Nemat-Nasser Am. Acad. Mech.), Pergamon Press 1975, **2**, 1–93

Bazant Z. P. (1988). *Mathematical modeling of creep and shrinkage of concrete*. John Wiley and Sons Ltd., New York, USA.

Bazant, Z. P. (1994). Creep and thermal effects in concrete structures: A conspectus of some new developments. *Proceedings of EURO-C 1994 International Conference*, Innsbruck, Austria, Pineridge Press, 461–480.

Bazant, Z. P. & Baweja, S. (2000). Creep and shrinkage prediction model for analysis and design of concrete structures: Model B3, *Adam Neville Symposium: Creep and Shrinkage-Structural Design Effects*, Al-Manaseer, A., ed., American Concrete Institute, Farmington Hills, Michigan, ACI SP-194, 1-83.

Bazant Z. P. & Cedolin L. (2003). *Stability of structures: Elastic, Inelastic, Fracture,*

and Damage Theories. Dover Publications INC., Mineola, New York, USA.

Bazant, Z. P. & Li, G. H. (2008). Unbiased statistical comparison of creep and shrinkage prediction models, *ACI Materials Journal*, **105**, No. 6, 610-619.

Bazant Z. P., Li G. H., & Yu Q. (2008). Prediction of creep and shrinkage and their effects in concrete structures: Critical appraisal. *Creep, Shrinkage and Durability Mechanics of Concrete and Concrete Structures* (Proceedings of 8th International Conference on creep, shrinkage and durability of concrete and concrete structures, Ise-Shima, Japan, T. Tanabe et al. eds.), CRC Press/Balkema, Taylor & Francis Group, Boca Raton–London, 1275-1289.

Bazant Z. P. & Osman E. (1976). Double power law for basic creep of concrete. *Materials and Structures (RILEM, Paris)*, **9**, 3-11.

Bazant Z. P. & Tsubaki T. (1980). Nonlinear creep buckling of reinforced concrete columns. *Journal of the Structural Division*. **106**, No. ST11, 2235-2258.

Behan J. E. & O'Connor C. (1982). Creep buckling of reinforced concrete columns. *Journal of the Structural Division*. **108**, No. 12, 2799-2818.

Bleich F. (1952). *Buckling Strength of Metal Structures*, McGraw-Hill Book Co., New York, USA.

Bockhold J. & Petryna Y. S. (2008). Creep influence on buckling resistance of reinforced concrete shells. *Computers & Structures*. **86**, 702-713.

Boresi A. P. & Schmidt R. J. (2003). *Advanced Mechanics of Materials, 6th ed.*, John Wiley & Sons Inc., USA.

Bradford M. A. (2005). Shrinkage and creep response of slender reinforced concrete columns under moment gradient: theory and test results. *Magazine of Concrete Research*. **57**, No. 4, 235-246.

Brooks J. J. & Al-Qarra H. (1999). Assessment of creep and shrinkage of concrete for the Flintshire Bridge. *The Structural Engineer*. **77**, No. 5, 21-26.

Brooks, J. J. & Neville, A. M. (1976). Relaxation of stress in concrete and its relation to creep, *ACI Journal*, **73**, No. 4, 227-232.

BSI. (2004). *Eurocode 2: Design of concrete structures*, European Committee for Standardization, BS EN European Standards 1992-1-1: Part 1-1: general rules and rules for buildings.

Cai S. H. (2007). *Modern steel tube confined concrete structures.* China

Communications Press, Beijing, China. (in Chinese).

Cassity P., Furrer M. & Price K. (1999). Synthesizing form and function—The Damen Avenue Arch Bridge was not simply an innovative engineering feat, but also a success as a new neighborhood landmark. *Modern Steel Construction*, December 1999

Chakrabarty J. (1998). *Theory of plasticity*, McGraw-Hill Book Co., Singapore.

Chang X., Cheng K. H., & Chen Y. J. (2009). Mechanical performance of eccentrically loaded pre-stressing concrete filled circular steel tube columns by means of expansive cement. *Engineering Structures*. No. 31, 2588-2597.

Chen B. C. (2007). *Concrete filled steel tubular arch bridge*, China communication press, Bei Jing, China. (in Chinese).

Chen S. F., Yang D. W., Yang X. S. (2007). Research on concrete creep effect of CFST arch rib concrete of Qiandao Lake Bridge. *Highway*, No. 6, 32-35. (in Chinese).

Cheng X. D. (2004). *Three-dimensional nonlinear analysis of long span concrete filled steel tube arch bridge by the method of laminated element*. Doctoral Thesis, Zhejiang University, Zhejiang, China (in Chinese).

Cheng, X. D., Li, G. Y. & Ye, G. R. (2005). Three-dimensional nonlinear analysis of creep in concrete filled steel tube columns, *Journal of Zhejiang University (Science)*, **6A**, No. 8, 826-835.

Chiorino M. A. (2005). A rational approach to the analysis of structural effects due to creep. *Shrinkage and creep of concrete*. (Gardner, J. and Weiss, J. (ed.)), ACI SP-227, 239-259.

Cluley N. C. & Shepherd R. (1996). Analysis of concrete cable-stayed bridges for creep, shrinkage and relaxation effects. *Computers & Structures*. **58**, No. 2, 337-350.

Cook D. J. & Chindaprasirt P. (1980). Influence of loading history upon compressive properties of concrete, *Magazine of concrete research*, **32**, No. 111, 89-100.

Comité Euro-International du Béton. (1993). *CEB-FIP Model Code 1990*, CEB bulletin d'Information, London: Thomas Telford.

Coutinho A. S. (1977). A contribution to the mechanism of concrete creep, *Materials and Structures*, **10**, No. 55, 3-16.

Cui J. (2003). *Structural Characteristic Study on Large Span CFST Arch Bridge.* Doctor Thesis, Zhe Jiang University, Zhe Jiang, China. (in Chinese).

Dhir R. K. & Sangha C. M. (1972). A study of the relationships between time, strength, deformation and fracture of plain concrete, *Magazine of concrete research*, **24**, No. 81, 197-208.

DL/T 5085-1999. (1999). *Code for design of steel-concrete composite structure*, State Economic and Trade Commission (SETC) of the People's Republic of China, China electric power press, Beijing, China. (in Chinese)

Faber H. (1927-28). Plastic yield, shrinkage and other problems of concrete and their effect on design. *Minutes Proc. Inst. Civ. Eng.*, London, England, **225**, 27-76, discussion, 75-130.

Freudenthal A. M. & Roll F. (1958). Creep and creep-recovery of concrete under high compressive stress, *ACI Journal*, No. 54, 1111-1142

Gardner N. J. & Lockman M. J. (2001). Design provisions for drying shrinkage and creep of normal strength concrete. *ACI Materials Journal.* **98**, No. 2, 159-167.

GB 50010-2002. (2002). *Code for design of concrete structures*, Ministry of Construction of the People's Republic of China, Bei Jing, China. (in Chinese).

Geng Y., Zhang S. M., Wang Y. Y. & Wang X. L. (2010). Static behaviour of a concrete filled steel tubular double X-shape arch bridge without wind braces under construction. *Proceedings of Ninth Pacific Structural Steel Conference.* Beijing, China, 906-910.

Gilbert, R. I. & Ranzi, G. (2011). *Time-dependent behaviour of concrete structures*, Spon Press, London, UK.

Goel R., Kumar R. & Paul D. K. (2007) Comparative study of various creep and shrinkage prediction models for concrete. *Journal of Materials in Civil Engineering.* **19**, No. 3, 249-260.

Goode C. D. (2006). A review and analysis of over one thousand tests on concrete filled steel tube columns. *8th International concrete on steel-concrete composite and hybrid structures proceedings.* Harbin, China, 17-23.

Gu A. B., Liu Z., Zhou S. X. (1999). Analysis of time dependent effects of concrete, geometrical nonlinearities, material nonlinearities of Wanxian Yangtze River Bridge. *Journal of Chong Qing Jiao Tong Institute*, **18**, No. 4, 1-7. (in Chinese).

Gu A. B., Yu W. J., Chen Q. J. & Liu C. C. (2005). Analysis on shrinkage and creep in large span concrete filled steel tube arch bridges. *Proceedings of the National Conference on Bridge Engineering*. China, 1014-1024. (in Chinese).

Gu J. Z., Liu X. L. & Chen W. F. (2001). Structure analysis with the effect of creep in CFT arch bridge. *Journal of Shanghai Jiaotong University*. **35**, No. 10, 1574-1577. (in Chinese).

Han B. & Wang Y. F. (2007). Creep analysis comparison of circular axially compressed concrete-filled steel tubular members. *China journal of highway and transport*, **20**, No. 2, 83-86. (in Chinese).

Han, L. H. (2007). *Concrete-Filled Steel Tubular Structures — Theories and Applications (2nd ed.)*. Science Press. Beijing, China. (in Chinese)

Han, L. H. & Yang, Y. F. (2003). Analysis of thin-walled steel RHS columns filled with concrete under long-term sustained loads, *Thin-Walled Structures*, **41**, No. 9, 849-870.

Han, L. H., Tao, Z. & Liu, W. (2004). Effects of sustained load on concrete-filled hollow structural steel columns, *Journal of Structural Engineering*, **130**, No. 9, 1392-1404.

Hellesland J. & Green R. A. (1972). Stress and time dependent strength law for concrete, *Cement and concrete research*, **2**, No. 3, 261-275.

Highway Planning and Design Institute in Sichuan Provincial Communications Department. (2008). *Guide to Design and Construction Technology of Road Steel Tube Concrete Bridge*. (Mo T. M., Zhuang W. L., Liang J. & Fan B. K. (ed.)). China Communications Press, Beijing, China. (in Chinese).

Howells, R. W., Lark, R. J. & Barr, B. I. G. (2005). A sensitivity study of parameters used in shrinkage and creep prediction models, *Magazine of Concrete Research*, **57**, No. 10, 589-602.

Hu, S. H. 2007. *The research on shrinkage creep and temperature effect of concrete filled steel tubes on long-span arch brdige. Master Thesis. University of Hunan.* (in Chinese).

Ichinose, L. H., Watanabe, E. & Nakai, H. (2001). An experimental study on creep of concrete filled steel pipes. *Journal of Constructional Steel Research*, **57**, No. 4, 453-466.

Jiang R. (2009). *Static & dynamic analysis of composite truss beem bridge with steel tube & concrete filled tube.* Master thesis, Southwest Jiaotong University, Si Chuan, China. (in Chinese)

JTG D60-2004. (2004). *General Code for Design of Highway Bridges and Culverts.* Ministry of Communications of the People's Republic of China, Beijing, China. (in Chinese).

JTG D62-2004. (2004). *Code for design of highway reinforced concrete and prestressed concrete bridges and culverts.* CCCC highway consultants CO., Ltd., Bei Jing, China, 2004 (in Chinese)

Jung S., Chaboussi J. & Marulanda C. (2007). Field calibration of time-dependent behaviour in segmental bridges using self-learning simulation. *Engineering Structures.* **29**, 2692-2700.

Keil S. & Benning O. (1979). On the evaluation of elsto-plastic strains measured with strain gages. *Experimental mechanics*, 265-270.

Khalil N., Cusens A. R. & Parker M. D. (2001). Tests on slender reinforced concrete columns. *Structural Engineer.* **79**, No. 18, 21-30.

Kim J. K., Kwon S. H., Kim S. Y. & Kim Y. Y. (2005). Experimental studies on creep of sealed concrete under multiaxial stresses, *Magazine of Concrete Research*, **57**, No. 10, 623-634.

Kitada T. (1997). Ultimate strength and ductility of state-of-the-art concrete-filled steel bridge piers in Japan. *Engineering Structures.* **20**, No. 4-6, 347-354.

Kwon, S. H., Kim, Y. Y. & Kim, J. K. (2005). Long-term behaviour under axial service loads of circular columns made from concrete filled steel tubes, *Magazine of Concrete Research*, **57**, No. 2, 87-99.

Kwon, S. H., Kim, T. H., Kim, Y. Y. & Kim, J. K. (2007). Long-term behaviour of square concrete-filled steel tubular columns under axial service loads, *Magazine of Concrete Research*, **59**, No. 1, 53-68.

Le Roy R., De Larrard F. & Pons G. (1996). The AFREM code type model for creep and shrinkage of high-performance concrete, *4th international symposium on utilization of high-strength/ high-performance concrete.* Paris, France, 387-396.

Li B. & Gu A. B. (2008). Creep analysis on concrete filled steel tubular structures under eccentric loading. *Journal of highway and transportation research and*

development. No. 3, 114-119. (in Chinese).

Li G. Y. & Wang Z. (2002). Mechanical behavior and microstructure feature of expansive concrete controlled in steel tube. *Building science research of Sichuan*. 28, No. 3, 59-61. (in Chinese).

Li Z. S. (1997). Applications of concrete filed steel tubular structures in Zi Dong Bridge. *Journal of Harbin University of Civil Engineering and Architecture*, **30**, No. 5, 174-178. (in Chinese).

Lin J. (2002). *The creep of core concrete and its influence on the mechanical performance of the axially compressed high strength concrete filled steel tubular member*, Master Thesis, University of Shantou, Guang Dong, China. (in Chinese).

Liu Q. (2008). Effect of initial stress and creep on bearing capacity of four-tube concrete filled steel tube arch bridge. Master Thesis, Chongqing Jiaotong University, Chong Qing, Chia. (in Chinese).

Liu Z., Li F. & Roddis W. M. K. (2002). Analysis Model of Long-Span Self-Shored Arch Bridge. *Journal of Bridge Engineering*. **7**, No. 1, 14-21

Marí A. R. & Valdés M. (2000). Long-term behavior of continuous precast concrete girder bridge model. *Journal of bridge engineering*. **5**, No. 1, 22-30.

Matsui C. (2006). Recent concrete filled steel tube structures in Japan, *8th International concrete on steel-concrete composite and hybrid structures proceedings*, Harbin, China, 24-29.

Minahen T. M. & Knauss W. G. (1993). Creep buckling of viscoelastic structures. *International Journal of Solids and Structures*. **30**, No. 8, 1075-1092.

McMillan F. R. (1916). Method of designing reinforced concrete slabs, discussion of A. C. Janni's paper, *Trans. ASCE*, **80**, 1738

Müller H. S. & Küttner C. H. (1996). Creep of high-performance concrete-characteristics and code type prediction model. *4th international symposium on utilization of high-strength/high-performance concrete*, Paris, France, 377-385.

Morino, S., Kswanguchi, J. & Cao, Z. S. (1996). Creep Behavior of Concrete Filled Steel Tubular Members. *Proceeding of an Engineering Foundation Confererence on Steel-Concrete Composite Structures*. ASCE. Irsee, 514-525.

Naguib, W. & Mirmiran, A. (2003). Creep modeling for concrete-filled steel tubes, *Journal of constructional steel research*, No. 59, 1327-1344.

Nakamura S. I. (2007). Static and aero-dynamic studies on cable-stayed bridges using steel pipe girders. *Structural Engineering International, Journal of IABSE.* **17**, No. 1, 68-71

Nakamura S. I., Momiyama T., Hosaka T. & Homma K. (2002). New technologies of steel/concrete composite bridges, *Journal of Constructional Steel Research.* **58**, 99-130

Nakamura S. I., Tanaka H. & Kato K. (2009). Static analysis of cable-stayed bridge with CFT arch ribs. *Journal of constructional steel research.* **65**, 776-783

Neville A. M. (1995). *Properties of Concrete, 4th and final ed.* Harlow, Essex, Longman.

Ohura T. & Kato M. (1993). Erection and field test of concrete arch bridge applying composite tube, *Journal of Construction Engineering and Management.* **119**, No.4, 666-680.

Robertson I. N. (2005). Prediction of vertical deflections for a long-span prestressed concrete bridge structure. *Engineering structures.* **27**, 1820-1827.

Sassone, M. & Chiorino, M. A. (2005). Design aids for the evaluation of creep induced structural effects, *Shrinkage and Creep of Concrete*, (Gardner, J. and Weiss, J. (ed.)), ACI SP-227, 239-259.

Šavor Z. & Bleiziffer J. (2008). From melan patent to arch bridges of 400m spans. *Long arch bridges, Chinese-Croatian joint colloquium*, Brijuni Islands, Croatia, 349-356

Shams M. & Saadeghvaziri M. A. (1997). State of the art of concrete-filled steel tubular columns. *ACI structural journal*, **94**, No. 5, 558-571.

Shanmugam N. E. & Lakshmi B. (2001). State of the art report on steel-concrete composite columns. *Journal of constructional steel research.* **57**, 1041-1080.

Shao X. D., Peng J. X., Li L. F., Yan B. F. & Hu J. H. (2010). Time-dependent behavior of concrete-filled steel tubular arch bridge. *Journal of bridge engineering.* **15**, No. 1, 98-107.

SIMULIA. (2007 a). *Abaqus Analysis User's Manual (Version 6.7). Volume IV: Elements.* ABAQUS help files, USA.

SIMULIA. (2007 b). *Abaqus Analysis User's Manual (Version 6.7). Volume II: Analysis.* ABAQUS help files, USA.

Somja H. & Goyet V. de ville de. (2008). A new strategy for analysis of erection stages including an efficient method for creep analysis. *Engineering structures.* **30**, 2871-2883.

Strasky J. Nazratil J. & Susky S. (2001). Applications of time-dependent analysis in the design of hybrid bridge structures. *PCI Journal.* **46**, No. 4, 56-74

Tan, S. J. & Qi, J. L. (1987). Experimental investigation of the effects on the strength of concrete filled steel tubular compressive members under standing load, *Journal of Harbin University of Civil Engineering and Architecture*, No. 2, 10-24. (in Chinese).

Terrey, P. J., Bradford, M. A. & Gilbert, R. I. (1994). Creep and shrinkage of concrete in concrete-filled circular steel tubes, *Proceeding of 6th International Symposium on Tubular Structures*, Melbourne, Australia, 293-298.

Tian Z. C., Liu X. F., Yan D. H. & Gu Y.Q. (2007). Discussion for creep calculation methods of concrete-filled steel tube arch bridge. *Journal of Hunan University of Science & Technology (Natural Science Edition).* **22**, No. 2, 48-51. (in Chinese)

Tomii M. (1991). Ductile and strong columns composed of steel tube, infilled concrete and longitudinal steel bars. *Proceedings of the 3rd International Conference on Steel-Concrete Composite Structure*, Fukuoka, Japan, 39-66

Uy B. (1997). Time effects in concrete-filled steel box columns in tall buildings, *The structural design of tall buildings*, **6**, 1-22.

Uy B. (2001). Static long-term effects in short concrete-filled steel box columns under sustained loading, *ACI Structural Journal*, **98**, No. 1, 96-104.

Uy B. (2005). High strength steel-concrete composite columns: Applications and design. *Proceedings of the Structures Congress and Exposition.* New York, United states, 1089-1100

Virlogeux M., Bouchon E., Berthellemy J. & Resplendino J. (1997). The Antrenas Tubular Arch Bridge, France, *Structural Engineering International*, **7**, No. 2, 107-109

Wang T., Bradford M. A. & Gilbert R. I. (2006). Creep buckling of shallow parabolic

concrete arches. *Journal of Structural Engineering*. **132**, No. 10, 1641-1649.

Wang Y. F. (2006). *Creep of concrete-filled steel tubes*. Science press, Beijing, China. (in Chinese).

Wang Y. F., Han B., Du J. S. & Liu K. W. (2007). Creep analysis of concrete filled steel tube arch bridges. *Structural engineering and mechanics*. **27**, No. 6, 639-650.

Wang Y. Y. & Hui Z. H. (2010). *Construction Process and Key Techniques of Concrete-Filled Steel Tubular Arch Bridges*. China Machine Press. Beijing, China. (in Chinese).

Wang Y. Y., Liu C. Y. & Zhang S. M. (2011). In-plane creep buckling for pin-ended concrete filled steel tubular circular arches. *Engineering Mechanics*. (accepted, in Chinese).

Wu X. S., Peng Y. F., Zhang X. F. (2010). Site rolling production technique of nonstandard size caliber steel tube in Ganhaizi Bridge. *Bridge*. No. 9, 74-76. (in Chinese).

Wang, Z. (1994). The creep for expansive concrete filled steel tube, *Journal of Harbin University of Civil Engineering and Architecture*, **27**, No. 3, 14-17. (in Chinese).

Wu B. & Qu G. Y. (1991). Computation of cross-sectional redistributed internal force produced by creep for concrete filled steel tube arch bridge. *Journal of Xi'an University of Highway*. **11**, No. 4, 22-28. (in Chinese).

Xie X. L. & Qin R. (2001). Theoretical research of shrinkage and creep's influence on CFT arch bridges. *Bridge construction*. No. 4, 1-4. (in Chinese).

Xie L. & Yin L. (2009). Finite element progressive analysis method of creep of axially compressed members of concrete filled steel tube. *Chonqing Architecture*. **8**, No. 7, 37-39. (in Chinese).

Xin B., Xu S. Q. (2003). Analysis of creep of long span steel tubular concrete arch bridge. *Railway Standard Design*. No. 4, 31-32. (in Chinese).

Xiong H. X. & Liu M. Y. (2005). FEM analysis of the creep and shrinkage in CFST arch bridge. *Journal of Wuhan University of Technology*. **27**, No. 4, 51-53 (in Chinese)

Yang H. C. & Yan P. (2008). Influence of creep on stress of CFST arch bridge with

dumbbell section. *Modern Transportation Technology*. **5**, No. 5, 41-43. (in Chinese).

Yao H. X. (2006). *Test research on shrinkage and creep of concrete filled steel tubes on long span arch bridge*. Master Thesis. University of Hunan, Hunan, China. (in Chinese).

Yao, H. X., Chen, Z. Q. & Li, Y. (2007). Experimental study on the shrinkage and creep of concrete filled steel tubes. *Journal of China & Foreign Highway*, No. 6, 133-136. (in Chinese).

Yang S. C., Wang F. M., Qu P. (2008). Brief introduction to the core concrete's empty influence on the mechanical performance of concrete filled steel tube components, *Journal of Chong Qing Jiao Tong University (Natural Science)*, **27**, No. 3, 360-365. (in Chinese).

Yin L., & Cao Y. (2007). Analysis of creep influence on CFST arch bridge. Technology of Highway and Transport. Suppl, 74-76. (in Chinese).

Yoshimura M., Wu Q. X., Takahashi K., Nakamura S. & Furukawa K. (2006). Vibration analysis of the Second Saikai Bridge—a concrete filled tubular (CFT) arch bridge, *Journal of Sound and Vibration*, **290**, No. 1-2, 388-409

Yu J. H., Sun J. Y. & Chen J. L. (2003). Analysis of aging effect of steel-concrete composite arch spans of the 4th Qiantangjiang River Double Dech Bridge. *Bridge construction*. No. 6, 30-33. (in Chinese).

Zeng Y. & Gu A. B. (2005). Exploitation of creep analysis software about concrete filled steel tube arch bridge. *Journal of chongqing jiaotong university*, **24**, No 2, 26-29. (in Chinese).

Zha X. X., Wang H. Y., Yu H. & Zhong S. T. (2010). Experimental infvestigation on the seismic behaviour of RC beam to CFST column connections and the influence of the concrete age during the construction of CFST structure. *Proceedings of Ninth Pacific Structural Steel Conference*. Beijing, China, 879-887

Zhang J. M., Zheng J. L. & Qin R. (2001). Time-dependent behavior analysis of long span CFST arch bridge. *Journal of Chongqing Jiaotong University*. **20**, No. 4, 11-15. (in Chinese)

Zhang Z. C. (2007). Creep analysis of long span concrete-filled steel tubular arch

bridges. *Engineering mechanics*. **24**, No. 5, 151-160. (in Chinese).

Zhao Y. L. (2005). *Seismic Response Analysis of Long Span Concrete Filled Steel Tube Arch Bridge. Master Thesis.* Zhe Jiang University, Zhe Jiang, China. (in Chinese).

Zhong S. T. (1987). The effects on the critical load of concrete filled steel tubular axial compressive members under standing load. *Journal of Harbin University of Civil Engineering and Architecture*, No. 4, 1-8. (in Chinese).

Zhong S. T. (1994). *Concrete-filled steel tubular structures (revised edition)*. Hei Longjiang Science and Technology Press, Hei Longjiang, China. (in Chinese).

Zhong S. T. (2000). Several problems in the design of concrete filled steel tubular (CFST) arch bridges. *Journal of Harbin University of C. E. & Architecture*. **33**, No. 2, 13-17. (in Chinese).

Zhong S. T. (2006). Application and research achievement of concrete filled steel tubular (CFST) structures in China. *8th International concrete on steel-concrete composite and hybrid structures proceedings*. Harbin, China, 24-29

Zhong S. T. & Zhang S. M. (1992). A new method from China to determine load-carrying capacity for CFST members, *Proceedings of an Engineering Foundation Conference, Part of Composite construction in steel and concrete II, ASCE*, Potosi, Missouri, America, 499-511.

Zhong S. T. & Zhang S. M. (1999). Application and development of concrete-filled steel tubes (CFST) in high rise buildings, *Advances in Structural Engineering*, **2**, No. 2, 149-159.

Zhou X. Y. & Cao G. H. (2008). Test study on the long-term mechanical behaviors of concrete-filled steel tube arch bridge with CFRP suspended cables. *China Railway Science*. **29**, No. 3, 34-39.

APPENDIX I CFST ARCH BRIDGES

The designing information for CFST arch bridges gathered through website, literature review and with the help of some designers are collected in the table below, in which the *l/f* denotes the span-to-rise ratio, $f_{ck\text{-}cube}$ represents the cubic characteristic strength of core concrete with the dimension of 150×150×150mm, f_y means the yielding strength of the steel tube, *D* refers to the diameter of the steel tube, and t_s is the thickness of the steel tube. The related references are presented at the end of this appendix.

No.	Name	Location	Year	Span (m)	*l/f*	Arch profile	Bridge type	Width (m)	Arch cross section				
									Shape	$f_{ck\text{-}cube}$ (MPa)	f_y (MPa)	*D* (mm)	t_s (mm)
1	He River No.1 Bridge	Si Chuan, China	Under construction	529	4.5	Catenary	Half-through	28.6	Four-tube truss	60	345	1320	22,26, 30
2	Wu Xia Long River Bridge	Si Chuan, China	2005	460	3.8	Catenary	Half-through	27.84	Four-tube truss	60	345	1220	22,25
3	Zhi Jing River Bridge	Hu Bei, China	2009	430	5.5	Catenary	Deck	13	Eight-tube truss	50	345	1200	35
4	Lian Cheng Bridge[1]	Hu Nan, China	2007	400	5.2	Parabolic	Half-through	34	Six-tube truss	50	345	850	22,24, 26
5	Yellow River Bridge[2]	Hekou to Long Kou, China	Under construction	380	5	Catenary	Deck	28	Four-tube truss	50	N/A	1500	N/A

No.	Name	Location	Year	Span (m)	*l*/*f*	Arch profile	Bridge type	Width (m)	Arch cross section				
									Shape	$f_{ck\text{-}cube}$ (MPa)	f_y (MPa)	D (mm)	t_s (mm)
6	Mao Cao Jie Bridge	Hu Nan, China	2005	368	5	Catenary	Half-through	16	Four-tube truss	50	345	1000	18,22, 28
7	Ya Ji Sha Bridge	Guang Zhou, China	2000	360	4.5	Catenary	Half-through	36.5	Six-tube truss	50	345	750	18,20
8	Wu Jiang Bridge (I) [3]	Chong Qing, China	N/A	360	4	N/A	N/A	22	Five-tube cluster	N/A	N/A	N/A	N/A
9	Yong He Bridge	Guang Xi, China	2004	338	4.5	Parabolic	Through	35	Horizontal dumbbell truss	50	345	1220	16,25
10	Xiao He Bridge[4]	Hu Bei, China	2009	338	5	Catenary	Deck	12.5	Six-tube truss	60	345	1100	16,28, 32
11	Tai Ping Hu Bridge	An Hui, China	2008	336	4.94	Catenary	Half-through	30.8	Horizontal dumbbell truss	50	345	1280	20,25
12	Nan Pu Bridge	Zhe Jiang, China	2003	308	5.5	Catenary	Half-through	12	Horizontal dumbbell truss	50	345	850	12,16
13	Xin Cheng Bridge	Zhe Jiang, China	2005	300	N/A	Catenary	Through	24.5	Truss	50	345	850	12
14	Meixi He Bridge	Chong Qing,China	2001	288	5	Catenary	Deck	17.5	Four-tube truss	60	345	920	14
15	Han Jiang 3rd Bridge	Hu Bei, China	2000	280	5	Catenary	Through	19	Four-tube truss	50		1000	12

No.	Name	Location	Year	Span (m)	*l*/*f*	Arch profile	Bridge type	Width (m)	Arch cross section				
									Shape	$f_{ck\text{-}cube}$ (MPa)	f_y (MPa)	D (mm)	t_s (mm)
16	Dong Guan Waterway Bridge	Guang Dong, China	2005	280	5	Catenary	Half-through	19.5	Horizontal dumbbell truss	50	345	1000	16,18
17	San An Yong Jiang Bridge	Guang Xi, China	1998	270	5	Catenary	Half-through	32.8	Horizontal dumbbell truss	50	345	1020	12,14
18	San Menkou North Gate Bridge	Zhe Jiang, China	2006	270	5	Catenary	Half-through	22	Four-tube truss	50	N/A	800	16,24
19	San Menkou Middle Gate Bridge	Zhe Jiang, China	2006	270	5	Catenary	Half-through	22	Four-tube truss	50	N/A	800	16,24
20	Rong Zhou Bridge	Si Chuan, China	2004	260	4.5	Catenary	Half-through	22.5	Four-tube truss	50	N/A	1020	16
21	Song ao Bridge[5]	Zhe Jiang, China	2007	260	5.44	Catenary	Half-through	20.49	Four-tube truss	50	345	800	14,20
22	Jing Yang He Bridge[6]	Hu Bei, China	2008	260	5	Catenary	Deck	9	Four-tube truss	50	235	1020	14
23	N/A[7]	N/A	N/A	260	3.8	Catenary	N/A	N/A	Four-tube truss	60	N/A	1220	22
24	Qingan He Bridge	Hu Bei, China	2002	256	4.95	Catenary	Half-through	11	Four-tube truss	50	345	1000	12
25	Qu Jiang Bridge[8]	Si Chuan, China	Under construction	256	4.5	Catenary	Half-through	21	Four-tube truss	50	N/A	920	16,18

No.	Name	Location	Year	Span (m)	*l*/*f*	Arch profile	Bridge type	Width (m)	Arch cross section				
									Shape	$f_{ck\text{-}cube}$ (MPa)	f_y (MPa)	D (mm)	t_s (mm)
26	Jiu Long Jiang Bridge	Fu Jian, China	Under construction	254	N/A	N/A	Half-through	38.5	N/A	N/A	N/A	N/A	N/A
27	Qian Island Lake Bridge	Zhe Jiang, China	2006	252	6.5	Catenary	Deck	23	Horizontal dumbbell truss	50	345	1000	20
28	Wu Jiang Bridge (II) [3]	Chong Qing, China	N/A	250	4	N/A	N/A	22	Five-tube cluster	N/A	N/A	N/A	N/A
29	Jian Tiao Bridge	Zhe Jiang, China	2001	245	5	Parabolic	Half-through	21	Horizontal dumbbell truss	50	345	800	14
30	Luo Jiao He Bridge	Gui Zhou, China	1998	240	4	N/A	Half-through	13.5	Five to four tube cluster	40	235	1200	12
31	Jiang Han 5th Bridge[9]	Hu Bei, China	2000	240	5	Catenary	Half-through	27	Horizontal dumbbell truss	50	345	1000	14
32	Xin Long Men Bridge	Si Chuan, China	2010	240	5	Catenary	Half-through	N/A	Horizontal dumbbell truss	50	345	1000	14
33	Tong Wa Men Bridge	Zhe Jiang, China	2001	238	4.82	Parabolic	Half-through	10	Two-tube truss	50	345	1150	12,14, 16
34	Bei Pan Jiang Bridge	Gui Zhou, China	2001	236	4	Catenary	Deck	7	Horizontal dumbbell truss	50	345	1000	16

No.	Name	Location	Year	Span (m)	*l*/*f*	Arch profile	Bridge type	Width (m)	Arch cross section				
									Shape	$f_{ck\text{-}cube}$ (MPa)	f_y (MPa)	D (mm)	t_s (mm)
35	Xu Zhou Jing Hang Canal Bridge	Jiang Su, China	2002	235	4	Catenary	Half-through	33.5	Four-tube truss	50	345	850	14
36	Second Saikai Bridge[10]	Japan	2006	230	4.79	N/A	Half-through	20.2	Three-tube truss	N/A	N/A	812.8	50
37	Sheng Mi Bridge	Jiang Xi, China	2005	228	4.5	Parabolic	Half-through	39	Horizontal dumbbell truss	50	345	900	20
38	Pu Shan Bridge[11]	He Nan, China	2009	225	5.14	Parabolic	Through	38.8	Six-tube truss	N/A	N/A	1000	16,18
39	Yu Jiang Bridge	Guang Xi, China	1999	220	5	Catenary	Half-through	25.1	Four-tube truss	50	345	820	12,14
40	Nan Nidu Bridge	Hu Bei, China	2002	220	5	Catenary	Deck	13	Four-tube truss	50	345	920	14
41	Long Tan He Bridge	Hu Bei, China	1999	208	4.94	Catenary	Half-through	11	Horizontal dumbbell truss	50	345	900	14
42	Meng Jiang Bridge	Si Chuan, China	N/A	206	N/A	N/A	Half-through	28	Four-tube truss	N/A	N/A	N/A	N/A
43	Fu Jiang Bridge	Si Chuan, China	1997	202	4.5	Parabolic	Half-through	26.5	Four-tube truss	40	N/A	N/A	N/A
44	Moon Island Bridge	Liao Ning, China	2003	202	5.46	Parabolic	Through	12.5	Two-tube truss	50	345	1100	12
45	N/A	Si Chuan, China	N/A	202	4.5	Catenary	Half-through	15.2	Four-tube truss	N/A	N/A	850	N/A
46	San Shan Xi Bridge	Guang Dong, China	1995	200	4.5	Catenary	Half-through	28	Four-tube truss	40	345	750	10

No.	Name	Location	Year	Span (m)	*l*/*f*	Arch profile	Bridge type	Width (m)	Arch cross section				
									Shape	$f_{ck\text{-}cube}$ (MPa)	f_y (MPa)	D (mm)	t_s (mm)
47	Jia Ling Jiang Bridge	Chong Qing, China	2002	200	4	Catenary	Half-through	23	Four-tube truss	50	345	760	13
48	You Shui He Bridge	Hu Nan, China	2003	200	5	Catenary	Half-through	N/A	Horizontal dumbbell truss	50	345	750	12
49	Hu Tuo He Bridge	He Bei, China	2010	200	N/A	N/A	Half-through	51.9	Horizontal dumbbell truss	N/A	N/A	N/A	N/A
50	Shen Xi Gou Bridge[12]	Si Chuan, China	2007	192	4.5	Catenary	Half-through	14.3	Four-tube truss	50	345	850	18
51	Yan He Bridge	Shan Xi, China	1998	190	6	Catenary	Half-through	25	Horizontal dumbbell truss	50	345	750	10
52	Na Mo Yong Jiang Bridge	Guang Xi, China	2002	190	4.5	Catenary	Half-through	26.8	Four-tube truss	50	345	820	12
53	Qian Jiang 4th Bridge	Zhe Jiang, China	2004	190	4	Parabolic	Through	32	Horizontal dumbbell truss	50	345	950	22
54	Tao Jia Du Bridge	Si Chuan, China	2005	190	4.5	Catenary	Half-through	24.1	Horizontal dumbbell truss	40,50	N/A	750	12
55	Gan Jiang Bridge	Jiang Xi, China	2005	188	3.3	Catenary	Half-through	28	Three-tube truss	50	345	1000 750	16 12

No.	Name	Location	Year	Span (m)	*l*/*f*	Arch profile	Bridge type	Width (m)	Arch cross section				
									Shape	$f_{ck\text{-}cube}$ (MPa)	f_y (MPa)	D (mm)	t_s (mm)
56	Cao E Jiang Bridge	Hu Nan, China	Under construction	185	4	Parabolic	Half-through	43	Four-tube truss	50	345	900	16
57	Qi Jia Du Yellow River Bridge[13]	Gan Su, China	2009	180	5	Catenary	Deck	12	Horizontal dumbbell truss	50	345	700	12
58	Zhenjiang Jing Hang Canal Bridge[14]	Xu Zhou to Shang Hai, China	2010	180	5	Parabolic	Through	11.9	Dumbbell	N/A	N/A	1100	20
59	Jinkou He Dadu He Bridge	Si Chuan, China	1999	175	5	N/A	Half-through	25	Horizontal dumbbell truss	N/A	N/A	700	10,12
60	Gui Jiang 3rd Bridge	Guang Xi,China	2000	175	4	Catenary	Half-through	25.6	Horizontal dumbbell truss	50	345	750	14
61	Huaxi No.1 Bridge[15]	Gui Zhou, China	2009	175	4.38	Catenary	Half-through	29.5	Three-tube truss	50		1000 700	30,34 20,24
62	Li Jiang Bridge	Guang Xi, China	2003	170	4.5	Catenary	Half-through	44.5	Horizontal dumbbell truss	50	345	711	13
63	Nan Huan Bridge	He Bei, China	2005	170	4.72	Catenary	Half-through	28	Horizontal dumbbell truss	45	345	750	15
64	Wu Lie He Rainbow Bridge	He Bei, China	2010	170	N/A	N/A	Half-through	28	N/A	N/A	N/A	N/A	N/A

No.	Name	Location	Year	Span (m)	*l*/*f*	Arch profile	Bridge type	Width (m)	Arch cross section				
									Shape	$f_{ck\text{-}cube}$ (MPa)	f_y (MPa)	D (mm)	t_s (mm)
65	Heng Meng Road Bridge Crossing Railway Station	Hu Nan, China	Under construction	168	4.5	Catenary	Through	28.6	Horizontal dumbbell truss	50	345	800	14,20
66	Hei Shi Pu Xiang Jiang Bridge	Hu Nan, China	2004	162	4	Parabolic	Half-through	34	Horizontal dumbbell truss	50	345	1000	14
67	Huang Bai He Bridge	Hu Bei, China	1996	160	5	Catenary	Deck	18.5	Dumbbell	50	345	1000	10,12
68	Xia Lao Xi Bridge	Hu Bei, China	1996	160	5	Catenary	Deck	18.5	Dumbbell	50	345	1000	10,12
69	Jiu Wan Xi Bridge	Hu Bei, China	1998	160	6	Catenary	Deck	10	Dumbbell	40	235	1000	12
70	Mao Zi Ping Da Du He Bridge	Si Chuan, China	1999	160	N/A	N/A	Half-through	14.1	Four-tube truss	N/A	N/A	600	14
71	Da Xian Zhou He Bridge	Si Chuan, China	2001	160	N/A	N/A	Half-through	N/A	N/A	N/A	N/A	N/A	N/A
72	Dong Yang Zhong Shan Bridge	Zhe Jiang, China	2002	160	5	Parabolic	Half-through	22	Four-tube truss	50	N/A	750	14
73	Chao Zhou Jin Shan Bridge	Guang Dong, China	2007	160 114	4.66	Parabolic	Half-through	26	Dumbbell	50	345	1200 950 800	24 22 20

No.	Name	Location	Year	Span (m)	*l*/*f*	Arch profile	Bridge type	Width (m)	Arch cross section				
									Shape	$f_{ck\text{-}cube}$ (MPa)	f_y (MPa)	*D* (mm)	t_s (mm)
74	Bin Hai Road 4th Bridge[16]	Liao Ning, China	N/A	160	4.32	Parabolic	Half-through	18.5	Obround, Single Circular	40	345	1500×3200 2000	25 25
75	Yi Tong He Bridge	Ji Lin, China	2009	158	4.23	Parabolic	Half-through	40	Single Circular	50	345	1800	28
76	Jun Zhou Bridge	Jiang Xi, China	2003	156	4.5	Catenary	Half-through	17.2	Horizontal dumbbell truss	50	345	750	12
77	Yun Zao Bang Bridge	Shang Hai, China	2007	156	5	N/A	Through	N/A	N/A	N/A	N/A	N/A	N/A
78	Ci Du Bridge	Jiang Xi, China	1997	150	5	Parabolic	Half-through	21	Dumbbell	N/A	235	1000	14
79	Gao Gu Wu Jiang Bridge	Si Chuan, China	1997	150	5	Catenary	Half-through	12	Horizontal dumbbell truss	50	235	600	10
80	Ming Cheng Bridge	Si Chuan, China	1998	150	5	N/A	Through	18	Four-tube truss	N/A	N/A	610	10
81	Kong Quehe Bridge	Xin Jiang, China	1998	150	4.5	N/A	Half-through	24.5	Four-tube truss	40	N/A	600	10
82	Shen Zhen Rainbow Bridge	Guang Dong, China	2000	150	4.5	Catenary	Through	23.5	Four-tube truss	50	345	750	12
83	Pan Jia He Bridge	Shan Xi, China	2003	150	4.5	N/A	Half-through	N/A	Horizontal dumbbell truss	40	N/A	600	10
84	Hai Kou Bridge	Yun Nan, China	2006	150	4.5	Catenary	Half-through	25.5	Four-tube truss	50	N/A	700	12,14

No.	Name	Location	Year	Span (m)	*l*/*f*	Arch profile	Bridge type	Width (m)	Arch cross section				
									Shape	$f_{ck\text{-}cube}$ (MPa)	f_y (MPa)	D (mm)	t_s (mm)
85	Xi Yang Ping Bridge	Fu Jian, China	2007	150	5	Catenary	Half-through	33	Truss	50	345	850	14,16
86	Wei Fang Wei He Bridge[17]	Shan Dong, China	2008	145	3.7	N/A	Through	N/A	Dumbbell	50	345	1500	N/A
87	Tian Jin Road Canal Bridge	Jiang Su, China	2007	143	N/A	N/A	Half-through	32	N/A	N/A	N/A	N/A	N/A
88	Hua Gang Bridge	Zhe Jiang, China	2000	141	5	Catenary	Half-through	N/A	Dumbbell	40	235	1020	12
89	E Bian Da Du He Bridge	Si Chuan, China	1995	140	5	Catenary	Through	13.5	Horizontal dumbbell truss	40	N/A	550	8
90	Xia Menkou Wu Jiang Bridge	Si Chuan, China	1996	140	4	N/A	Half-through	13.5	Five to four tube cluster	40	235	700	8
91	Hun He Chang Qing Bridge	Liao Ning, China	1997	140	4	Catenary	Half-through	32.5	Four-tube truss	50	345	700	10
92	Pu Bu Gou Bridge	Si Chuan, China	2004	140	5	Catenary	Half-through	14	Horizontal dumbbell truss	50	N/A	760	12
93	Wen Feng Road Overpass	He Nan, China	1995	138	5	Catenary	Through	31.4	Truss	40	345	720	12
94	Shi Tan Xi Bridge	Fu Jian, China	1997	136	5	Catenary	Half-through	13.1	Four-tube truss	40	235	550	8

No.	Name	Location	Year	Span (m)	*l*/*f*	Arch profile	Bridge type	Width (m)	Arch cross section				
									Shape	$f_{ck\text{-}cube}$ (MPa)	f_y (MPa)	D (mm)	t_s (mm)
95	Sheng Zhou Cao EZhe Jiang Bridge	Jiang, China	2004	136	5	Parabolic	Through	36	Dumbbell	50	345	750	14,16
96	Ge Chou Gou Bridge[18]	Shan Xi, China	Under construction	136	N/A	N/A	Through	N/A	Dumbbell	N/A	235	1100	N/A
97	Cheng Jiang Town Bridge[3]	Chong Qing, China	N/A	135	4	N/A	N/A	14	Five tube cluster	N/A	N/A	N/A	N/A
98	Qing Long Chang Overpass	Si Chuan, China	1997	132	5	Catenary	Through	30.7	Dumbbell	50	235	1100	12
99	La Xi Wa Yellow River Bridge	Qing Hai, China	2003	132	6.5	Catenary	Deck	14.5	Dumbbell	50	345	1000	12
100	Hua Qing Bridge	Jiang Su, China	2005	132	4	Catenary	Through	40	Dumbbell	50	N/A	1500	16
101	Chang Feng Bridge	Zhe Jiang, China	2009	132	N/A	Parabolic	Through	41.2	Single circular	N/A	N/A	N/A	N/A
102	Fu He Bridge	Si Chuan, China	2001	130	4	Catenary	Half-through	40.84	Dumbbell	50	N/A	920	12
103	Nan He Bridge	Jiang Su, China	2003	130	5	Parabolic	Through	15.25	Dumbbell	40	345	1100	14
104	Long He Bridge	N/A	N/A	130	3	N/A	N/A	20	Five tube cluster	N/A	N/A	N/A	N/A
105	Gao Yang Bridge[19]	Hu Bei, China	Under construction	129.5	3.5	Catenary	Half-through	17.5	Four-tube truss	50	345	351	12,16
106	Ping Wei Bridge	Guang Xi, China	2000	128	4	Catenary	Half-through	14.5	Dumbbell	40	345	920	12

No.	Name	Location	Year	Span (m)	*l*/*f*	Arch profile	Bridge type	Width (m)	Arch cross section				
									Shape	$f_{ck\text{-}cube}$ (MPa)	f_y (MPa)	D (mm)	t_s (mm)
107	Gong Boxia Yellow River Bridge	Qing Hai, China	2001	128	4	Catenary	Half-through	16.2	Dumbbell	50	345	1200	N/A
108	Da Fenbei Waterway Bridge	Guang Dong, China	2005	128	5	Catenary	Through	24	Two-tube truss	50	345	1050	14
109	Shi Tan Bridge[20]	Guang Dong, China	N/A	128	5	N/A	Half-through	30.8	Dumbbell	50		1200	14
110	Bai Nihe Bridge[21]	Guang Dong, China	N/A	128	5	Parabolic	Through	11	Dumbbell	N/A	N/A	N/A	N/A
111	Yan Yan Yellow River Bridge	Gan Su, China	2003	127	5	Parabolic	Through	16.75	Dumbbell	50	345	1200	14
112	Nian Yuwan 22# Oil Berth Bridge[22]	Liao Ning, China	2010	126	N/A	N/A	Through	N/A	N/A	N/A	N/A	N/A	N/A
113	Arco del Escudo Bridge[23]	Spain	N/A	126	8.24	N/A	Deck	N/A	Horizontal two tube truss	N/A	N/A	N/A	N/A
114	Zhong Shan 2nd Bridge[24]	Guang Dong, China	1995	125	5	N/A	Half-through	N/A	Box shaped	30	235, 345	250×250 250×350	N/A
115	Hong Fu Road Bridge	Guang Dong, China	2003	125	5	Catenary	Through	32	Dumbbell	50	345	1200	20

No.	Name	Location	Year	Span (m)	*l*/*f*	Arch profile	Bridge type	Width (m)	Arch cross section				
									Shape	$f_{ck\text{-}cube}$ (MPa)	f_y (MPa)	*D* (mm)	t_s (mm)
116	Tianzi Shan Bridge[25]	Hu Nan, China	2003	125	5	Catenary	Deck	12	Dumbbell	50	345	1000	12
117	Da Zhihe Bridge[26]	Shanghai, China	2009	125	5	Parabolic	Through	21.2	Dumbbell	50	345	1000	16
118	Rizhao-Yizheng Oil Pipeline Accessory Approach Bridge	Shan Dong, China	Under construction	125	6	N/A	Through	N/A	N/A	N/A	N/A	N/A	N/A
119	Ye Sanhe Bridge[27]	Hu Bei, China	2008	124	4.4 3.5	Catenary	Half-through Through	13.1	Four-tube truss	50	N/A	800	16,20 ,24
120	Hua Zhou Bridge[28]	Guang Xi, China	2008	123	N/A	Parabolic	Half-through	15.5	Single circular	50	345	1580	24,26
121	Cao Feidian Oil Discharging Dock Trestle	Hebei, China	2007	122	6	N/A	N/A	9.95	N/A	N/A	N/A	N/A	N/A
122	Wang Jiang Bridge	Zhe Jiang, China	1994	120	4	Parabolic	Half-through	10	Dumbbell	40	345	800	10,12 ,14
123	Shuhe Han Jiang Bridge	Shan Xi, China	1997	120	5	Catenary	Half-through	13	Dumbbell	40	235	820	12
124	Tai He Bridge	Zhe Jiang, China	1998	120	N/A	N/A	Half-through	20	N/A	N/A	N/A	N/A	N/A
125	Qin Bridge	Zhe Jiang, China	2001	120	5	Parabolic	Through	33	Obround	40	345	3300×2000	N/A
126	Yang Jiagou Bridge	Si Chuan, China	2001	120	N/A	N/A	Half-through	N/A	N/A	N/A	N/A	N/A	N/A

No.	Name	Location	Year	Span (m)	*l*/*f*	Arch profile	Bridge type	Width (m)	Arch cross section				
									Shape	$f_{ck\text{-}cube}$ (MPa)	f_y (MPa)	D (mm)	t_s (mm)
127	Moshan Overpass	Jiang Xi, China	2003	120	5	Catenary	Through	18.7	Dumbbell	50	345	1100	14
128	Wuchang Yu Bridge	Hu Bei, China	2003	120	6	Catenary	Through	24	Dumbbell	50	345	1100	14
129	Nanpu Hong Bridge[29]	Hu Bei, China	2003	120	6	Catenary	Through	24	Dumbbell	50	345	1100	14
130	Jiang Wan Bridge	Ji Lin, China	2004	120	5	Catenary	Half-through	31	Four-tube truss	40	345	700	14
131	Zhong Shan 1st Bridge[30]	Guang Dong, China	2004	120 100	6 3.8	Parabolic	Through Half-through	40	Obround	N/A	N/A	1400×2200 1200×1800 1200×2200	N/A
132	Lu Jia Zhi Bridge	Zhe Jiang, China	2005	120	N/A	N/A	Through	N/A	N/A	N/A	N/A	N/A	N/A
133	Chao Yang East Bridge	Liao Ning, China	2005	120	4.5	Catenary	Half-through	26	Four-tube truss	50	345	700	14
134	Cai Ling Road Bridge	Jiang Su, China	2006	120	3.75	Parabolic	Half-through	35.8	Dumbbell	50	345	1100	20
135	Dong Fang Bridge[31]	Jiang Su, China	2007	120	3.75	Parabolic	Half-through	32	Dumbbell	50	345	1100	20
136	Yang He Bridge[32]	Jiang Su, China	2008	120	6	Parabolic	Through	N/A	Dumbbell	40	N/A	1000	14
137	Ying Zhou Bridge[33]	He Nan, China	2009	120	3.5	N/A	Half-through	N/A	Three tube truss	50	345	1500	20
138	Kang Funan Road Bridge	Hu Nan, China	2006	120	4.44	N/A	Through	N/A	Dumbbell	50	N/A	1200	10
139	Mo Zi Wan Bridge	Si Chuan, China	N/A	120	5.5	Catenary	Half-through	7.5	Dumbbell	N/A	N/A	800	12

No.	Name	Location	Year	Span (m)	*l*/*f*	Arch profile	Bridge type	Width (m)	Arch cross section				
									Shape	$f_{ck\text{-}cube}$ (MPa)	f_y (MPa)	*D* (mm)	t_s (mm)
140	Ling Hu Bridge	Zhe Jiang, China	Under construction	120	5	Parabolic	Through	32	Obround	50	345	3500×1500	N/A
141	Bin Hai Road 1st Bridge[34]	Liao Ning, China	N/A	120	N/A	Catenary	N/A	N/A	Dumbbell	N/A	N/A	N/A	N/A
142	Bridge Crossing Neiyi Railway	Si Chuan, China	N/A	120	N/A	N/A	Half-through	N/A	N/A	N/A	N/A	N/A	N/A
143	Bridge Crossing Ying Sha Railway[35]	Fu Jian, China	N/A	118	4	Catenary	Through	N/A	N/A	40	N/A	N/A	N/A
144	Luan He Bridge	He Bei, China	2007	116	N/A	N/A	Half-through	N/A	N/A	N/A	N/A	N/A	N/A
145	Wang Cang East River Bridge	Si Chuan, China	1990	115	5	Catenary	Through	13	Dumbbell	30	235	800	10
146	Lian Tuo Bridge	Hu Bei, China	1996	114	3	Catenary	Half-through	20	Dumbbell	50	345	1200	14
147	Fo Chen Bridge	Guang Dong, China	1994	113	5	Catenary	Through	26	Dumbbell	30	345	1000	14
148	Dong Shao Xi Bridge	Zhe Jiang, China	2005	112	5	Catenary	Through	16	Dumbbell	50	345	1000	16
149	Jiu Qu He Bridge[36]	Jiang Su, China	2007	112	5	N/A	Through	N/A	Dumbbell	50	N/A	1000	14
150	Hu Jia Wan Bridge[37]	Hu Bei, China	2009	112	5	Catenary	Through	16.2	Dumbbell	55	N/A	1200	18

No.	Name	Location	Year	Span (m)	*l*/*f*	Arch profile	Bridge type	Width (m)	Arch cross section				
									Shape	$f_{ck\text{-}cube}$ (MPa)	f_y (MPa)	D (mm)	t_s (mm)
151	Hua Cheng Bridge	Liaoning, China	1998	110	5	Parabolic	Half-through	7.5	Two tube truss	50	345	600	8,10
152	Yu Feng Bridge[38]	Jiang Su, China	2004	110	5.5	Parabolic	Half-through	24	Three tube truss	N/A	N/A	1100	N/A
153	Ling Jiang 3rd Bridge	Zhe Jiang, China	Under construction	110	N/A	N/A	Half-through	N/A	N/A	N/A	N/A	N/A	N/A
154	An Ning He Bridge	Si Chuan, China	N/A	110	5	Catenary	Half-through	9	Dumbbell	50	N/A	N/A	N/A
155	Wen Hui Bridge	Guang Xi, China	1995	108	4	Catenary	Half-through	18.5	Dumbbell	N/A	N/A	900	N/A
156	Chao Bai He Bridge	Bei Jing, China	1999	108	5	Circle	Half-through	27	Dumbbell	50	345	1000	14
157	Zhou Jia Gou 1st Bridge	He Bei, China	2000	108	5	Catenary	Deck	27	Dumbbell	50	345	1000	16
158	Zi Jiang 3rd Bridge	Hu Nan, China	2001	108	4	Parabolic	Half-through	24.5	Dumbbell	50		1300	14
159	Qiong Zhou Bridge	Hai Nan, China	2003	108	4.5	Parabolic	Through	23	Dumbbell	40	345	1100	14,16
160	Nian Yu Wan Trestle[39]	Liao Ning, China	2004	108	6	N/A	Through	N/A	Two tube truss	50	345	800	12
161	La Sa He Bridge[40]	Tibet, China	2005	108	N/A	N/A	Through	N/A	Tow tube truss	N/A	N/A	900	N/A
162	Si Ma Xiang Bridge	Zhe Jiang, China	2006	108	4	Parabolic	Half-through	24	Dumbbell	40	N/A	850	16
163	Nan Xi Jiang Bridge	Zhe Jiang, China	1999	105	5	Catenary	Through	14.4	Dumbbell	40	235	800	10
164	Tai Cang Tang Bridge	Jiang Su, China	2007	105	N/A	N/A	Half-through	36.5	N/A	N/A	N/A	N/A	N/A
165	Jin Gang Bridge	Tian Jin, China	1996	101	5	Parabolic	Half-through	18.4	Dumbbell	40	N/A	900	14

No.	Name	Location	Year	Span (m)	l/f	Arch profile	Bridge type	Width (m)	Arch cross section				
									Shape	$f_{ck\text{-}cube}$ (MPa)	f_y (MPa)	D (mm)	t_s (mm)
166	Xie Gang Bridge	Jiang Su, China	1995	100.5	7	Parabolic	Through	19.5	Obround	N/A	235	2000×900	10
167	Gao Ming Bridge	Guang Dong, China	1991	100	4	Catenary	Half-through	12	Dumbbell	30	235	750	10
168	Chang'an University Footbridge[41]	Shan Xi, China	1995	100	9.6	Parabolic	Half-through	N/A	Single circular	30	235	650	10
169	Yuan Shui Bridge	Hu Nan, China	1996	100	3	Catenary	Half-through	N/A	Three tube cluster	40	N/A	N/A	N/A
170	Mu Dan Jiang Bridge	Hei Long Jiang, China	1997	100	4	Catenary	Half-through	11.8	Three tube truss	50	345	600	12
171	Hong Zhou Bridge	Si Chuan, China	1999	100	4	Parabolic	Half-through	16	Three tube cluster	40	235	1200	10
												700	8
172	Yang En University Footbridge	Fu Jian, China	2002	100	5	Catenary	Half-through	5.5	Dumbbell	N/A	N/A	500	8
173	Yang Ma Island Bridge[42]	Shan Dong, China	2004	100	5	Parabolic	Through	28.2	Dumbbell	50	345	1200	16
174	Zheng Zhou Yellow River 2nd Bridge	He Nan, China	2004	100	4.5	Catenary	Through	24.4	Dumbbell	50	345	1000	16
175	Xiang Wang Bridge	Jiang Su, China	2005	100	N/A	N/A	Through	28.2	Dumbbell	N/A	N/A	1100	14
176	Yin Zhou Bridge	Zhe Jiang, China	2005	100	N/A	Parabolic	Half-through	43	Dumbbell	55	345	800	14
177	Wu Chi Gou Bridge[43]	Shang Hai, China	2005	100	4	N/A	Through	37.1	Obround	N/A	N/A	1600×2600	16

No.	Name	Location	Year	Span (m)	*l*/*f*	Arch profile	Bridge type	Width (m)	Arch cross section				
									Shape	$f_{ck\text{-}cube}$ (MPa)	f_y (MPa)	D (mm)	t_s (mm)
178	Han Zhong Qiao Zha Bridge	Shan Xi, China	2006	100	N/A	Catenary	Through	28.1	Dumbbell	N/A	N/A	1000	N/A
179	Shu Yuan He Bridge	He Bei, China	2007	100	N/A	N/A	Half-through	55	N/A	N/A	N/A	N/A	N/A
180	Fu Ning Road 2nd Bridge[44]	Fu Jian, China	2009	100	5	Parabolic	Through	49	N/A	50	N/A	600	10
181	Yang Mei Bridge[45]	Fu Jian, China	2009	100	4.5	Parabolic	Through	21.4	Dumbbell	50	235	1100	14
182	Xuan Tian Bridge	Yun Nan, China	Under construction	100	5	N/A	Through	16.7	Truss	50	N/A	1200	16
183	Ci Cheng Bridge[46]	Zhe Jiang, China	N/A	100	6	Parabolic	Through		Dumbbell	N/A	N/A	N/A	N/A
184	He Chang Bridge[47]	Fu Jian, China	N/A	100	5	Catenary	Half-through	5.5	Dumbbell	40	345	500	8
185	Kuo Kou Bridge	Fu Jian, China	2004	99	5	Parabolic	Through	16.35	Dumbbell	40	235	800	14
186	Xiang Jiang Road Bridge	Hu Nan, China	2001	98	4	Parabolic	Half-through	16	Dumbbell	40	235	900	12
187	Yuan Zhou Bridge	Jiang Xi, China	1996	96	5	Catenary	Half-through	22.7	Dumbbell		345	850	12
188	Dan Tai Hu Bridge	Jiang Su, China	2003	96	N/A	N/A	Through	N/A	N/A	N/A	N/A	N/A	N/A
189	Bao An Rainbow Bridge[48]	Shan Xi, China	2008	96	4	Catenary	Half-through	14	Dumbbell	45	345	900	16
190	Hui He Bridge[49]	An Hui, China	Under construction	96	5	Catenary	Through	N/A	Dumbbell	N/A	N/A	1000	16
191	N/A	N/A	N/A	96	5	Parabolic	N/A	13.2	Dumbbell	N/A	N/A	1100	16

No.	Name	Location	Year	Span (m)	*l*/*f*	Arch profile	Bridge type	Width (m)	Arch cross section				
									Shape	$f_{ck\text{-}cube}$ (MPa)	f_y (MPa)	D (mm)	t_s (mm)
192	Cao Fei Dian Ore Dock Trestle	He Bei, China	2005	94	N/A	N/A	Through	17.6	N/A	N/A	N/A	800	12
193	Long Tun Overpass	Guang Xi, China	2004	92.5	4.5	Catenary	Through	24	Dumbbell	N/A	345	900	20
194	Qing Fang Bridge	Zhe Jiang, China	1994	92	4	Parabolic	Through	28.4	Dumbbell	40	N/A	900	12
195	Zheng Zhou Yellow River Railway Bridge Approach Bridge[50]	He Nan, China	N/A	92	5	N/A	Through	N/A	Two tube truss	50	N/A	1000	20
196	Hua Bu Bridge	Zhe Jiang, China	N/A	90.5	N/A	N/A	Half-through	12.8	N/A	N/A	N/A	N/A	N/A
197	Ming Xuan Bridge	Fu Jian, China	1995	90	4.5	Parabolic	Half-through	14	Dumbbell	N/A	N/A	800	10
198	Ji Nan Viaduct Dong Zhan Overpass	Shan Dong, China	1998	90	5	Catenary	Through	25.5	Four tube truss	50	345	650	10
199	Yi He Bridge	Shan Dong, China	1998	90	5	Parabolic	Through	19	Dumbbell	40	N/A	750	10
200	Xi Xia Bridge	Jiang Su, China	1999	90	4.5	Parabolic	Through	34	Obround	40	345	2400×1200	20
201	Ma Gang Bridge	Guang Dong, China	1999	90	4	Parabolic	Through	18	Dumbbell	N/A	345	800	12
202	Xi Yi Jing Hang Canal Bridge	Jiang Su, China	2002	90	5	Parabolic	Through	16.05	Dumbbell	50	345	1000	14

No.	Name	Location	Year	Span (m)	*l*/*f*	Arch profile	Bridge type	Width (m)	Arch cross section				
									Shape	$f_{ck\text{-}cube}$ (MPa)	f_y (MPa)	D (mm)	t_s (mm)
203	Bei Chuan He Bridge[51]	Qing Hai, China	2002	90	5	Catenary	Half-through	25.5	Four tube truss	50	345	650	10
204	Li Shui Taxia Bridge	Zhe Jiang, China	2004	90	N/A	N/A	Through	25.5	Dumbbell	N/A	N/A	N/A	N/A
205	Viaduct Crossing Hu Hang Yong Road	Zhe Jiang, China	2004	90	4	Catenary	Half-through	29	Dumbbell	50	345	900	16
206	Bridge Crossing Hang Yong Canal	Zhe Jiang, China	2006	90	N/A	N/A	Through	29	N/A	N/A	N/A	N/A	N/A
207	Qing Xi He Bridge[52]	Hu Bei, China	2008	90	6	Parabolic	Through	N/A	Dumbbell	N/A	N/A	N/A	N/A
208	Shang Zhai 2nd Viaduct[53]	Guang Dong, China	2010	90	7	Parabolic	Deck	N/A	Dumbbell	50	N/A	1000	14
209	Feng Huang Shan Bridge[54]	Zhe Jiang, China	2006	88	4	Catenary	Through	N/A	Dumbbell	40	N/A	800	14
210	Jiang Nan Gong Tie Overpass	Ji Lin, China	2000	85	3.5	Catenary	Half-through	30.5	Four-tube truss	N/A	345	402	11
211	Yun Zao Bang Bridge	Shang Hai, China	2004	85	5	Parabolic	Through	40	Obround	40	235	2400×1350	20
212	Zhao Jia Gou Bridge[55]	Shang Hai, China	2004	85	5.67	Parabolic	Through	44.4	Rectangular	N/A	N/A	1400×2000	N/A
213	Xi Ping 3rd Bridge[56]	Zhe Jiang, China	2009	85	4	Catenary	Half-through	19	Dumbbell	50	345	1000	20
214	Yan He Road Bridge[57]	Jin Lin, China	N/A	85	4	Parabolic	Half-through	22	Three tube truss	50	345	650	12

No.	Name	Location	Year	Span (m)	*l*/*f*	Arch profile	Bridge type	Width (m)	Arch cross section				
									Shape	$f_{ck\text{-}cube}$ (MPa)	f_y (MPa)	D (mm)	t_s (mm)
215	Zhang Jia Gang Bridge	Jiang Su, China	N/A	85	N/A	N/A	Through	32	Three tube truss	40	N/A	500	N/A
216	Jin Chuan Bridge	Inner Mongolia, China	2001	84	N/A	Parabolic	Through	45.5	Dumbbell	40	N/A	1100	14
217	Yuan Shi Bridge[58]	Zhe Jiang, China	2002	84	2.447	Parabolic	Through	55	Rectangular	50	N/A	1600×800 1600×1200	8 25
218	Ma Yun Bridge	Jiang Su, China	2003	84	4	N/A	Half-through	38.5	N/A	N/A	N/A	N/A	N/A
219	Wo He 3rd Bridge	An Hui, China	1999	83.98	4	Parabolic	Through	20.9	Dumbbell	40	345	800	12
220	Chu He Bridge[59]	Jiang Su, China	2009	83	5	Parabolic	Through	23	Dumbbell	40	345	750	12
221	Chuan Yang He Bridge[60]	Shang Hai, China	2009	83	N/A	N/A	Through	32.5	Rectangular	N/A	N/A	1600×2000	24,20
222	Gao You 2nd Bridge	Jiang Su, China	2002	82.88	4.65	N/A	Through	12.4	N/A	N/A	N/A	N/A	N/A
223	Jiu Jiu Bridge[61]	Zhe Jiang, China	2007	81.7	N/A	N/A	Through	28	Obround	50	345	2000×1000	N/A
224	Sheng Li Bridge[62]	Inner Mongolia, China	2009	81.3	5	Parabolic	Through	24.2	Dumbbell	50	345	1200	14
225	Yin Shan Bridge	Jiang Su, China	1996	80.5	6	N/A	Through	19.5	Obround	N/A	N/A	N/A	N/A
226	Footbridge crossing the 2nd Ring Road in Fu Zhou City[63]	Fu Jian, China	N/A	80.46	5	Catenary	Half-through	6	Single circular	40	N/A	1300	14
227	Li Yu Jiang Bridge	Hu Nan, China	1994	80	4	Parabolic	Half-through	20.1	Dumbbell	40,50	345	900	10,16

No.	Name	Location	Year	Span (m)	*l*/*f*	Arch profile	Bridge type	Width (m)	Arch cross section				
									Shape	$f_{ck\text{-}cube}$ (MPa)	f_y (MPa)	D (mm)	t_s (mm)
228	Huang Yuan Bridge	Zhe Jiang, China	1995	80	5	Parabolic	Through	29	Obround	40	N/A	2000×800	20
229	Fu Zhou Jie Fang Bridge	Fu Jian, China	1996	80	5	Parabolic	Half-through	14	Dumbbell	N/A	N/A	800	10
230	Bai Ma Shi Liang He Bridge	Si Chuan, China	1996	80	2.5	N/A	Half-through	12.5	Two tube cluster	40	235	N/A	N/A
231	Guang Zhou Jie Fang Bridge	Guang Dong, China	1997	80	5	Parabolic	Through	25	Dumbbell	30	345	950	14
232	Bin Wang Bridge	Zhe Jiang, China	1997	80	5	Parabolic	Through	32.7	Two tube truss	N/A	N/A	1400	16
233	Shan Yang Wa 1st Bridge	Bei Jing, China	1998	80	5	Catenary	Deck	13	Dumbbell	N/A	N/A	750	N/A
234	Lan Xi Bridge	Fu Jian, China	1999	80	5	Parabolic	Through	15	Dumbbell	40	235	800	10
235	Fu Rong Bridge	Shen Zhen, China	2000	80	5	Parabolic	Through	23.5	Dumbbell	50	345	950	14
236	Fu Ding Shan Qian Bridge	Fu Jian, China	2000	80	5	Parabolic	Through	14	Single circular	40	345	1200	16
237	Qing Dao Cheng Yang Overpass	Shan Dong, China	2001	80	5	Parabolic	Through	N/A	Dumbbell	40	235	750	12
238	Jiang Shan Cheng Zhong Bridge	Zhe Jiang, China	2002	80	N/A	N/A	Half-through	22	Dumbbell	40	N/A	850	12

No.	Name	Location	Year	Span (m)	*l*/*f*	Arch profile	Bridge type	Width (m)	Arch cross section				
									Shape	$f_{ck\text{-}cube}$ (MPa)	f_y (MPa)	D (mm)	t_s (mm)
239	Bai Qi Hu Bridge	Fu Jian, China	2006	80	5	Catenary	Through	21.2	Dumbbell	50	345	900	14
240	Feng Hui Bridge[64]	Zhe Jiang, China	2007	80	4	Parabolic	Through	N/A	Dumbbell	50	345	800	14
241	San Dian Tang Bridge[65]	Zhe Jiang, China	2007	80	5	Parabolic	Through	17	Rectangular	N/A	N/A	1200×2000	16
242	Yue Hai Bridge[66]	Ning Xia, China	2008	80 80 30	2.5 3 5	Parabolic	Through	10.8	Dumbbell	N/A	N/A	650	16
243	Tong Yang Canal Bridge[67]	Jiang Su, China	2009	80	5	Parabolic	Through	19.4	Dumbbell	40	345	750	14
244	Jia Li Chen Bridge	Zhe Jiang, China	2004	80	5	Parabolic	Through	21	Dumbbell	N/A	N/A	800	20
245	N/A[68]	China	N/A	80	4	Parabolic	Half-through	22	Dumbbell	40	345	850	14
246	Hai Hu Bridge	Qing Hai, China	N/A	80	N/A	N/A	Half-through	N/A	N/A	40	N/A	1600	N/A
247	N/A[69]	China	N/A	80	5	Parabolic	Through	N/A	Obround	50	N/A	1800×1400	20
248	Xin Tang Bridge	Zhe Jiang, China	1997	78.42	4.5	Parabolic	Through	38.5	Obround	N/A	N/A	2000×1200	20
249	Nan Tang He Bridge	Zhe Jiang, China	2004	76.5	5	Parabolic	Through	32.5	Obround	40	345	2000×1200	20
250	Yu Rong Bridge	Fu Jian, China	1995	76	4	Parabolic	Half-through	28.4	Dumbbell	N/A	N/A	800	10
251	Shi Tang Wan Bridge	Jiang Su, China	2002	75	5	Parabolic	Through	N/A	Dumbbell	50	N/A	900	14
252	Tong Shan Bridge	Fu Jian, China	2003	75	5	Parabolic	Through	21	Dumbbell	40	345	800	12

No.	Name	Location	Year	Span (m)	*l*/*f*	Arch profile	Bridge type	Width (m)	Arch cross section				
									Shape	$f_{ck\text{-}cube}$ (MPa)	f_y (MPa)	*D* (mm)	t_s (mm)
253	Zheng Pu Bridge	Shang Hai, China	2003	75	5	Parabolic	Through	11.6	N/A	50	345	1000	16
254	Xian You Bridge	Fu Jian, China	2009	75	N/A	N/A	Half-through	N/A	N/A	N/A	N/A	N/A	N/A
255	Yin Jiang He Bridge	Jiang Su, China	1996	74	5.88	Parabolic	Through	13	Single circular	40	N/A	1000	20
256	Xing Chun Bridge[70]	Jiang Su, China	2004	73.5	4.38	N/A	Through	N/A	Three tube truss	N/A	N/A	N/A	N/A
257	Jian Bi Jing Hang Canal Bridge	Jiang Su, China	2001	72.8	5	Parabolic	Through	28.5	Single circular	40	235	900	16
258	Shi Mian Rainbow Bridge	Si Chuan, China	1996	72	N/A	Catenary	Half-through	N/A	Dumbbell	N/A	N/A	650	10
259	Yong Feng Bridge	Jiang Xi, China	1998	72	5	N/A	Through	32	Single circular	N/A	N/A	1400	14
260	Jian He Bridge	He Nan, China	2001	72	5	Parabolic	Through	15	Single circular	40	345	1200	16
261	Xi Tang Bridge	Zhe Jiang, China	2002	72	N/A	N/A	Through	N/A	N/A	40	345	N/A	N/A
262	Wei He Bridge	Shan Xi, China	2003	72	5	Parabolic	Through	26	Obround	40	N/A	1800×900	16
263	Mian Jiang Bridge	Jiang Xi, China	2004	72	5	Catenary	Through	36.1	Dumbbell	50	345	800	14
264	San Qiao Gang Bridge	Zhe Jiang, China	N/A	72	4.5	Parabolic	Through	N/A	Single circle	N/A	345	1600	10
265	Tang Qi Canal Bridge	Zhe Jiang, China	N/A	72	4.5	Parabolic	Through	N/A	Obround	40	N/A	1600×800	16
266	Bei Ta Bridge	Fu Jian, China	2000	70.3	3	Parabolic	Half-through	24.4	Dumbbell	50	N/A	900	16
267	Si Yang 2nd Bridge	Jiang Su, China	2002	70	5	Parabolic	Through	28.2	Single circle	50	345	1060	14

No.	Name	Location	Year	Span (m)	*l*/*f*	Arch profile	Bridge type	Width (m)	Arch cross section				
									Shape	$f_{ck\text{-}cube}$ (MPa)	f_y (MPa)	D (mm)	t_s (mm)
268	Xin He Bridge[71]	Jiang Su, China	2002	70	N/A	Parabolic	Through	40	Three tube truss	50	N/A	N/A	N/A
269	Long Chuan 2nd Bridge[45]	Jiang Su, China	2004	70	N/A	N/A	N/A	N/A	N/A	N/A	N/A	N/A	N/A
270	Hou Xi 1st Bridge[72]	Zhe Jiang, China	2008	70	N/A	Catenary	Half-through	N/A	Single circular	40	345	1200	20
271	N/A[73]	China	N/A	70	5	N/A	Through	N/A	Dumbbell	40	N/A	800	12
272	Xi Huan Road Yan Tang He Bridge	Jiang Su, China	N/A	70	N/A	N/A	Through	17.4	N/A	N/A	N/A	N/A	N/A
273	She Yang He Bridge	Jiang Su, China	1996	68.5	4	Parabolic	Through	13	Dumbbell	N/A	N/A	700	10
274	Overpass crossing Qing Yin Road	Shan Dong, China	N/A	68	4	Parabolic	Half-through	25	Dumbbell	40	N/A	750	12
275	Xin Dian Overpass[74]	Fu Jian, China	N/A	68	4	Parabolic	Half-through	12.3	Obround	N/A	N/A	1500×800	12
276	Dan Yang People Bridge	Jiang Su, China	1996	67.6	6	Parabolic	Through	14	Single circular	50	345	900	20
277	Arch bridge crossing the Brno-Vienna Expressway[75]	Czech Republic	1998	67.5	5.19	Circular	Deck	10.9	Single circular	N/A	N/A	900	30
278	Tai Xing Bridge[76]	Jiang Su, China	2007	67	4	Parabolic	Through	34	Dumbbell	40	345	850	16
279	Hulu Dazhihe Bridge[77]	Shang Hai, China	2004	66	5	N/A	Through	29.5	Rectangular	50	N/A	1500×1500	N/A
280	Jian Hu Bridge[78]	Jiang Su, China		65.6	5.42	Parabolic	Through	9.7	Single circular	50	235	1016	16

No.	Name	Location	Year	Span (m)	*l*/*f*	Arch profile	Bridge type	Width (m)	Arch cross section				
									Shape	$f_{ck\text{-}cube}$ (MPa)	f_y (MPa)	D (mm)	t_s (mm)
281	Pu Dong Canal Bridge[79]	Shang Hai, China	1997	65	5	N/A	Through	N/A	Dumbbell	40	N/A	550	10
282	Cai Hua Jing Bridge	Zhe Jiang, China	N/A	64.6	5.5	Parabolic	Through	40.5	N/A	N/A	N/A	N/A	N/A
283	Xi Shi Bridge	Zhe Jiang, China	1996	64	4	Parabolic	Half-through	27	Obround	N/A	N/A	1600×720	10
284	Lan Xi Bridge	Fu Jian, China	1997	64	3.2	Parabolic	Half-through	27.7	Dumbbell	N/A	N/A	750	10
285	Su Zhou He Bridge	Shang Hai, China	1998	64	4	Parabolic	Half-through	12.5	Obround	55	235	1200×700	16
286	Guang Hua Bridge	Guang Dong, China	2002	63.8	5	Parabolic	Through	23.4	Obround	50	345	1600×1200	14
287	Da Feng Overpass	Jiang Su, China	2005	63.1	4	Parabolic	Through	15.5	Dumbbell	50	N/A	800,700	14
288	Tun Xi Bridge	An Hui, China	1995	63	3.5	Parabolic	Through	27	Dumbbell	N/A	N/A	800	12
289	Xiao Yi He Bridge	Shan Dong, China	Under construction	62.7	N/A	N/A	N/A	17.8	N/A	50	N/A	N/A	N/A
290	Zui Liang Jiang Bridge	Zhe Jiang, China	2003	61.8	N/A	N/A	Through	N/A	N/A	N/A	N/A	N/A	N/A
291	Yao Jiang Bridge	Zhe Jiang, China	2003	61.8	N/A	N/A	Through	N/A	N/A	N/A	N/A	N/A	N/A
292	Xi Dao Kou Bridge	Ji Lin, China	2001	61	5	Parabolic	Through	13.6	Dumbbell	50	N/A	600	N/A
293	Xin An Bei Bridge	Jiang Su, China	1993	60	6	Parabolic	Through	15	Single circular	N/A	N/A	800	16
294	Hang Shen Xian Bridge	Zhe Jiang, China	2002	60	5	Parabolic	Through	30	Obround	40	345	1400×800	10
295	Xin Hui He Bridge	An Hui, China	2003	60	5	Parabolic	Through	20.8	Single circular	40	345	1000	12

No.	Name	Location	Year	Span (m)	*l*/*f*	Arch profile	Bridge type	Width (m)	Arch cross section				
									Shape	$f_{ck\text{-}cube}$ (MPa)	f_y (MPa)	D (mm)	t_s (mm)
296	E Hu Bridge[80]	Jiang Xi, China	2008	60	N/A	N/A	Through	N/A	N/A	N/A	N/A	N/A	N/A
297	Min Le Xin Bridge	Guang Dong, China	N/A	60	5	Parabolic	Through	22.5	Three tube truss	40	345	600	12
298	Sheng Li Qu Bridge	Xin Jiang, China	N/A	58	4.5	N/A	Half-through	13.45	Dumbbell	40	N/A	650	10
299	Dong Men Bridge	Fu Jian, China	1998	57.5	4	Parabolic	Half-through	N/A	Dumbbell	40	N/A	900	N/A
300	Dian Pu He Bridge[72]	Shang Hai, China	2005	55	4	Parabolic	Half-through	21.1	Rectangular	N/A	N/A	1500×1500	N/A
301	Huai Yin Canal 2nd Bridge	Jiang Su, China	1997	54.8	6	Parabolic	Through	8.8	Single circular	40	N/A	700	15
302	Lao Da He Bridge	Xin Jiang, China	2000	52	8	Catenary	Deck	25.5	Four tube truss	50	345	345	10
303	Gang Yue He Bridge	Jiang Su, China	2002	52	5	Parabolic	Through	20	Single circular	N/A	N/A	N/A	N/A
304	Yan Tang He Bridge	Jiang Su, China	1998	50	4	N/A	Through	14	Single circular	N/A	N/A	920	N/A
305	Zheng Chang Bridge	Jiang Su, China	2000	50	5	Circular	Through	N/A	Single circular	40	N/A	800	14
306	You Dun Gang Bridge[81]	Shang Hai, China	2003	50	3	N/A	Half-through	36.6	Rectangular	N/A	235	1500×1500	16
307	Guang Wu Kua Xian Footbridge[82]	Guang Dong, China	2010	50	5	Parabolic	Deck	4.5	Single circular	50	N/A	1200	16
308	Huan Shui He Bridge[83]	Qing Hai, China	2007	48	4.2	Parabolic	Through	10.8	Dumbbell	N/A	N/A	650	16
309	Bridge on Wuguang Road crossing Railway[84]	China		40	5	Parabolic	Through	12.9	Single circular	40	345	800	12

No.	Name	Location	Year	Span (m)	l/f	Arch profile	Bridge type	Width (m)	Arch cross section				
									Shape	$f_{ck\text{-}cube}$ (MPa)	f_y (MPa)	D (mm)	t_s (mm)
310	Bei Gang Bridge[85]	Liao Ning, China	2006	38	4	Parabolic	Through	13.5	Single circular	55	345	600	16
311	Bang Shan Ducao Bridge[86]	Guang Dong, China	2010	32.3	4	Parabolic	Through	7.8	Single circular	50	345	700	16
312	Wang Jia Ba Bridge[3]	Si Chuan, China	N/A	30	3	N/A	N/A	24	Single circular	N/A	N/A	N/A	N/A
313	Double Rainbow Bridge	Shang Hai, China	2009	N/A	N/A	N/A	N/A	N/A	N/A	N/A	N/A	N/A	N/A

REFERENCES

[1] Peng M. (2008). *The Research on the Design Parameters Optimization for Cable-stayed Arch Bridge*. Master Thesis, Hunan University of Science and Technology, Hunan, China. (in Chinese).

[2] Yang K. J., Li F. Q. & Zhang Y. L. (2008). Research on the Design of Large Span Deck Steel Tube Concrete Arch Bridge. *Journal of Railway Engineering Society,* No.12, 66-71. (in Chinese).

[3] Tang G. D., Xie L. L., Chen X. D., Liang S. X. & Mou C. Y. (1997). Cluster concrete filled steel tubular arch bridges. *Highway*. No. 4, 17-19. (in Chinese).

[4] Huang Z. Q. (2009). *Study on Arch Structure Optimization of Long-span CFST Arch Bridge*. Master Thesis. Chongqing Jiaotong University, Chongqing, China. (in Chinese).

[5] Zheng Y. W. (2008). *Simulation Analysis of the Songao Bridge's Stability and Dynamic Performance*. Master Thesis. Zhejiang University, Zhejiang, China. (in Chinese).

[6] Xu K. M., Zhang M. Z. & Wang J. (2008). Nonlinear Stability Analysis of Long-span CFST Arch Bridge under Construction. *Journal of Xian University of Architecture and Technology*. (Natural Science Edition), **40**, No.4, 556-560. (in Chinese).

[7] Su G. R. (2010). *Study on Condition Monitoring Scheme of Long Span Concrete-filled steel tube arch bridge*. Master Thesis. Chongqing Jiaotong University, Chongqing, China. (in Chinese).

[8] Zhang D. P. (2007). *Study on construction control of concrete-filled steel tubular arch bridge with long span*. Master Thesis. Chongqing University. Chong Qing, China. (in Chinese).

[9] Yang X. (2009). *Calculation Model of Concrete-filled Steel Tubular Arch Bridge*. Master Thesis. Chongqing Jiaotong University, Chongqing, China. (in Chinese).

[10] Wu Q. X., Chen B. C. & Takahashi. (2008). Nonlinear Seismic analysis of New Saikai Bridge. *Journal of Earthquake Engineering and Engineering Vibration*, **28**, No.5, 55-64. (in Chinese).

[11] Liang X. C. & Liang Z. X. (2009). Upper Structure Construction Technology of Lingnan Highway of Pushan. *Railway Standard Design,* 58-61. (in Chinese).

[12] Chen L. W. (2008). *Study on the Simulation Analysis of the Construction Control of Shen xingou Bridge*. Master Thesis. Wuhan University of Technology, Wuhan, China. (in Chinese).

[13] Zhao H. Q., Liu S. Z. & Wu W. H. (2006). Design of Qijiadu Yellow River Bridge. *Steel Construction*, **21**, No.4, 69-71. (in Chinese).

[14] Tang Z. (2009). *The Deflection caused by temperature or shrinkage and creep of continuous beam concrete-filled steel tubular arch bridge affects the track irregularity and the dynamic response of the vehicle-bridge system*. Master Thesis. Central South University, Hunan, China. (in Chinese).

[15] Liu R. & Liu C. (2008). Space Finite Element Analysis of Guiyang Highway 1 # bridge. *Railway Standard Design*, No.10, 35-38. (in Chinese).

[16] Chen Y. Q., Xing Y., Yang J. Q. & Hu Y. Q. (2007). Design of Long Span Half-Through Concrete Filled Steel Tube Arch Bridge. *World Bridges*, No.3, 18-20. (in Chinese).

[17] Qian W. H. (2009). *Finite Element Simulation Analysis of CFST Arch Bridge*. Master Thesis. Chang'an University, Shanxi, China. (in Chinese).

[18] Gai X. H. (2009). Study of the Arch Rib Section of Concrete-filled Steel Tube Tied Arch Bridge. *Railway Construction On Technology*, No.9, 27-29. (in Chinese).

[19] Yang D. Y. (2008). *Linear Optimization and Analysis of Structural Characteristics of Concrete Filled Steel Tubular Arch Bridge with Inverse Bending Arch*. Master Thesis. Chang'an University, Xi'an, China. (in Chinese). (in Chinese).

[20] Liu J. (2006). The Comparing of the Designs of Zengcheng Shitan Bridge. *Science Information,* No.7, 52. (in Chinese).

[21] Cao W. J. (2010). The Design of Guangzhou Zhuhai Railway Southwest Continuous Arch Bridge with 128 m. *Transportation Science & Technology*, No.3, 35-37. (in Chinese).

[22] Miao D. (2007). *Static and Dynamical Characteristics and TMD Damping Research of the Concrete Filled Steel Tubular Arch Bridge*. Master Thesis. Dalian University of Technology, Dalian, China. (in Chinese).

[23] Šavor Z. & Bleiziffer J. (2008). From melan patent to arch bridges of 400m spans. *Long arch bridges, Chinese-Croatian joint colloquium*, Brijuni Islands, Croatia, 349-356.

[24] Yu J. L. & Xu K. J. (1996) Upper Bridge Construction Technique of Zhongshan 2 #. *Science & Technology Academic Conference of the Bridge,* 222-227. (in Chinese).

[25] He J. J. & Chen X. L. (2004). The Design and Construction of the Tianzi Shan Concrete-filled Steel Tube Arch Bridge. *Journal of China & Foreign Highway*, **24**, No.6, 68-70. (in Chinese).

[26] Li F. K. (2009). *Stability Analysis of Concrete Filled Steel Tubular Arch Bridge*. Master Thesis. Hefei University of Technology, Hefei, China. (in Chinese).

[27] Gai H. H. (2007). *Study on Half-through and Deck-type Unsymmetrical Concrete-filled Steel Tube Arch Bridge*. Master

Thesis. Central South University, Hunan, China. (in Chinese).

[28] Xie K. Z., Lin H. Y. & Liang S. Z. (2010). A Method for Damage Detection of Concrete-filled Steel Tube Basket Handle Arch. *Journal of Guangxi University (Natural Science Edition)*, **35**, No.1, 96-100. (in Chinese).

[29] Zhao Y. S. (2007). *Design Optimization on Axial Cord of Concrete Filled Steel Tube Arch Bridge*. Master Thesis. Wuhan University of Technology, Wuhan, China. (in Chinese). (in Chinese).

[30] Yang Y. (2008). *Study on Three-arch Rib Concrete-filled Steel Tube Arch Bridge Construction Technique and Construction Control*. Master Thesis. Central South University, Hunan, China. (in Chinese).

[31] Cai G. F., Wang L. G., Zhu H. P. & Bian J. (2009). Analysis on Spatial Structure Stabilization of the Eastern Bridge. *Journal of Nanjing University of Technology. (Natural Science Edition),* **31**, No.6, 36-40. (in Chinese).

[32] Lian X. B. & Dong Y. X. (2009). Integral Installation Technology for Steel Tube Concrete Tied Arch of 120m Main span of Yanghe Bridge. *Technology of Highway and Transport,* No.4, 91-99. (in Chinese).

[33] Han S. L. (2009). Control Techniques of Fabrication and Assemblage of Crescent Arch. *Municipal Engineering Technology,* **27**, No. 6, 564-568. (in Chinese).

[34] Liu W. Y. (2010). Cable Erection Construction Technology of CFST Arch Bridge. *Northern Communications*, No.5, 95-98. (in Chinese).

[35] Lin Q. (2008). Design Conception of Sanming Chang'an YingSha Railway acrossing the Overpass. *China Water Transport*, **8**, No.8, 216-218. (in Chinese).

[36] Li Q., Tian X. M. & Zhang Q. H. (2003). A Model Test on Long-span X-style Tied Arch Bridge on Railway. *China Railway Science*, No.1, 88-93. (in Chinese).

[37] Zhang Y. Z. & Guo Y. P. (2008). Stability Analysis of Concrete-filled Steel Tubular Arch Bridge. *Science and Technology of West China*, **7**, No.28, 34-36. (in Chinese).

[38] Xiao R. C., Sun H. T., Jia L. J., Sun B., Chen L. & Fan X. L. (2004). Double X-shape Arch Bridge. *Shanghai Highway*,

22-27. (in Chinese).

[39] Shi C. T. (2009). Application of Concrete-filled Steel Tubular Arch Bridge on the sea. *Technological Application*, 38-40. (in Chinese).

[40] Li F. Q. & Wang Z. (2005). Structural Design of Main Bridge of Lhasa River Bridge. *Bridge Construction*, No.5, 8-12. (in Chinese).

[41] Chen H. (2009). *The Seismic Response Analysis of Concrete Filled Steel Tubular Arch Bridge*. Master Thesis. Chang'an University, Xi'an, China. (in Chinese).

[42] Song J. X. (2005). Construction Technology of Flexibly Tied Steel Pipe Concrete Arch. *Journal of Shijiazhuang Railway Institute*, **18**, 78-81. (in Chinese).

[43] Jin C. D. (2006). Design and Construction of Concrete Filled Steel Tubular Arch Bridge with Prestressed Concrete Tied bars. *Shanghai Highways*, 1-6. (in Chinese).

[44] Lin Z. M. (2009). Research of Care and Maintenance System for Long-span Concrete-filled Steel Tubular Arch Bridges. *Fujian Architecture & Construction*, No.10, 110-114. (in Chinese).

[45] Fan W. Q. (2008). *The Design Parameters Analysis of the Double X-arch Bridge*. Master Thesis. Chang'an University, Xi'an, China. (in Chinese).

[46] Li M. G. (2008). Study on Concrete-filled Steel Tube Arch Bridge Construction Control. *Journal of Liaoning Provincial College of Communications*, **10**, No. 1, 4-6. (in Chinese).

[47] Guo Y. F. (2007). Research of the Inclination Angle Effect on the Internal Force Distribution of Lift-basket CFST Arch Bridge. *Fujian Architecture & Construction*, No. 11, 39-40. (in Chinese).

[48] Wang T. (2009). *Research on Static and Dynamic Load Test of CFST Arch Bridge*. Master Thesis. Chang'an University, Xi'an, China. (in Chinese).

[49] Li W. B. (2010). Study on the Construction Technique of Bowstring Arch Bridge across Hui River in Beijing-Shanghai

High-speed Railway. *Bridge and Tunnel Engineering,* 72-77. (in Chinese).

[50] Li B. (2008). *Research on Seismic Action Based Concrete-filled Steel Tube Arch Bridge of High-speed Railway Bridge Vibration*. Master Thesis. Central South University, Hunan, China. (in Chinese).

[51] Lin. L. Q. (2009). Study on the Anti-corrosive and Anti-rust Construction Technology of the Steel Tubular Arch Bridge. *Shanxi Architecture*, **35**, No. 2, 156-158. (in Chinese).

[52] Xu J. L., Zheng Z. J. & Xiang M. S. (2008). Analysis of Effect of Uncertain Factors on Reliability of Concrete-filled Steel Tube Arch Bridge with Collar Beam. *Computer and Communications,* 107-110. (in Chinese).

[53] Yuan W. G., Liu M. Y. & Sun X. D. (2009). Distinctive Design of Overpass Arch Bridge on the Highway from Guangzhou to Wuzhou. *The World of Building Materials,* **30**, No. 5, 109-114. (in Chinese).

[54] Li N. (2009). *Research on Calculating Methods of Concrete Filled Steel Tubular Arch Bridge*. Master Thesis. Wuhan University of Technology, Wuhan, China. (in Chinese).

[55] Jin C. D. (2006). Design and construction of concrete filled steel tubular arch bridge with prestressed concrete tied bars. *Shanghai Highways*. No. 99, 1-6. (in Chinese).

[56] Zhang J. J. (2009). *Concrete-filled Steel Tube Arch Bridge Construction Technology in the Application of the Third Bridge of Xiping*. Master Thesis. Chang'an University, Xi'an, China. (in Chinese).

[57] Zhang D. Q., Zhang P., Sun W. M., Sun L. & Luo R. (2007). Analysis Research on Shock Absorption Effect on CFST Arch Bridge with Damping Support. *Journal of Disaster Prevention and Mitigation Engineering*, **27**, supplement, 266-271. (in Chinese).

[58] Yu Y. Y. (2002). Construction of prestressed reinforcement and suspending bar of steel pipe concrete through arch bridge. *Construction Technology*. **31**, No. 7, 24-25. (in Chinese).

[59] Zhou C. L. (2007). *Construction Monitoring of Concrete Filled Steel Tube Tied Arch Bridge*. Master Thesis. Nanjing Forestry University, Nanjing, China. (in Chinese).

[60] Huang Z. H., Tao N. C., Zhang W. J. & Zhang D. W. (2010). Analysis of steel tube stress in course of pouring concrete of steel tube concrete arch bridge. *Bridges & Structures*. No. 3, 52-54. (in Chinese).

[61] Fan W. X. (2006). *Optimization and Structure Analysis of the Construction Procedure for Concrete-filled Steel Tubular Arch Bridge*. Master Thesis. Zhejiang University, Zhejiang, China. (in Chinese).

[62] Wang J. (2009). *Steel Tube Reinforced Concrete Arch Bridge Simulation Analysis During the Perfusion Construction Stage*. Master Thesis. Xi'an University of Architecture and Technology, Xi'an, China. (in Chinese).

[63] Li Z. X. (2009). Stability Analysis of Single Concrete-filled Steel Tubular Arch Bridge. *Industrial Construction,* **39**, supplement, 616-619. (in Chinese).

[64] Liu F. (2009). *Finite Element Simulation Analysis of Concrete Filled Steel Tubular Arch Bridge Construction Technology*. Master Thesis. Hubei University of Technology, Hubei, China. (in Chinese).

[65] Luo H. F. (2008) Design of Bowstring Arch Bridge for Sandiantang Bridge. *Urban Roads Bridges & Flood Control*, No. 10, 78-81. (in Chinese).

[66] Yang N. Y. (2009). *Study on the Balance about Tied Bar to the Pier Horizontal Thrust of Concrete-Filled Steel Tube "Fly-Bird-Type" Arch Bridge*. Master Thesis. Chang'an University, Xi'an, China. (in Chinese).

[67] Guo Z. H. (2008). *The Analysis of Foot of Concrete-filled Steel Tubular Arch Bridge*. Master Thesis. Nanjing Forestry University, Nanjing, China. (in Chinese).

[68] Liu B. (2008). Effect of concrete pouring sequence on dumbbell concrete-filled steel tube arch bridge. *Modern Transportation Technology*. **5**, No. 2, 39-42. (in Chinese).

[69] Liu B. D. (2009). *Dynamic characteristic study of under-supported concrete-filled steel tube tied arch bridge*. Master Thesis. Xi'an University of Architecture and Technology, Xi'an, China. (in Chinese).

[70] Xiao R. C., Sun H. T., Jia L. J., Sun B., Chen L. & Fan X. L. (2004). Double X-shape Arch Bridge. *Shanghai Highway*, 22-27. (in Chinese).

[71] Zhang X. Y., Chen S. J. & Kong F. L. (2004). Construction for Double Basket Type Concrete Steel Pipe Tied Arch Bridge. *East China Highway,* No. 1, 24-26.

[72] Yang M. Z. (2009) *Concrete-filled Steel Tubular Arch Bridge Construction Boom Tension Control Analysis and Optimization*. Master Thesis. Chang'an University, Xi'an, China. (in Chinese).

[73] Zhang Y. (2007). Steel tube concrete arch hardness value's influence on motive feature. *Shanxi Architecture*. **33**, No. 20, 71-73. (in Chinese).

[74] Zhang J. (2007). Design of Xin Dian Overpass. *Science and Technology Consulting Herald,* No. 25, 41-42. (in Chinese).

[75] Strasky J., Nazratil J. & Susky S. (2001). Applications of time-dependent analysis in the design of hybrid bridge structures. *PCI Journal*. **46**, No. 4, 56-74.

[76] Yuan X. Y. (2006). *Research on the Design and Calculation Method of an X-Shaped Arch Bridge*. Master Thesis. Nanjing Forestry University, Nanjing, China. (in Chinese).

[77] Li F. K. (2009). *Stability Analysis of Concrete Filled Steel Tubular Arch Bridge*. Master Thesis. Hefei University of Technology, Hefei, China. (in Chinese).

[78] Wang S. M., Qian Z. D. & Chen J. B. (2006). Stress Analysis of Arch Rib of Jianhu Arch Bridge on Monitoring. *Journal of University of Science and Technology of Suzhou(Engineering and Technology)*, **19**, No. 2, 10-13. (in Chinese).

[79] Han L. H. Some recent applications and researches in concrete-filled steel tubular structures. http://www.paper.edu.cn, 1-17. (in Chinese).

[80] Chen J. H. (2007). Technology Research on Arch Rib Construction of Concrete-filled Steel Tubular Arch Bridge. *Chinese and Overseas Architecture*, 113-116. (in Chinese).

[81] Jin C. D. (2006). Design and Construction of Concrete Filled Steel Tubular Arch Bridge with Prestressed Concrete Tied bars. *Shanghai Highways,* 1-7. (in Chinese).

[82] Liu M. Y., Gong K., Sun X. D. & Yuan W. G. (2009). Dynamic Characteristics Analysis of Single Rib Braces CFST Arch

Bridge. Journal of *Wuhan University of Technology (Transportation Science & Engineering)*, **33,** No. 6, 1104-1107. (in Chinese).

[83] Zhang X., Wu Y. P. & Chen W. (2009). Static Load Test of Xiaxiahuangshui River Steel Pipe Concrete Arch Bridge at Lanqing Railway Line. Journal of *Changzhou Institute of Technology,* **22**, No .6, 1-3. (in Chinese).

[84] Xie X. (2008). *Static and Dynamic Characters Analysis On Through Concrete-filled Steel-tabular Arch Bridge*. Master Thesis. Southwest Jiaotong University, Sichuan, China. (in Chinese).

[85] Chen Z. C. (2007). Construction of Concrete-filled Steel Tabular Arch Bridge. *Railway Engineering,* No. 3, 36-38. (in Chinese).

[86] Yuan W. G., Liu M. Y. & Sun X. D. (2009), Distinctive Design of Overpass Arch Bridge on the Highway from Guangzhou to Wuzhou. *The World of Building Materials,* **30**, No. 5, 109-112. (in Chinese).

APPENDIX II CONCRETE MODELS

II.1. EC2 MODEL

Creep:

$$J(t,t_0)=\frac{1}{E_c(t_0)}+\frac{\phi(t,t_0)}{1.05\times E_{ci}} \tag{II-1}$$

where

$$E_{ci}=E_{c0}\left[f_{cm28}/f_{cm0}\right]^{0.3} \tag{II-2}$$

$$E_{c0}=2.2\times10^4 \tag{II-3}$$

$$f_{cm0}=10 \tag{II-4}$$

$$E_c(t)=\beta_E(t)E_{ci} \tag{II-5}$$

$$\beta_E(t)=\left[\beta_{cc}(t)\right]^{0.3} \tag{II-6}$$

$$\beta_{cc}(t)=\exp\left\{s\left[1-\left(\frac{28}{t/t_1}\right)^{1/2}\right]\right\} \tag{II-7}$$

$$t_1=1 \tag{II-8}$$

$$\phi(t,t_0)=\phi_{RH}\cdot\beta(f_{cm28})\cdot\beta(t_0)\cdot\beta_c(t-t_0) \tag{II-9}$$

$$\phi_{RH}=\begin{cases}1+\dfrac{1-RH/100}{0.1(h)^{1/3}} & \text{for } f_{cm28}\le 35\text{MPa}\\ \left[1+\dfrac{1-RH/100}{0.1(h)^{1/3}}\cdot\alpha_1\right]\cdot\alpha_2 & \text{for } f_{cm28}>35\text{MPa}\end{cases} \tag{II-10}$$

$$h=\frac{2A_c}{u} \tag{II-11}$$

$$\beta(f_{cm28})=\frac{16.8}{f_{cm28}^{\ 0.5}} \tag{II-12}$$

$$\beta(t_0) = \frac{1}{0.1 + (t_{0,c} / t_1)^{0.2}} \tag{II-13}$$

$$t_{0,c} = t_{0,T} \cdot \left[\frac{9}{2 + t_{0,T}^{1.2}} + 1 \right]^{\alpha} \geq 0.5 \tag{II-14}$$

For $0°C \leq T \leq 80°C$

$$t_{0,T} = t_0 \tag{II-15}$$

For $T<0°C$ or $T>80°C$

$$t_{0,T} = \sum_{i=1}^{n} \Delta t_i \cdot \exp\left[13.6 - \frac{4000}{273 + T(\Delta t_i)} \right] \tag{II-16}$$

$$\alpha = \begin{cases} -1 & \text{for cement Class S} \\ 0 & \text{for cement Class N} \\ 1 & \text{for cement Class R} \end{cases} \tag{II-17}$$

$$\beta_c(t - t_0) = \left[\frac{(t - t_0)/t_1}{\beta_H + (t - t_0)/t_1} \right]^{0.3} \tag{II-18}$$

For $f_{cm28} \leq 35MPa$

$$\beta_H = 150\left[1 + \left(1.2\frac{RH}{100} \right)^{18} \right]\frac{h}{100} + 250 \leq 1500 \tag{II-19}$$

For $f_{cm28} \geq 35MPa$

$$\beta_H = 150\left[1 + \left(1.2\frac{RH}{100} \right)^{18} \right]\frac{h}{100} + 250 \cdot \alpha_3 \leq 1500 \cdot \alpha_3 \tag{II-20}$$

$$\alpha_1 = \left[\frac{35}{f_{cm28}} \right]^{0.7} \quad \alpha_2 = \left[\frac{35}{f_{cm28}} \right]^{0.2} \quad \alpha_3 = \left[\frac{35}{f_{cm28}} \right]^{0.5} \tag{II-21}$$

Shrinkage:

$$\varepsilon_{ca}(t) = \beta_{as}(t) \cdot \varepsilon_{ca}(\infty) \tag{II-22}$$

where

$$\beta_{as}(t) = 1 - \exp\left(-0.2t^{0.5}\right) \tag{II-23}$$

$$\varepsilon_{ca}(\infty) = 2.5(f_{cm28} - 18) \times 10^{-6} \tag{II-24}$$

The input data necessary to perform calculation are:

- f_{cm28} mean 28-day standard cylinder compression strength [MPa]
- s coefficient related to the type of cement
- RH relative humidity expressed as percentage
- A_c section cross area [mm^2]
- u section perimeter [mm]
- t age of concrete [days]
- t_0 age of concrete at loading [days]
- α power which depends on type of cement
- t_s age of the concrete at the beginning of drying shrinkage, normally at the end of curing [days].

Note:

If experimental value of f_{cm28} is not available, it can be calculated by the following equation:

$$f_{cm28} = f_{ck28} + \Delta f \quad \Delta f = 8 \tag{II-25}$$

which is considered as a part of the model formulation.

II.2. MC90 MODEL

Creep:

$$J(t,t_0) = \frac{1}{E_c(t_0)} + \frac{\phi(t,t_0)}{E_{ci}} \tag{II-26}$$

where

$$E_{ci} = E_{c0}\left[f_{cm28} / f_{cm0}\right]^{1/3} \tag{II-27}$$

$$E_{c0} = 2.15 \times 10^4 \tag{II-28}$$

$$f_{cm0} = 10 \tag{II-29}$$

$$E_c(t_0) = \beta_E(t_0) E_{ci} \tag{II-30}$$

$$\beta_E(t_0) = [\beta_{cc}(t_0)]^{0.5} \tag{II-31}$$

$$\beta_{cc}(t_0) = \exp\left\{ s\left[1 - \left(\frac{28}{t_0/t_1} \right)^{1/2} \right] \right\} \tag{II-32}$$

$$t_1 = 1 \tag{II-33}$$

$$\phi(t,t_0) = \phi_{RH} \cdot \beta(f_{cm28}) \cdot \beta(t_0) \cdot \beta_c(t-t_0) \tag{II-34}$$

$$\phi_{RH} = 1 + \frac{1 - RH/100}{0.46(h/h_0)^{1/3}} \tag{II-35}$$

$$h = \frac{2A_c}{u} \tag{II-36}$$

$$h_0 = 100 \tag{II-37}$$

$$\beta(f_{cm28}) = \frac{5.3}{(f_{cm28}/f_{cm0})^{0.5}} \tag{II-38}$$

$$\beta(t_0) = \frac{1}{0.1 + (t_{00}/t_1)^{0.2}} \tag{II-39}$$

$$\beta_c(t-t_0) = \left[\frac{(t-t_{00})/t_1}{\beta_H + (t-t_{00})/t_1} \right]^{0.3} \tag{II-40}$$

$$\beta_H = 150\left[1 + \left(1.2\frac{RH}{100} \right)^{18} \right]\frac{h}{h_0} + 250 \le 1500 \tag{II-41}$$

$$t_{00} = t_{0,T} \cdot \left[\frac{9}{2 + t_{0,T}^{1.2}} + 1 \right]^{\alpha} \ge 0.5 \tag{II-42}$$

For $-20°C \le T \le 40°C$

$$t_{0,T} = t_0 \tag{II-43}$$

For $-20°C \le T \le 40°C$

$$t_{0,T} = \sum_{i=1}^{n} \Delta t_i \cdot \exp\left[13.65 - \frac{4000}{273 + T(\Delta t_i)} \right] \tag{II-44}$$

$$\alpha = \begin{cases} -1 & \text{for SL} \\ 0 & \text{for N and R} \\ 1 & \text{for RS} \end{cases} \tag{II-45}$$

SL, N, R, and RS stands for slowly hardening, normal, rapid hardening and rapid hardening high strength cements, respectively, same infra.

Shrinkage:

$$\varepsilon_{cs}(t) = \varepsilon_s(f_{cm28}) \cdot \beta_{RH} \cdot \beta_s(t - t_s) \tag{II-46}$$

where

$$\varepsilon_s(f_{cm28}) = \left[160 + 10\beta_{sc}\left(9 - \frac{f_{cm28}}{f_{cm0}} \right) \right] \times 10^{-6} \tag{II-47}$$

$$\beta_{sc} = \begin{cases} 4 & \text{for SL} \\ 5 & \text{for N and R} \\ 8 & \text{for RS} \end{cases} \tag{II-48}$$

$$\beta_{RH} = \begin{cases} -0.25 & \text{for } RH \geq 99\% \\ 1.55\left[1 - \left(\frac{RH}{100} \right)^3 \right] & \text{for } 40\% \leq RH < 99\% \end{cases} \tag{II-49}$$

$$\beta_s(t - t_s) = \left[\frac{(t - t_s)/t_1}{350(h/h_o)^2 + (t - t_s)/t_1} \right]^{0.5} \tag{II-50}$$

The input data necessary to perform calculation are:

- f_{cm28} mean 28-day standard cylinder compression strength [MPa]
- s coefficient related to the type of cement
- RH relative humidity expressed as percentage
- A_c section cross area [mm^2]
- u section perimeter [mm]
- t age of concrete [days]
- t_0 age of concrete at loading [days]
- t_s age of the concrete at the beginning of drying shrinkage, normally at the end of curing [days].

Note:

If experimental value of f_{cm28} is not available, it can be calculated by the following equation:

$$f_{cm28} = f_{ck28} + \Delta f \quad \Delta f = 8 \tag{II-51}$$

which is considered as a part of the model formulation.

II.3. AFREM MODEL

Creep:

$$J(t,t_0)=\frac{1}{E_c(t_0)}+\frac{\phi_b(t,t_0)}{E_{i28}} \tag{II-52}$$

where

$$E_c(t)=\beta_E(t)E_{ci} \tag{II-53}$$

$$\beta_E(t)=\left[\beta_{cc}(t)\right]^{0.5} \tag{II-54}$$

$$\beta_{cc}(t)=\exp\left\{s\left[1-\left(\frac{28}{t/t_1}\right)^{1/2}\right]\right\} \tag{II-55}$$

$$t_1=1 \tag{II-56}$$

$$\phi_b(t,t_0)=\phi_{b0}\frac{\sqrt{t-t_0}}{\left[\sqrt{t-t_0}+\beta_{bc}\right]} \tag{II-57}$$

$$\phi_{b0}=\begin{cases}\dfrac{3.6}{f_c(t_0)^{0.37}} & \text{for silica-fume concrete}\\ 1.4 & \text{for non silica-fume concrete}\end{cases} \tag{II-58}$$

$$\beta_{bc}=\begin{cases}0.37\exp\left(2.8\dfrac{f_c(t_0)}{f_{ck28}}\right) & \text{for silica-fume concrete}\\ 0.40\exp\left(3.1\dfrac{f_c(t_0)}{f_{ck28}}\right) & \text{for non silica-fume concrete}\end{cases} \tag{II-59}$$

$$f_c(t)=\frac{t}{1.4+0.95t}f_{ck28} \tag{II-60}$$

$$E_{i28}=E_{c0}\left[\left(f_{ck28}+\Delta f\right)/f_{cm0}\right]^{1/3} \tag{II-61}$$

$$E_{c0}=2.15\times10^4 \tag{II-62}$$

$$\Delta f=8 \tag{II-63}$$

$$f_{cm0} = 10 \tag{II-64}$$

Shrinkage:

For t<28days

$$\varepsilon_{ca}(t) = \begin{cases} 0 & \text{for } \dfrac{f_c(t)}{f_{ck28}} < 0.1 \\ \left(f_{ck28} - 20\right)\left(2.2\dfrac{f_c(t)}{f_{ck28}} - 0.2\right)\times 10^{-6} & \text{for } \dfrac{f_c(t)}{f_{ck28}} \geq 0.1 \end{cases} \tag{II-65}$$

For t≥28days

$$\varepsilon_{ca}(t) = \left(f_{ck28} - 20\right)\left[2.8 - 1.1\exp(-t/90)\right]\times 10^{-6} \tag{II-66}$$

The input data necessary to perform calculation are:

f_{ck28} standard cylinder concrete characteristic compressive strength at 28 days [MPa]

s coefficient related to the type of cement

RH relative humidity expressed as percentage

t age of concrete [days]

t_0 age of concrete at loading [days]

Note:

$E_c(t)$ and E_{i28} are calculated according to the provisions from model CEB-FIP (1993)

If mean 28-day standard cylinder compression strength (f_{cm28}) is available, f_{ck28} is calculated by the formula suggested by CEB-FIP (1993):

$$f_{ck28} = f_{cm28} - \Delta f \quad \Delta f = 8 \tag{II-67}$$

which is considered as a part of the model formulation.

II.4. B3 MODEL

Creep:

$$J(t,t_0) = q_1 + C_o(t,t_0) \tag{II-68}$$

where

$$q_1 = 0.6\times 10^6 / E_{28} \tag{II-69}$$

$$E_{28} = 4734\sqrt{f_{cm28}} \tag{II-70}$$

$$C_o(t,t_0) = q_2 Q(t,t_0) + q_3 \ln\left[1+(t-t_0)^{0.1}\right] + q_4 \ln(t/t_0) \tag{II-71}$$

$$q_2 = 185.4c^{0.5} f_{cm28}{}^{-0.9} \tag{II-72}$$

$$q_3 = 0.29(w/c)^4 q_2 \tag{II-73}$$

$$q_4 = 20.3(a/c)^{-0.7} \tag{II-74}$$

$$Q(t,t_0) = Q_f(t_0)\left[1+\left(\frac{Q_f(t_0)}{Z(t,t_0)}\right)^{r(t_0)}\right]^{-1/r(t_0)} \tag{II-75}$$

$$Q_f(t_0) = \left[0.086(t_0)^{2/9} + 1.21(t_0)^{4/9}\right]^{-1} \tag{II-76}$$

$$Z(t,t_0) = \begin{cases} (t_0)^{-0.5}\ln\left[1+(t-t_0)^{0.1}\right] & \text{for } t \neq t_0 \\ (t_0)^{-0.5}\ln\left[1+(\Delta t)^{0.1}\right] & \text{for } t = t_0 \end{cases} \tag{II-77}$$

$$\Delta t = 10^{-4} t_0 \tag{II-78}$$

$$r(t_0) = 1.7(t_0)^{0.12} + 8 \tag{II-79}$$

The input data necessary to perform calculation are:

- f_{cm28} mean 28-day standard cylinder compression strength [MPa]
- t age of concrete [days]
- t_0 age of concrete at loading [days]
- w water content of concrete mix [kg/m^3]
- c cement content of concrete mix [kg/m^3]
- a aggregate content of concrete mix [kg/m^3]

Note:

The autogenous shrinkage here is assumed to be small enough to be neglected.

APPENDIX III MATERIAL PARAMETERS

III.1. STEP-BY-STEP PROCEDURE

$$E_{c1k} = \frac{2}{J(t_k,t_k)+J(t_k,t_{k-1})} \tag{III-1}$$

$$E_{c2kj} = \begin{cases} \dfrac{J(t_k,t_1)-J(t_k,t_0)}{J(t_k,t_k)+J(t_k,t_{k-1})} & \text{for } j=0 \\ \dfrac{J(t_k,t_{i+1})-J(t_k,t_{i-1})}{J(t_k,t_k)+J(t_k,t_{k-1})} & \text{for } j=1,\ldots,k-1 \end{cases} \tag{III-2}$$

III.2. EFFECTIVE MODULUS (EM) METHOD

$$E_{c1k} = \frac{E_c(t_0)}{1+\varphi(t_k,t_0)} \tag{III-3}$$

$$E_{c2k} = 0 \tag{III-4}$$

III.3. MEAN STRESS (MS) METHOD

$$E_{c1k} = \frac{2}{J(t_k,t_k)+J(t_k,t_0)} \tag{III-5}$$

$$E_{c2k} = \frac{J(t_k,t_k)-J(t_k,t_0)}{J(t_k,t_k)+J(t_k,t_0)} \tag{III-6}$$

III.4. AGE-ADJUSTED EFFECTIVE MODULUS (AAEM) METHOD

$$E_{c1k} = \frac{E(t_0)}{1+\chi(t_k,t_0)\cdot\varphi(t_k,t_0)} \tag{III-7}$$

$$E_{c2k} = \varphi(t_k,t_0)\cdot\frac{\chi(t_k,t_0)-1}{1+\chi(t_k,t_0)\cdot\varphi(t_k,t_0)} \tag{III-8}$$

The input data necessary to perform calculation are:

t_k age of concrete at step k [days]

t_0 age of concrete at loading [days]

$\varphi(t_k, t_0)$ creep coefficient representing the ratio of the creep strain at time t_k over the elastic strain at time t_0

$\chi(t_k, t_0)$ aging coefficient

Based on Bazant & Baweja (2000)

$$\chi(t_k,t_0) = \frac{E_c(t_0)}{E_c(t_0)-\dfrac{0.992}{J(t_k,t_0)}+\dfrac{0.115}{J(t_m,t_m-1)}\cdot\left[\dfrac{J(t_m,t_0)}{J(t_k,t_m)}-1\right]} - \frac{1}{\varphi(t_k,t_0)} \tag{III-9}$$

$$t_m = \frac{(t_k+t_0)}{2} \tag{III-10}$$

Based on Brooks & Neville (1976)

$$\chi(t_k,t_0) = \frac{1}{1-e^{-[0.09+0.686\varphi(t_k,t_0)]}} - \frac{1}{\varphi(t_k,t_0)} \tag{III-11}$$

APPENDIX IV CROSS-SECTIONAL PROPERTIES

$$AE_j = \int_{A_c} E_{c1j}\,\mathrm{d}A + \int_{A_s} E_s\,\mathrm{d}A + \sum_{a=1}^{n_r}\int_{A_{r(a)}} E_{r(a)}\,\mathrm{d}A = A_c E_{c1j} + A_s E_s + \sum_{a=1}^{n_r} E_{r(a)} A_{r(a)} \qquad \text{(IV-1)}$$

$$BE_j = \int_{A_c} yE_{c1j}\,\mathrm{d}A + \int_{A_s} yE_s\,\mathrm{d}A + \sum_{a=1}^{n_r}\int_{A_{r(a)}} yE_{r(a)}\,\mathrm{d}A = B_c E_{c1j} + B_s E_s + \sum_{a=1}^{n_r} y_{r(a)} E_{r(a)} A_{r(a)} \qquad \text{(IV-2)}$$

$$IE_j = \int_{A_c} y^2 E_{c1j}\,\mathrm{d}A + \int_{A_s} y^2 E_s\,\mathrm{d}A + \sum_{a=1}^{n_r}\int_{A_{r(a)}} y^2 E_{r(a)}\,\mathrm{d}A = I_c E_{c1j} + I_s E_s + \sum_{a=1}^{n_r} y_{r(a)}^2 E_{r(a)} A_{r(a)} \qquad \text{(IV-3)}$$

The input data necessary to perform calculation are:

A_c	cross-sectional area of concrete [mm^2]
B_c	the first moment of area to the x-axis for concrete [mm^3]
I_c	the second moment of area to the x-axis for concrete [mm^4]
A_s	cross-sectional area of steel tubes [mm^2]
B_s	the first moment of area to the x-axis for steel tubes [mm^3]
I_s	the second moment of area to the x-axis for steel tubes [mm^4]
E_{c1j}	defined in Appendix III